Rudder, Propeller and Hull Interaction by RANS

Claus D. Simonsen

PhD thesis

May 2000

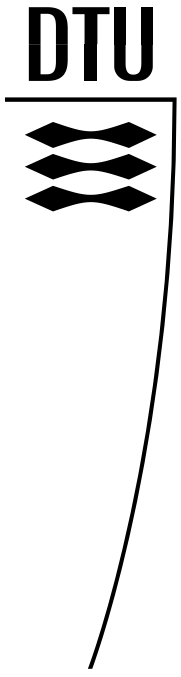

DEPARTMENT OF
NAVAL ARCHITECTURE
AND OFFSHORE ENGINEERING

Rudder, Propeller and Hull Interaction by RANS

Claus Daniel Simonsen

DEPARTMENT OF NAVAL ARCHITECTURE AND OFFSHORE ENGINEERING
TECHNICAL UNIVERSITY OF DENMARK · LYNGBY
APRIL 2000

Department of Naval Architecture and Offshore Engineering
Technical University of Denmark
Studentertorvet, Building 101E, DK-2800 Kongens Lyngby
Denmark
Phone +45 4525 1360, Telefax +45 4588 4325
e-mail ish@ish.dtu.dk, Internet http://www.ish.dtu.dk/

Published in Denmark by
Department of Naval Architecture and Offshore Engineering
Technical University of Denmark

Publication Reference Data

Simonsen, C. D.
Rudder, Propeller and Hull Interaction by RANS.
PhD thesis.
Department of Naval Architecture and Offshore Engineering
Technical University of Denmark
ISBN 87-89502-33-7

Preface

This thesis is submitted as a partial fulfillment of the requirements for the Danish Ph.D. degree and as part of the Danish Industrial Ph.D. Fellowship Programme administered by the Committee on Industrial Ph.D. Fellowship under the Danish Academy of Technical Sciences (ATV). The work was carried out at the Department of Naval Architecture and Offshore Engineering, the Technical University of Denmark, and at the Danish Maritime Institute in Lyngby, Denmark, during the period of February 1997 to April 2000.

The study was financially supported by the Danish Maritime Institute and by the Danish Agency for Trade and Industry under the Ministry of Business and Industry. This support is gratefully acknowledged.
Also the support granted by the Ministry of Research through the Danish Natural Science Research Council, which made it possible to apply the super computer facilities at Uni•C in Lyngby, is gratefully acknowledged.

During the study Professor Fred Stern gave me the opportunity to visit the Iowa Institute of Hydraulic Research at the University of Iowa. A very inspiring period - I thank the staff of the department for their help and kindness during my stay in Iowa.

Thanks to my colleagues at the University and at the Danish Maritime Institute, friends and family, and especially to my supervisors Poul Andersen from the University and Jakob Buus Petersen from Danish Maritime Institute, for invaluable help and support.

Claus Daniel Simonsen
Lyngby, April 25, 2000

This page is intentionally left blank.

Executive Summary

In an attempt to increase the safety at sea more attention has been focused on the requirements of the education of the officers sailing the ships and of the maneuverability of the ships. This has of course increased the interest in the numerical maneuvering simulators, which are a strong tool for investigation of the maneuverability of the ship and for the training of the crew members. Consequently, the increased interest has resulted in stronger requirements of the quality, accuracy and reliability of the maneuvering models behind the simulators. The simulators are doing well today, but there are still areas where additional knowledge could be useful to improve the models. One of these areas is the interaction between the rudder, propeller and hull, which plays an important role for successful modeling of the maneuvering problem.

Today the state of the art in maneuvering simulation covers the full mission simulators based on numerical solution of the equations of motion in conjunction with experimental hydrodynamic data which is mainly determined by means of captive model testing techniques like the planar motion mechanism (PMM). A study of the maneuvering model and the PMM model testing technique applied to the data generation revealed that a comprehensive set of experimental input data was required in order to perform a maneuvering simulation and model the rudder, propeller and hull interaction.
As regards the rudder, propeller and hull interaction there are two approaches which can be applied to the study of the interaction effects: The first consists of systematic experimental parameter studies of the hydrodynamic forces. However, since the investigation is carried out at the integral level, this approach provides information about how the forces vary, but it does not provide information about what actually causes the interaction. The second approach is a detailed numerical study of the flow patterns. This approach gives the data lacking in the first approach, which can probably help to understand better the complex flow phenomena. In order to exemplify the first approach and to provide an experimental basis for a numerical investigation, i.e. the second approach, a full PMM test program was designed and a PMM test was carried out in the towing tank at the Danish Maritime Institute with a model of the tanker Esso Osaka. Some of the results for the straight-ahead sailing model condition were used to determine basic interaction effects like the hull-on-propeller and hull-on-rudder interaction, represented by the effective wake fraction and the rudder-on-hull interaction found by means of the local and global rudder forces.

The application of numerical methods to investigation of maneuvering related flow problems is rather new. A few inviscid methods based on potential theory have been applied, but when viscous effects are to be included, very little information is available.

Since the objective was to study the local flow features it was necessary to apply the latter type of method, which included real fluid effects. Therefore, all the numerical calculations were performed by use of the CFD code CFDSHIP-IOWA, developed at the Iowa Institute of Hydraulic Research at the University of Iowa. The CFD code is a so-called RANS code, which is based on solution of the Reynolds-averaged Navier-Stokes equations. The turbulence was modeled by the isotropic algebraic Baldwin Lomax turbulence model, while the effect of the propeller was represented by a prescribed body force distribution calculated from the Hough-Ordway model. By use of this type of numerical method the purpose was to investigate the future possibility of applying a RANS code to maneuvering related flows. Thus, it could be studied if the integral quantities, i.e. the hydrodynamic forces acting on the rudder and the hull, could be determined numerically and if knowledge of the flow pattern could be gained, which might be used to improve the maneuvering models.

Initially, it was attempted to generate a complete model including the rudder, propeller and hull in one step, but it was not possible to obtain a converged solution due to the complexity and size of the model. Instead a new stepwise procedure was proposed. It covered: 1) 2-D rudder profile, 2) 3-D rudder in free stream, 3) 3-D rudder behind a propeller, 4) bare hull, 5) hull with rudder and 6) hull with rudder and propeller. However, due to the time limitations of the project it was impossible to finish items 5 and 6.

In the 2-D rudder profile case, the flow around an NACA0012 profile was calculated for different angles of attack and different Reynolds numbers. The computed lift and drag were compared with experimental data and fair agreement was found if the experiments were performed with leading edge roughness. Finally, the method was verified by means of a grid study and validated at a 10 % level for the zero rudder angle case.

In the study of the rudder in free stream, the flow was calculated around two NACA0020 rudders with different aspect ratios at different rudder angles and a Reynolds number equal to 0.4 million. The computations showed a tendency to over-predict the lift coefficient by 2 to 16 percent when compared with experimental and empirical data. The largest deviation was detected for the experimental data, but it was partly caused by differences between the boundary conditions for the numerical and the experimental model. Concerning the drag, the calculations were generally in fair agreement with the empirical expression, while the agreement with the experiments to a large degree seemed to depend on the applied leading edge roughness. The effect of changing the aspect ratio was also reflected in the numerical results, which showed that if the aspect ratio was increased, the lift curve slope increased accordingly, while the drag coefficient was relatively unaffected. As regards the field quantities, the code appeared to be capable of capturing the gross features of the rudder flow with respect to reversed flow and the vortex developing at the tip of the rudder. As in the 2-D case, the calculation was verified and validated at a 11 % level for the zero rudder angle case.

In the case of the rudder behind the propeller, the flow around the same two rudders as in the free stream case was calculated numerically for 12 different combinations of rudder angles and propeller loads. The propeller was represented by a prescribed body force distribution. As to the interaction effects between the rudder and the propeller, the study showed that the presence of the propeller increased the axial velocity over the part of the rudder placed in the slipstream, and that it introduced a swirl in the flow which changed the local angle of attack over the rudder. Consequently, the magnitude of the pressure and the suction peaks on the rudder surface was increased over the part of the

rudder in the slipstream, resulting in increased lift compared to the free stream rudder. The propeller also seemed to help drive the cross flow around the tip, even though the effect was reduced when the aspect ratio was increased and the tip was moved away from the slipstream. Regarding the forces on the rudder, the increased aspect ratio caused the drag to decrease, while the lift was relatively unaffected. The numerical integral quantities were compared with experimental data and the numerical method was capable of giving a reasonable estimate of the lift, while the drag was predicted too low. Moreover, it was found that with the grid resolution applied in this study, the method would give a qualitative picture of the flow patterns in the rudder-propeller flow, but that the grid needed to be redistributed in order to investigate if the forces could be calculated more accurately.

Finally, the flow around the tanker Esso Osaka was calculated in model scale on the assumption that the free surface could be neglected and a mirror image applied instead. The limiting streamlines, the pressure distribution on the hull surface and the axial velocity contours and cross flow vectors at the propeller plane were compared with other experimentally visualized tanker flows, and qualitative agreement with the numerical results was generally found. A resistance test was carried out on the model of the Esso Osaka and the experimental resistance was compared with the calculated data. The comparison showed that the numerical method underpredicted the resistance. The deviation was probably caused by three factors: First the omission of the free surface, second the insufficient grid resolution and third the insufficiency of the applied Baldwin-Lomax turbulence model.

This page is intentionally left blank.

Synopsis

Som et led i bestræbelserne på at øge sikkerheden til søs, er man i løbet af de seneste år begyndt at fokusere mere på krav til øget træning af de officerer, som sejler skibene samt på krav til selve skibets manøvreevne. Dette har naturligvis øget interessen for de numeriske manøvresimulatorer, som på billig og sikker måde dels giver mulighed for at undersøge skibenes manøvreevne, og dels giver mulighed for at træne officerernes sejlfærdigheder i forskellige kritiske situationer. Konsekvensen af den øgede interesse for simulatorerne har naturlivis også været skrappere krav til kvaliteten, præcisionen og pålideligheden af manøvremodellerne, som ligger til grund for simulatorerne. Set i relation til disse krav klarer simulatorerne sig generelt fint i dag, men der findes dog stadig områder inden for hvilke, der ønskes mere viden for eventuelt at kunne forbedre modellerne. Et af disse områder dækker vekselvirkningen mellem ror, propeller og skrog, som spiller en vigtig rolle for, at man er i stand til at løse manøvreproblemerne på en tilfredsstillende måde.

De mest avancerede metoder inden for manøvresimulering dækker i dag de såkaldte "full mission" simulatorer, som er baseret på numerisk løsning af skibets bevægelsesligninger sammen med en lang række hydrodynamiske kræfter, som hovedsageligt er bestemt eksperimentelt i slæbetanken ved hjælp af forskellige modelforsøgsteknikker som for eksempel Planar-Motion-Mechanism-(PMM-)teknikken. I forbindelse med dette viste et studium af en sådan eksisterende manøvremodel samt af PMM-teknikken, der bruges til generering af inputdata til simulatoren, at der på nuværende tidspunkt kræves et omfattende sæt af eksperimentelle data for, at man kan gennemføre en simulering og samtidig modellere vekselvirkningen mellem ror, propeller og skrog.
Set i relation til denne vekselvirkning synes der at eksistere to fremgangsmåder, som kan anvendes ved en nærmere undesøgelse af vekselvirkningseffekterne. Den første involverer systematiske, eksperimentelle parameterstudier af de hydrodynamiske kræfter. Da en sådan fremgangsmåde udføres på integralt niveau, det vil sige på kraftniveau, giver den information om, hvordan kræfterne varierer men ikke om de fænomener i selve strømningen, der opstår i forbindelse med vekselvirkningen. Den anden fremgangsmåde består af et detaljeret numerisk studium af selve strømningen. Denne fremgangsmåde skulle i teorien give den detaljerede information om strømningen, som manglede i det første tilfælde, og den skulle herved gøre det muligt at øge forståelsen af det komplekse strømningsfænomen. For at eksemplificere den første fremgangsmåde og for at skabe en eksperimentel basis for den numeriske undersøgelse, det vil sige den anden fremgangsmåde, blev der udarbejdet et komplet PMM-testprogram og et PMM-forsøg blev efterfølgende udført i slæbetanken på Dansk Maritimt Institut i Lyngby med en model af tankskibet Esso Osaka. Nogle af

forsøgsresultaterne for modellen i en kondition svarende til ligeudsejlads blev derefter brugt til bestemmelse af nogle af de grundliggende vekselvirkningseffekter. Disse dækkede effekter hidrørende fra "skrog-på-ror"- og "skrog-på-propeller"-vekselvirkning repræsenteret ved medstrømskoefficienten samt "ror-på-skrog"-vekselvirkning, som blev fundet ud fra de lokale og globale rorkræfter.

Anvendelsen af numeriske metoder i forbindelse med undersøgelse af manøvrerelaterede strømningsproblemer for skibe er relativ ny. Nogle få inviskose potentialteoretiske metoder har være anvendt, men når det kommer til metoder, som medtager viskose effekter, er brugen meget begrænset. Da ideen med nærværende projekt blandt andet var at undersøge de lokale strømningsfænomener, var det nødvendigt at bruge en af de sidstnævnte metoder for at kunne modellere vandets virkelige egenskaber. Alle beregningerne præsenteret i dette projekt er defor foretaget med CFD-koden CFDSHIP-IOWA, som er udviklet på Iowa Institute of Hydraulic Research, University of Iowa i USA. CFD-koden hører til de såkaldte RANS-koder, der er baseret på løsning af de Reynolds-midlede Navier-Stokes-ligninger og turbulensen blev modelleret med den isotrope algebraiske Baldwin-Lomax turbulensmodel. I de tilfælde, hvor effekten af en propeller i strømningen var krævet, blev denne modelleret ved hjælp af en foreskreven volumenkraftfordeling beregnet ud fra en model foreslået af Hough og Ordway. Det kan i denne forbindelse også nævnes, at da manøvrerelaterede strømninger som sagt er et relativt nyt anvendelsesområde for denne type numeriske metode, var ideen udover det detaljerede strømningsstudium også at undersøge, om det ad numerisk vej var muligt at bestemme de integrale størrelser, det vil sige de hydrodynamiske ror- og skrogkræfter, som bruges til input til simulatoren.

Til at begynde med blev det i ét step forsøgt at opbygge en komplet numerisk model, som indeholdt både ror, skrog og propeller. Det viste sig dog efter nogen tid, at det ikke var muligt at opnå en konvergeret løsning på grund af størrelsen og kompleksiten af modellen. I stedet blev det besluttet at nedbryde problemet i mindre dele, som dækkede følgende delopgaver: 1) 2D rorprofil, 2) 3D ror i fristøm, 3) 3D ror bag propeller, 4) skrog alene, 5) skrog med ror og endelig 6) skrog med ror og propeller. Det bør nævnes, at det på grund af projektets tidslige begrænsning ikke var muligt at færdigøre 5) og 6).
Med hensyn til strømningen omkring 2D rorprofilet blev denne beregnet for forskellige indfaldsvinkler og Reynoldstal. De beregnede løft- og modstandskoefficienter blev herefter sammenlignet med eksperimentelle værdier, og det viste sig, at der var pæn overensstemmelse, hvis eksperimentet var udført med ruhedskorn på ledende kant. Endelig blev metoden verificeret ved hjælp af et netstudium og bagefter valideret på et 10% niveau for tilfældet med nul graders indfaldsvinkel.
For tilfældet med ror i fristrøm, blev strømningen beregnet omkring to ror bestående af samme NACA0020 profil men med forskellige sideforhold. Rorene blev undersøgt ved forskellige rorvinkler, mens Reynoldstallet blev holdt konstant lig 0.4 millioner. Beregningerne viste en tendens til at give løftkoefficienter der var 2 til 16% for høje ved sammenligning med eksperimentelle og empiriske data. De største afvigelser blev observeret for de experimentelle værdier, men dette kunne delvis forklares ved forskelle i randbetingelserne for den eksperimentelle og numeriske model. Med hensyn til modstandskoefficienterne, gav beregningerne resultater, som generelt var i god overensstemmelse med de empiriske data. For de eksperimentelle datas vedkommende, afhang overensstemmelsen i høj grad af de anvendte ruhedskorn på den ledende kant af

roret. Effekten af ændringer i rorets sideforhold, blev også reflekteret i de numeriske beregninger. For løftkoefficientens vedkommende førte en øgning af sideforholdet til en øget hældning af løftkurven, mens modstandskoefficienten ikke viste nogen markant ændring. Endelig kan det nævnes at med hensyn til feltstørrelserne, det vil sige hastigheder og tryk, lod det til, at den numeriske metode var i stand til at prediktere overordnede karakteristika i strømningen såsom hvirvlen omkring tippen af roret og reverseret strømning på sugesiden af roret. Som det var tilfældet for det todimensionelle rorprofil, blev rorberegningen også verificeret og valideret på et 11% niveau for tilfældet med nul graders rorvinkel.
Med hensyn til den numeriske ror-propeller konfiguration, blev strømningen omkring de samme to ror som i fristrømstilfældet beregnet for ialt 12 forskellige rorvinkler og propellerbelastninger og som nævnt tidligere, blev propelleren repræsenteret ved en foreskreven volumenkraftfordeling. Set i relation til vekselvirkningen mellem roret og propelleren viste beregningerne, at tilstedeværelsen af den arbejdende propeller dels øgede strømningshastigheden over den del af roret, som befandt sig i propellerstrålen, og dels introducerede en rotation i strømningen, som ændrede den lokale indfaldsvinkel over roret. Konsekvensen var, at størrelsen af de lokale trykmaksima og -minima øgedes, hvilket resulterede i en øget løftkraft sammenlignet med roret i fristøm. Udover dette lod det også til, at propelleren hjalp med til at drive strømningen omkring tippen af roret, selvom denne effekt blev reduceret, når tippen blev flyttet væk fra propellerstrålen ved at ændre sideforholdet på roret. Set i relation til kræfterne på roret, bevirkede en forøgelse af sideforholdet at modestandskoefficienten blev mindre, mens løftkoefficienten forblev relativ uændret. Ved sammenligning af de numeriske løft- og modstandskoefficienter med eksperimentelle værdier viste det sig, at den numeriske metode kunne give et rimeligt bud på løftkraften, mens modstanden var for lille. Sluttelig blev det fundet, at det med den anvendte netfinhed ville være muligt at give et kvalitativt billede af strømningsmønsteret omkring roret, men også at netpunkterne på roret burde fordeles anderledes for at undersøge, om kræfterne på roret kunne beregnes mere præcist.
Endelig blev strømningen omkring skroget af tankeren Esso Osaka beregnet i modelskala under antagelsen om, at den frie overflade kunne negligeres og erstattes af en symmetribetingelse. Bagefter blev strømlinierne over skroget samt trykfordelingen på skrogoverfladen plus de aksielle hastighedskonturer og crossflow-vektorerne over et tværskibsplan svarende til propellerpositionen sammenlignet med eksperimentelt visualiserede strømninger for to andre tankskibsmodeller. Sammenligningen viste, at den aktuelle beregning rent kvalitativt forudsagde de samme karakteristika, som var observeret for de to andre strømninger. Med hensyn til skrogets slæbemodstand, blev der udført et modstandsforsøg ved en modelkondition svarende til den beregnede, og den målte modstand blev sammenlignet med den beregnede. Det viste sig, at den numeriske metode beregnede en modstand, som var mindre end den målte, hvilket kunne skyldes tre faktorer, nemlig udeladelsen af den frie overflade, følsomhed overfor netfinhed samt den relativt simple Baldwin-Lomax turbulensmodel.

Man kan konkludere, at med hensyn til anvendelse af viskose numeriske metoder til beregning af manøvrerelaterede strømningsproblemer omkring skibe har de et potentiale i fremtiden, selvom de er beregningsmæssigt krævende. Det er ikke sandsynligt, at de i nærmeste fremtid vil kunne konkurrere med modelforsøget med hensyn til generering af de omfattende sæt af hydrodynamiske inputdata, som simulatorene kræver. Det er muligt, at metoderne kan beregne de integrale størrelser korrekt, men dette kræver

nærmere studier i form af verificering og validering. Potentialet i metoderne ligger indenfor visualisering af strømningen, hvor de er i stand til at fange de detaljerede strømningsmønstre og herved kan være med til at øge forståelsen omkring de komplekse strømningsfænomener.

Contents

List of Nomenclature

A	Characteristic area
A^+	Closure coefficient
A_C	Characteristic lateral underwater area of ship
A_e	Expanded area of propeller disk
A_P	Area of propeller disk
A_R	Lateral rudder area
A_S	Area of portion of rudder in propeller slipstream
B_{mld}	Moulded breadth
C	Inflow velocity
C_A	Allowance factor
C_b	Block coefficient
C_{cp}	Closure coefficient
C_D	Drag coefficient
C_{D0}	Frictional rudder drag coefficient
$C_{\varepsilon i}$	Closure coefficients, i=1, 2
C_F	Non-dimensional force coefficient
C_f	Frictional resistance coefficient
C_{fx}	Numerically calculated frictional x-force component
C_f^m	Frictional resistance coefficient for model
C_f^s	Frictional resistance coefficient for ship
C_G	Correction factor applied for verification
C_{Kleb}	Closure coefficient
C_L	Lift coefficient
C_M	Non-dimensional moment coefficient
C_p	Pressure coefficient, pressure resistance coefficient
C_{ppx}	Numerically calculated pressure x-force component
C_Q^*	Non-dimensional propeller torque
C_q	Resistance coefficient accounting for the shape of the rudder tip
C_R	Residual resistance coefficient
C_T	Resistance coefficient
C_T^*	Non-dimensional propeller thrust

C_{Th} Thrust loading coefficient
C_{totx} Numerically calculated total *x*-force component
C_{toty} Numerically calculated total *y*-force component
C_X Non-dimensional resistance coefficient
C_{wk} Closure coefficient
C_{YP}^* Non-dimensional propeller force in *y*-direction
C_{YR} Non-dimensional rudder lift force in *y*-direction
C_{YR}^{Global} Non-dimensional rudder lift force in *y*-direction measured on ship
C_{YR}^{Local} Non-dimensional rudder lift force in *y*-direction measure on rudder
C_{iR} Non dimensional rudder force coefficient, $i = X, Y, N$
$C_{i\beta}$ Non-dimensional drift force coefficient, $i = X, Y, N$
$C_{i\gamma}$ Non-dimensional yaw force coefficient, $i = X, Y, N$
$C_{i\beta\gamma}$ Non-dimensional yaw-drift cross-coupling force coefficient, $i=X, Y, N$
CF_∞ Fitted numerical solution at infinite number of iterations
D Propeller diameter, rudder drag force, experimental data
E Comparison error
F Force
F_D Relaxation force
$F_{fric,x}$ Computed frictional *x*-force component
F_{Kleb} Intermittence function
$F_{press,x}$ Computed pressure *x*-force component
$F_{tot,x}$ Computed total *x*-force component
Fn Froude number
Fn_0 Froude number at approach speed
Fn_{Lwl} Froude number based on the length of the ship at the waterline
F_{wk} Wake function
J Advance coefficient
J_T Advance coefficient for propeller in open water
J_V Advance coefficient for propeller behind ship
K Turbulent kinetic energy
K_Q Torque coefficient
K_T Thrust coefficient
L Length of the ship, rudder lift force
L_C Characteristic length of the ship
L_{PP} Length between perpendiculars
L_{WL} Length of ship in waterline
M Moment
N Yaw moment
N_0 Nominal number of propeller revolutions at self propulsion
N_{PMM} Number of revolution of the PMM equipment
N_{tot} Total number of computational cells
P Non-dimensional mean pressure

P/D Propeller pitch ratio
$P_{0.7}/D$ Propeller pitch ratio at 0.7 R_P
P_G Estimated order of accuracy of numerical method
P_{th} Theoretical order of accuracy of numerical method
Q Propeller torque
R Model tow resistance
Re Reynolds number
Re_{eff} Effective Reynolds number
Re_k Roughness based Reynolds number
RES_ϕ Residual, ϕ=*u*, *v*, *w*, *p*
R_G Grid convergence ratio
R_h Radius of propeller hub
R_p Radius of propeller
S Wetted surface area, simulated data
S_C Numerical benchmark
S_L Lower limit of oscillating solution
S_m Wetted surface area of the model
S_U Upper limit of oscillating solution
T Propeller thrust, time interval, true value
T_m Mean draught of the ship
T_r Taper ratio
U Total ship speed, uncertainty, free stream velocity
U_0 Approach speed to manoeuvre
U_C Carriage speed during model tests
U_{diff} Velocity difference
U_D Experimental data uncertainty
U_E Uncertainty of comparison error
U_G Grid uncertainty
U_{G1} Grid uncertainty of fine grid
U_{G2} Grid uncertainty of medium grid
U_I Iterative uncertainty
U_{mean} Axial mean velocity in propeller slipstream
U_{reqd} Required level of validation
U_S Simulation uncertainty
U_{SM} Simulation modeling uncertainty
U_{SN} Simulation numerical uncertainty
U_V Validation uncertainty
X Force in *x*-direction
V Characteristic velocity, model speed
V_m Model approach speed
$\boldsymbol{V}$ Instantaneous velocity vector
Y Force in *y*-direction

Y_H	Non-dimensional propeller hub radius
Z	Number of blades on propeller
a	Characteristic arm
a_H	Interaction coefficient describing the rudder-on-hull interaction
b	Geometric span of double rudder model
b_e	Effective span of double rudder model
c	Rudder cord
c_f	Local frictional coefficient
c_m	Mean rudder cord
c_n	Sectional normal force coefficient
c_p	Local pressure coefficient
c_r	Rudder cord at root
c_t	Rudder cord at tip
f_{bi}	Body force term, $i = x, \theta$
g	Acceleration of gravity
$\boldsymbol{g}$	Vector of acceleration of gravity
h	Water depth, width of wind tunnel, fine grid spacing
k	Form factor, diameter of roughness grain
k_m	Factor accounting for variation of the propeller slipstream diameter
l	Mixing length, turbulent length scale, arc length of rudder profile
l_{mix}	Mixing length in Cebeci-Smith and Baldwin-Lomax turbulence models
n	Number of propeller revolutions, iteration parameter
p	Instantaneous pressure, non-dimensional mean pressure
$\hat{p}$	Non-dimensional Piezometric pressure
$\overline{p}$	Mean pressure
p'	Pressure fluctuation
p_∞	Reference pressure
r	Yaw rate
r_G	Grid refinement factor
$\dot{r}$	Yaw acceleration
r'	Non-dimensional yaw rate
r^*	Non-dimensional propeller radius
s	Rudder span
t	Thrust deduction fraction, time
t_0	Thrust deduction fraction at self propulsion point, time
u	Surge velocity, non-dimensional mean velocity component in x-direction
$\underline{u}$	Surge velocity difference
$\dot{u}$	Acceleration in x-direction
u'	Non-dimensional surge velocity
$\underline{u'}$	Non-dimensional surge velocity difference
u_a	Effective axial advance velocity at propeller
u_e	Velocity on the edge of the boundary layer
u_i	Instantaneous and non-dimensional mean velocity components, i = 1,2,3
$\overline{u}_i$	Mean velocity components, i = 1,2,3

u_i'	Fluctuating velocity components, i = 1,2,3
u_P	Longitudinal ship velocity component at propeller
u_s	Propeller slipstream velocity
Δu_∞	Slipstream velocity increment far downstream
v	Sway velocity, non-dimensional mean velocity component in y-direction
$\dot{v}$	Acceleration in y-direction
v'	Non-dimensional sway velocity
v^*	Wall friction velocity
v_P	Transverse ship velocity component at propeller
w	Effective wake fraction, non-dimensional mean velocity component in z-direction
w_0	Effective wake fraction at self propulsion point
Δx	Thickness of propeller disc in RANS grid
x_H	Change of longitudinal center of pressure due to rudder-on-hull interaction
x_i	Cartesian coordinates, i = 1,2,3
x_P	Propeller x-coordinate in the ship's coordinate system
x_R	Rudder x-coordinate in the ship's coordinate system
y	Wall distance
y_m	Position of change between inner and outer eddy viscosity formulation
y^+	Non-dimensional wall distance
y_P	Propeller y-coordinate in the ship's coordinate system
y_R	Rudder y-coordinate in the ship's coordinate system

Greek letters

Δ	Displacement
Λ	Geometric aspect ratio of rudder
Λ_e	Effective aspect ratio of rudder
α	Closure coefficient, angle of attack
β	Drift angle, twist angle in propeller slipstream
β'	Propeller loading angle
β^*	Hydrodynamic pitch angle
β_P	Local drift angle at propeller
β_{Re}	Local drift angle at rudder
$\beta_{R\beta}$	Local drift angle at rudder due to drift
$\beta_{R\gamma}$	Local drift angle at rudder due to yaw
β_{theory}	Theoretical twist angle in propeller slipstream
δ	Geometric rudder angle, boundary layer thickness
δ_D	Error of experimental data
δ_e	Effective rudder angle
δ_G	Grid error
δ_{G1}	Grid error of fine grid

δ_{ij}	Kronecker delta
δ_I	Iterative error
$\delta_{\max}$	Maximal rudder angle
$\delta_{RE,G}$	First order estimate of grid error
$\delta_{RE,G1}$	First order estimate of grid error for fine grid
$\delta_{RE,G2}$	First order estimate of grid error for medium grid
δ_S	Error of simulation
δ_{SM}	Simulation modeling error
δ_{SN}	Simulation numerical error
δ^*	Displacement thickness
ε	Dissipation of turbulent kinetic energy, relative change of solution
ε_{21}	Change of solution between medium and fine grids
ε_{32}	Change of solution between coarse and medium grids
κ	Correction for longitudinal variation of axial velocity in propeller slipstream, closure coefficient
γ	Yaw velocity angle, intermittence function
η	Non-orthogonal curvilinear coordinate
ξ	Rudder loading angle, non-orthogonal curvilinear coordinate
μ	Viscosity of fluid
ν	Kinematic viscosity of fluid
ν_t	Eddy viscosity
ν_{ti}	Inner layer eddy viscosity
ν_{to}	Outer layer eddy viscosity
ω	PMM frequency, vorticity
ρ	Fluid density
σ_ε	Closure coefficient
σ_K	Closure coefficient
τ_{ij}	Fluid stress tensor
τ_w	Wall shear stress
ζ	Non-orthogonal curvilinear coordinate

Subscripts used at forces and moments (*X*, *Y* and *N*)

0	Constant term in Taylor expansion of the forces
AC	Hydrodynamic force from acceleration
H	Hydrodynamic force from hull
HPR	Hydrodynamic force from hull-propeller-rudder interaction
P	Hydrodynamic force from propeller
R	Hydrodynamic force from rudder
Fn	Force due to tow resistance
$\dot{u}, \dot{v}, \dot{r}$	Derivation with respect to acceleration
u, v, r	Derivation with respect to velocity

β	Force or moment due to drift
γ	Force or moment due to yaw
$\beta\gamma$	Force or moment due to cross-coupling between yaw and drift
δ	Derivation with respect to rudder angle

This page is intentionally left blank.

Chapter 1

Introduction

1.1 Overview and Background

Since transportation of goods by ships over long distances is the cheapest transport method available today, the traffic at sea is expected to increase all over the world in the coming years. Of course, this expectation has enhanced the focus on the possibilities of improving the safety at sea, which among other things depends on the maneuverability of the ships and the skills of the officers sailing them.
Both shipowners and shipyards have been affected by the requirements of improved safety, so tools are needed which can be applied to solution of maneuvering related problems. Furthermore, IMO (The International Maritime Organization) has adopted a standard of the maneuverability of ships leading to requirements for prediction of the maneuverability of ships even before they are built. However, it is common to all the affected parties that they focus on a technically well founded method for simulation of the maneuverability of ships, which is both reliable and accurate. Thus, even though the ship simulators today are considered as an efficient tool for education of cadets, in-service training and investigation of the maneuverability of the ship, there is still a need for improving the mathematical models in order to satisfy the requirements made by the users and maritime organizations.

Historically, the maneuvering simulation was initiated in the 1960s when Professor Abkowitz, who was one of the pioneers in the prediction of ship maneuverability, at the Danish Maritime Institute first measured the forces acting on the ship as a function of its motions and then integrated the equations of motion to provide the path of the ship, while it performed some predefined standard maneuvers. In the following years, the mathematical models and the experimental techniques were improved, but the method applied to solution of the equations of motion was the same. Therefore, this work continued until the late 1970s where the introduction of computers made it possible to develop a maneuvering simulator enabling simulations in real time. This increased the interest in the simulators and in the 1980s and the 1990s much effort was spent on research and development in numerical maneuvering models. Consequently, maneuvering simulators are used all over the world today and they are all able to describe the maneuverability of ships at a general level. Most of the mathematical models behind the simulators are based on more or less empirical methods, consisting of

experience gained in the place where they are developed. The input data of the models is obtained partly from captive model testing techniques and partly from databases with information about maneuvering coefficients or full-scale maneuvers.
The quality of the maneuvering models depends primarily on two factors: 1) The complexity of the model, i.e. the number of independent variables and the way they are composed, and 2) the quality of the input data to the model. Regarding the complexity of the model, the rudder-propeller-hull interaction is important, due to its influence on the generality of the maneuvering model and the accuracy of the simulated results. However, the interaction phenomenon between rudder, propeller and hull, which occurs in the complex flow around the ship, is not yet fully understood, so additional knowledge is required in order to improve the maneuvering models.
Most of the simulator input data and the influence of the interaction effects on the maneuverability are today primarily known from experimental work, where relations between the rudder, propeller and hull forces are measured and analyzed. However, numerical methods begin to appear and much effort is spent on the establishment of numerical methods, which can describe the flow around sailing ships. The work covers research into methods for determination of propeller efficiency and cavitation, of the resistance of the ship where the influence of the propeller on the hull is included and of the response of the ship due to waves, other ships, quays etc., and it generally seems that progress and promising results are obtained in all the areas. Concerning maneuvering related flow problems, effort is also spent on the development of methods for description of the maneuverability of ships and progress is observed, but the results may not yet be as promising as in the other areas mentioned above. In the report from the 21st International Towing Tank Conference (ITTC96), the Committee on Maneuvering concluded that promising results had been obtained. But it also concluded that these methods cannot determine the forces, acting on the hull during maneuvering, with sufficient accuracy for ships with special hull forms, so that work has still to be done in this area.

1.2 Objectives and Scope of the Work

The present work is focused on application of numerical methods to investigation of the interaction effects between the rudder, propeller and hull in connection with numerical maneuvering simulation. In summary, the objectives of the project are as follows:

- Investigation of the possibility of generating a complete numerical rudder, propeller and hull model, by means of an existing numerical method. In theory the current method should be able to model the problem, but the application to maneuvering related flow problems is new, so more knowledge of this area is useful.

- A systematic study of the details of the flow in order to provide information about the rudder, propeller and hull related flow phenomena, which can hopefully help to understand the rudder, propeller and hull interaction better, and which possibly can be used to improve the mathematical maneuvering model.

- Investigation of the possibility of numerical data generation to the simulator. Since simulator data today is mainly generated by means of experiments, it is interesting to

investigate if the numerical methods can determine the hydrodynamic forces with enough accuracy to be used in the simulator.

The results of the work are described in the present thesis, which consists of 14 Chapters divided into two parts. The first part, which covers Chapters 2 to 5, focuses on different aspects of maneuvering simulation to give an overview forming a basis for the numerical flow study. The work is initiated by a presentation of the results from a literature study given in Chapter 2. The study is intended as an overview of different methods applied for maneuvering simulation in order to define state of the art in maneuvering simulation. The overall study is followed by a more detailed study of an advanced maneuvering model in Chapter 3 and a study of the experimental method applied to data generation to the simulator in Chapter 4. The purpose is to investigate how the rudder, propeller and hull interaction is modeled in the mathematical maneuvering model and to identify the necessary experimental data for the model and study how it is generated. Thus, it should be possible to identify a relevant flow situation, which can be applied to the numerical interaction study and possibly also to a future investigation with respect to experimental uncertainty assessment which is important in relation to validation of numerical methods. The uncertainty assessment is not treated in this context. Finally, the results of a PMM model test are presented in Chapter 5, as an illustration of some of the interaction effects and in order to generate experimental data to be used as a basis for the numerical study.

The second part of the work, consisting of Chapters 6 to 13, deals with the topics related to the flow study, which is based on a numerical method including real fluid effects. Since the work is based on a so-called RANS method, Chapter 6 gives a general description of the methodology, but it also deals with the practical application of viscous numerical methods in order to describe the status of the use of this kind of method in ship related flow problems.

Since the results from the RANS method are sensitive to many parameters, it is difficult to judge the accuracy of the calculated results by direct comparison with experimental data. Therefore, Chapter 7 is dedicated to a description of a methodology, which systematically quantifies the errors and uncertainties, for the purpose of verification and validation of the numerical method.

Finally, the CFD code concerned is briefly described with respect to numerical model, boundary conditions and propeller model in Chapter 8 together with the pre- and post-processing tools.

The computational work starts in Chapter 9, where the initial work on the complete rudder, propeller and hull model is described. Besides, a stepwise procedure for modeling of the problem is proposed in order to obtain the experience of grids and limitations of the method necessary for completion of the model.

The first step in the proposed procedure is a study of the flow around a two-dimensional rudder profile as described in Chapter 10. This work is followed by a study of the flow around a rudder in free stream in Chapter 11, where the flow is studied and experience of the rudder model is gained before the propeller is included. The rudder related work is continued in Chapter 12, where the rudder is placed behind a propeller and the flow around and the interaction between the two components are studied. Finally, the bare hull is dealt with in Chapter 13 to gain knowledge of the performance of the code when applied to a ship’s geometry.

The thesis is rounded off by Chapter 14, in which the drawn conclusions are presented together with recommendations for future work.

Chapter 2

State of the Art in Maneuvering Simulation

2.1 Introduction

When a maneuvering simulation or prediction is performed different approaches can be applied depending on the complexity and the type of the simulation, which can for instance be general maneuvers or the set of standard maneuvers proposed by IMO. In the present chapter the different approaches will be presented and discussed briefly to give an overview of the methods available for maneuvering prediction at the present time of writing. A literature study of state of the art methods for maneuvering simulation, led to three approaches for the purpose of maneuvering simulation: The free-running model test, maneuvering prediction on the basis of databases and finally numerical simulation. These three approaches are briefly described below.

2.2 Free-running Model Test

The free-running model test is used to determine the maneuvering performance of a ship during standard maneuvers like zigzag and turning tests by letting a free-sailing model carry out the maneuver. The method has the advantage of providing the maneuvering motion directly and it is still used today. However, the method has also some disadvantages. First, it requires a large maneuvering basin so it is difficult to perform the test in the traditional narrow towing tank. Second, the free-running model test gives information, which enables the naval architect to determine whether a given design is suitable or not. But in case improvements are required, it does not say anything about the reason for the observed behavior. Third, it is difficult to avoid scale effects during the free-running model test, since the relatively thick boundary layer around the model, compared to the ship, changes the inflow field to the propeller and results in model propeller and rudder forces which are not in agreement with the full-scale quantities. The problem can be reduced by means of relaxation, which is an additional force helping the propeller to move the ship. However, since the model is free, it is not easy to apply the extra force. More information about the free-running model test, is found in Crane et. al. (1989) and the references listed there.

2.3 Databases

Databases are often used for estimation of the maneuvering performance of a ship in the design phase. The method does not require a physical model of the ship, as existing model test or full scale data is to be used as a basis for estimation of maneuvering characteristics of the new ship. As regards the database concept two approaches can be adopted. The first is to estimate the hydrodynamic forces acting on the ship and then use them in a simulation as explained later. The second is to use databases containing the maneuvering characteristics such as the head reach, the tactical diameter, the overshoot angle etc. If these parameters are grouped by ship type, size, displacement etc. it should be possible to estimate the maneuvering performance of the new ship, when its type, size etc. are known. Data for maneuvering parameters can be found in Landsburg et al. (1983) and in Jensen and Martinussen (1987).

2.4 Numerical Simulation

The third approach, which can be applied to maneuvering simulation, comprises the numerical methods, usually including two activities. One of course concerns calculation of the motion of the ship, found by solving the equations of motion. The other concerns determination of the external forces acting on the ship during the maneuver, since these forces are necessary to solve the equations of motion. The numerical approach is widely used today and it is described below.

2.4.1 Solution of the Equations of Motion

Generally, simulation of a maneuvering ship is based on solution of the equations of motion, which describe the motions of the ship as a function of the external hydrodynamic forces. Some years ago, it was difficult to handle the equations, since they could not be solved analytically for practical applications. However, later the development of fast and powerful computers has made it possible to solve the equations of motion numerically in the time domain and thus give a description of the time history of the position, velocity and acceleration of the ship.
The equations of motion, for instance found in Abkowitz (1964), make it possible to couple 6, 4 or 3 degrees of freedom (DOF) at a time by locking 0, 2 or 3 degrees of freedom in the general 6-DOF system of equations. Most of the methods used for maneuvering simulation are based on the 3-DOF system, which couples surge, sway and yaw motions. The simplification inherent in the use of a 3-DOF system is acceptable for maneuvering simulation of most cargo ships as long as they are not sailing too fast and the sea is calm. The 4-DOF system, which couples surge, sway, yaw and roll, is used for simulation of high-speed vessels, such as naval combatants and fast container ships, because it is necessary to include a fourth degree of freedom to account for the roll effect, when these fast ships are turning. Finally, the 6-DOF system couples all six degrees of freedom, i.e. surge, sway, yaw, roll, heave and pitch, and it is used if wave effects and squat have to be accounted for in simulations with surface ships or if simulations with submarines are performed.

Basically, the different simulation approaches use the same general sets of equations of motion, so that the differences between the simulation methods appear in the way the external forces are determined as well as in the numerical methods used for the solution of the equations of motion. The latter subject is not within the scope of this project and will not be treated further, while the first is described below.

2.4.2 External Forces Acting on the Ship

A maneuvering ship is influenced by a number of external forces which can be divided into two groups: Environmental forces and control devices. The first group includes uncontrollable forces from the environment, i.e. forces from for instance wind and waves. The second group consists of controllable forces and it can consequently be used for maneuvering purposes. The group of control devices contains hydrodynamic forces on rudder, hull and propeller, tug forces, forces from thrusters etc. The present project focuses on the hydrodynamic forces acting on hull, rudder and propeller in calm water and especially on the interaction between the three parts. Therefore, only methods used in this particular area are dealt with.
As mentioned in the previous section there are three systems of equations of motion but several ways to determine the external forces. Since the simulation methods are based on the same governing equations, the quality and the range of validity of the individual simulation method to a large degree depend on the choice of method used for determination of the external hydrodynamic hull, rudder and propeller forces and of the method for modeling the interaction between the three parts. Range of validity means that the forces can be valid for either 1-quadrant maneuvers, i.e. maneuvers with forward-sailing ship with forward-going propeller or 4-quadrant maneuvers, which allow the ship to sail ahead or astern with forward-going or backing propeller. There are three approaches to determination of the hydrodynamic forces. The first is based on model tests, the second is a combined mathematical/numerical approach and the third is semi-empirical. In the following, a description of available methods for determination of external hydrodynamic forces will be given.

2.4.2.1 Model Test Approach

The model test approach is the oldest of the three. It has been used for many years because of its ability to generate comprehensive sets of hydrodynamic data in a relatively simple way. It has also commonly been believed that the data was rather accurate, but it is important to confirm this by means of experimental uncertainty assessment. During the last 20 years the model testing technique has been improved by computers used for data sampling as well as electronic measuring methods. Usually, the hydrodynamic forces applied to maneuvering simulation are represented as functions of the motion parameters, the rudder angle and the propeller loading and they are found by expansion of the individual forces in multidimensional Taylor series. The model tests are used to determine the (hydrodynamic) derivatives or coefficients in the series. The DMI simulator DEN-Mark1 is an exception because it is based on look-up tables, which makes it capable of using the measurements directly from the tank.

Two types of model tests can be used for determination of the hydrodynamic forces in maneuvering simulation, namely the so-called Planar Motion Mechanism (PMM) test and the rotating arm test. The application of the PMM method is dealt with in Key (1993), Abkowitch (1964), Strøm-Tejsen and Chislett (1966) and Kose (1982) while the rotating arm method is treated in Abkowitch (1964), Kose (1982) and Crane (1989). The two model tests are characterized as captive model tests, because the forces are measured while the model is forced through the tank in a fixed condition where the motion and the rudder and propeller settings are known. Both methods make it possible to gain information about propeller, rudder and hull forces. The PMM testing technique used at DMI is described later.
Hydrodynamic forces determined by the model test approach of course include some experimental uncertainties as mentioned above, but with the measuring techniques used today, these uncertainties are hopefully acceptable. However, it is necessary to perform experimental uncertainty assessment in order to quantify the uncertainties and judge if they are acceptable or not. Even though the model tests give good results some difficulties are associated with the method. The first is the scale effect. When a model test is carried out, it is done with the same Froude number for ship and model but with different Reynolds numbers. The result is that the gravity dominated effects are scaled correctly between model and ship while the viscous effects are not. Thus, the wave system is scaled correctly while the boundary layer is not. This scale effect will most likely introduce some errors when the model test results are later scaled to be used for the ship. Another problem is that it is difficult to cover all the intervals of independent variables necessary for making the forces valid for a general 4-quadrant simulation. Finally, the method is expensive because a model has to be manufactured for each ship and the measurements require people and facilities for carrying out the test.
Although the model test approach has some disadvantages, it yields rather good results, which is also the reason that the approach is widely used for determination of forces to simulators as well as for validation of other methods. The model test is therefore probably state of the art within data generation for maneuvering simulators.

2.4.2.2 Mathematical Approach

The mathematical approach is based on a mathematical description of the hydrodynamic forces. The mathematical expressions are often too complicated to be solved analytically, so that computers are required to solve the problem. Therefore, the use of this approach is rather new. The numerical methods are usually characterized as Computational Fluid Dynamics or CFD methods. The CFD methods are used to determine the hydrodynamic forces directly as well as to calculate the hydrodynamic derivatives used in the previously mentioned Taylor expansions. Below some of the methods are summarized.
In Söding (1982) a method based on potential flow theory is presented. The method does not applay the Taylor expansion, so instead explicit expressions for the hydrodynamic forces acting on the hull, rudder and propeller are derived and afterwards inserted in the equations of motion. The expressions describing the forces are based on contributions from ideal fluid effects (potential flow without viscous effects) and from real fluid effects (viscosity). The method is almost purely mathematical, so that use of empirical constants is avoided as far as possible. For practical use the few empirical constants

should be taken from experiments on ships of the same type as the one in the calculation.
In Hearn and Clarke (1993), Fujino (1996) and Nonaka (1993), a method based on slender body theory is dealt with. The theory is used to approximate the flow along a long slender body elongated in the direction of the flow (e.g. a ship). The method applies the potential flow theory and treats the calculation of the hydrodynamic forces as a lifting potential problem in which a free vortex layer separates from the hull of the ship. The slender body theory makes it possible to approximate the three-dimensional flow around the hull by a two-dimensional cross flow problem at each cross-section of the hull. Since the method includes the separating vortex layer, the accuracy of the method is dependent on the position of the lines of separation of the flow along the ship, which means that the largest problem with the method is modeling of the separation of the flow. According to Nonaka (ibid.), it seems that a complete model for this problem has not yet been found.
Finally, two types of methods remain. The first is represented by the 3-D panel methods mentioned in Gronarz (1993), Zou and Söding (1994), Zou (1995) and Yasukawa et al. (1996). These methods are also based on the potential flow theory. Gronarz (1993) uses an existing 3-D panel code (WAMIT) developed at MIT, while Zou and Söding (1994) propose their own method for determination of the hydrodynamic forces on a yawed ship sailing in deep water without rudder and propeller. The method uses Rankine singularities for the calculation of the steady three-dimensional lifting potential flow around the ship and it is assumed that the flow is inviscid. The method has some limitations. One is that the calculations are limited to ships with small drift angles β, and another is that the method becomes inaccurate when the flow separates along the ship. In Zou (1995) the method applied in Zou and Söding (1994) is extended to predictions of the hydrodynamic forces acting on a ship sailing in shallow water. The results of the calculations show qualitative agreement with model test measurements, but they lack quantitative agreement. Yasukawa's method gives the forces acting on the ship while it is sailing straight ahead with deflected rudder. It is described in the section on interaction effects below. As mentioned, the panel methods are usually based on a potential theory solution which is inviscid. But a correction for frictional effects can be made as it is done in Yasukawa et al. (1996).

The second mathematical approach comprises the methods based on numerical solution of the Navier-Stokes equations by means of different discretization schemes as described in Gronarz (1993) and Fujino (1996). In their basic form, the Navier-Stokes equations describe the flow around the ship exactly, i.e. they include phenomena like turbulence and friction. But unfortunately they cannot be solved directly on this form with respect to ship related problems, since the required grid resolution is so fine that it is not practically possible to solve the problem numerically. However, by averaging the equations and introducing different kinds of turbulence models the size of the numerical problem can be reduced considerably. Thus, the method can be used for numerical calculation of the flow around the ship in the fields of resistance, propulsion and maneuvering. Still, it should be mentioned that even with the averaging and the turbulence models the numerical solution of the Navier-Stokes equations for a full scale ship requires computers which are much faster and much more powerful than the computers available today, so the equations are solved for ships in model scale. As regards the field of maneuvering, the Navier-Stokes based methods should have a

potential for investigation of interaction effects between rudder, propeller and hull as well as for calculation of the hydrodynamic forces, but so far they have mainly been applied to bare hulls. Generally, the method has shown qualitative agreement between computation and experiment for the field quantities and in some cases quantitative agreement for the integral quantities. A more detailed study of the application of Navier-Stokes based methods to ship and maneuvering related flow problems is presented in Chapter 6.

If the inviscid and viscous methods are seen in relation to each other the potential based panel methods have the advantage of being computationally easy to handle, while the Navier-Stokes solvers are more difficult to deal with since 1) they require powerful computers and much CPU time and memory and 2) they are time consuming to implement and the number of trained users is limited. But on the other hand the Navier-Stokes methods account for real fluid effects which are difficult to include in the panel methods and, moreover they represent a possibility of studying the flow itself, which can be useful in order to understand the complex flow phenomena often occurring in ship related flow problems. However, in comparison with the numerical approaches, the model test approach is still most widely used. At first sight the numerical methods seem to have the advantage of being cheaper than the model test approach, because no physical model has to be manufactured. But with the computer programs available today, a great deal of time for preparation of the numerical model must be expected and the costs of this task appear about the same as those for model manufacturing. Furthermore, the amount of hydrodynamic data required for a maneuvering simulation is so large that it would not be possible to calculate the necessary forces within a reasonable time. Finally, the model test approach covers flow situations which are very difficult or impossible to handle by the numerical methods available today. Therefore, the numerical methods are not expected to be an alternative to the model tests, but they may be useful for isolated studies of different flow problems related to maneuvering and they therefore seem to have a potential in the future.

2.4.2.3 Semi-empirical Approach

The third and final approach used for determination of the hydrodynamic forces is based on the semi-empirical methods. These methods are normally used at the early design stage where the maneuvering performance of a ship is to be estimated. Hooft and Nienhuis (1994) and Hooft and Quadvlieg (1996) mention a method which bases the calculation of the hull related hydrodynamic derivatives on integration of the local cross flow drag along the hull. When the hull form is known the idea is to model the hull with a number of different hull sections, each with known cross flow properties. The local cross flow properties are found by use of model tests with segmented models. The method is used for determination of the non-linear contributions to the hydrodynamic forces acting on the hull. The linear contributions can be calculated by means of the empirical expressions proposed by Kijima et al. (1993). These expressions are derived on the basis of analysis of experimental data and they give the linear derivatives as functions of the main particulars of the ship.
In Fujino (1996) a method which uses databases containing hydrodynamic derivatives from old model tests is treated. A new set of hydrodynamic derivatives for a new ship at

the design stage is developed by means of existing model data stored in a database. Finally, Kose et al. (1996) propose another method called “TYPE SHIP” consisting of a combination of numerical calculations (slender body theory) and existing model test results stored in a database. When the geometry of the new ship design is known, a prototype ship which is as similar as possible is found in the database. The two geometries are used in a numerical calculation to find the differences in their hydrodynamic performance. The numerically determined changes are then added to the prototype ship in order to obtain the performance of the new ship.
It should be noted that the method proposed by Kijima et al. (1993) is widely used by shipbuilders today. The expressions for the hydrodynamic forces depend on the main particulars but not on the hull form. But, according to Kose et al. (1996), the hull form has a significant influence on the maneuverability of the ship, so he includes the hull form in his calculations. Ishiguro et al. (1996) made an accuracy study of Kijima’s method and it was found that this method yields satisfactory results for course stable ships but less satisfactory results for ships with poor course stability. The reason for this is, according to Ishiguro et al. (ibid.), that Kijima’s method does not take the hull form into account. Finally, Ishiguro et al. (ibid.) propose some modifications of Kijima’s method.
To round off the presentation of methods for determination of hydrodynamic forces a few comments should be given. The methods above are divided into the three approaches in order to categorize the methods, but of course some of the authors use combinations of the methods. It is apparent that the model test approach is still the most accurate and fastest way to determine the hydrodynamic forces and that it will still be used in the future. The numerical methods are used more and more and they show promising results, but they still need to be improved to reach the desired level of accuracy. For prediction of the maneuverability of ships at the design stage the methods based on databases are most widely used.

2.4.3 Hull, Rudder and Propeller Interaction

When the numerical maneuvering simulation approach based on solution of the equations of motion in conjunction with the hydrodynamic forces is used, it is important to include the effects of the interaction between rudder, propeller and hull in the model. The reason is that the input forces for the rudder, propeller and hull are determined for a limited number of discrete conditions, which in theory should be used to cover an infinite number of combinations of forces during the simulation. Therefore, to provide the necessary freedom to combine the forces it is important to have knowledge of how they affect each other and to be able to model the interaction. Usually, the hull-on-propeller, hull-on-rudder and propeller-on-hull interactions are accounted for in the maneuvering models by the effective wake fraction *w* and the thrust deduction fraction *t*. The rudder-on-hull interaction is often accounted for by the interaction coefficients a_H and x_H which can be explained physically as follows: When the rudder works behind the hull, the interaction causes the rudder lift to decrease and the lateral hull force to increase. The result is that the total transverse force acting on the ship increases by a factor $(1+a_H)$ compared to the local rudder force, where a_H is the interaction coefficient. The altered rudder and hull forces change the overall force distribution with

the result that the center of attack of the total transverse force moves a distance x_H forward in the ship, which affects the total yaw moment acting on the ship. It should be noted that if the contribution to the transverse hull force from changes in the rudder angle is extracted and used as rudder force, the use of a_H and x_H can be omitted. However, a comprehensive set of hydrodynamic data is still required to generate the necessary interaction data for a maneuvering simulation, and even then the problem is not modeled completely. The methods used for determination of the interaction effects are today mainly based on data from model experiments and empirical formulas as illustrated by Kose (1982), Hooft and Nienhuis (1994) and Kijima et al. (1993), who all account for the interaction effects during the simulations by use of empirically and experimentally determined values of *w*, *t*, a_H and x_H.

However, a few numerical methods which can be used for investigation of the interaction phenomena and for data generation have been proposed. Some of these methods are listed in the following. Fujino (1996) discusses different models based on the panel method for calculation of the interaction between rudder, propeller and hull. One of these methods is proposed by Yasukawa et al. (1996). The method is used for calculation of the forces on the ship as well as for investigation of the interaction effects for a ship sailing straight ahead with deflected rudder. Thus it is a numerical alternative to a part of the experimental PMM test. The method is based on the potential flow theory, but it is corrected for fluid viscosity by superposition of the velocity components based on fluid viscosity and the potential velocity components. The propeller is modeled by a simplified propeller theory where it is assumed to have an infinite number of blades, and it is represented by distributions of bound and free vortices on the propeller disk. The rudder and the hull are modeled by a panel method based on thick wing theory. The interaction between rudder, propeller and hull is modeled by combining the potentials for the three parts. By this method it is possible to calculate the thrust deduction fraction *t* and the effective wake fraction *w*, as well as the two interaction coefficients a_H and x_H. The method is almost purely theoretical, but it uses an experimentally determined nominal wake distribution. Yasukawa et al. (ibid.) propose that the wake could be determined by a numerical method as well, in order to obtain a totally theoretical method. A comparison with experimental data shows that the forces calculated by the method agree with the measurements, while the interaction coefficients are determined less accurately.

Turnock (1996) also proposes a panel method for calculation of interaction effects, but he only investigates a propeller-rudder unit without hull. The theory is based on a lifting surface panel method where both rudder and propeller geometries are modeled by 3-D panels. The interaction between rudder and propeller is accounted for by modification of the inflow fields for the two components. The calculation procedure is carried out in the following manner. First the propeller flow problem is solved and the influence on the rudder is found. Then the rudder flow problem is calculated with the propeller-induced inflow field and the influence on the propeller is found. Then the propeller flow is calculated again with the new inflow and so on. The procedure is repeated until convergence is reached. The effect of viscosity is included in the model by means of skin friction. The skin friction coefficient is calculated from approximate expressions as a function of the local Reynolds number, which is calculated on the basis of the velocities from the potential solution. Finally, the frictional force is added to the pressure force found by the potential solution. The method gives the best results for small rudder angles because of the limitations of the model used for the frictional forces.

Li and Dyne (1995) also investigate a rudder-propeller unit. The method calculates the stationary forces of the rudder-propeller unit working in a uniform flow. The propeller is assumed to have an infinite number of blades, and it is modeled by a bound vortex sheet at the propeller plane, a hub vortex filament and a series of free vortex sheets behind the propeller, which are assumed to be undisturbed by the rudder. The rudder is represented by vortex and sink-source filaments placed on the mean plane of the rudder. The propeller and rudder performances are estimated by a lifting line method and a vortex lattice method, respectively. The solution of the interaction is arrived at by solving the propeller and rudder flow in an iterative manner until convergence is reached. The viscous forces of the propeller are accounted for by an empirical expression. The viscous forces acting on the rudder are also calculated empirically. Two important simplifications have been made in the model. One is that the contraction of the propeller slipstream tube is neglected. This influences the accuracy for at least heavily loaded propellers. The second is that the free vortex sheets behind the propeller are assumed to be undisturbed by the rudder. Thus, the presence of the rudder does not deform the slipstream, which is a very rough assumption. This is also reflected in the accuracy of the method not being the best when compared with experiments.

2.5 DEN-Mark1 Simulator at DMI

The literature study also included a study of the model behind the DEN-Mark1 simulator used at DMI. The hydrodynamic part of this model is based on the model test approach so that input data is generated by model tests. Instead of using the above-mentioned hydrodynamic derivatives, the model uses look-up tables including basic forces and functions for correction of for instance water depth, trim etc. The model employs a general and exact set of 6-DOF equations of motion, but it is possible to work with 3- or 4-DOF systems by locking the degrees of freedom describing respectively roll, heave and pitch or heave and pitch.
Based on experimental data, the model is also able to include the interaction between rudder, propeller and hull by splitting the interaction effects up in the following parts: hull-on-propeller, hull-on-rudder, propeller-on-hull, propeller-on-rudder, rudder-on-propeller and rudder-on-hull. The DEN-Mark1 model is relatively flexible and with the right input data the interaction between rudder, propeller and hull can be described rather well. The model is briefly described in Chislett (1996) and Jensen (1993).
The captive model test method used to generate the hydrodynamic input data to DEN-Mark1 is the PMM test. See Abkowitch (1964) and Strøm-Tejsen and Chislett (1966). The objective of the method is to force the model through the water while each relevant parameter (for instance rudder or drift angle) is varied. For each parameter setting the corresponding forces and moments are measured. Afterwards the hydrodynamic derivatives are determined by polynomial curve fairing to the resultant force and parameter sets. The hydrodynamic derivatives are determined for appended models, which means that the hull is equipped with both rudder and propeller during the test. It was mentioned earlier that DEN-Mark1 uses look-up tables including forces, while the PMM test gives hydrodynamic derivatives. The problem is solved by a numerical transformation from derivatives to forces. A more detailed description of the DEN-Mark1 model and its relation to the model test is given in Chapters 3 and 4.

2.6 Summary

It appears from the findings in the present chapter that there are several approaches with different levels of complexity to maneuvering simulation. The methods range from free-running model tests and simple empirical models yielding the maneuvering performance directly, to complex models, which give detailed information about the motion of the maneuvering ship. The latter category, which appears to be state of the art, requires numerical solution of the equations of motion for the ship and comprehensive model testing to lead to the necessary hydrodynamic rudder, propeller and hull forces used as input to the simulator. Since the hydrodynamic forces are split up into contributions from rudder, propeller and hull, an important subject as regards these complex numerical models is the rudder-propeller-hull interaction. Most of the interaction models used today are based on empirical data or experimental data derived on the basis of the hydrodynamic forces. Thus, they are based on knowledge of the overall behavior of the flow rather than on knowledge of the flow field itself, which of course is difficult to obtain.

Concerning generation of hydrodynamic input data to the simulator, the experimental PMM testing technique is apparently the state of the art at the present time of writing and one of the few methods which can give the sufficient amount of data for a simulation within a reasonable time. Different numerical methods do exist which should be able to give both the hydrodynamic forces and information about the interaction phenomena, but at present they cannot provide the required amount of hydrodynamic input data to the simulator. They are divided into two categories covering the inviscid potential theory based methods and the viscous Navier-Stokes based methods. The methods based on potential theory are relatively easy to handle with regard to the requirements of computational power and user training. However, they lack the real fluid effects and even though corrections are made in compensation, the accuracy of the results still needs to be improved. The viscous methods include the real fluid effects, but they are at the same time more difficult to use. They have mainly been applied to bare hull calculations and even in this case they require large computers. The accuracy of the results obtained by these methods also needs to be improved. But even though they cannot lead to the desired accuracy, they have the advantage of giving a visual impression of the flow, which can lead to a better understanding of the flow problems.

Chapter 3

Mathematical Maneuvering Model

3.1 Introduction

In summary the objective of the present project is 1) to focus on numerical investigation of the interaction effects taking place between rudder, propeller and hull for ships in maneuvering situations, since this is important to the area of maneuvering simulation and 2) to investigate the possibility of numerical generation of the hydrodynamic input data to maneuvering simulators. According to the findings in Chapter 2, the models applied to maneuvering simulation are based on experimental input data and they already include different models to account for the interaction, but they are usually empirical or based on the measured hydrodynamic forces. Since the forces are integral quantities, they do not provide much information about the flow phenomena causing the interaction, and there is a need for more detailed studies of the flow in order to understand the problem better. However, the problem is complex and it is difficult to find out where to begin. Therefore, it is a good idea to start out with a study of an existing maneuvering model to see how the model works and which input data it requires. Thus, some flow situations of interest with respect to numerical investigation could be identified.
The considered maneuvering model is the DEN-Mark1 model, based on a general and exact set of non-linear equations of motion describing six degrees of freedom (DOF). But it is also possible to work with 3- or 4-DOF systems by locking the degrees of freedom which describe respectively roll, heave, pitch and heave, pitch. The hydrodynamic part of the maneuvering model, which is applied at DMI, is based on input data generated by model tests and empirical methods. Instead of using the traditional hydrodynamic derivatives, the model uses look-up tables containing basic forces and functions for correction of for instance water depth, trim etc. Each component of the hydrodynamic forces is tabulated as a function of one or two independent variables which consist of the relevant motion or control parameters. The model is designed so that the hydrodynamic forces can be split into different contributions from for instance rudder, propeller and hull. Thus, the individual force components are first inserted separately in the model and then added to a total force by means of the superposition principle. The model is also capable of including the interaction between rudder, propeller and hull by splitting the interaction effects up into different components.

A description of the rudder, propeller and hull forces and of the model of the interaction between them is presented below. For simplification of the problem, the 3-DOF case is considered.

3.2 Hydrodynamic Forces

As mentioned, the present project is limited to investigation of ships with three degrees of freedom, which means that the ship is allowed to surge, sway and yaw. According to the DEN-Mark1 model, the external hydrodynamic forces and moments acting on a 3-DOF ship during the maneuver can be expressed as

$$\begin{aligned} X &= X_{AC} + X_H + X_P + X_R + X_{HPR} \\ Y &= Y_{AC} + Y_H + Y_P + Y_R + Y_{HPR} \\ N &= N_{AC} + N_H + N_P + N_R + N_{HPR} \end{aligned} \tag{3.1}$$

where X and Y are the forces in the x- and y-directions and N is the yaw moment about the z-axis. Figure (3.1). The subscript at each force component indicates contribution to the force from the following: *AC*: acceleration (added mass), *H*: hull, *P*: propeller, *R*: rudder and *HPR*: hull, propeller and rudder interaction. The acceleration forces are shown for completion of the overview, but apart from this, they are not considered in the present project. Each component of the remaining *H*, *P* and *R* forces is dependent on several parameters, which is described in the following sections.

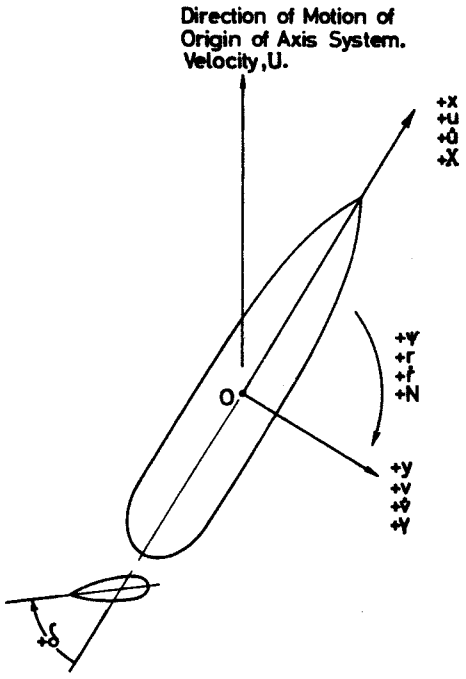

Figure (3.1) *Definitions of motion, orientation and force parameters.*

It should be noted that the *HPR* contributions to practical applications are not separate force contributions as indicated in (3.1), but that they are usually included in the individual *H*, *P* and *R* contributions.

3.2.1 Interaction Effects

The objective of the mathematical interaction model is to divide the interaction effects into a number of separate contributions, which according to the Mathematical Model Description (1993), cover

Hull-on-propeller interaction	: Effective wake fraction and relative rotative efficiency
Propeller-on-hull interaction	: Thrust deduction fraction for zero rudder angle and steering action of the propeller
Rudder-on-propeller interaction	: Effective wake fraction
Propeller-on-rudder interaction	: Change of effective axial inflow velocity to rudder
Hull-on-rudder interaction	: Change of effective inflow angle to rudder
Rudder-on-hull interaction	: Pressure on hull due to non-zero rudder angle, the effect is included in the rudder forces

In the list of interaction contributions shown above the physical parameters, used for implementation of the effects in the model, are also listed. The practical inclusion of the interaction effects in the hull, propeller and rudder forces is illustrated in the sections below.

3.2.2 Hull Forces

The hull forces for a 3-DOF ship are represented by X_H, Y_H and N_H. According to the Mathematical Model Description (ibid.), the three force components can be defined as

$$\begin{aligned} X_H &= X_{Fn} + X^*_{\beta\gamma} \\ Y_H &= Y_{Fn} + Y^*_{\beta\gamma} \\ N_H &= N_{Fn} + N^*_{\beta\gamma} \end{aligned} \qquad (3.2)$$

where the subscript *Fn* indicates the resistance of the ship without propeller as a function of the ship speed. For port and starboard symmetry Y_{Fn} and N_{Fn} are zero, while X_{Fn} for deep water and zero trim is defined by

$$X_{Fn} = C_X(Fn)\, ½\, \rho\, u^2\, S \qquad (3.3)$$

where $C_X(Fn)$ is the experimentally determined resistance coefficient, which can be obtained by means of the resistance test in the towing tank. ρ is the water density, u is the longitudinal ship speed, S is the area of the wetted surface of the ship at zero speed and Fn is the Froude number defined by

$$Fn = \frac{u}{\sqrt{g\,L}} \tag{3.4}$$

where L is the length of the ship and g is the acceleration of gravity.
The subscript $\beta\gamma$ at the forces in (3.2) symbolizes the components of the hull forces due to sway, yaw and cross-coupling between the two modes. By application of the superposition principle $X^*_{\beta\gamma}$, $Y^*_{\beta\gamma}$ and $N^*_{\beta\gamma}$ can be written as a sum of three components

$$\begin{aligned} X^*_{\beta\gamma} &= X_\beta + X_\gamma + X_{\beta\gamma} \\ Y^*_{\beta\gamma} &= Y_\beta + Y_\gamma + Y_{\beta\gamma} \\ N^*_{\beta\gamma} &= N_\beta + N_\gamma + N_{\beta\gamma} \end{aligned} \tag{3.5}$$

All the force and moment components on the right hand side of (3.5) can be related to dimensionless coefficients by means of the following general relations:

$$\begin{aligned} F &= C_F \; ½\, \rho\, A\, V^2 \\ M &= C_M \; ½\, \rho\, A\, V^2\, a \end{aligned} \tag{3.6}$$

where F and M are the forces and the moments, C_F and C_M are dimensionless force and moment coefficients, ρ is the density, A and a are the characteristic area and arm, respectively and, finally, V is a characteristic velocity of the flow problem. The experimentally determined dimensionless coefficients C_F and C_M used in DEN-Mark1 are naturally calculated on the basis of the relation (3.6), but they are not constant since they are dependent on the Froude number Fn, the drift angle β and the yaw rate angle γ:

$$\begin{aligned} C_{i\beta} &= f(Fn, \beta) \\ C_{i\gamma} &= f(Fn, \gamma) \\ C_{i\beta\gamma} &= f(Fn, \beta, \gamma) \end{aligned} \tag{3.7}$$

where the subscript i can be replaced by X, Y and N. All the nine coefficients $C_{i\beta}$, $C_{i\gamma}$ and $C_{i\beta\gamma}$ are determined by the PMM technique, which is described in Chapter 4. $C_{i\beta}$ is determined by the "static drift" test, $C_{i\gamma}$ by the "pure yaw" test and $C_{i\beta\gamma}$ by the "yaw and drift" test. The Froude number is defined in (3.4) while the drift and yaw rate angles are defined by

$$\beta = Arctan^{s}\left(\frac{-v}{u}\right) \tag{3.8}$$

$$\gamma = Arctan^{s}\left(\frac{½\, r\, L_c}{U}\right) \tag{3.9}$$

where U is the total ship speed defined as shown in Figure (3.2) and L_c is a characteristic length. The superscript *s* denotes that the angles must be calculated so that the sign of the angles corresponds to the current flow situation. An illustration of β can be seen in Figure (3.2).
The characteristic area and arm used in the model are respectively the characteristic lateral underwater area of the hull A_C and the characteristic length of the ship L_c. Usually, the perpendicular length L_{PP} is used as characteristic length. Finally, the characteristic velocities remain to be dealt with. For the coefficient $C_{i\beta}$ the characteristic squared velocity is defined as

$$V^2 = u^2 + v^2 \tag{3.10}$$

and for $C_{i\gamma}$ and $C_{i\beta\gamma}$ it is defined as

$$V^2 = u^2 + v^2 + \left(\frac{r\, L_c}{2}\right)^2 \tag{3.11}$$

where *u* and *v* are the surge and sway velocities, respectively and *r* the yaw rate as illustrated in Figure (3.1).

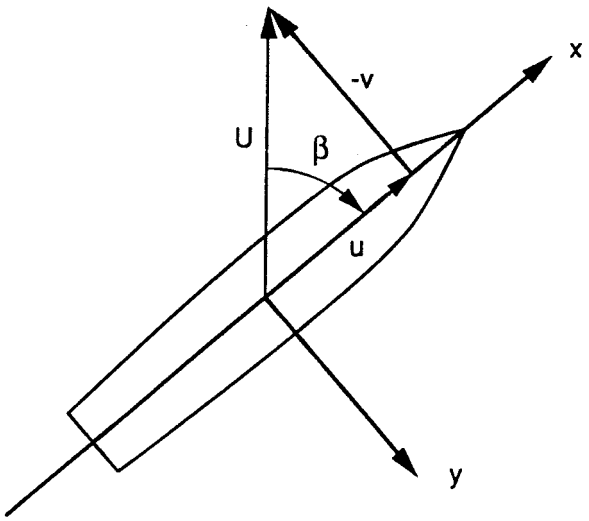

Figure (3.2) *Definition of drift angle.*

3.2.3 Propeller Forces

In DEN-Mark1 each of the propeller forces X_P, Y_P and N_P is assumed to be a function of the propeller diameter, the number of propeller revolutions, the propeller pitch and the axial inflow velocity to the propeller. These parameters are gathered in a set of independent variables which is defined in the Mathematical Model Description (ibid.). The independent variables are summarized as follows:

$$\beta^* = Arctan^s\left(\frac{u_a}{0.7\,\pi\;n\;D}\right) \tag{3.12}$$

is the hydrodynamic pitch angle and

$$\beta_p = Arctan^s\left(\frac{-v_P}{u_P}\right) \tag{3.13}$$

is the local drift angle at the propeller and

$$\beta' = Arc\tan^s\left(\frac{u_P}{0.7\,\pi\;n\;D}\right) \tag{3.14}$$

is the propeller loading angle. In these expressions *n* is the rate of propeller revolutions, *D* is the propeller diameter, v_P and u_P are respectively the transverse and longitudinal velocity components of the ship at the propeller, and u_a is the effective axial velocity of advance defined by

$$u_a = u_P(1-w) \tag{3.15}$$

where *w* is the effective wake fraction, which is assumed to be based on a thrust identity. With a definition of these independent variables, it is possible to return to the forces and moments generated by the propeller. The first force is the longitudinal force X_P, which according to the Mathematical Model Description (ibid.) is defined as

$$X_P = T(1-t) \tag{3.16}$$

where *T* is the thrust at the propeller shaft and *t* is the thrust deduction fraction, which is also assumed to be based on a thrust identity. The thrust *T* is obtained from the following expression:

$$T = C_T^*\;\tfrac{1}{2}\;\rho\;\left[u_a^2 + (0.7\,\pi\;n\;D)^2\right]\;A_p \tag{3.17}$$

where ρ and A_P are the density of the water and the propeller disk area, respectively. C_T^* is the thrust coefficient calculated from the well known open water coefficient K_T.

C_T^* is treated as a function of the hydrodynamic pitch angle β^* and the pitch *P/D* of the propeller:

$$C_T^* = f(\beta^*, P/D) \tag{3.18}$$

Both the effective wake fraction *w* and the thrust deduction fraction *t* have to be known for the calculation of X_P. These two factors are assumed to be influenced by the flow conditions, which means that they vary during the simulation. In the model *w* is assumed to be a function of the propeller loading, water depth, local drift angle and rudder angle, but since this project only deals with ships in deep water the water depth correction is omitted ($f(\beta', T_m/h) = 1$) and *w* turns out to be

$$w = f(\beta')\, f(\beta', \beta_P) + f(\beta', \delta) \tag{3.19}$$

The thrust deduction fraction is assumed to be dependent on propeller loading and water depth, but independent of the rudder angle δ. If the water depth correction is omitted, *t* becomes

$$t = f(\beta') \tag{3.20}$$

As regards the interaction effects it is seen that three of the contributions to X_{HPR} from Section 3.2.1 are included. The effective wake fraction accounts for both hull-on-propeller and rudder-on-propeller interaction, while the thrust deduction fraction accounts for the propeller-on-hull interaction.

Even though the model is prepared for the variable effective wake fraction and the thrust deduction fraction, only sparse information about the influence of β', β_P and δ on *w* and of β' on *t* is available today. The only available information of the β' dependence is some empirical diagrams and tables created by Harvald, who based a method on model tests. Harvald's results can be found in Harvald (1967) and Harvald (1976). By applying this method it is possible to create a table containing the effective wake fraction or thrust deduction fraction as a function of β', when the wake fraction w_0 or the thrust deduction fraction t_0 at forward service speed is known. w_0 and t_0 are determined experimentally by means of the self-propulsion model test. Information about the influence of drift and rudder angle on *w* is even sparser because no information is available in the literature and only a few unpublished model test results have been obtained at DMI. Therefore, the influence of β_P and δ on *w* is normally ignored in the simulations.

The remaining propeller force Y_P and moment N_P form the so-called steering action of the propeller. They are both described in the Mathematical Model Description (1993) but the results are summarized here. Both Y_P and N_P are assumed to be independent of the rudder angle. This is done to avoid overlapping of the different forces and moments when all the contributions are superposed.

The transverse force Y_P is due to the propeller-on-hull interaction. When the propeller rotates behind the ship, it induces a pressure difference between the two sides of the aft ship, which results in a transverse force Y_P on the hull. Y_P has, according to the

Mathematical Model Description (ibid.), the following form for deep water and no heel or trim:

$$T = C_{YP}^{*} \; ½ \; \rho \; \left[u_a^2 + (0.7 \; \pi \; n \; D)^2 \right] \; A_P \tag{3.21}$$

All the involved parameters except C_{YP}^{*} are defined above. C_{YP}^{*} can be determined by PMM model tests as a function of the hydrodynamic pitch angle and the pitch of the propeller:

$$C_{YP}^{*} = f(\beta^{*}, P/D) \tag{3.22}$$

However, experience obtained at DMI has shown that when no other information is available, the force Y_P can be approximated by 1 percent of the propeller thrust for forward propeller actions and 10 percent for backing propeller. For a clockwise rotating propeller the Y_P force is positive for ahead-running propeller and negative for astern-running propeller. Finally, the yaw moment N_P can be found. The moment results from the transverse Y_P force and the thrust *T* and it has the form

$$N_P = Y_P \; x_P - T \; (1-t) \; y_P \tag{3.23}$$

where the new parameters x_P and y_P are the propeller coordinates in the coordinate system of the ship.

3.2.4 Rudder Forces

The rudder forces used in the maneuvering model are also described in the Mathematical Model Description (ibid.) and the results valid for a ship with a single rudder and a single propeller are briefly described below to illustrate the idea behind the model. When a rudder is placed in a uniform flow field, the lift or drag coefficients are usually determined by non-dimensionalizing the lift or drag forces with the lateral rudder area A_R, the inflow velocity *C* and the fluid density ρ:

$$C_L = \frac{L}{½ \; \rho \; A_R \; C^2} \tag{3.24}$$

However, when the rudder is placed in the slipstream of the propeller, the inflow field is no longer uniform and it is necessary to apply a characteristic velocity and area, which reflect the variations in the rudder inflow field. The method must therefore account for the extension of the part of the rudder in the slipstream, but it must also include the actual velocity in the slipstream, which reflects the propeller loading. In the maneuvering model the problem is solved by applying a characteristic velocity weighting the slipstream and free stream velocities with the slipstream and free stream areas of the rudder:

$$C^2 = \frac{A_s u_s^{S2} + \left(A_R - A_s\right) u_a^{S2}}{A_R} \tag{3.25}$$

where A_s and $(A_R - A_s)$ are the portions of the rudder area in the slipstream and the free stream, respectively. A_R is the total lateral rudder area, while u_s and u_a are the velocities at the rudder inside and outside the slipstream, respectively. The signed square at the velocities is used to account for situations where the slipstream and the free stream velocities are oppositely directed, e.g. when the ship is sailing forward with backing propeller during a stop maneuver. The signed square is defined as

$$x^{S2} = |x|\, x \tag{3.26}$$

This leads to the following expressions for the components of the rudder forces X_R, Y_R and N_R which can be found in the Mathematical Model Description (ibid.):

$$X_R = C_{XR}(\xi, \delta)\ ½\ \rho \left[A_s u_s^{S2} + \left(A_R - A_s\right) u_a^{S2}\right] \tag{3.27}$$

$$Y_R = C_{YR}(\xi, \delta)\ ½\ \rho \left[A_s u_s^{S2} + \left(A_R - A_s\right) u_a^{S2}\right] \tag{3.28}$$

$$N_R = C_{NR}(\xi, \delta)\ ½\ \rho\, L_{PP} \left[A_s u_s^{S2} + \left(A_R - A_s\right) u_a^{S2}\right] \tag{3.29}$$

The slipstream velocity u_s in the Expressions (3.27) to (3.29) is calculated by use of the momentum theory, which is the simplest of the propeller theories:

$$u_s = u_a + \kappa \Delta u_\infty \qquad \text{for } T \geq 0 \tag{3.30}$$

$$u_s = u_a + (1 - \kappa \Delta u_\infty) \qquad \text{for } T < 0 \tag{3.31}$$

where κ accounts for the variation of u_s with the distance from the propeller and the direction of the thrust. T is the thrust and Δu_∞ is the slipstream velocity increment far downstream determined from

$$u_a + \Delta u_\infty = \left[u_a^{s2} + \frac{8\,T}{\rho\, D^2 \pi}\right]^{S\,½} \tag{3.32}$$

The expression shown in (3.32) can be used for both negative and positive thrust because the signed square and square root are used. The definition of the signed square is found in (3.26) while the signed square root is defined by

$$(x)^{S\,1/2} = (\,|x|\,)^{1/2}\, \frac{x}{|x|} \tag{3.33}$$

The area of the rudder in the slipstream A_s applied in (3.27) to (3.29) is calculated from the slipstream diameter, which is also determined on the basis of the momentum theory. The slipstream area is represented by a square with a side length which equals the slipstream diameter. The calculation of A_s is divided into two parts. The first is a definition of A_s for the zero rudder angle:

$$A_s = A_R \frac{(Rudder\ span\ in\ slipstream)}{(Total\ rudder\ span)} \tag{3.34}$$

The second part is a definition of A_s for non-zero rudder angles:

$$A_s = \frac{(Projected\ rudder\ area\ in\ slipstream)}{|sin\ \delta|} \tag{3.35}$$

C_{XR}, C_{YR} and C_{NR} are non-dimensionalized rudder force coefficients determined experimentally by use of the PMM test called “static rudder”. They are determined for the ship moving straight ahead with deflected rudder and they are tabulated as functions of the independent variables δ and ξ. These variables are respectively the rudder inflow angle and the rudder loading angle. The latter is defined as

$$\xi = Arctan^s\left(\frac{u_a}{u_s}\right) \tag{3.36}$$

where u_a is the effective axial advance velocity at the propeller and u_s is the velocity in the slipstream of the propeller.
The experimentally determined rudder forces used in the simulation, are measured for the ship moving straight ahead, but the behavior of the rudder on a maneuvering ship must be expected to be somewhat different since the ship experiences yaw and drift. It is not possible to separate the influence of straight ahead and oblique sailing in model tests, so the problem is solved by introducing an effective rudder angle δ_e instead of the geometric rudder angle δ. The effective rudder angle is defined as

$$\delta_e = \delta + \beta_{Re} \tag{3.37}$$

δ_e is influenced by the sway velocity and the yaw rate, which can be accounted for in the local drift angle β_{Re} by means of the two separate drift angles $\beta_{R\beta}$ and $\beta_{R\gamma}$:

$$\beta_{R\beta} = Arctan^s\left(\frac{-v}{u}\right) \tag{3.38}$$

$$\beta_{R\gamma} = Arctan^s\left(\frac{-x_R r}{u - y_R r}\right) \tag{3.39}$$

where x_R and y_R are the rudder coordinates in the ship's coordinate system and *v* and *r* are respectively the sway velocity and the yaw rate. This leads to the following tabulated function for β_{Re}

$$\beta_{Re} = f(\beta_{R\beta}, \xi)\, cf_1(\beta_{R\gamma}, \xi) + f(\beta_{R\gamma}, \xi)\, cf_2(\beta_{R\beta}, \xi) \tag{3.40}$$

where the *cf* functions are corrections for the influence of yaw on drift and vice versa. However, experiences obtained at DMI have shown that the influence of drift on the effective rudder angle is usually not significant. This must be seen in relation to the flow straightening effect of both hull and propeller on the rudder flow, which results in a decreasing value of the yaw and drift based β_{Re}. Therefore, the geometric rudder angle is often used without corrections.
As regards the interaction effects, it is seen that the incorporation of the local drift angle β_{Re} and the application of u_a account for the hull-on-rudder interaction and that the rudder-in-propeller slipstream idea accounts for the propeller-on-rudder interaction.

3.3 Summary

In the present chapter, an overview of the mathematical maneuvering model DEN-Mark1 was given. The purpose was not to describe the equations of motion, but instead to find out which hydrodynamic rudder, propeller and hull forces are used as input to the

Necessary input parameter	Nomenclature	Dependent of	Independent variables
Hull forces and moment	X_H, Y_H, N_H	Longitudinal speed Drift Yaw	Fn β γ
Rudder forces and moment	X_R, Y_R, N_R	Rudder angle Drift angle at rudder due to drift Drift angle at rudder due to yaw Rudder loading angle	δ $\beta_{R\beta}$ $\beta_{R\gamma}$ ξ
Steering action of propeller	Y_P, N_P	Hydrodynamic pitch angle Pitch of propeller	β^* P/D
Effective wake fraction	w	Propeller loading angle Local drift angle Rudder angle	β' β_P δ
Thrust deduction fraction	t	Propeller loading angle	β'
Thrust	T	Hydrodynamic pitch angle Pitch of propeller	β^* P/D

Table (3.1) *Overview of the input parameters to the maneuvering model.*

simulator, and how the interaction effects between the three components are included in the model.

Table (3.1) summarizes the necessary dependent forces and parameters and the corresponding independent variables to be determined before a simulation can be performed. Explanations and definitions are found in Section 3.2. It is seen from Table (3.1) that many parameters have to be determined in order to provide data for a simulation. At the present time of writing most of this data is generated experimentally by means of model tests. The most important model test for determination of the hydrodynamic data for the maneuvering model appears to be the PMM test, which is described in more detail in Chapter 4.

It was found that, except for the thrust deduction fraction and the effective wake fraction, it was difficult to extract explicit information about the interaction effects between the rudder, propeller and hull, since they are to a large degree included in the forces either by the non-dimensionalization or directly when they are measured. Thus, it was difficult to find a way to quantify the interaction, which could be used directly as a basis for numerical study of the interaction effects. However, two approaches can be adopted in order to study the rudder, propeller and hull interaction: The first is investigation of the interaction effects at simulator level, i.e. at the integral level where the forces are considered. This requires a comprehensive set of hydrodynamic data to investigate the overall relations between the different forces and parameters, and it must be done experimentally since it is not realistic to produce this amount of data by the numerical methods available today. A study of this kind would have to be based on systematic parameter studies to illustrate the tendencies and variations of the forces and parameters. However, the approach only provides overall information and not data which help understand the flow phenomena causing the interaction effects. The approach is illustrated later by a few examples in Chapter 5.

The second approach consists of numerical investigation of the interaction effects at the flow field level, i.e. it provides information about the flow itself. The idea is to select a ship condition and vary one independent parameter systematically and see how this influences the forces, as in the first approach, but at the same time observe how the flow behaves accordingly and thus explain why the other parameters vary. By adopting this approach it would be possible to 1) see if the numerical method is capable of predicting the forces and thus investigate if it can be used for data generation to the simulator, and 2) gain knowledge of the complex flow phenomena in the stern region of the ship and maybe be able to improve the maneuvering model.

Finally, a comment should be made on the selection of a ship condition. The description of the maneuvering model, given in the present chapter, showed that many relations could be examined, but also that basic information about rudder forces, effective wake fraction, and thrust deduction fraction was generally extracted for straight-ahead sailing. The simplification introduced by neglecting yaw and drift might be useful in a numerical study.

Chapter 4

Generation of Hydrodynamic Input Data to the Simulator

4.1 Introduction

According to Chapter 3 the simulator input data, which describes the hydrodynamic parameters and forces, must be determined before the simulation of a maneuvering ship can be performed. At the time of writing most of the hydrodynamic data is found by use of model tests. The present chapter deals with the primary method applied for this purpose, namely the PMM test. By describing the test it is attempted to provide an overview of the method and its relation to the simulator. But also to identify the involved flow situations, which can be used for a study of the interaction effects as illustrated in the following chapters.

4.2 PMM Model Testing Technique

The PMM model test method is a so-called captive model testing method, which means that the model is forced through the water while the hydrodynamic forces are measured. The method is described in detail in Abkowitz (1964) and Strøm-Tejsen and Chislett (1966), but a summary of the method is presented here. The PMM testing technique enables determination of the hydrodynamic forces and moments as functions of different independent variables as for instance rudder angle, speed or number of propeller revolutions. This can also be expressed as

$$\left.\begin{matrix} X \\ Y \\ N \end{matrix}\right\} = f(\dot{u}, \dot{v}, \dot{r}, u, v, r, \delta, n) \qquad (4.1)$$

where u and v are the surge and sway velocities and r is the yaw rate. The dots denote differentiation with respect to time i.e. accelerations. δ is the rudder angle and n is the number of propeller revolutions. X, Y and N are the longitudinal x-force, the transverse

y-force and the yaw moment, respectively. As mentioned in the previous chapter, work on the acceleration forces is not included in the present project. Therefore, focus is placed on the tests used for determination of the forces and moments related to the velocities and the rudder angle.
The measurements are performed with an appended ship, which means that the ship is equipped with both rudder and propeller during the test. Usually the propeller is running at the self-propulsion point. The model is locked in all degrees of freedom except for translation in the *z*-direction and rotation around the *y*-axis, so that the model is allowed to squat and pitch. The idea of the method is to force the model through the water, following a precisely controlled path, while one or two of the relevant rudder and motion variables are varied systematically. For each parameter-setting the corresponding forces and moments are measured.
The first step in the procedure is to measure the forces and moments while one parameter is varied. The resulting forces and moments are then expressed as functions of the single parameters. The next step is to vary two parameters at a time and measure the corresponding forces and moments. If the forces are different from the superimposed results of the individually measured forces, the difference is expressed in a two-dimensional function, which depends on the current parameters. This function accounts for the so-called cross-coupling.
The measurements can be carried out in two modes: Static or dynamic. The static mode is applied to determination of the influence from rudder angle alone, drift angle alone and from combinations of rudder and drift angle. The dynamic mode is obtained by oscillating bow and stern of the model from side to side, while the model travels through the tank. Depending on whether the bow and stern are oscillated in or out of phase, the dynamic mode is used for determination of the influence on the forces from sway alone and yaw alone. Furthermore, the cross-coupling effects can be obtained from combinations of yaw and rudder, drift and rudder, yaw and drift and finally yaw and drift and rudder. Finally, the dynamic mode is also used for determination of the acceleration forces and moments, but as mentioned earlier this is beyond the scope of the project. A more detailed description of the individual tests can be found in a later section.
The PMM test is developed to generate input data to a coefficient based maneuvering model and, as mentioned in Chapter 2 about state of the art methods, such a model is based on expansion of the hydrodynamic forces in multidimensional series including the necessary linear and non-linear combinations of independent variables. Thus, the forces and moments measured during the PMM test are used to determine the coefficients, often refered to as hydrodynamic derivatives, of these series. It is done by polynomial curve fairing to the resultant force and parameter sets.
It should be noted that the description above covers tests which are used for data generation to simulations with 3-DOF ships, but the PMM facility at DMI is also capable of measuring the fourth degree of freedom, roll. However, inclusion of this degree of freedom in the model is beyond the scope of the present project.

4.3 Transformation and Range of Validity of Data

When hydrodynamic input data is generated to DEN-Mark1, most of it is found by means of the PMM model test. However, DEN-Mark1 uses one- or two- dimensional look-up tables containing the non-dimensionalized forces and moments split up into

contributions from rudder, propeller and hull, while the PMM test represents the total hydrodynamic forces and moments in polynomial form by application of non-dimensionalized hydrodynamic derivatives. Besides, two different sets of independent variables are used. The problem with the two different representations is solved by a numerical transformation of the independent variables and of derivatives to forces.

4.3.1 Hull Forces

The nomenclature used in connection with the PMM test is found in the Mathematical Model Description (1993), where the set of independent variables is defined as

$$u' = \frac{u}{U} \qquad v' = \frac{v}{U} \qquad r' = \frac{r\,L_{PP}}{U} \qquad \underline{u'} = \frac{\underline{u}}{U} = \frac{u - U_0}{U} \tag{4.2}$$

Here u and v are the surge and sway velocity, respectively, r is the yaw rate, U is the total speed of the ship, U_0 is the approach speed of the ship and L_{PP} is the perpendicular length of the ship. It is seen that U must be different from zero, which means that the traditional PMM nomenclature cannot be used for U=0m/s. The corresponding independent variables used in the DEN-Mark1 nomenclature are defined in Chapter 3, but their relation to the PMM nomenclature is according to the Mathematical Model Description (ibid.) as follows:

$$\beta = Arctan\left(\frac{-v'}{u'}\right) \qquad \gamma = Arctan\left(\frac{r'}{2}\right) \qquad \frac{Fn}{Fn_0} = \frac{u'}{u' - \underline{u'}} \tag{4.3}$$

where β, γ and Fn are the drift angle, the yaw angle and the Froude number, respectively. Before the input data is generated and transformed, it is necessary to determine whether the simulation shall cover linear, 1-quadrant or 4-quadrant maneuvers. The linear maneuver is used for investigation of the course stability of the ship, while both the 1- and 4-quadrant maneuvers are used for simulation of more general maneuvers. The linear part involves simulation of the ship sailing straight ahead at approach speed with only small deviations from the equilibrium state. The 1-quadrant part simulates the maneuvering ship, but it is restricted to forward speeds and fixed forward propeller setting and, finally, the 4-quadrant simulation covers all maneuvering situations, so that it is valid for both ahead and astern speeds and propeller actions. To ensure that the input data is valid for the chosen type of simulation, the independent variable must lie in certain intervals. According to the Mathematical Model Description (ibid.) these intervals are

PMM	linear to DEN-Mark1	
$-0.04 \le v' \le 0.04$	or approximately	$-2° \le \beta \le 2°$
$-0.07 \le r' \le 0.07$	-	$-2° \le \gamma \le 2°$
$\underline{u'} = 0.0$	-	$Fn/Fn_0 = 1.0$

PMM	1-quadrant to DEN-Mark1	
$-0.4 \le v' \le 0.4$	or approximately	$-25° \le \beta \le 25°$
$-1.0 \le r' \le 1.0$	-	$-25° \le \gamma \le 25°$
$-3.0 \le \underline{u'} \le 0.0$	-	$0.3 \le Fn/Fn_0 \le 1.0$

PMM	4-quadrant to DEN-Mark1	
$-1.0 \le v' \le 1.0$	or approximately	$-180° \le \beta \le 180°$
$-\infty \le r' \le \infty$	-	$-90° \le \gamma \le 90°$
$-1.0 \le u' \le 1.0$	-	$-1.0 \le Fn/Fn_0 \le 1.0$

4.3.2 Propeller and Rudder Forces

The independent variables ξ, β' and β^* used in the description of propeller and rudder forces and moments in Chapter 3 must also lie in certain intervals depending on the type of simulation. These intervals are shown in Table (4.1).

	Linear simulation	1-quadrant simulation	4-quadrant simulation
β'-range (deg.)	0 to 90	0 to 90	-180 to 180
β^*-range (deg.)	0 to 90	0 to 90	-180 to 180
ξ-range (deg.)	0 to 90	0 to 90	-180 to 180

Table (4.1) *Ranges for independent DEN-Mark1 variables for different simulations.*

During the linear simulation the three angles are not varying. Thus, each angle represents one single point in the intervals above. Although, it is impossible to say where the points are when the ship is not known, it is certain that the values are found in the intervals shown above. For the remaining two types of simulations, the variables cover more points.

4.3.3 Transformation

When the forces and moments have been measured and brought on a non-dimensional form by means of the PMM format, it is necessary to transform them from non-dimensional hydrodynamic derivatives to non-dimensional forces in DEN-Mark1 format. The first step in this procedure is to identify the hydrodynamic derivatives contributing to each of the forces and moments (on rudder, propeller or hull) used in DEN-Mark1. When this has been done, each of the non-dimensionalized derivatives is dimensionalized from the PMM format. Afterwards they are non-dimensionalized in the DEN-Mark1 format and tabulated as functions of the relevant independent variables. Further information about the transformations is found in the Mathematical Model Description (ibid.), while the forces and moments to be determined are summarized in Section 3.3 in Chapter 3.

4.4 Description of the Individual Tests

The PMM tests performed today usually involve a number of different tests to cover the different types of motions and cross-coupling effects, which are used in the simulator during the simulation. To know what kind of test is required for determination of the different forces (hydrodynamic derivatives) and to design a test program, it is necessary 1) to have an overview of these tests and 2) to know in which parameter ranges the test should be performed. In order to provide this information the different components of the PMM test are described below together with some guidelines for the model test planning. Later these results will be used to design a test program for a PMM test with the model used as test case in the present project.
Initially, it should be mentioned that it is difficult to lay down a set of general guidelines which can be used when a test program is designed, because the program is dependent on the type of simulated maneuver. For simulation of complex maneuvers which for instance involve a ship maneuvering in a harbor it is not possible to say much about the test program, since this requires more detailed knowledge of the case concerned. However, it is most likely that the program must cover speeds and propeller revolutions in all four quadrants, i.e.:

$u > 0$ and $n > 0$	or	$0 < \beta^* \cap \beta' < 90$	1^{st} quadrant
$u > 0$ and $n < 0$	or	$90 < \beta^* \cap \beta' < 180$	2^{nd} quadrant
$u < 0$ and $n < 0$	or	$-180 < \beta^* \cap \beta' < -90$	3^{rd} quadrant
$u < 0$ and $n > 0$	or	$-90 < \beta^* \cap \beta' < 0$	4^{th} quadrant

where u is the longitudinal ship speed and n is the number of propeller revolutions. In the following sections emphasis will be put on 1-quadrant simulations.

4.4.1 Relaxation and Number of Propeller Revolutions

Before the PMM tests are described a few general comments on relaxation and the number of propeller revolutions, which are common to all the tests, will be presented. Relaxation is an additional tow force applied to the model during the test to reduce the scale effects between the full-scale ship and the model. Since the flow problem is scaled on the basis of Froude similarity and therefore does not fulfill Reynolds law, the flows in the stern region of the model and the ship are not hydrodynamically similar. Consequently, the boundary layer is relatively thicker on the model than on the ship, which results in a field of reduced inflow velocity to the propeller. The reduced inflow velocity leads to higher propeller loading and higher slipstream velocity, which again results in overprediction of the rudder performance at the self-propulsion point. In order to reduce this effect, it is commonly tried to reduce the propeller loading by adding an extra tow force to the model, so that the model sails partly under its own power. At DMI the additional tow force F_D is determined as the difference between the frictional resistance coefficient for the model and the ship at the self-propulsion point, i.e.

$$F_D = \frac{1}{2}\rho S_m V_m^2 \left[C_f^m - \left((1+k) C_f^s + C_A \right) \right] \tag{4.4}$$

where ρ is the density, S_m the wetted surface area of the model and V_m the model approach speed. C_f^m and C_f^s are the frictional resistance coefficients for the model and the ship, respectively and, finally, k and C_A are the form and allowance factors, respectively. The friction coefficients are calculated on the basis of the ITTC 1957 friction line:

$$C_f = \frac{0.075}{(\log_{10}(Re) - 2)^2} \tag{4.5}$$

where *Re* is the Reynolds number.
During the PMM test used as a basis for 1-quadrant simulations the number of propeller revolutions is kept constantly equal to the nominal number of revolutions N_0. When the relaxation is estimated by means of (4.4) the number of model propeller revolutions N_0 is determined experimentally in the beginning of the model test. The purpose is to find a number of revolutions resulting in a thrust which outbalances the model resistance minus the relaxation. In many cases the nominal number of propeller revolutions N_0 is used during the whole test, but depending on the ship concerned this may have to be changed. Since a ship usually loses some speed during the maneuver the propeller loading can increase so much that if the real ship performed the maneuver, the main engine would not be able to produce the necessary propeller torque to keep the number of revolutions. Even though it is not done very often, this effect can be modeled. At DMI it is done by applying a "diesel engine simulator" in some of the PMM tests. This simulator is capable of reducing the number of propeller revolutions as function of the propeller torque.

4.4.2 Static Tests

4.4.2.1 "Static Rudder" Test

The basic rudder data is obtained by the so-called "static rudder" test where the model sails straight ahead in the x_0-direction, while the rudder angle δ and the model speed are varied systematically as illustrated in Figure (4.1).

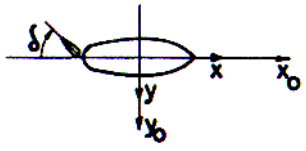

Figure (4.1) *"Static rudder" test.*

For simulations of standard maneuvers like the turning circle test or the zigzag test, which are restricted to straight-ahead sailing and forward-going propeller, it is difficult to define the program exactly. But a few things have to be kept in mind. When the ship initiates the maneuver it sails at the self-propulsion point at a certain speed called the approach speed U_0 and with a nominal number of propeller revolutions N_0. However, since the hydrodynamic forces on the ship increase during the maneuver and the rate of propeller revolutions is kept constant, it is normal to observe that the ship loses some of its speed during the maneuver. In order to capture this effect it is therefore necessary to consider speeds lower than the approach speed.

Rudder effect	Speed effect	Rudder-speed effect
X_0, Y_0, N_0	X_u, X_{uu}, X_{uuu}	$X_{\delta u}$, $Y_{\delta u}$, $N_{\delta u}$
X_δ, Y_δ, N_δ		$X_{\delta\delta u}$, $Y_{\delta\delta u}$, $N_{\delta\delta u}$
$X_{\delta\delta}$, $Y_{\delta\delta}$, $N_{\delta\delta}$		$X_{\delta\|\delta\|u}$, $Y_{\delta\|\delta\|u}$, $N_{\delta\|\delta\|u}$
$X_{\delta\|\delta\|}$, $Y_{\delta\|\delta\|}$, $N_{\delta\|\delta\|}$		$X_{\delta\delta\delta u}$, $Y_{\delta\delta\delta u}$, $N_{\delta\delta\delta u}$
$X_{\delta\delta\delta}$, $Y_{\delta\delta\delta}$, $N_{\delta\delta\delta}$		

Table (4.2) *Hydrodynamic derivatives found by the "static rudder" test.*

So, it is not unusual to perform the "static rudder" test for four to five different u'-values in the range from 0.4 to 1.0, when data is generated for 1-quadrant simulations. The rudder angle δ should be varied systematically at each model speed so that the whole range of angles from maximum starboard to maximum port rudder angle is covered. Usually, steps of five degrees are used to cover the range from $-\delta_{max}$ to δ_{max}. The hydrodynamic derivatives found in the "static rudder" test are shown in Table (4.2).

4.4.2.2 "Static Drift" Test

For determination of the hydrodynamic drift forces acting on the ship during the maneuver, the "static drift" test is carried out. In this test the model travels through the towing tank in the x_0-direction at a preset drift angle β, while the rudder angle is kept constantly equal to zero as illustrated in Figure (4.2).

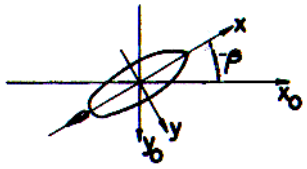

Figure (4.2) *"Static drift" test.*

As in the case of the "static rudder" test, the speed loss experienced throughout the maneuver is taken into account so that the considered speeds should correspond to u'-values in the range from 0.4 to 1.0. During the test the drift angle is varied systematically within a range of -30 to 30 degrees depending on the speed of the model, meaning that small drift angles are used at the high speeds while larger angles are considered at the lower speeds. The idea is that in the beginning of the maneuver, where

the ship speed is close to U_0, only small drift angles are experienced, while the larger drift angles are not observed until later in the maneuver when the ship has lost some of its speed. Usually, drift angles between -4 and 4 degrees are considered in the linear range at U_0 while angles between -10 and 10 degrees are tested at $0.8U_0$.

Drift effects	Speed effects
X_{vL}, Y_{vL}, N_{vL} (L indicates linear)	X_{uv}, Y_{uv}, N_{uv}
X_v, Y_v, N_v	
X_{vv}, Y_{vv}, N_{vv}	
$X_{v\|v\|}$, $Y_{v\|v\|}$, $N_{v\|v\|}$	
X_{vvv}, Y_{vvv}, N_{vvv}	

Table (4.3) *Hydrodynamic derivatives found by the "static drift" test.*

For the remaining speeds the drift angles lie in the range from -30 to 30 degrees. As regards the linear derivatives, they express the slopes of the *X(v)*-, *Y(v)*- and *N(v)*-curves in the linear range, which covers β-values in the narrow interval around β=0°. When the small drift angles in this range at the approach speed U_0 are tested it is important to use a fine resolution and change β in small steps (0.5 to 1 degree). The reason is that the dynamic course stability of the ship is determined on the basis of the linear derivatives for *Y* and *N*, which means that a good prediction of these derivatives is essential for the ability to predict the maneuvering characteristics of the ship. For the larger drift angles at lower speeds larger steps can be used (2, 4 or 6 degrees). The hydrodynamic derivatives found in the "static drift" test are shown in Table (4.3).

4.4.2.3 "Rudder and Drift" Test

The last static case considered in the PMM test is the so-called "rudder and drift" test. This test involves runs where the model travels through the towing tank in the x_0-direction, while the rudder and drift angles are varied as illustrated in Figure (4.3).

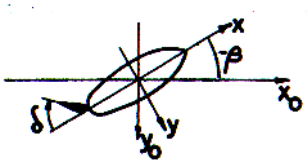

Figure (4.3) *"Rudder and drift" test.*

The purpose of the test is to determine the cross-coupling effects between rudder and drift forces. On the basis of comparison of the combined "rudder and drift" measurements with the "static rudder" and "static drift" results information about the cross-coupling can be extracted. However, in order to do so the "rudder and drift" experiment must contain the same conditions as the "static rudder" and "static drift" tests. Thus, for a given carriage speed the considered rudder and drift angle combinations should contain the same ranges of rudder and drift angles as used in the "static rudder" and "static drift" tests. Usually, the β-values in the range from 10 to 30

degrees are tested at the same rudder angles as in the "static rudder" case. This means that the tests are performed at the low speeds, i.e. u'-values in the range of 0.4 to 0.6, since the large drift angles are to be used here. The hydrodynamic derivatives found in the static "rudder and drift" test are shown in Table (4.4).

"Rudder and drift" effects
$X_{v\delta}$, $Y_{v\delta}$, $N_{v\delta}$
$X_{\delta vv}$, $Y_{\delta vv}$, $N_{\delta vv}$
$X_{v\delta\delta}$, $Y_{v\delta\delta}$, $N_{v\delta\delta}$

Table (4.4) *"Rudder and drift" derivatives.*

In order to round off the description of the static PMM tests it should be mentioned that besides providing information about the forces from the rudder and the drift and the cross-coupling between the two, the tests can also provide useful information about some of the rudder-propeller-hull interaction effects. For instance it is possible to investigate how the effective wake fraction, which plays an important role in relation to propeller and rudder forces, is influenced by changes in the propeller loading, the rudder angle and the drift angle, but also to investigate the rudder-on-hull interaction. However, this requires measurement of both the propeller forces and the local rudder forces during the PMM test.

4.4.3 Dynamic Tests

The dynamic tests are used for determination of the hydrodynamic forces and moments acting on the ship when it is in a sway or yaw motion or in a combined yaw and drift motion. Again as in the static case it is not possible to create a standard test plan which is valid for the 4-quadrant maneuvering simulation, but some guidelines for the planning of the more restricted 1-quadrant simulation are proposed to ensure that the measured forces cover the relevant parameter intervals. However, before the dynamic tests are described, two restrictions on the frequency of the cyclic PMM motions should be mentioned. First resonance in the towing tank must be avoided, i.e. standing waves which disturb the measurements. Hence, the PMM frequency must satisfy

$$\frac{\omega U}{g} \neq \frac{1}{4} \tag{4.6}$$

where ω is the PMM frequency, U is the speed and g is the gravitational constant. Second the model must be sailing in undisturbed water all the time. This can be exemplified as follows. If the model speed is equal to zero, the model will oscillate at the same x_0-position all the time and thus end up in the same region of disturbed water after each oscillation. If the frequency is kept constant and the model instead is given a sufficiently high forward speed, it is possible for the model to return to a region with undisturbed water at an x_0-position where it has not been before. (4.7) ensures that, when the model returns to a y_0-position after one oscillation, the stern of the model is approximately one ship's length in front of the position where the bow was when the oscillation was initiated.

$$\frac{\omega L_{PP}}{U} < 3 \text{ to } 4 \qquad (4.7)$$

In (4.7) ω is the PMM frequency, L_{PP} is the perpendicular length of the model, and U is the ship speed.

4.4.3.1 "Pure Sway" Test

The first dynamic test is the "pure sway" test, which is applied when the acceleration related hydrodynamic derivatives, originating from the sway acceleration, are determined. The test is conducted so that bow and stern are oscillated in phase, which means that the model is sailing straight ahead while it is forced from side to side in order to obtain the pure sway motion, as illustrated in Figure (4.4).

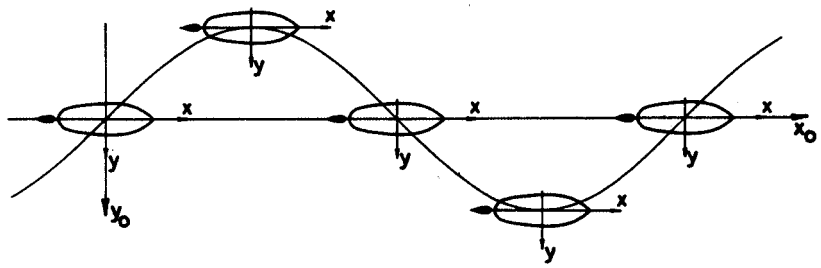

Figure (4.4) *Pure sway test.*

4.4.3.2 "Pure Yaw" Test

The "pure yaw" test is used for determination of the hydrodynamic derivatives with respect to the yaw rate and the yaw acceleration. The test is carried out by oscillating the bow and stern out of phase while the model travels through the tank in the x_0-direction, as illustrated in Figure (4.5). The phase angle is chosen so that the center line of the ship is tangent to the path traveled during the run. The result is a pure yaw motion.

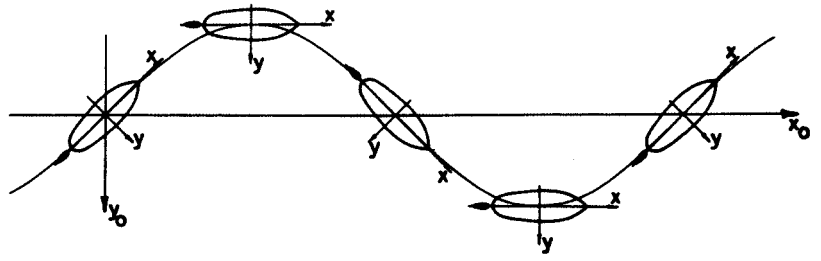

Figure (4.5) *"Pure yaw" test.*

In order to obtain pure yaw and avoid cross-coupling effects the rudder angle δ, the sway velocity v and the drift angle β are kept equal to zero during the test.
The design of the test program should ensure that yaw rates in the range from 0 to 1 are covered. It is most likely that the ship will experience the small yaw rates in the

beginning of the maneuver, while the large yaw rates will occur later, when the ship has lost some of its speed due to the increased forces occurring during the maneuver. This is accounted for by considering different speeds as in the "static drift" test. r'-values are considered in the range from 0.05 to 0.3 at the approach speed U_0 while r' is varied in steps of 0.05 to 0.1. The larger r'-values must cover the range from 0.15 to 1.0 at speeds in the range from $0.4U_0$ to $0.6U_0$. In this case the r'-step size should be chosen in the range of 0.1 to 0.2. Table (4.5) shows the hydrodynamic derivatives obtained by the "pure yaw" test.

"Pure yaw"	Correction for speed influence
X_{rL}, Y_{rL}, N_{rL} (L indicates linear)	X_{ru}, Y_{ru}, N_{ru}
X_r, Y_r, N_r	X_{ru}, Y_{ru}, N_{ru}
X_{rr}, Y_{rr}, N_{rr}	$X_{\|u\|r}$, $Y_{\|u\|r}$, $N_{r\|u\|}$
X_{rrr}, Y_{rrr}, N_{rrr}	X_{urr}, Y_{ruu}, N_{ruu}
$X_{r\|r\|}$, $Y_{r\|r\|}$, $N_{r\|r\|}$	

Table (4.5) *"Pure yaw" related hydrodynamic derivatives.*

4.4.3.3 "Drift and Yaw" Test

When the ship performs a turn it experiences a yaw motion. However, it is not pure yaw because the ship is drifting at the same time. The effect of cross-coupling between drift and yaw is found by means of the "yaw and drift" test. The cross-coupling is found as the difference between the forces measured in the "drift and yaw" test and the sum of the forces measured in the "pure yaw" and "pure drift" tests. The yaw motion in the test is generated in the same manner as in the "pure yaw" test, while the drift contribution is included by turning the model so that it travels with a constant angle to the tangent of the traveled path as illustrated in Figure (4.6).
When the test is performed it is again important to cover r'-values in the range from 0 to 1.0 and to include the effect of the speed loss by considering the approach speed as well as the lower speeds. To extract the cross-coupling effects it is necessary to perform the test at speeds, drift angles and yaw rates in the same ranges as used in the "pure drift" and "pure yaw" tests. Table (4.6) shows the hydrodynamic derivatives to be determined in this test.

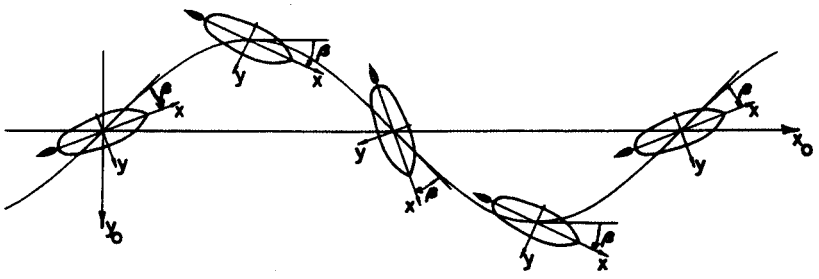

Figure (4.6) *"Drift and yaw" test.*

Derivatives for influence of "yaw and drift" cross-coupling
X_{vr}, Y_{vr}, N_{vr}
$X_{v\|r\|}$, $Y_{v\|r\|}$, $N_{v\|r\|}$
Y_{vrr}, N_{vrr}
$Y_{\|v\|r}$, $N_{\|v\|r}$
Y_{vvr}, N_{vvr}

Table (4.6) "Yaw and drift" derivatives.

The description of the PMM test shown above is relatively detailed. But further information about standard PMM tests can be found in ITTC (1996) and ITTC (1999), where guidelines for test facilities, model, testing technique and analysis of measurements are given.

4.5 Summary

In the present chapter different subjects related to the PMM testing technique, which is the primary method for generation of hydrodynamic input data to the maneuvering simulator, were described to give an overview of the method. First, the description briefly dealt with the range of validity of the test results for a certain type of maneuver and the transformation between the two different data representations of the DEN-Mark1 and the PMM nomenclatures. Second, the individual components of the PMM test were described in more detail and it was seen that the test involved various tests in order to generate sufficient amounts of hydrodynamic data for the simulation. Third, guidelines to be used in model test program design were proposed together with comments on relaxation and critical PMM frequencies. Finally, it should be noted that the results from the present chapter were applied to the design of a PMM test program, which was used for the PMM test described in Chapter 5.

Chapter 5

Experimental Investigation of Interaction Effects

5.1 Introduction

Today most of the rudder-propeller-hull interaction effects used in maneuvering simulation are determined on the basis of experiments where the integral quantities like the propeller thrust and torque, the rudder forces and the hull forces are measured. Thus, general tendencies of the overall behavior of the forces can be determined and information about the rudder, propeller and hull interaction can be derived on the basis of the forces. However, detailed information about the flow phenomena causing the interaction effects are difficult to obtain, because this would require comprehensive measurements of the field quantities in the flow field, which is time-consuming and expensive, or alternatively numerical investigations of the flow field.

In the present chapter it is tried to illustrate some of the interaction effects determined at the integral level by use of experimental results from measurements in the towing tank at the Danish Maritime Institute in connection with the present project. The model test is conducted with a model of the tanker Esso Osaka which is used as a benchmark case in maneuvering simulation. In Chapter 3 an overview of the rudder-propeller-hull model in DEN-Mark1 was provided, including the interaction effects between rudder, propeller and hull, and in Chapter 4 the experimental methods used for generation of data for this purpose were described. Based on the findings presented in these two chapters, a model test program was designed and a PMM test was carried out in order to provide the necessary data for the investigation of the interaction effects.

The work in the present chapter focuses on the following topics: Investigation of the hull-on-propeller and hull-on-rudder interactions by means of the effective wake fraction w, considered for different propeller loads and rudder angles, illustration of the propeller-on-rudder and the rudder-on-hull interaction effects by means of the global hull forces and the local rudder forces for different propeller loads and rudder angles and, finally, illustration of the rudder-on-propeller interaction by means of the propeller forces for different rudder angles. Unfortunately, it has not been possible to investigate the propeller-on-hull interaction, which is expressed by the thrust deduction fraction t. The thrust deduction fraction is calculated on the basis of the thrust and the model

resistance, but due to some technical problems with the *X*-force measurement, this force was not measured and, consequently, *t* could not be calculated.

5.2 Selection of the Esso Osaka as Test Case

In the area of maneuvering simulation it is difficult to validate the results of full-scale maneuvering simulations, which are usually based on model test data. The reason is that full-scale data is usually sparse since it is expensive and difficult to perform detailed full-scale measurements. However, in 1977 Exxon, the U. S. Coast Guard et al. performed a comprehensive full scale test in the Gulf of Mexico with the 278,000 DWT tanker Esso Osaka to provide a set of detailed maneuver data, which could be used to improve the quality of the numerical maneuvering models. The results were presented in Crane (1979). In 1981, four years after the tests had been performed, the maneuverability committee under ITTC laid down the first recommendations about use of the Esso Osaka tanker as a benchmark case in research on the model-to-ship correlation for maneuvering simulations. In the following years, much work was carried out in order to develop and test the numerical maneuvering models and to study subjects like the model-to-ship correlation and deep/shallow water effects by comparison of the simulations with the full-scale data.
Most of the research on maneuvering has been concentrated on the maneuvering simulation itself, i.e. the simulation of full-scale maneuvers based on overall hydrodynamic forces *measured* in the towing tank. However, lately numerical methods have been focused on to a higher degree for *calculation* of the hydrodynamic simulator input data, but also for detailed investigations of the flow field itself in order to improve the understanding of phenomena like the rudder-propeller-hull interaction. It is most likely that the Esso Osaka will again be a part of this research since the 22nd ITTC has established a separate committee dedicated to concentrate on Esso Osaka. On the basis of these facts, it was decided to concentrate on the Esso Osaka in the present project and use it for both the experimental and numerical work even though it is a full form ship, which requires more of the numerical method than for instance a slender hull form. The body plan and the main particulars of the Esso Osaka are shown in Appendix A.

5.3 Description of Model Test

The concept of the PMM testing technique was described in Chapter 4, so more information about this topic should be found in that chapter and the references listed there. The present section is used for a brief description of the practical aspects of the model test.

5.3.1 Model Condition

The PMM test was carried out in the 240 meters long, 12 meters wide and 5.5 meters deep towing tank at Danish Maritime Institute (DMI) with a model of the Esso Osaka built in the model scale 1:43.8783, corresponding to a length between the perpendiculars

equal to 7.475m and a displacement of 3.791 tons. In accordance with the full-scale ship the model was equipped with a rectangular rudder with heel. The full-scale rudder was mounted in two bearings: One at the rudder stock and one at the heel, but to be able to measure the local rudder forces, the model rudder was only mounted at the rudder stock. The real ship was equipped with a five-bladed propeller, but it was not possible to find an existing five-bladed model propeller matching the full-scale propeller with respect to pitch ratio and area ratio. Therefore, a four-bladed propeller with approximately the same pitch and area ratios was used instead. The propeller was driven by an electric motor, which allowed the number of propeller revolutions to be adjusted during the test. The rudder-propeller arrangement of the model is shown in Figure (5.1.b). The model particulars are shown in Appendix A together with the rudder and propeller data.
When low speed models are tested in the towing tank, it can be difficult to obtain a turbulent boundary layer with an extension over the model, which is similar to the full-scale ship. Usually, the boundary layer on the relatively rough surface of the ship becomes turbulent close to the bow, while the transition on the smooth model occurs further downstream along the hull. Since the resistance is influenced by the extension of the turbulent boundary layer it is important to ensure, that the boundary layer is turbulent over most of the model to be able to match the full-scale condition. For this purpose different turbulence triggering devices were applied to the model. At the bow a set of standard studs was mounted as illustrated in Figure (5.1.a) and, in addition to this, two 2mm wires were mounted around the hull at stations 3 and 6 corresponding to 2.243m and 4.485m forward of AP.

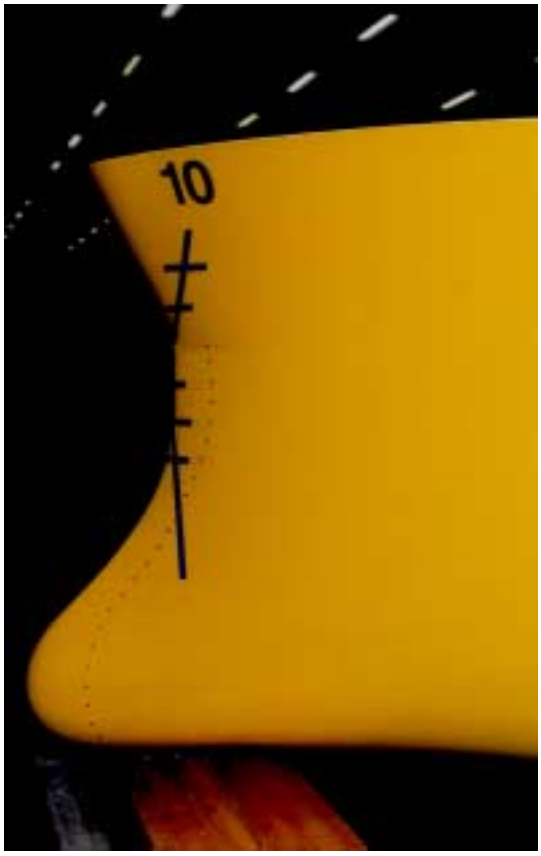

a. *Turbulence triggering studs.*

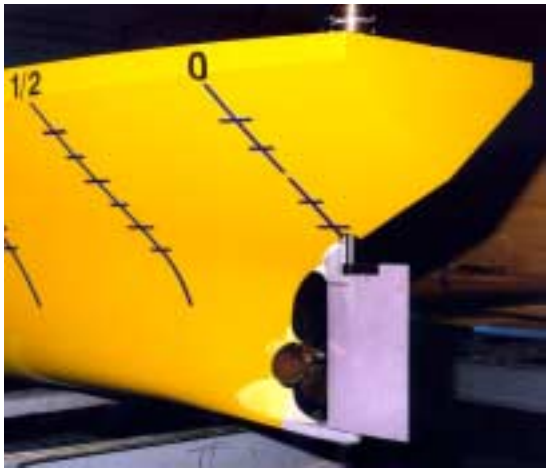

b. *Rudder-propeller arrangement.*

Figure (5.1) *Model of the Esso Osaka.*

Figure (5.2) *Model mounted in the PMM below the carriage.*

5.3.2 Model Test

During the test the model was attached to the planar motion mechanism where it was free to heave and pitch in the vertical plane, but otherwise constrained. The set-up is illustrated in Figure (5.2). The model was connected to the PMM by two gauge arrangements, which measured the longitudinal and the transverse global forces acting on the model plus the squat. The forward force gauge was placed 1.499m forward of the midship section while the aft force gauge was placed 1.501m aft of the midship section. In addition to the global forces, the local lift and drag forces acting on the rudder, the propeller thrust and torque, the number of propeller revolutions, the carriage speed and the rudder angle were also measured.
The model test was carried out at an approach speed (the speed of the ship as it initiates the maneuver) corresponding to 10 knots in full-scale. On the basis of scaling by Froude's law the result was a model approach speed equal to U_0=0.780m/s. In order to account for the Reynolds related scale effects mentioned in Chapter 4, the test was carried out with a relaxation equal to F_D=9.82N. With this relaxation the nominal number of model propeller revolutions was found to be N_0=310rpm. The complete test program, which was generated on the basis of the content of Chapter 4, is shown in Appendix B.

5.4 Experimental Investigation of Interaction Effects

According to the description of the maneuvering model in Chapter 3, some of the basic information about the rudder-propeller-hull interaction effects initially could be extracted from the straight-ahead condition and then later corrected for oblique flow occurring from drift and yaw. In order to illustrate some of these basic interaction phenomena and use them as a basis for the numerical study of the interaction effects, the results presented in this section were all obtained for the straight-ahead condition modeled by the tests called: "Static rudder" and "Runs for estimation of effective wake

fraction: δ=0° and β=0°" in the test program shown in Appendix B. Figure (5.3) shows the model during the static rudder test.

Figure (5.3) *Static rudder test.*

5.4.1 Effective Wake Fraction

As seen from Chapter 3 one of the important quantities in rudder-propeller-hull interaction is the effective wake fraction *w*, used for calculation of the speed of advance u_a, which is again used for calculation of the rudder and propeller forces in the DEN-Mark1 maneuvering model. The effective wake fraction is mainly introduced to account for the retarding influence of the hull on the inflow velocity field to the propeller and rudder, and it can be determined experimentally by application of the thrust or torque identity methods. On the basis of the thrust identity method used in the present project, *w* is found from the relative difference between the advance coefficient for a propeller in open water J_T and a propeller behind the model J_V when they yield the same thrust. This can also be expressed as

$$w = 1 - \frac{J_T}{J_V} \tag{5.1}$$

The two advance coefficients are defined as

$$J_T = \frac{u_a}{n D} \tag{5.2}$$

and

$$J_V = \frac{V}{n D} \tag{5.3}$$

where u_a is the speed of advance and D is the propeller diameter. The procedure for calculation of w consists of the following steps: First the thrust T, the number of propeller revolutions n and the model speed V are measured in the considered model condition. Then J_V is calculated from (5.3) and K_T from

$$K_T = \frac{T}{\rho n^2 D^4} \tag{5.4}$$

where ρ is the density of the water. Afterwards, the calculated K_T is used together with the open water propeller diagram to determine J_T and, finally, the two known J values are inserted in (5.1) to determine w.

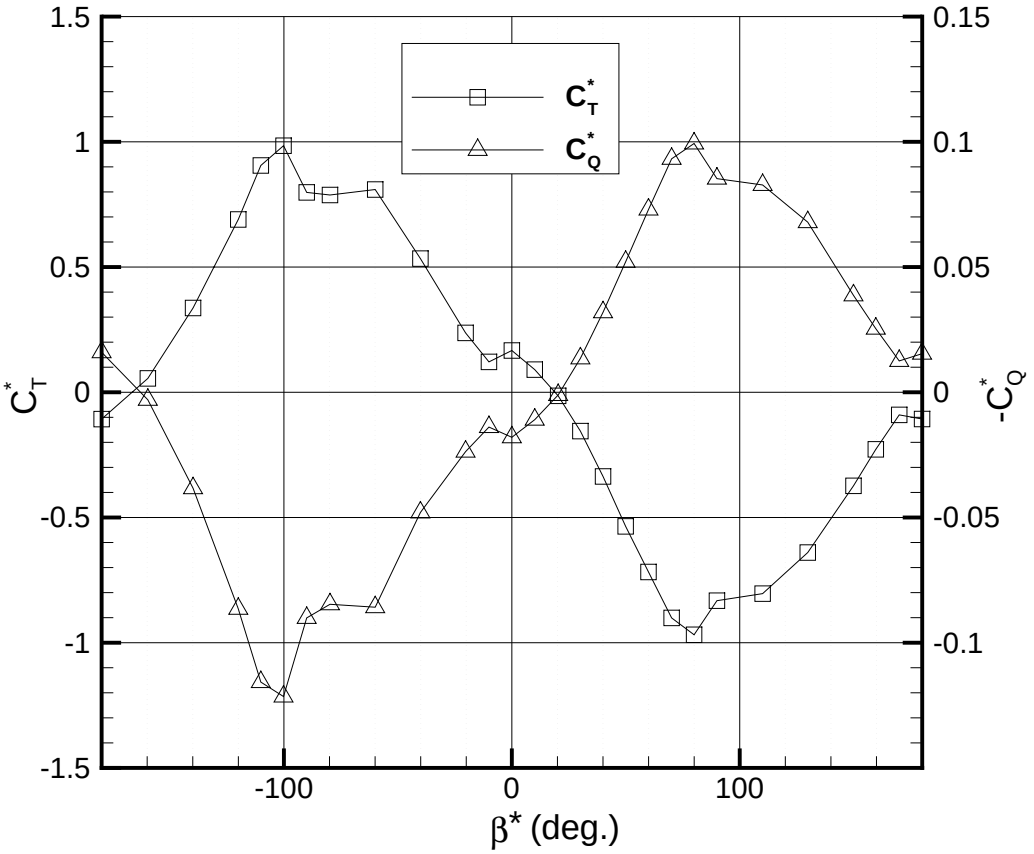

Figure (5.4) *4-quadrant open water propeller diagram.*

However, according to the findings in Chapter 3, w is not constant since it depends on the propeller loading, the rudder angle and the maneuvering motion. Thus, if w is to be used in a maneuvering simulation, it must be calculated for the conditions, which the ship is expected to experience during the simulation, in order to cover the variations in w. Usually, the PMM test program is designed to cover these conditions, so it should be possible to determine w for the simulation on the basis of the thrust measured during the test.

Since the calculation of the effective wake fraction also requires the open water characteristics for the model propeller, an open water test was carried out. The resulting open water curves are shown in Figure (5.4). The propeller diagram contains all four quadrants which means that the propeller was tested in the conditions described in Table (5.1). It should be noted that the thrust *T* and the torque *Q* were non-dimensionalized in DEN-Mark1 format, so instead of using *J*, K_T and K_Q the corresponding DEN-Mark1 variables β^*, C_T^* and C_Q^*, which are defined in Chapter 3, were applied.

Sailing direction	Propeller rotation	β^* in degrees	Quadrant
Astern	Backing	-180 to -90	III
Astern	Forward	-90 to 0	IV
Ahead	Forward	0 to 90	I
Ahead	Backing	90 to 180	II

Table (5.1) *Test conditions for 4-quadrant open water test.*

It should also be noted that if the 4-quadrant diagram is related to the traditional propeller diagram, applied to the self-propulsion test, the data in the range from β^* equal to 0 to approximately 20 degrees corresponds to the traditional test.

5.4.1.1 Effective Wake Fraction, without Rudder Angle

If the investigation of the effective wake fraction is returned to, it was mentioned that *w* was assumed to depend on the propeller loading, the drift angle and the rudder angle in the maneuvering model, but since the study was limited to straight-ahead sailing, the drift angle dependence was not investigated. Therefore, the first interaction effect covered the influence of the propeller loading on *w*, when the model was sailing straight ahead with zero rudder angle. Based on the open water data and the relevant PMM data from the "Runs for estimation of effective wake fraction: δ =0° and β=0°" test, the results shown in Figure (5.5.a), were found. The figure shows the normalized effective wake fraction w/w_0 as a function of the propeller loading angle β'. The effective wake fraction was normalized with the effective wake fraction w_0 =0.51, corresponding to the self-propulsion point at the approach speed, U_0=10 knots or β'=18.3°. Results for two different conditions were considered. First, a number of 1st quadrant conditions corresponding to ahead-sailing ship and forward-going propeller. It was found that when the propeller loading was increased to a heavier load than the one corresponding to self-propulsion the effective wake fraction was decreasing, while the effective wake fraction was increasing when the propeller loading was decreased to a lighter one than the self-propulsion loading. Second, a few 2nd quadrant conditions corresponding to ahead-sailing ship with backing propeller occurring when the ship performs a crash stop maneuver. Again it was observed that the effective wake fraction was decreasing with increasing propeller loading. Generally, there was a relatively large variation in the effective wake fraction, which indicated the necessity for taking it into account in the simulation. The behavior as regards decreasing effective wake fraction as a function of increasing propeller loading seemed qualitatively reasonable, because the same behavior was observed in model test results for the Esso Osaka presented by Kijima et al. (1985).

However, quantitatively it was difficult to compare the results since the effective model wake fractions were different due to different model sizes. The length of the model applied by Kijima et al. (ibid.) was 2.5m compared to 7.475m for the present model. In order to get an idea of the quantitative level, the effective wake fraction at the self-propulsion point, w_0 =0.51 from the present model test, was compared with w_0 =0.55 for a 7.222m model presented in HSVA (1986). If it is taken into account that the propellers and the model lengths of the two models were not exactly the same, the agreement appeared to be fair.

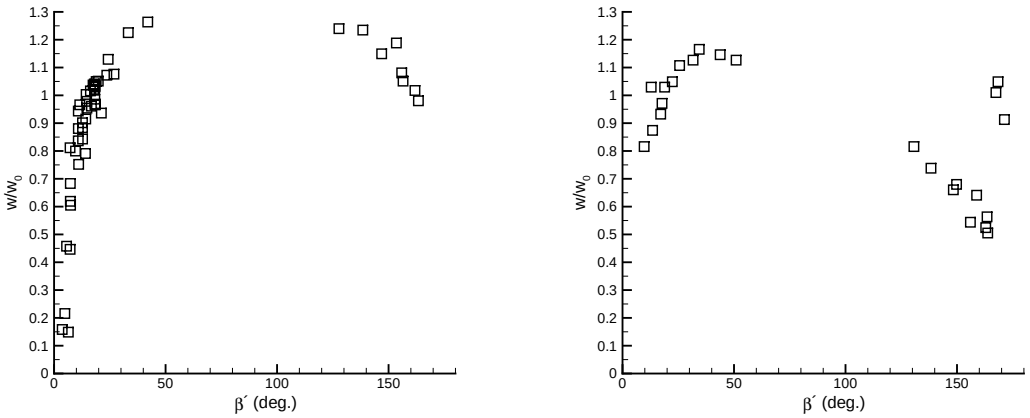

a. Present experiment for Esso Osaka *b. Data for bulk carrier, Harvald (1976)*
Figure (5.5) *Influence of propeller loading on effective wake fraction.*

Since experimental effective wake fraction data is relatively sparse for extreme propeller loadings, it could be interesting to compare the measured data with some of the sparse existing data. Therefore, the measured effective wake fractions for the Esso Osaka were compared with data measured for a bulk carrier model of approximately the same size as the Esso Osaka model. The bulk carrier was equipped with spade rudder and a four-bladed propeller with a pitch ratio equal to 0.65 and developed blade area ratio equal to 0.533, which was different from the Esso Osaka model propeller (See Appendix A). The data for the bulk carrier, found in Harvald (1976), was plotted in Figure (5.5.b) after normalization with w_0 =0.51, which for this data corresponded to β' =18.3°. From the two plots in Figure (5.5) it is found that for the β'-values in the range from 0 to 60 degrees, the effective wake fraction follows the same tendency for both ships, even though the Esso Osaka data is higher than the bulk carrier data. As to the backing propeller, i.e. for β' in the range of 120 to 180 degrees, the picture is somewhat different, since w/w_0 is sometimes lower than the Esso Osaka data and in a few other cases is of approximately the same magnitude. It is difficult to point out the exact cause of the difference on the basis of data for only two ships, but it can be that w/w_0 is more sensitive to differences in hull form, rudder arrangements and propeller parameters when the propeller is backing than when the ship is sailing ahead with forward-going propeller.

5.4.1.2 Effective Wake Fraction, with Rudder Angle

The next investigation involved a study of the influence of the rudder angle on the effective wake fraction for constant propeller loading angle and the ship sailing straight ahead. Figure (5.6) shows the normalized effective wake fraction for different rudder angles δ at four fixed 1st quadrant propeller loading angles. For each propeller loading the effective wake fraction was normalized with *w* corresponding to δ=0° at the considered propeller loading angle, in order to remove the variation caused by the influence from the propeller loading. The results show that *w* was generally influenced by changes in the rudder angle and that the influence appeared to be most significant for the largest rudder angles. The increase in *w* was not symmetric around δ=0°, but this effect was most likely caused by the asymmetric flow introduced by the rotating propeller. For all the β′-values ranging from 10.9° to 18.3° the effective wake fraction was found to increase with increased rudder deflection. It followed a tendency where changes in δ in general appeared to affect *w* less with increasing propeller loading for large negative rudder angles. For the large positive rudder angles it was difficult to describe the tendency because of the scatter in the data, but the opposite behavior might be observed for large positive rudder angles, i.e. the heavier propeller loading, the larger influence on the effective wake fraction by the rudder angle.

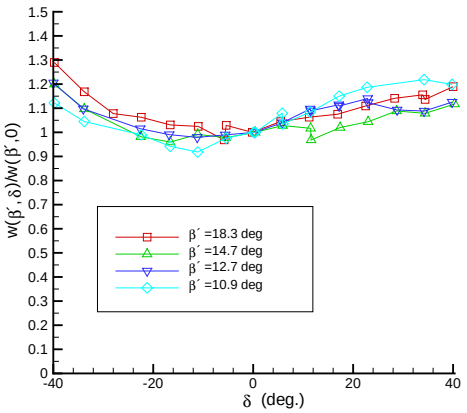

Figure (5.6) *Influence of rudder angle on the effective wake fraction.*

5.4.2 Rudder Forces

For an examination of the local influence of the propeller loading on the rudder, placed in the slipstream of the propeller, the lift and drag forces were measured directly on the rudder while the propeller loading was varied. The measured forces were non-dimensionalized by means of the speed of advance u_a and the slipstream velocity u_s as described in Chapter 3, and the resulting lift and drag coefficients, C_{YR} and C_{XR} were plotted as functions of the rudder loading angle ξ in Figures (5.7) and (5.8), respectively.

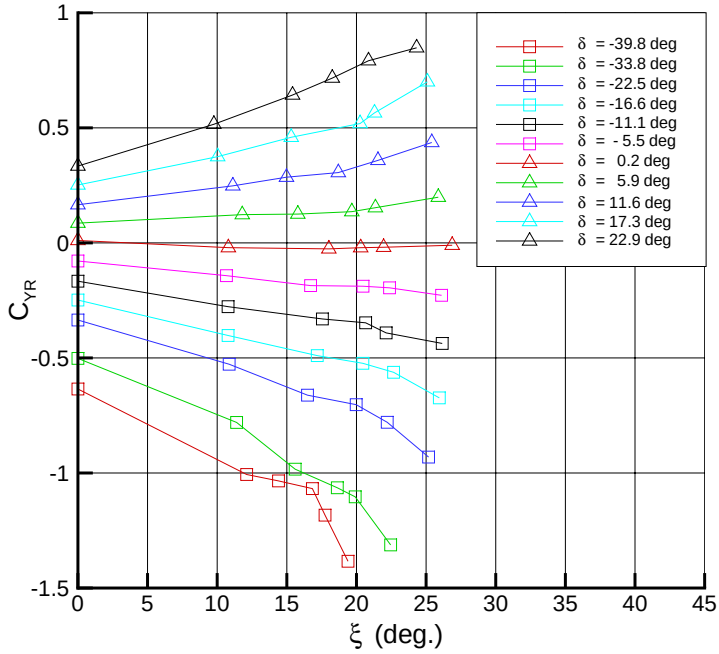

Figure (5.7) *Influence of propeller loading on local rudder lift force.*

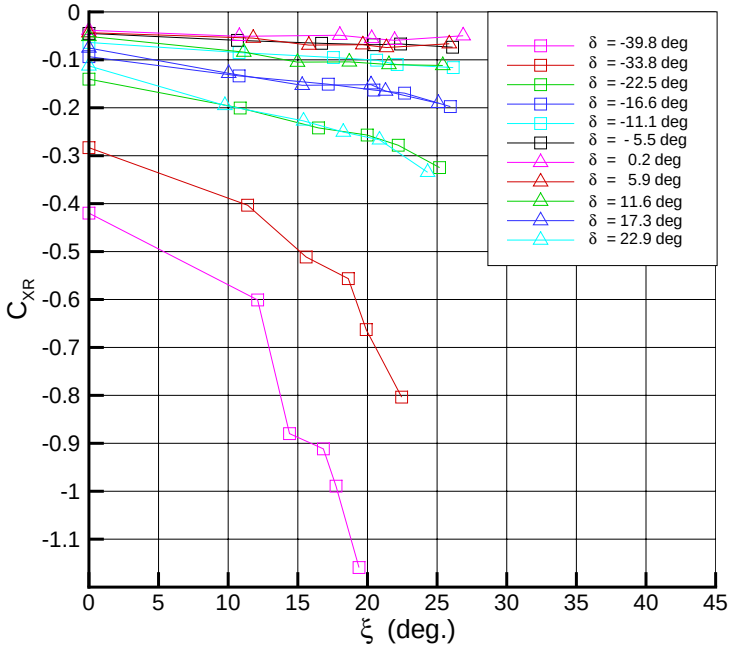

Figure (5.8) *Influence of propeller loading on local rudder drag force.*

According to the definition of the rudder loading angle (5.5), ξ does not directly involve the propeller loading, but it includes the propeller slipstream velocity, which is an expression for the propeller loading:

$$\xi = Arctan^{s}\left(\frac{u_a}{u_s}\right) \tag{5.5}$$

Concerning the lift, the results in Figure (5.7) show that for fixed rudder angle, C_{YR} was affected by changes in the rudder loading angle and consequently also by the propeller loading. The tendency was that the *Y*-force coefficient was increasing with increasing rudder loading angle. Moreover, it is seen that the lift or *Y*-force coefficient was generally negative for δ=0.2° even though the rudder angle was positive. However, this could be explained by the rotation of the flow in the propeller slipstream, which changed the local angle of attack at the rudder. The drag force coefficient C_{XR}, which is shown in Figure (5.8), was also found to be influenced by the propeller loading and it generally showed the same behavior as C_{YR}, i.e. increasing force coefficient with increased rudder loading angle.

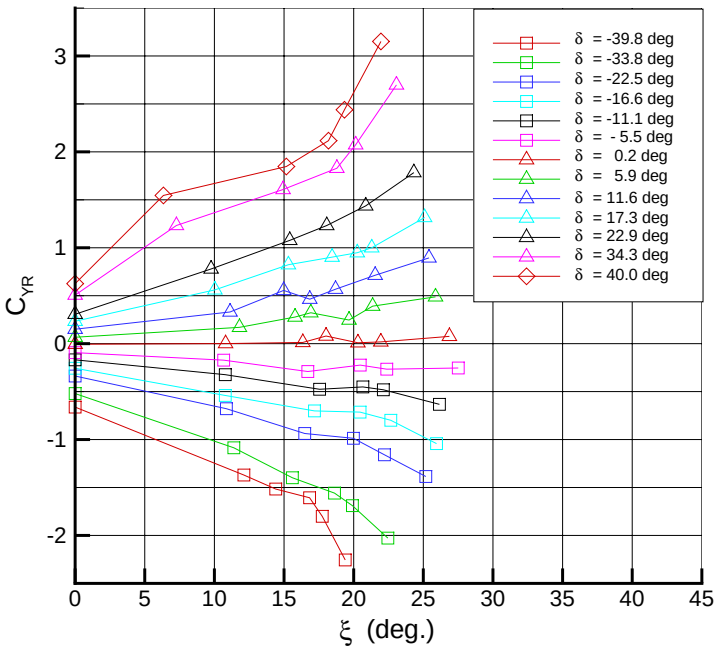

Figure (5.9) *Influence of propeller loading on global rudder lift force.*

When the rudder is turned under the straight-ahead sailing condition, the *Y*-force measured locally on the rudder should be expected to be equal to the *Y*-force measured globally on the total model. But this is not the case, because as mentioned in Chapter 2 the presence of the turned rudder behind the ship increases the global transverse force on the model compared to the local transverse force measured directly on the rudder. From a maneuvering point of view the transverse *Y*-force plays an important role, so in order to investigate this in more detail, the overall or global transverse hull force coefficient was plotted in Figure (5.9) under the same test conditions as the local rudder force in Figure (5.7). Figure (5.9) shows that the global C_{YR} behaved as the local ditto with respect to the influence of the propeller loading, but as expected it also seemed to be

higher. This effect is more clearly seen in Figure (5.10) where the global (Gl.) and local (Lo.) force coefficients were plotted together for some of the rudder angles.

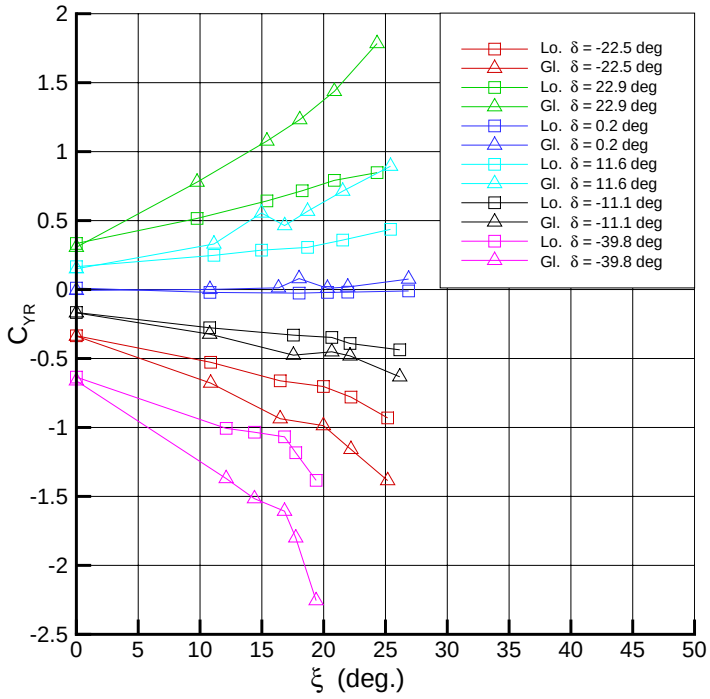

Figure (5.10) *Comparison between local and global rudder lift forces.*

Depending on the mathematical maneuvering models this rudder-hull effect can be included in the simulation in different ways. In the DEN-Mark1 simulator no separate model for this interaction effect is implemented, so in order to include the effect the global forces are used directly. In other models, like the one applied Kose et al. (1985), also known as the MMG model, the local rudder forces are used together with an experimentally determined factor $(1+a_H)$, which accounts for the interaction by means of the relation

$$C_{YR}^{Global} = (1+a_H)\, C_{YR}^{Local} \qquad (5.6)$$

In an attempt to quantify the rudder-on-hull interaction and investigate how it was influenced by propeller loading and rudder angle, a_H was calculated for some of the measured rudder forces by use of (5.6) and the resulting a_H values were plotted in Figure (5.11.a) for negative rudder angles and in Figure (5.11.b) for positive rudder angles.

From the results in Figure (5.11) it is seen that the interaction depends on both the rudder angle δ and the rudder loading angle ξ. With respect to the rudder angle influence it is found that the interaction is different for positive and negative rudder angles, since the a_H values seems to be larger when δ is positive than when it is negative. This behavior is most likely caused by the rotation of the propeller. Besides, there is a tendency towards the negative rudder angles, which indicates, that a_H is increasing with the rudder angle. For the positive rudder angles, the opposite behavior is observed. However, due to the fluctuations in the data it is difficult to obtain a clear picture of the

relation. Concerning the influence of the rudder loading angle, the interaction is found to be relatively small for the bullard pull condition corresponding to ξ=0°, but also that it becomes stronger with increasing rudder loading angle. Without detailed knowledge of the flow, it is difficult to explain exactly why the global rudder forces are larger than the local ditto, but it is possible that the presence of the rudder changes the flow in a way which influences the pressure field on the hull surface, with increased transverse hull forces as a result.

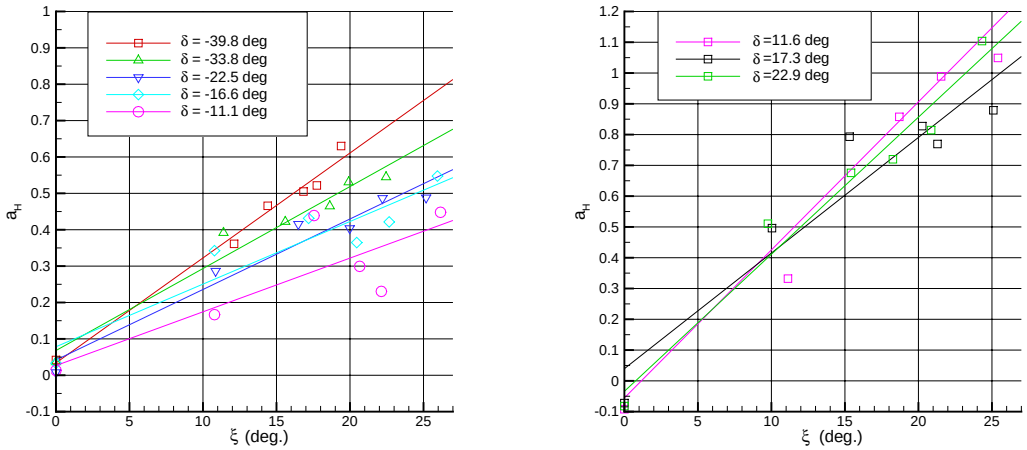

a. Negative rudder angles *b. Positive rudder angles*

Figure (5.11) *Influence of rudder on hull forces.*

To relate the a_H-values in the present work to results presented in the literature, it should be noted that Kijima et al. (1990), based on model tests, suggest $a_H \approx 0.81$ for $C_b \approx 0.81$. Moreover, Kose et al. (1986) summarize different experimental data obtained by Yoshimura et al. and Haseqawa et al.. The first suggest $a_H \approx 0.61$ while the latter suggest a_H to be in the range from 0.1 to 1, depending of the propeller loading and the rudder angle. Compared to the results shown in Figure (5.11) it seems that the a_H-values from the literature and the present findings are in the same range.

5.4.3 Propeller Forces

The last experimental results presented in this chapter concern the propeller thrust and torque measured during the straight-ahead part of the PMM test. The measurements are presented to illustrate how the rudder influenced the propeller forces, when the model speed and the number of propeller revolutions were kept constant while the rudder angle was varied. The measured thrust T and torque Q for five different propeller loading angles were non-dimensionalized to DEN-Mark1 format by

$$C_T^* = \frac{T}{½\ \rho\ \left[u_a^2 + (0.7\ \pi\ n\ D)^2\right]\ A_p} \qquad (4.7)$$

$$C_Q^* = \frac{Q}{½\ \rho\ \left[u_a^2 + (0.7\ \pi\ n\ D)^2\right]\ A_p\ D} \tag{4.8}$$

where u_a, n, D, A_P and ρ are the speed of advance, the number of propeller revolutions, the propeller diameter, propeller disk area and the density, respectively. The resulting coefficients C_T^* and C_Q^* are plotted in Figure (5.12), which shows that the thrust and the torque coefficients are influenced by variations in the rudder angle and that they vary in the same manner. Generally it seems that both C_T^* and C_Q^* are increasing with increasing rudder angle, which may be explained by the rudder blocking an increasingly larger part of the propeller slipstream, the more the rudder was turned. This probably caused the propeller load to increase. Additionally, the variation of C_T^* and C_Q^* is not symmetric around δ=0°, since the influence appears to be largest at large negative rudder angles. This most likely has to be explained by the rotational direction of the propeller in conjunction with the presence of the hull above the rudder. Finally, it is found that the rudder angle influence seems to be more significant at the propeller loading angle β'=18.3°, corresponding to the self-propulsion point than at β'=0° corresponding to the bullard pull condition.

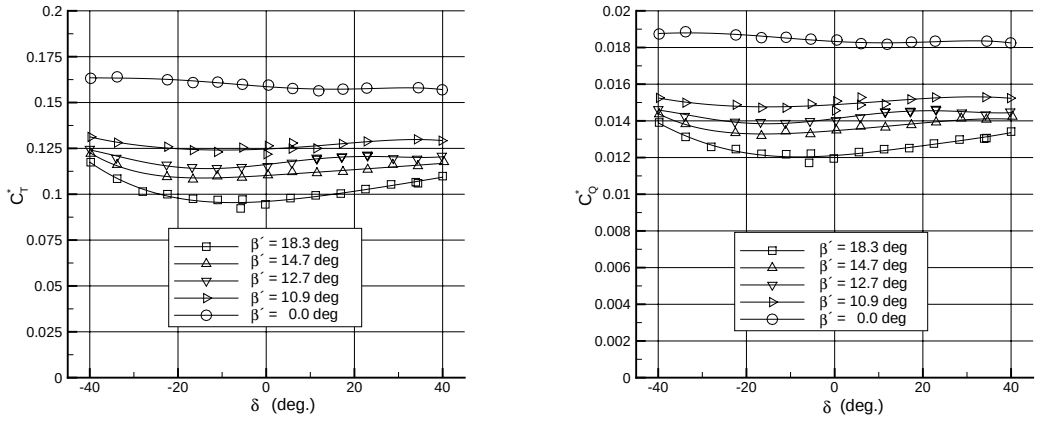

a. *Thrust* b. *Torque*

Figure (5.12) *Influence of rudder angle on propeller forces.*

5.5 Summary

In the present chapter data measured by use of the PMM technique was extracted and presented. The objective was to illustrate some of the interaction effects occurring between the rudder, propeller and hull for the straight ahead-condition and to provide data which could be used as a basis for a numerical study of the interaction effects. The experimental investigation was performed on an integral basis, so that all the presented data either consisted of the measured forces themselves or was derived from the forces. Therefore, it could only provide information about the overall behavior of the effects and not about the features in the flow causing the effects. All the results were presented in the DEN-Mark1 format, which was described in Chapter 3.

The first considered quantity was the effective wake fraction *w*, which usually accounts for the retarding effect of the hull on the propeller inflow when the propeller is working behind the ship. The effective wake fraction was derived from the measured thrust for the open water propeller and the propeller behind the ship. The results showed that *w* could not be assumed to be constant during the simulation, since it varied with both propeller loading and rudder angle.
The next results concerned the local rudder lift and drag forces measured directly on the rudder. Since the rudder was placed in the propeller slipstream it was found that the propeller loading had a relatively strong influence on both lift and drag. A further study of the global *Y*-forces, measured on the model under the same conditions as the rudder forces, showed that the global forces followed the same tendency regarding the influence from the propeller loading, but also that they were larger than the local rudder forces. The increase in the forces could be explained by the influence of the rudder and the propeller on the hull surface pressure. It was quantified by the factor a_H laying in the range from approximately 0 to 1.2, indicating that the global forces in some cases were more than twice as high as the local rudder forces. Unfortunately, it was not possible to present data for the global *X*-forces, due to technical problems during the model test.
Finally, the propeller thrust and torque were measured for constant model speed and number of propeller revolutions and it was found that the rudder, probably because of the blocking effect, influenced both thrust and torque when it was turned.

As seen from the experimental results above, different kinds of rudder, propeller and hull interaction effects appear when the rudder and the propeller are working behind the ship. These effects need to be modeled in order to perform a good manoeuvering simulation. However, to be able to suggest new or improve the existing interaction models, a good understanding, not only of the overall behavior of the hydrodynamic forces, but also of the details of the flow pattern in the stern region of the ship, is important. Seen in relation to this, the applied experimental method gave information of the overall behavior of the hydrodynamic forces, but it did not give any flow field data, which made it difficult to explain the phenomena causing the interaction. In order to obtain this kind of detailed information about the properties of the flow field around the ship a comprehensive experimental study could be conducted. However, an experimental study of this kind is probably too comprehensive and expensive, so another method is needed. This other method could be a numerical interaction model like the one applied in the present project. The benefit of a numerical method is that it can provide both the same integral quantities as the experiment and the desired field data for most of the flow field. It may be that the method cannot predict the integral forces quantitatively correctly, but if it could give a good qualitative picture of the flow field, it could be used for a study of the flow in order to obtain information about the interaction at this level. Hopefully, the knowledge gained by such a study could lead to a better understanding of the interaction phenomena, which again could be used for improving the mathematical interaction models in the DEN-Mark1 simulator. The work, which was carried out to investigate the possibility of applying a numerical model to the study of rudder, propeller and hull interaction, is presented in the following chapters.

This page is intentionally left blank.

Chapter 6

Viscous CFD Methods

6.1 Introduction

The purpose of the present chapter is to summarize the results of a literature study covering the viscid CFD methods used in ship hydrodynamics today. It is intended to provide an overview of the state of the art as regards the use of CFD for hydrodynamic input data generation for maneuvering models. Models which can be used for investigations of rudder-propeller-hull interaction are of special interest.
Methods used in the field of Computational Fluid Dynamics are often designated by the abbreviation CFD methods, which cover two types: the inviscid and the viscous ones. The inviscid methods are usually based on potential theory while the viscous methods are usually based on solution of the Navier-Stokes equations. The inviscid methods were described in Chapter 2 where focus was placed on the state of the art within maneuvering, while this chapter is dedicated to the viscid methods. Since a viscid method is applied to the calculations in the present project a brief description of the theory behind these methods will be presented in the first part of the chapter. Subsequently, the results of a literature study will be presented in order to provide an overview of the practical application of viscid methods today.

6.2 Methods Based on Solution of the Navier-Stokes Equations

The viscous methods have traditionally been used for calculations of flow problems where turbulence, boundary layer, wake and viscous resistance are important. The methods are based on numerical solution of the Navier-Stokes and the continuity equations. During the past years different solution approaches as e.g. direct solution of the Navier-Stokes equations and solution of the Reynolds-averaged Navier-Stokes equations have been tried. But, especially the presence of turbulence complicates the solution. A brief summary of the theory used for description of the flow, i.e. the governing Navier-Stokes and continuity equations, Reynolds-averaging, turbulence modeling and boundary conditions, is given below.

6.2.1 Governing Equations

The fluid flow is governed by the Navier-Stokes (NS) equations, which form a set of non-linear partial differential equations describing the transport of momentum. By use of tensor notation the unsteady NS equations for incompressible flow can be written as

$$\frac{D\boldsymbol{V}}{Dt} = \boldsymbol{g} - \frac{1}{\rho}\nabla p + \frac{\partial}{\partial x_j}\left[\nu\left(\frac{\partial u_i}{\partial x_j} + \frac{\partial u_j}{\partial x_i}\right)\right] \tag{6.1}$$

where the indices i and j run from 1 to 3, the velocity vector $\boldsymbol{V}$ represents the instantaneous velocity components u_1, u_2 and u_3, p is the pressure, ρ is the density of the fluid, ν is the kinematic viscosity of the fluid and $\boldsymbol{g}$ is the vector acceleration of gravity. The operator D/Dt is the particle or substantive derivative defined by

$$\frac{D}{Dt} = \frac{\partial}{\partial t} + (\boldsymbol{V}\cdot\nabla) \tag{6.2}$$

Besides the NS equations the fluid must also fulfill the continuity equation. This equation ensures conservation of mass and it has the following form:

$$\frac{\partial u_j}{\partial x_j} = 0 \tag{6.3}$$

The Einstein summation convention, saying that repetition of an index in a term denotes summation with respect to that index over its range, is applied.

By using (6.1) and (6.2) with the right boundary conditions it should be theoretically possible to calculate the flow around any ship. However, the fact is that it is practically impossible to solve the equations in the case of problems of engineering interest and therefore many attempts to simplify the equations have been made. In the beginning the simplifications were made in a way which enabled analytical solution of the equations for a few simple geometries. Later when the computers were introduced numerical solution was tried. The numerical solution of the equations works well when the flow is laminar, but when turbulence occurs the flow becomes too complicated for calculation. For the turbulent case there are three approaches to numerical solution of the governing equations. These approaches are based on direct solution of the NS equations, Large eddy simulation and solution of the Reynolds-averaged NS equations.

Direct Solution

Few attempts to solve the NS equations directly for simple geometries in turbulent flow have been made by means of supercomputers. But, even for low Reynolds numbers this requires unrealistically large computational time, because the grid must be extremely fine to capture all flow structures in the turbulent flow.

Large Eddy Simulation

Large eddy simulation is related to direct numerical simulation. According to Wilcox (1994) the idea behind the method is to filter out eddies smaller than the mesh size used during simulation. By doing this, calculation of the flow is possible if the remaining

large-scale eddies are calculated directly and the small-scale (or subgrid scale) eddies are modeled by means of wall functions or for instance an eddy viscosity model. The result is that it is possible to solve the Navier-Stokes and continuity equations with a mesh size which allows computations to be carried out within a reasonable time. The method seems to have a potential in the future, but it has not been used much in ship hydrodynamics.

Reynolds-averaged Navier-Stokes Equations

Another approach is to use time-averaging as proposed by Reynolds. If the Navier-Stokes and continuity equations are time-averaged and the turbulent fluctuations are modeled, the mean properties of the flow can be calculated. This procedure is widely used today and it is described below.

6.2.2 Reynolds-averaged Navier-Stokes Equations

By applying time-averaging to the basic equations of motion shown in the previous section, a new set of equations expressed in terms of both mean flow and fluctuation quantities is obtained. The derivation of the equations will not be carried out here, but the results will be given. A derivation of the equations can for instance be found in White (1991).

It is assumed that the fluid is in a randomly unsteady turbulent state and that the time-averaged or mean value $\overline{Q}$ of any fluctuating quantity Q is defined to be

$$\overline{Q} = \frac{1}{T}\int_{t_0}^{t_0+T} Q\,dt \tag{6.4}$$

where the time interval T must be large compared to the period of the fluctuations. If an incompressible flow is considered the fluctuating velocity and pressure quantities can be assumed to have the form

$$\begin{aligned} u_1 &= \overline{u}_1 + u_1' \\ u_2 &= \overline{u}_2 + u_2' \\ u_3 &= \overline{u}_3 + u_3' \\ p &= \overline{p} + p' \end{aligned} \tag{6.5}$$

where $\overline{u}_i$ and $\overline{p}$ represent the mean flow velocities and the mean pressure, respectively. u_i' and p' represent the fluctuations in velocity and pressure around the mean level. If the expressions for u_1, u_2 and u_3 are substituted into the continuity equation and the resulting expression is time-averaged, a new continuity equation for the mean flow is obtained:

$$\frac{\partial \overline{u}_j}{\partial x_j} = 0 \tag{6.6}$$

Based on the same idea, substitution of u_1, u_2, u_3 and p into the Navier-Stokes equations followed by time-averaging yields the Reynolds-Averaged Navier-Stokes (RANS) equations:

$$\frac{D\overline{V}}{Dt}+\frac{\partial}{\partial x_j}(\overline{u_i'u_j'})=\boldsymbol{g}-\frac{1}{\rho}\nabla\overline{p}+\frac{\partial}{\partial x_j}\left[\nu\left(\frac{\partial\overline{u}_i}{\partial x_j}+\frac{\partial\overline{u}_j}{\partial x_i}\right)\right] \tag{6.7}$$

It is seen that the new mean momentum equations have the same form as the instantaneous equations, except for one new term involving the turbulent inertial tensor $\overline{u_i'u_j'}$, which introduces nine new unknowns. Rearranging the terms so that the turbulent inertial forces appear as if they were stresses yields

$$\frac{D\overline{V}}{Dt}=\boldsymbol{g}-\frac{1}{\rho}\nabla\overline{p}+\nabla\tau_{ij} \tag{6.8}$$

where the stress tensor τ_{ij} has the form

$$\tau_{ij}=\nu\left(\frac{\partial\overline{u}_i}{\partial x_j}+\frac{\partial\overline{u}_j}{\partial x_i}\right)-(\overline{u_i'u_j'}) \tag{6.9}$$

It is seen that the stress tensor consists of two terms. The first is the Newtonian viscous stresses and the second term is the turbulent stress tensor. The latter is often referred to as the Reynolds stress tensor and, as mentioned earlier, it contains nine unknown variables which have to be modeled in order to solve the flow problem. This is described in the next section.

6.2.3 Turbulence Modeling

Modeling of the components in the Reynolds stress tensor is rather difficult, because it requires detailed and usually unavailable information about the turbulent structures in the flow. Besides, the components do not only depend on the physical properties of the fluid, but also on the local conditions of the flow like velocity, geometry, surface roughness and upstream history. However, attempts to model the turbulence have been made and some of the most popular models will be presented in the following to illustrate the different levels of complexity of the models available today.

6.2.3.1 Eddy Viscosity

One of the ideas in turbulence modeling is based on the assumption that the Reynolds stresses can be related to the mean flow in the same way as the Newtonian viscous stresses, i.e. by means of an apparent (eddy) viscosity and the local mean flow gradient. Besides, it is assumed that the turbulence is isotropic. The idea was originally proposed

by Boussinesq, who, according to Cebeci and Smith (1974), expressed the Reynolds stress tensor as

$$-\overline{u_i' u_j'} = \nu_t \left(\frac{\partial \overline{u}_i}{\partial x_j} + \frac{\partial \overline{u}_j}{\partial x_i} \right) - \frac{2}{3} \delta_{ij} K \tag{6.10}$$

where ν_t is the eddy viscosity, δ_{ij} is Kronecker's delta and $K = (\overline{u_i' u_i'})/2$ represents the turbulent kinetic energy. The eddy viscosity approach is widely used today and many models for the eddy viscosity have been proposed. Some of the basic ideas behind these models are presented below.

6.2.3.2 Mixing Length Related Eddy Viscosity

One suggestion for an eddy viscosity model is Prandtl's mixing length concept. It is proposed that each turbulent fluctuation can be related to a velocity gradient and a length scale describing the mean eddy size. According to Cebeci and Smith (1974), this can be expressed as

$$-\overline{u_i' u_j'} = l^2 \left(\frac{\partial \overline{u}_i}{\partial x_j} + \frac{\partial \overline{u}_j}{\partial x_i} \right) \left(\frac{\partial \overline{u}_i}{\partial x_j} + \frac{\partial \overline{u}_j}{\partial x_i} \right) - \frac{2}{3} \delta_{ij} K \tag{6.11}$$

where l is the so-called mixing length. Comparison of Boussinesq's and Prandtl's expressions for the Reynolds stresses shows that the eddy viscosity can be modeled with the relation

$$\nu_t = l^2 \left(\frac{\partial \overline{u}_i}{\partial x_j} + \frac{\partial \overline{u}_j}{\partial x_i} \right) \tag{6.12}$$

The idea of the two models is then to insert either the eddy viscosity related Reynolds stresses represented by (6.10) or the mixing length related Reynolds stresses represented by (6.11) into the RANS Equations (6.7), and thus obtain a set of equations which either involves the mean flow quantities and the eddy viscosity or the mean flow quantities and the mixing length. Afterwards a model for either the eddy viscosity or the mixing length must be found in order to obtain closure of the flow problem. The term including the turbulent kinetic energy K is often neglected. These types of models belong to the so-called algebraic or zero equation models and several algebraic models for the eddy viscosity and the mixing length can be found in the literature, e.g. Cebesi and Smith (1974) and Wilcox (1994), but only two of the most popular will be presented here. These two are the Cebeci-Smith and the Baldwin-Lomax turbulence models. Both models are two-layer models, which means that two different expressions are used for the eddy viscosity in the inner and the outer regions of the boundary layer. Thus, the eddy viscosity can be expressed by

$$\nu_t = \begin{cases} \nu_{ti} & y \le y_m \\ \nu_{to} & y \ge y_m \end{cases} \tag{6.13}$$

where ν_{ti} and ν_{to} are the inner and the outer eddy viscosity, respectively, y is the distance to the wall and y_m is the value of y where $\nu_{ti} = \nu_{to}$.

In the Cebeci-Smith model the inner eddy viscosity is based on Prandtl's mixing length concept:

$$\nu_{ti} = (l_{mix})^2 |\omega| \tag{6.14}$$

where $|\omega|$ is the magnitude of the vorticity vector defined by

$$|\omega| = \left[\left(\frac{\partial \overline{v}}{\partial x} - \frac{\partial \overline{u}}{\partial y} \right)^2 + \left(\frac{\partial \overline{w}}{\partial y} - \frac{\partial \overline{v}}{\partial z} \right)^2 + \left(\frac{\partial \overline{u}}{\partial z} - \frac{\partial \overline{w}}{\partial x} \right)^2 \right]^{1/2} \tag{6.15}$$

and l_{mix} is the mixing length, which is calculated by a model based on an extension of the mixing length model proposed by van Driest. The model can be found in Cebeci and Smith (1974), where l_{mix} is defined as

$$l_{mix} = \kappa y \left(1 - \exp\left(-\frac{y^+}{A^+} \right) \right) \tag{6.16}$$

Here κ is a closure coefficient assigned the value κ=0.40, and the non-dimensionalized y-coordinate y^+ is defined to be

$$y^+ = \frac{y \tau_w}{\nu \rho} \tag{6.17}$$

where τ_w is the wall friction, $\tau_w = \mu \, du/dy \big|_{y=0}$. A^+ is also a closure coefficient. Sometimes, it is assumed to be a constant, $A^+ = 26$. Modifications for the influence of parameters like pressure gradient, wall mass transfer, streamline curvature, surface roughness etc. can be found in Cebeci and Smith (1974).

The outer layer expression for the eddy viscosity ν_{to} is defined to be

$$\nu_{to} = \alpha u_e \delta^* \gamma(y, \delta) \tag{6.18}$$

where α is a closure coefficient with the value α= 0.0168, δ is the boundary layer thickness, u_e is the velocity at the edge of the boundary layer, δ^* is the displacement thickness:

$$\delta^* = \int_0^{\delta} \left(1 - u/u_e\right) dy \tag{6.19}$$

and, finally, $\gamma(y,\delta)$ is the Klebanoff intermittence function:

$$\gamma(y,\delta) = \left(1 + 5.5\left(\frac{y}{\delta}\right)^6\right)^{-1} \tag{6.20}$$

A close look at the Baldwin-Lomax mixing length model reveals that it uses the same expression for the inner eddy viscosity as the Cebeci-Smith model. But in the outer layer the eddy viscosity is modeled differently. According to Wilcox (1994), ν_{to} is expressed by

$$\nu_{to} = \alpha C_{cp} F_{wk} F_{Kleb} \tag{6.21}$$

where α=0.0168 and C_{cp} =1.6 are closure coefficients. F_{Kleb} is a modified version of the Klebanoff intermittence function used in the Cebeci-Smith model, where δ is substituted by y_{max}/C_{Kleb}:

$$F_{Kleb} = \left(1 + 5.5\left(C_{Kleb}\frac{y}{y_{max}}\right)^6\right)^{-1} \tag{6.22}$$

where C_{Kleb} =0.3. Finally, F_{wk} is the wake function:

$$F_{wk} = \min\left(y_{max}F_{max}; C_{wk}y_{max}\frac{U^2{}_{diff}}{F_{max}}\right) \tag{6.23}$$

Where the first and the second expressions in F_{wk} are used in attached and separated flow, respectively. C_{wk}=0.25 is an empirical constant, while F_{max} is used for determination of the velocity scale. It is determined as the maximum value of the function

$$F(y) = y|\omega|\left(1 - \exp\left(-\frac{y^+}{A^+}\right)\right) \tag{6.24}$$

y_{max} is the value of the y-coordinate corresponding to F_{max}. Finally, U_{diff} is the difference between the maximum and minimum velocity:

$$U_{diff} = \sqrt{\left(\overline{u}^2 - \overline{v}^2\right)_{max}} - \sqrt{\left(\overline{u}^2 - \overline{v}^2\right)_{min}} \tag{6.25}$$

The primary difference between the Cebeci-Smith and the Baldwin-Lomax models is in the outer layer eddy viscosity. The Cebeci-Smith model involves boundary layer

properties like δ, δ^* and u_e in the calculation of the turbulent length scale in the outer layer, while the Baldwin-Lomax model avoids this by relating the length scale to the vorticity, ω, in the layer. Since the boundary layer properties are difficult to determine in separated flows it seems that the Baldwin-Lomax model is easier to use in such flows. However, difficulties often arise when algebraic models are used in calculations of separated flows. But since they can be tuned to the actual flow to provide greater accuracy and they are easy to implement, they are used widely today.

6.2.3.3 *K*-based Turbulence Model

Another approach to the eddy viscosity modeling belongs to the one-equation models. It is based on the turbulent kinetic energy K and a turbulent length scale l describing the "mean size" of the turbulent structures. The consequence of involving the turbulent kinetic energy in the model is that a transport equation for K must be derived. According to Wilcox (1994), the rate of change of turbulent kinetic energy is described by

$$\underset{I}{\frac{DK}{Dt}} = \underset{II}{-\overline{(u_i'u_j')}\frac{\partial \bar{u}_i}{\partial x_j}} \underset{III}{-\nu\overline{\frac{\partial u_i'}{\partial x_k}\frac{\partial u_i'}{\partial x_k}}} + \frac{\partial}{\partial x_j}\left[\underset{IV}{\nu\frac{\partial K}{\partial x_j}} \underset{V}{-\frac{1}{2}\overline{(u_i'u_i'u_j')}} \underset{VI}{-\frac{1}{\rho}\overline{p'u_j'}}\right] \tag{6.26}$$

As it is seen from Equation (6.26) the introduction of the turbulent kinetic energy results in a new complicated differential equation, which even introduces two new unknown correlations, namely a triple correlation between the velocity fluctuations and a correlation between the velocity and pressure fluctuations. If the individual terms in the equation are looked at more closely they have the following meaning: Term (*I*) represents the rate of change of turbulent kinetic energy. Term (*II*) represents the production, i.e. the rate at which kinetic energy is transferred from the mean flow to the turbulence. Term (*III*) represents the dissipation, i.e. the rate at which turbulent kinetic energy is converted into thermal energy. The dissipation term is often called ε. Term (*IV*) is the molecular diffusion caused by the natural molecular transport process of the fluid and finally the terms (*V*) and (*VI*) represent the convective diffusion caused by velocity and pressure fluctuations. If the convective diffusion is related to the gradient of the kinetic energy by the following assumption

$$\frac{1}{2}\overline{(u_i'u_i'u_j')} - \frac{1}{\rho}\overline{p'u_j'} = \frac{\nu_t}{\sigma_K}\frac{\partial K}{\partial x_j} \tag{6.27}$$

and ε represents the dissipation of turbulent kinetic energy, the following transport equation for the turbulent kinetic energy is obtained:

$$\frac{DK}{Dt} = -\overline{(u_i'u_j')}\frac{\partial \bar{u}_i}{\partial x_j} - \varepsilon + \frac{\partial}{\partial x_j}\left[\left(\nu + \frac{\nu_t}{\sigma_K}\right)\frac{\partial K}{\partial x_j}\right] \tag{6.28}$$

Again ν_t is the eddy viscosity while σ_K is a constant used for closure of the flow problem. With the expression for *K* it is possible to return to the turbulence model where it is assumed that the eddy viscosity ν_t and the dissipation ε can be expressed as

$$\nu_t = \sqrt{K}\, l \qquad \varepsilon \approx K^{3/2}\, l \tag{6.29}$$

where *l* is the turbulent length scale mentioned in the beginning of this section.
The equations for ε, ν_t and *K* combined with the RANS and continuity equations provide a set of equations which can be used for calculation of the mean flow velocity components, the mean pressure and the kinetic energy. However, the system of equations requires a model for *l* to be closed and it seems that such a model is rather complex to formulate. The results obtained by this model are not better than those obtained by the best zero equation models, because it is very difficult to find a proper model for the turbulent length scale *l*. Hence, that the one equation model is not used very much today.

6.2.3.4 *K*-ε Turbulence Model

The *K*-ε model belongs to the two-equation models based on the idea of using transport equations for *both* the turbulent kinetic energy *K and* the dissipation of turbulent kinetic energy ε instead of for *K* alone. However, this approach requires that equations for the rate of change of both *K* and ε are formulated. The expression for ε is derived from the NS equations and the resulting expression can be found in Wilcox (1994).

$$\begin{aligned}\frac{D\varepsilon}{Dt} = &-2\nu\left[\overline{u'_{i,k}u'_{j,k}} + \overline{u'_{k,i}u'_{k,j}}\right]\frac{\partial \overline{u}_i}{\partial x_j} - 2\nu\,\overline{u'_k u'_{i,j}}\,\frac{\partial^2 \overline{u}_i}{\partial x_k \partial x_j} \\ &-2\nu\,\overline{u'_{i,k}u'_{i,m}u'_{k,m}} - 2\nu^2\,\overline{u'_{i,km}u'_{i,km}} \\ &\frac{\partial}{\partial x_j}\left[\nu\frac{\partial \varepsilon}{\partial x_j} - \nu\,\overline{u'_j u'_{i,m}u'_{i,m}} - 2\frac{\nu}{\rho}\overline{p'_{,m}u'_{j,m}}\right]\end{aligned} \tag{6.30}$$

where the subscript "," denotes differentiation. For instance $u_{,m}$ means the same as $\partial u/\partial x_m$. The terms in the equation contribute to different effects. The first line of the right side describes the production of dissipation, the second line describes the dissipation of dissipation, and the third line describes the sum of molecular diffusion of dissipation and turbulent transport of dissipation. The equation is very complex and it includes many unknown double and triple correlations of velocity, pressure and velocity gradient fluctuations, which have to be related to the dissipation in different ways. According to Wilcox (1994), one example of a resulting expression for the rate of change of dissipation becomes

$$\frac{D\varepsilon}{Dt} = -C_{\varepsilon 1}\frac{\varepsilon}{K}\overline{(u'_i u'_j)}\frac{\partial \overline{u}_i}{\partial x_j} - C_{\varepsilon 2}\frac{\varepsilon^2}{K} + \frac{\partial}{\partial x_j}\left[\left(\nu + \frac{\nu_t}{\sigma_\varepsilon}\right)\frac{\partial \varepsilon}{\partial x_j}\right] \tag{6.31}$$

where $C_{\varepsilon 1}$, $C_{\varepsilon 2}$ and σ_ε are closure coefficients.

With transport equations for both the turbulent kinetic energy and for the dissipation of turbulent kinetic energy, it is possible to express the eddy viscosity in terms of K and ε. Therefore, ν_t is assumed to be related to the turbulent kinetic energy K and the dissipation of turbulent kinetic energy ε:

$$\nu_t \approx \frac{K^2}{\varepsilon} \tag{6.32}$$

The K-ε method is rather general because it has the advantage of not using an expression for the length scale. But it often fails in the viscous near wall layer, which means that corrections are necessary. It is often tried to solve this problem by application of wall functions, which describe the mean velocity profile in the near wall layer. However, this introduces weaknesses in the model when it is applied to flow calculations with adverse pressure gradient and separated flow. In order to avoid this problem another two-equation model can be used. The model is the K-ω turbulence model described in Wilcox (1994), which does not require special treatment in the near wall layer.
Compared to the algebraic methods the two-equation models should be more accurate, but at the same time they are also more difficult to implement and solve. Like the algebraic models these methods also need tuning to the actual flow problem, but not as often and not as fine as in the case of the algebraic models. Finally, the two-equation methods omit the use of the length scale, but it must be kept in mind that they are still based on Boussinesq's eddy viscosity approach and therefore possess the limitations of this model.

6.2.3.5 Reynolds Stress Transport Model

This type of model is a so-called second order closure model and it does not involve the eddy viscosity and velocity gradient concept. Instead the Reynolds stresses are calculated directly by either algebraic stress models or by a differential equation for the rate of change of stress. According to White (1991), the Reynolds stress equation describing the rate of change of stress has the form

$$\overset{I}{\frac{D\overline{u_i'u_j'}}{Dt}} = -\left[\overset{II}{\overline{u_j'u_k'}\frac{\partial \overline{u}_i}{\partial x_k} + \overline{u_i'u_k'}\frac{\partial \overline{u}_j}{\partial x_k}}\right] - 2\nu\overset{III}{\overline{\frac{\partial u_i'}{\partial x_k}\frac{\partial u_j'}{\partial x_k}}} + \overset{IV}{\overline{\frac{p'}{\rho}\left(\frac{\partial u_i'}{\partial x_j} + \frac{\partial u_j'}{\partial x_i}\right)}} - \frac{\partial}{\partial x_k}\left[\overline{u_i'u_j'u_k'} - \nu\overset{V}{\frac{\partial \overline{u_i'u_j'}}{\partial x_k}} + \overline{\frac{p'}{\rho}\left(\delta_{jk}u_i' + \delta_{ik}u_j'\right)}\right] \tag{6.33}$$

The terms with roman numerals are interpreted in the following way: Term (*I*) represents the rate of change of Reynolds stress, term (*II*) is the generation of stress, term (*III*) is the dissipation of stress, term (*IV*) is the pressure strain effect and term (*V*) is the

diffusion of Reynolds stress. The method avoids use of eddy viscosity and mixing length, but instead it requires modeling of the correlations of velocity, pressure and velocity gradient fluctuations occurring in the terms (*III*), (*VI*) and (*V*). The models must relate the correlations to the Reynolds stresses to obtain closure and some of the models used today can be found in Wilcox (1994). The method avoids use of the assumption about isotropic turbulence as it was the case of Boussinesq's eddy viscosity concept and it is able to capture more flow details, at least qualitatively, than the eddy viscosity models. However, like other methods this one has also certain problems when it is used with separated flows, and more research into these methods is still needed.

6.2.3.6 Comments on Turbulence Models

To round off the study of the turbulence models a few comments should be given. When a turbulence model is to be chosen it is worth considering whether a complicated or a simple model should be used. The choice can be based on both physical and numerical considerations. The physical considerations may for instance concern the form of the considered body in the flow. The flow around a slender body is relatively smooth and it leaves the body without too much disturbance. For full bodies the flow leaving the body is much more disturbed. It is therefore necessary to choose a turbulence model which can model the current flow problem.
The numerical considerations concern the level of complexity to be chosen to obtain satisfactory results with a reasonable computational effort. Complicated models are often computationally heavy to use and the boundary conditions for the different transport equations are difficult to set up. Simple models, which are easy to handle numerically, can often be adjusted to the specific problem and provide sufficient results. Finally, it should be noted that each time a turbulence model is applied to a problem which has not been investigated before, it is important to validate the model by experimental data.

6.2.4 Methods for Solution and Boundary Conditions

The numerical solution of the governing equations in CFD requires that the continuous flow problem is discretized. Today this can be done by four different methods: Finite difference, finite volume, finite element or finite analytic. In ship hydrodynamics the most popular method is probably finite volume, but also finite difference and finite analytic methods are used, the finite element method is hardly used at all in ship hydrodynamics today. A description of the numerical methods used for solution of the flow problems will not be given here, but descriptions of many of the methods can be found in Ferziger and Peric (1996).
The boundary conditions for the considered calculation domain are necessary to specify when the governing differential equations are solved. Usually, the conditions consist of known pressure and velocity distributions on the boundaries of the computational domain. In the field of ship hydrodynamics additional boundary conditions may be required if the free surface is included in the simulation. There are generally two conditions on the free surface: The dynamic condition given by the surface stress boundary condition and the kinematic boundary condition that particles on the surface

stay there during the surface deformation. Depending on the current turbulence model it can also be necessary to specify values for the turbulent kinetic energy K, the dissipation of turbulent kinetic energy ε or the Reynolds stresses $-\overline{u_i u_j}$.

Finally, it should be noted that the flow problems are often transformed from Cartesian to curvilinear coordinates to make it easier to apply the boundary conditions to for instance the complicated hull geometry.

6.3 Practical Application of Viscous CFD Methods

A look at the literature shows that most of the Navier-Stokes-based methods are used for calculation of the flow around bare hulls in straight-ahead sailing conditions. The primary purpose of these methods is calculation of the viscous tow resistance and wave resistance and investigation of the stern flow, i.e. calculation of the wake field. Few of the methods are used in calculations for ships in maneuvering situations, e.g. oblique sailing ships. A few methods are capable of including hull and propeller in the calculations and they are used for simulation of self propulsion tests.
A brief summary of some of the methods is given below.

6.3.1 Methods for Calculations of Hull Flows Alone

Ohmori and Miyata (1993) presented a method called WISDAM-V, which is used for calculation of the flow around an oblique towed ship without rudder and propeller. The WISDAM-V method is based on time marching solution of the Navier-Stokes equations and the flow problem is discretized by the finite volume method. The turbulence is modeled by large eddy simulation where the model of the subgrid scale eddies is based on the eddy viscosity concept. The turbulent length scale in the eddy viscosity model is determined by means of the smallest grid spacing.
The method is applied to three ship models sailing with a drift angle of 5°, and the resulting velocity field and pressure distribution from the flow calculations are used for calculations of the longitudinal and transverse forces and the yaw moment acting on the ship. The results seem reasonable when compared with experimental data. However, improvements are still needed since the free surface is neglected and a mirror image is applied instead. Moreover, the turbulence model could be improved.

In Ishikawa (1994) a CFD method is used for prediction of the viscous resistance and nominal wake of a ship model. This method is based on solution of the Reynolds-averaged Navier-Stokes equations and the continuity equation. The latter includes a pseudo-compressibility to compensate for the missing pressure dependence in the continuity equation. Discretization is carried out by the finite volume technique. The turbulence model is the algebraic Baldwin-Lomax model, which is based on the eddy viscosity concept. Finally, the free surface is neglected by using a mirror image.
The results obtained by this method have also been compared with experimentally determined data, and it is shown that the viscous resistance is predicted with enough accuracy for practical use, while the calculated nominal wake fraction is 10-20% lower than the value found by experiments. This indicates that the turbulence model is not

sufficient to model the complex flow around the stern and that improvements are therefore required.
In Sotiropoulos and Patel (1995) stern and wake flows of two different ships are investigated by a RANS-based method where the governing equations are discretized by the finite difference method. The investigations which concern calculations of velocity and pressure fields are performed by two different turbulence models and the results are compared with experimental data. One of the turbulence models is a seven-equation Reynolds stress transport model, and the other is a two-equation K-ε model used together with wall functions for correction of near wall effects. Finally, this method also neglects the free surface and uses a double body approximation.
When the numerical and the experimental results are compared, it turns out that the Reynolds stress model compared with experiments reproduces most of the flow features in the stern region. The K-ε method predicts the tendencies in the stern flow, but it calculates an inflow to the propeller plane which is more uniform than that measured. The explanation of the uniform inflow may be found in the wall functions, which most likely fail near the stern where the flow is very complex and the assumption about isotropic turbulence no longer holds. However, the much more complicated Reynolds stress model requires more computational power than to the K-ε model and, besides, it is difficult to extend it to free surface flows because no experimental information on the Reynolds stresses is available.

In proceedings of the CFD workshop in Tokyo 1994, it is tried to identify the state of the art of CFD methods used in ship hydrodynamics. A number of CFD methods based on solution of the Navier-Stokes equations have been used for calculations of the flow around the Series 60 and the HSVA tanker hulls, and the results have been compared with experimental data.
Nine of the viscous CFD methods in the proceedings deal with free surface flows and they have been used for calculations of waves, resistance, wake fields, velocity and pressure fields for the Series 60 hull. Six of the methods use the algebraic Baldwin-Lomax turbulence model, two use the two-equation K-ε model and, finally, one uses an eddy-viscosity-based subgrid scale model. Based on the results presented on the Tokyo workshop one of the best methods seems to be the one which is proposed by Tahara and Stern (1996) and which is based on solution of the RANS equations together with the Baldwin-Lomax turbulence model. However, concerning the general performance of the methods comparison with experimental data shows that the calculated results from most of the methods capture the tendencies in the near field flow around the ship. The wave profiles along the side of the hull agree well with measurements, while problems arise with the wave contours around the ship and with the wake fields in the stern region where, the flow is very complex because of the turbulence. The poor wave contour prediction may be caused by a too rough grid solution on the free surface while the bad wake field may be caused by the turbulence models, which do not describe the turbulence sufficiently. Finally, it should be mentioned that the resistance calculations agree well with the measurements even though the wave contours are predicted wrongly, which might indicate that the error originating in the wave resistance is maybe canceled out by other errors in the model.
Fourteen methods deal with flows without free surface and use instead the double hull approximation. Concerning the turbulence modeling, it can be mentioned that six

models use algebraic Baldwin-Lomax or Cebeci-Smith models, seven methods use the K-ε model and a single one uses a second order closure Reynolds stress model.
The flow calculations are performed on the hull of the HSVA tanker and they are mainly used for investigations of the wake field around the stern of the ship. It seems that the methods capture most of the tendences in the flow qualitatively. However, again the stern flow gives rise to difficulties in the calculations of the wake fields. A more detailed discussion of the results is found in the proceedings.

6.3.2 Hull and Propeller Models

In Tzabiras (1997) CFD is used for investigations of the influence of different bulb shapes on the resistance and self-propulsion of a ship equipped with propeller. Again the free surface is neglected and the double body approximation is used. The calculations are performed by a method based on solution of the RANS equations and the continuity equation and the problem is discretized by means of a finite volume method. The turbulence model used in this context is the K-ε model with associated wall functions.
In the model the propeller is represented by an actuator disk approximation. The propeller forces are introduced in the momentum equations as external body forces acting in the control volumes placed on the propeller disk. It is here assumed that the circumferential and radial body forces may be neglected. Thus, only the axial momentum is affected by the propeller action. The longitudinal distribution of the propeller forces through the propeller disk is found by experimental measurements on a hydrofoil.
The calculations are performed for different bulb shapes in both model and full scale and the results show differences in both resistance and self-propulsion factors. Unfortunately, there is no comparison with experimental results, which makes it impossible to say anything about the accuracy of the method.

Stern et al. (1996) present a CFD method, which calculates the flow by means of the RANS and the continuity equations with the algebraic Baldwin-Lomax turbulence model. The problem is discretized by a finite analytic method. The CFD method is used for calculation of surface-ship boundary layers, wakes and waves and besides it provides the possibility of including hull-propeller interaction. The elevation of the free surface is calculated during the simulation and each time a new elevation is found the grid is adapted to the new surface. The boundary conditions used for the free surface include a kinematic and a dynamic condition. The kinematic condition requires that fluid particles on the surface stay there during the simulation and the dynamic condition requires that normal and tangential stresses are continuous across the surface. The propeller is included by means of body forces applied in the momentum equations. The body force available in Stern et al. (ibid.) is obtained from a prescribed distribution suggested by Hough and Ordway.
However, in Stern et al. (1994) a RANS model is coupled with a propeller performance code so that the body forces are obtained from a propeller model based on a vortex-lattice method. Both the axial and the circumferential body force components are calculated while the radial component is neglected. During the simulation the propeller program is working together with the RANS solver in an iterative manner to capture the effect of interaction between the propeller and the hull. The effective inflow obtained by

the viscous solution is used in the propeller program, which calculates the body forces. These forces are then used in a new viscous calculation to obtain a new inflow field to the propeller program and so on. The calculations are continued until convergence is obtained.
A comparison with experimental data shows reasonably agreement between calculations and measurements for both methods.

In Zhang et al. (1991) it is tried to predict the stern flow of a ship with operating propeller. The CFD code, called SHIPFLOW, is based on solution of the Reynolds-averaged Navier-Stokes equations discretized by means of a finite analytic method. Turbulence is modeled by the standard two-equation K-ε turbulence model. The effect of the propeller is obtained by means of body forces imposed on the grid at the location of the propeller disk. The forces applied in both axial and tangential directions are calculated by a lifting line propeller performance method, while the radial forces are neglected. As in the method proposed by Stern et al. (1994) the propeller performance program is working interactively with the viscous Navier-Stokes solver. The inflow velocity field and the body force distribution are calculated in turn until convergence is obtained.
The method has been applied in two cases: An axisymmetric body with propeller and the Series 60 hull with propeller. For the axisymmetric body case the results seem to agree well with experiments and, besides, differences between the with and without propeller condition are captured. The calculations of the three-dimensional flow around the Series 60 hull with propeller capture most of the flow features qualitatively, but when it comes to quantitative agreement with experimental data accuracy is missing.

6.4 Status of Viscid CFD Methods

From the study presented above it is seen that in the case of the viscid methods most effort is spent on calculations of the flow around bare hulls in a straight-ahead sailing condition. The goal is to be able to optimize the designs with respect to waves, resistance and inflow to the propeller plane.
In the field of calculations on ships in maneuvering situations the use of viscid methods is very sparse. Only a single method for calculation of the forces acting on an oblique sailing hull has been found, but it was not able to include neither free surface, rudder nor propeller. It is most likely that some of the other methods mentioned above can be used for oblique conditions by applying the right boundary conditions, but no examples have been found in the literature. Three methods are capable of including the propeller in the calculations and thus of making investigations of hull-propeller interaction possible. However, the model is still without the rudder.
Cases cannot be found where a viscid method is applied to calculations of the flow around rudder, propeller and hull at the same time. It may be that the hull-propeller methods mentioned above can handle a rudder too, but it has not been tried yet.

This page is intentionally left blank.

Chapter 7

Verification and Validation Methodology

7.1 Introduction

When a CFD code is applied to a complex flow problem, it is often useful to compare the numerical results with experiments to see how well the code models the reality and thus get an indication of how much confidence should be placed in the results. However, it is not just a question of comparing the two sets of data, because both the simulations and the experiments can be influenced by different kinds of errors resulting in a misleading picture of the code performance.
In the case of good agreement between simulations and experiments it is a question, if this is really caused by a good numerical model or if it is a result of cancellation of errors in the code or large uncertainty in the experiments. On the other hand, in the case of deviation it is a question, if this is caused by poor quality of the experimental data or if the numerical model needs to be improved.
The problem has gained more attention lately and it has been realized that procedures for verification and validation of numerical methods are needed. One method is suggested by Stern, Coleman, Wilson and Paterson (1999), and it was decided to follow their approach to verification and validation of the numerical results obtained in this work. In the present chapter a brief summary of the methodology is provided to illustrate the idea behind the method and to present the equations necessary for estimation of the numerical uncertainty and error or just one of the components.

7.2 Concept of Verification and Validation

In comparisons of simulated data S and experimental data D it is usually impossible to know how accurate they are, i.e. how close they are to the true value T. The difference between the simulated or experimental value and the truth can be quantified by the error δ. Since the error is usually unknown in practical applications it has to be estimated. However, if the error is based on an estimate it is necessary to know how good the estimate is. For this purpose the uncertainty U is introduced. This quantity is an estimate

of an error U so that the true value of δ lies within the uncertainty interval bounded by $\pm U$, 95 times out of 100. The uncertainty interval does not provide information about the sign of the error, which means that it only indicates the magnitude of the error. However, in some cases there is sufficient information to estimate both magnitude and sign of the error and then use it for a correction of the data considered.
As seen from the section above a major task in the verification and validation procedure is assessment of the simulation and experimental uncertainties and possibly also the errors, i.e. U_S, δ_S, U_D and δ_D. Assessment of δ_D and U_D is done by experimental uncertainty analysis, which is not included in this chapter since it emphasizes the validation and the verification of the numerical method, i.e. assessment of U_S and δ_S.

According to Stern et al. (1999), the simulation error δ_S, which is the difference between the simulation S and the true value T, can be divided into two distinct components: A modeling error δ_{SM} and a numerical error δ_{SN}:

$$\delta_S = S - T = \delta_{SM} + \delta_{SN} \tag{7.1}$$

The modeling error originates from the assumptions and approximations made in the mathematical representation of the physical problem and it covers mathematical equations, boundary conditions, turbulence models etc., but also inclusion of previous data like fluid properties. The other error source, the numerical error, is introduced when the mathematical problem is solved numerically, and it consists of errors from discretization, incomplete iterative and grid convergence, artificial dissipation, computer rounding-off etc.
The equation for the simulation uncertainty U_S corresponding to the equation above can be expressed as

$$U_S^2 = U_{SM}^2 + U_{SN}^2 \tag{7.2}$$

where U_{SM} and U_{SN} are the uncertainties related to the modeling and the simulation, respectively.
From (7.1) and (7.2) it is seen that in order to estimate U_S and possibly also δ_S both the numerical and the modeling uncertainty must be assessed and possibly also the error contributions. The procedures for assessing these data are called verification and validation. The verification is the procedure for assessing the numerical uncertainty and the sign and magnitude of the numerical errors if the conditions allow it. Usually, the process is based on systematic parameter studies and convergence studies where different numerical parameters like grid size, time step and number of iterations can be varied. U_{SN} and possibly also δ_{SN} are normally estimated by means of the multiple solutions obtained from the parameter study. The validation is the process used for assessment of the modeling uncertainty and again also the sign and magnitude of the error if possible. U_{SM} and δ_{SM} cannot be estimated on the basis of numerical solutions as in the case of the verification. Instead they are found by a comparison with experimental benchmark data where the experimental uncertainty and possibly also the error are taken into account. Both the verification and validation procedures are described below.

7.3 Verification Methodology

As mentioned above the numerical uncertainty and error may have a number of different sources. Two of the important ones with respect to this work are the uncertainties and errors introduced by the discretization, i.e. the grid, and by the iterative solution method applied in the CFD code. Therefore, the description of the verification procedure will be focused on assessment of iterative and grid uncertainties and errors. Application of the approach presented by Stern et al. (ibid.) leads to the following expressions for U_{SN} and δ_{SN}:

$$\delta_{SN} = \delta_I + \delta_G \qquad U_{SN}^2 = U_I^2 + U_G^2 \tag{7.3}$$

where δ_I and δ_G are the numerical errors introduced by the iteration and the grid, respectively, and U_I and U_G are the uncertainties introduced by the iteration and the grid, respectively. It has to be kept in mind that it is not always possible to calculate the error because of lacking confidence in the data used for the error estimation. In these cases only U_{SN} will be estimated. However, in some cases the conditions allow estimation of δ_{SN}, and it is then possible to correct the numerical solution S for the numerical error by

$$S_C = S - \delta_{SN} = S - (\delta_I + \delta_G) \tag{7.4}$$

and use this value for comparison with experimental data. S_C is the corrected solution.

7.3.1 Assessment of Iterative Uncertainties and Errors

In the present project only steady state solutions were calculated by applying an iterative solution method to the RANS equations. The idea behind the method is to start from an initial guess and then perform time marching or iterations, until the steady state solution has been reached. In some cases the solution will diverge due to numerical instabilities caused by the grid and result in a solution which is useless, but in other cases the solution will converge towards the steady state solution and iterative convergence will be achieved. When a solution shows iterative convergence it is necessary to know when the steady state has been reached and the calculation can be stopped. Usually, the residuals are used as stopping criteria and ideally the solution should not be stopped before the residuals have reached machine zero. However, for practical applications, which usually involve complex geometries, this is not possible, so a drop in the residuals of three to four decades to a level between 10^{-3} and 10^{-4} is assumed to be acceptable.
According to Stern et al. (ibid.), the iterative convergence can be split into three categories when the iterative uncertainties and errors are estimated. Depending on the behavior of the convergence history of the solution, the following cases can be observed: a) oscillatory, b) convergent and c) mixed oscillatory/convergent. Based on a graphic estimation of the uncertainties and errors the following approach can be used:
In the case of *oscillatory iterative convergence*, the solution will keep oscillating around a mean value as the number of iterations is increased. In this case the iterative

uncertainty and possibly also the error are estimated on the basis of the solution envelope by

$$\delta_I = S - \frac{1}{2}(S_U + S_L) \qquad U_I = \left|\frac{1}{2}(S_U + S_L)\right| \tag{7.5}$$

where S_U and S_L are the maximum and minimum values of the oscillating solution.
In the case of *convergent iterative convergence*, the solution will converge towards a value in an exponential manner as the number of iterations is increased. In this case the iterative uncertainty and possibly also the error are estimated on the basis of an exponential function found from a curve fit for a large number of iterations by means of

$$\delta_I = S - CF_\infty \qquad U_I = \left|S - CF_\infty\right| \tag{7.6}$$

where CF_∞ is the value of the fitted function for the number of iterations going towards infinity.
Finally, in the case of mixed *convergent/oscillatory iterative convergence*, the solution will oscillate but the oscillations will decay as the number of iterations is increased. Again the iterative uncertainty and possibly also the error are estimated on the basis of the solution envelope. Since the amplitudes of the oscillation are decaying as the number of iterations is increased, the solution envelope will do the same. By using the range of the envelope the following expressions are defined:

$$\delta_I = S - \frac{1}{2}(S_U + S_L) \qquad U_I = \left|\frac{1}{2}(S_U + S_L)\right| \tag{7.7}$$

where S_U and S_L are the maximum and minimum values of the solution envelope at the ending iteration.

7.3.2 Assessment of Grid Uncertainties and Errors

When CFD calculations are performed it is important to keep in mind that the quality of the solution is strongly influenced by the quality of the grid and to investigate the errors and uncertainties introduced by the applied grid. Today most of the grid generation is done by use of interactive computer programs where the user can see the grids during the generation process. This makes the grid generation easier, but it does not ensure that the grid has a good quality, since this usually depends on the skills and the experience of the user. When a grid is generated, it is often impossible to tell if it is fine enough, if the cells are good enough to ensure numerical stability or if it is refined at the right locations, and the more complex the geometry becomes, the more difficult it is to find the right answer.
Usually, tools for checking cell aspect ratios, skewness and jacobians are available in the grid generation programs, but there are no requirements of the values of these quantities, so it is up to the user to judge if it looks realistic. Thus, the grid generation often relies on visual judgment based on the experience of the user.

When a grid has been generated it is usually necessary to perform a calculation to investigate if the grid results in a stable solution, i.e. the solution shows iterative convergence as described above. However, iterative convergence is not enough to ensure a good solution, because it is also necessary to know if the grid is fine enough, i.e. to know how close the solution, obtained by the current grid, is to the grid-independent solution and which errors and uncertainties the grid introduces. This requires a grid study where the grid is refined systematically in all three coordinate directions, using the same refinement factor:

$$r_G^{i,j,k} = \frac{\Delta X_A}{\Delta X_B} \tag{7.8}$$

where X represents the grid line distance and the subscript refers to the basic (A) and refined (B) grid. For investigation of grid convergence a minimum of three grids needs to be generated: coarse (3), medium (2) and fine (1). The same refinement factor should be used in going from coarse to medium and from medium to fine. In Stern et al. (ibid.), it is suggested that a grid refinement factor of $r_G = \sqrt{2}$ or r_G =2 could be used. However, for complex grids, which usually contain many cells, these factors will result in grids too coarse or too fine. Therefore, it is sometimes necessary to use smaller r values, for instance in the range from r_G =1.1 to 1.2.

After the solutions for the three grids have been calculated, it can be determined if grid convergence is obtained. This is done by consideration of the R_G ratio, which is defined as

$$R_G = \frac{\varepsilon_{21}}{\varepsilon_{32}} \tag{7.9}$$

where $\varepsilon_{21} = S_2 - S_1$ and $\varepsilon_{32} = S_3 - S_2$ express the changes in the solutions between medium-fine and coarse-medium grids, respectively. Depending on the value of R_G three cases are possible:

$$\begin{aligned} &(i) \quad \textit{Converging condition}: 0 < R_G < 1 \\ &(ii) \quad \textit{Oscillatory condition}: R_G < 0 \\ &(iii) \quad \textit{Diverging condition}: 1 < R_G \end{aligned} \tag{7.10}$$

Regarding estimation of error or uncertainty, the three conditions are treated separately. According to Stern et al. (ibid.), generalized Richardson extrapolation is used for the estimation of condition (*i*). Based on Taylor expansion of the coarse, medium and fine grid solutions around the grid-independent solution S_C, it is possible to estimate the first order error for the fine grid by

$$\delta_{RE,G1} = \left(\frac{\varepsilon_{21}}{r_G^{P_G} - 1} \right) \tag{7.11}$$

where ε_{21} is the change in solution between medium and fine grid, r_G is the grid refinement factor and P_G is the estimated order of accuracy defined as

$$P_G = \frac{\ln(\varepsilon_{32}/\varepsilon_{21})}{\ln(r_G)} \tag{7.12}$$

According to Stern et al. (ibid.), it is important to estimate P_G accurately when the error and possibly also the uncertainty are calculated, so the authors suggest a correction based on verification for analytical benchmarks which should account for overprediction or underprediction of the error caused by inaccurate prediction of P_G. The correction factor C_G is defined as

$$C_G = \frac{r_G^{P_G} - 1}{r_G^{P_{th}} - 1} \tag{7.13}$$

where P_{th}=2 is the theoretical order of accuracy of the method. Depending on the value of C_G two different situations can arise. If C_G turns out to be close to 1, meaning that the solutions are in the asymptotic range, both the magnitude and the sign of the error δ_{G1} and the uncertainty U_{G1} should be estimated from

$$\delta_{G1} = C_G \, \delta_{RE,G1} \tag{7.14}$$

$$U_{G1} = \left|(1 - C_G)\,\delta_{RE,G1}\right| \tag{7.15}$$

If C_G turns out to be too far away from 1, indicating that the first order estimate overpredicts (C_G<1) or underpredicts (C_G>1) the error and that the solutions are not in the asymptotic range, only the uncertainty U_{G1} should be estimated from

$$U_{G1} = \left|C_G \, \delta_{RE,G1}\right| + \left|(1 - C_G)\,\delta_{RE,G1}\right| \tag{7.16}$$

As regards application of the corrected expressions it should be noted that, according to Stern et al. (ibid.), there may be reasons for lack of confidence in Expressions (7.13) and (7.14) for complex three-dimensional flows, when C_G is far away from 1. The two expressions therefore still needs further testing for practical applications involving complex three-dimensional flows.

For condition (*ii*) in (7.10) it is only possible to estimate the uncertainty, but it is more comprehensive than in the case of condition (*i*), because it requires calculations for more than three grids. However, the idea is to perform calculations enough to be able to determine the upper and lower bounds of the oscillating solution and then calculate the uncertainty from

$$U_G = \frac{1}{2}(S_U + S_L) \tag{7.17}$$

where S_U and S_L are the upper and lower bounds of the oscillating solution.
Finally, in case condition (*iii*) in (7.10) should occur it should be noted that it is not possible to estimate the error and the uncertainty. Instead the grid quality should be improved to obtain the converging (*i*) or oscillating (*ii*) condition.

7.4 Validation

After presenting the method used for verification, i.e. assessment of the numerical error and uncertainty, the next step is assessment of the modeling uncertainty and error. As mentioned earlier this requires experimental benchmark data and estimates of the experimental uncertainty and possibly also the error. However, in this chapter the experimental uncertainty U_D and error δ_D are assumed to be known in the process of assessing the simulation modeling uncertainty U_{SM} and error δ_{SM}. According to Stern et al. (ibid.), the validation procedure is based on the comparison error *E* and the validation uncertainty U_V as described below. In the reference it is assumed that the modeling uncertainties and errors consist of two components, namely one from the modeling assumptions and one from use of previous data. Since the error from previous data is not considered separately in this context all modeling errors and uncertainties are treated as one component.
One of the central quantities in the validation procedure is the comparison error *E*, which is defined as the difference between the simulated data *S* and the experimental data *D*:

$$E = D - S \tag{7.18}$$

If this expression is rewritten *E* can be related to the errors in the data and in the simulation, including the modeling error δ_{SM}. By means of the numerical error δ_N and the experimental error δ_D it is possible to relate the simulated data *S* and the experimental data *D* to the true value *T*:

$$T = S - \delta_S \tag{7.19}$$

$$T = D - \delta_D \tag{7.20}$$

If these two expressions are subtracted and the result is inserted in (7.18), it results in the following expression for *E*:

$$E = D - S = \delta_D - \delta_S \tag{7.21}$$

According to (7.1) and (7.3), δ_S can be rewritten and *E* can be expressed as

$$E = \delta_D - (\delta_{SM} + \delta_I + \delta_G) \tag{7.22}$$

From this expression it is seen that *E* is the resultant of all the errors introduced by the experimental data and the simulation.

A straightforward method for validating a CFD code would be to estimate the comparison error *E* from (7.18) and the uncertainty of *E* from

$$U_E^2 = U_D^2 + U_{SN}^2 + U_{SM}^2 \tag{7.23}$$

and then postulate that the code was validated if the absolute value of *E* was smaller than U_E. However, according to Stern et al. (ibid.), there is no method for estimation of the simulation modeling uncertainty U_{SM}. This means that U_E cannot be estimated, so instead the validation uncertainty U_V is introduced. U_V or the noise is the combination of all the known uncertainties related to the data and the simulation uncertainties and it can be expressed as

$$U_V^2 = U_E^2 - U_{SM}^2 = U_D^2 + U_{SN}^2 \tag{7.24}$$

The idea is then to compare $|E|$ and U_V. According to Stern et al. (1999), it is postulated that in case $|E|$ is smaller than U_V, the combination of all the errors in the data and the simulation is smaller than the estimated validation uncertainty and validation has been achieved at the U_V level.
From (7.24) it is seen that the more inaccurate the data and the simulation are, the greater is the validation uncertainty. Thus validation is easier to achieve, even though it is at a high level U_V. For practical applications where a certain accuracy may be required, it can therefore be necessary to establish a required level of validation U_{reqd}. This leads to six different cases which may occur during the validation process of a CFD code:

1. $|E| < U_V < U_{reqd}$
2. $|E| < U_{reqd} < U_V$
3. $U_{reqd} < |E| < U_V$
4. $U_V < |E| < U_{reqd}$
5. $U_V < U_{reqd} < |E|$
6. $U_{reqd} < U_V < |E|$

(7.25)

For conditions 1, 2 and 3 it is seen that $|E|$ is smaller than U_V. This means that validation has been achieved at the U_V level and that the comparison error is below the noise level. Seen from a point of view of uncertainty there would be no reason for improving the model assumptions in the CFD method in order to decrease δ_{SM} in this case, because the effect of doing so would disappear in the noise. For conditions 4, 5 and 6 validation is not achieved since $|E|$ is greater than U_V. According to Stern et al. (ibid.), δ_{SM} can be calculated from (7.22) in this case by using the sign and magnitude of *E*. If the conditions have permitted calculation of δ_{SM} and if the corrected solution S_C therefore has been used for calculation of *E* in (7.18), it is most likely that *E* will correspond to δ_{SM}. IF $|E| >> U_V$, E will correspond to the modeling assumption error, δ_{SM}, and the error can be determined unambiguously.

7.5 Relation to the Present Work

As mentioned in the beginning of this chapter, it is generally difficult to judge the performance of a CFD code based on comparison between experimental and numerical results, because many errors can influence both the experiments and the simulations. Especially, in the case of lacking agreement it is difficult to point out the causes of the problems. However, the procedures for verification and validation proposed by Stern et al. (1999), which are summarized in this chapter, should provide a tool taking the errors and uncertainties into account in a systematic way, when experimental data and simulations are compared. Since one of the tasks in the present project is to investigate the possibility of numerical generation of maneuvering data by comparison between experiments and calculations it seems to be a good idea to adopt this approach to validation of some of the calculations. Especially, in the case of lack of agreement it would be interesting to be able to identify the reasons.

This page is intentionally left blank.

Chapter 8

Description of Numerical Method

8.1 Introduction

In numerical investigations of rudder-propeller-hull interaction it is important to apply a method which is capable of predicting relatively correct the complex flow in the stern and wake regions of the ship and the flow around the rudder and propeller. Due to the rapid change in the cross-sectional shape of the hull form, the flow in these regions is usually characterized by phenomena like strong, induced pressure gradients, formation of vortices, three-dimensional separation and a thick boundary layer, which influence the inflow field to the propeller and the rudder. Moreover, the flow around the propeller and the rudder is also very complex. On the one hand, the propeller flow involves tip vortices developing at the tip of the blades, boundary layers on each blade, separation, strong pressure gradients due to the load on the propeller and, finally, blade interference. On the other hand, the rudder flow is complicated, because the flow involves a boundary layer on the rudder surface, the vortex developing at the tip of the rudder, separation of the flow on the rudder surface and, finally, strong pressure gradients occurring when the rudder is deflected. Furthermore, a part of the rudder is working in the propeller slipstream, which is highly rotational and therefore results in a complicated pressure and velocity field around the part of the rudder placed in the slipstream region.
As seen from this list of flow features, a combined rudder, propeller and hull model is extremely complicated, and it requires an advanced numerical method in order to model the flow. According to the findings in Chapter 6, different kinds of CFD methods have been developed during the past years to be able to deal with the effects mentioned above. It appears that one of the most widely used methods is based on numerical solution of the continuity equation and the Reynolds-averaged Navier-Stokes (RANS) equations in conjunction with a turbulence model. The RANS method seems to perform well for ship flows, and it was decided to use this method for the flow study in the present project. However, a RANS model including a physical representation of both rudder, propeller and hull would require a complex computational grid consisting of millions of cells, which is difficult to generate by the existing grid techniques, and which is impossible to handle with most of the computers available today. In order to simplify the problem, it was therefore decided to apply an approach where the rudder and the hull were modeled by real geometries, while the propeller was represented by a body force distribution applied to the propeller disk. Concerning the turbulence model, it

was initially decided to apply the algebraic Baldwin-Lomax model, which, according to Chapter 6, produces fair results even though it is relatively simple. It was therefore assumed that this model would be sufficient for the initial studies and, besides it is relatively stable and does not introduce additional transport equations which have to be solved and therefore require extra computational power and time. If necessary, it should be possible to change to a two-equation turbulence model later, when the grids had been generated and the model seemed to be working.
Finally, it should be mentioned that the purpose of this project is not to develop a numerical method, but to apply an existing method to the flow study. The study is therefore based on application of the flow solver implemented in the CFD code CFDSHIP-IOWA, which is developed at Iowa Institute of Hydraulic Research at the University of Iowa. The method is briefly described below and the description covers governing equations, turbulence model, coordinate transformation, discretization, pressure equation, boundary conditions and the applied propeller model. It should be noted that two different versions of the code have been applied in the project. With reference to the work presented in later chapters, the two-dimensional rudder profile calculations were made with version2.1, discretized by means of the finite analytic method, while the bare hull, the rudder and the rudder-propeller calculations were made with version3.0, discretized by means of higher order finite differences.

8.2 Governing Equations and Turbulence Model

CFDSHIP-IOWA is based on numerical solution of the non-dimensionalized form of the unsteady three-dimensional Reynolds-averaged Navier-Stokes (RANS) equations and the continuity equation, which are described by Equations (6.6) and (6.7) in Chapter 6. Concerning the Reynolds stresses in the RANS equations, these are related to the mean flow quantities by the Boussinesq approximation in Equation (6.10), which is also described in Chapter 6. By inserting the expression for the Reynolds stresses (6.10) in the RANS Equations (6.7) and afterwards non-dimensionalizing the resulting expressions by means of the reference speed U_0, the length L and the density ρ, it is possible to obtain the following set of governing equations expressed in Cartesian tensor notation:

$$\frac{\partial u_i}{\partial x_i} = 0 \tag{8.1}$$

$$\frac{\partial u_i}{\partial t} + u_j \frac{\partial u_i}{\partial x_j} = -\frac{\partial P}{\partial x_i} + \frac{1}{Re_{eff}} \frac{\partial^2 u_i}{\partial x_j \partial x_j} + \frac{\partial \nu_t}{\partial x_j}\left(\frac{\partial u_i}{\partial x_j} + \frac{\partial u_j}{\partial x_i} \right) + f_{b_i} \tag{8.2}$$

In these equations, which are solved in the CFD code, $u_i = (u, v, w)$ are the non-dimensional mean velocity components and $x_i = (x, y, z)$ are the Cartesian coordinates. It should be mentioned that the bars, which denoted mean properties in Chapter 6, are omitted for the sake of convenience. The body force term f_{bi} is in the present case used for inclusion of the tangential and axial body force components $f_{b\theta}$ and f_{bx}, modeling the effect of the propeller. The non-dimensional mean pressure P is defined as

$$P = \hat{p} + \frac{2}{3}K \tag{8.3}$$

where K is the turbulent kinetic energy and $\hat{p}$ is the piezometric pressure:

$$\hat{p} = p + \frac{z}{Fr^2} \tag{8.4}$$

where p is the pressure, ν is the kinematic viscosity of the fluid and Fr is the Froude number. The effective Reynolds number Re_{eff} in (8.2) is defined by

$$\frac{1}{Re_{eff}} = \frac{1}{Re} + \nu_t \tag{8.5}$$

where Re is the Reynolds number and ν_t is the isotropic eddy viscosity. For all the calculations performed in the present project, the eddy viscosity is calculated by means of the algebraic Baldwin-Lomax turbulence model, which is based on a two-layer approximation. The two layer model uses two different expressions for the eddy viscosity depending on the position in the boundary layer and the eddy viscosity is therefore expressed by

$$\nu_t = \begin{cases} \nu_{ti} & y \le y_m \\ \nu_{to} & y \ge y_m \end{cases} \tag{8.6}$$

where ν_{ti} and ν_{to} are the inner and outer eddy viscosity, respectively. The distance to the wall is y and y_m is the y-position where ν_{ti} equals ν_{to}. In the inner layer the eddy viscosity is based on a mixing length relation

$$\nu_{ti} = \left(l_{mix}\right)^2 |\omega| \tag{8.7}$$

where l_{mix} is the mixing length and ω is the vorticity. The mixing length is determined on the basis of van Driest modified version of Prandtl's mixing length theory. This is described in more detail in Chapter 6. In the outer layer the eddy viscosity is determined by

$$\nu_{to} = \alpha C_{cp} F_{wk} F_{Kleb} \tag{8.8}$$

where α=0.0168 and C_{cp}=1.15 are empirical constants, while F_{wk} and F_{Kleb} are the wake function and the Klebanoff intermittence function, respectively. The turbulence model is described in more detail in Chapter 6 and more information about the individual terms can be found here.

The continuity equation and the momentum equations are not solved in the Cartesian space. Instead the equations are transformed from Cartesian coordinates (x, y, z) in the

physical domain to non-orthogonal curvilinear coordinates (ξ, η, ζ) in the computational domain. The transformation is partial since only the independent variables are transformed. The velocity components u_i are kept in Cartesian coordinates, meaning that u_1, u_2 and u_3 are still the velocity components in the *x*-, *y*- and *z*-directions, respectively. Detailed information about the transformation relations and the resulting equations can be found in Stern et al. (1996).

8.3 Numerical Method

In order to be able to solve (8.1) and (8.2) numerically, the equations are reduced to algebraic form. As mentioned earlier two versions, 2.1 and 3.0, of CFDSHIP-IOWA have been applied to the calculations. Both codes are based on the same set of governing differential equations, but they are discretized in different ways.

Version2.1 solves the equations on a regular (i.e. variable-collocated) grid and applies the finite analytic method to spatial discretization and a first order backward difference to temporal discretization. The idea behind the method is to analytically derive a set of solution-dependent coefficients by solving the linearized momentum equations on a computational cell with the dimensions 2*l* in the ξ-direction, 2*k* in the ζ-direction and 2*h* in the η-direction. This is done by means of a hybrid method which combines a two-dimensional analytic solution in the $\zeta\eta$-plane with a one-dimensional analytic solution in the ζ-direction. By specifying boundary conditions on the cell faces as combinations of exponential and linear functions and by using separation of variables, it is possible to evaluate the solution at the center note (at (*l*, *k*, *h*)) of the cell and obtain a 12-point finite analytic formula which expresses the solution in a grid point by the nodal values in the neighboring points. The use of the regular grid approach when solving the incompressible RANS equations results in problems with odd-even decoupling of the pressure and velocity fields. The problems are solved by special treatment of the pressure equation, which is derived on the basis of the generalized continuity equation discretized on a staggered-grid control volume by means of second order central differences.

In order to handle the velocity-pressure coupling, the overall solution procedure for the governing equations and the pressure equation is based on the fully implicit pressure implicit split operator method PISO, where both pressure equation and momentum equations are solved in an iterative manner by use of the method of lines with underrelaxation. A comprehensive description of the numerical model used in version2.1 is found in Stern et al. (1996).

Version3.0 also solves the equations on a regular grid, but instead of using the finite analytic method the code is based on higher order finite differencing. This means that the equations are reduced to algebraic form by discretization based solely on different kinds of finite difference schemes. For the steady state calculations, which are performed in this project, the temporal discretization is based on a first order backward Euler difference. The spatial discretization is performed by a second order upwind scheme for the convective terms, while all other first derivatives and viscous terms are discretized by a standard second order central difference scheme. In order to avoid the decoupling introduced by the collocated grid approach the pressure and the velocities are

coupled by means of the projection method, where a pressure equation is derived by taking the divergence of the momentum equations and by projecting the velocity into a divergence-free field at the time level (*n*). The oscillations caused by the decoupling are prevented by adding fourth order dissipation. Since the method is fully implicit it requires an iterative solution procedure. In the code the line-ADI scheme with underrelaxation is used to solve the algebraic equations originating from the discretization of the governing equations and the pressure equation. Further details about the numerical method used in version3.0 should be found in Wilson et al. (1998).

Since both versions of the code described above are based on iterative methods, it is necessary to apply a convergence criterion to stop the calculation when the solution is assumed to be good enough. In case of unsteady calculations several iterations are required within each time step to ensure that the pressure and the velocities converge and satisfy the momentum and pressure equations. However, in the present case, where steady state solutions are considered, convergence in each time step is not required. Instead few iterations in each time step are applied and the time step is used as an iteration parameter. When this approach is adopted the change in the solution between two time steps reflects how close the solution is to the steady state solution. Therefore, the convergence criterion is based on the residuals, which express the change in the solution between two successive time steps. The residuals for the flow variables are defined as the 1-norms of the change in the calculated variables between time steps (*n*) and (*n*+1), i.e.

$$RES_{\phi} = \frac{\sum_{i}^{Ntot} \left| \phi_i^n - \phi_i^{n-1} \right|}{Ntot} \tag{8.9}$$

where ϕ represents *u*, *v*, *w*, or $\hat{p}$ and *Ntot* is the total number of grid points. Usually, a solution is assumed to be converged when the residuals have dropped at least three to four decades to a level around 10^{-3} and 10^{-4}.

8.4 Boundary Conditions

Before the governing differential equations can be solved, a set of boundary conditions is required. For the present calculations several conditions are applied and they are briefly described below.

Far Field

Sufficiently far away from the body the disturbance caused by the body itself should disappear and leave the velocity components with their free stream values. Since it is not possible to prescribe both velocity and pressure on the same boundary, a zero gradient condition must be used for the pressure normal to the surface of the domain. The two conditions are expressed as

$$u_i = (1,0,0) \quad and \quad \frac{dp}{dn} = 0 \tag{8.10}$$

No-slip
On the body itself the velocity components of the fluid particles relative to the body must be equal to zero. This effect is obtained by use of a no-slip boundary condition saying that

$$u_i = (0,0,0) \quad and \quad \frac{dp}{dn} = 0 \tag{8.11}$$

where the condition for the pressure again says that the pressure gradient normal to the surface must be equal to zero.

Exit
In the wake behind the body, both the velocity components and the pressure are unknown and it is therefore impossible to prescribe the values of the variables in this region. However, sufficiently far downstream of the body there should be no changes in the flow variables when going in the *x*-direction or the free-stream flow direction. This exit condition can be expressed as

$$\frac{\partial(u,v,w,p)}{\partial x} = 0 \tag{8.12}$$

Mirror Image instead of Free Surface
Since the free surface elevation is neglected in the calculations, there is no need for applying the free surface boundary condition. Instead a mirror image or symmetry condition is used. This condition says that there is no flow through the surface and that the gradients of *u*, *v* and *p* in the *z*-direction must be equal to zero, i.e.

$$\frac{\partial(u,v,p)}{\partial z} = 0 \quad and \quad w = 0 \tag{8.13}$$

Multi-block Boundary Conditions
In cases with complex geometries it is convenient to split the flow domain into smaller subdomains or blocks to obtain larger flexibility in the grid generation. However, this requires a method for exchanging boundary data between neighboring blocks. When the multi-block approach is used there are two ways of handling the exchange of data, depending on how the blocks are connected. One is the case where the blocks are connected point to point (patched multi-block) and another is the case where blocks with different dimensions are connected and therefore need to be overlapping (overlapped multi-block).
As regards the patched multi-blocks the value of the flow variable at a common boundary point of two blocks is determined by a weighted average of the two values from the neighboring points found in the direction normal to the two boundaries.
In the case of overlapped multi-blocks the value of the flow variable at a point at the boundary of the considered block is determined by three-dimensional linear interpolation in the neighboring block. This approach requires that the blocks are overlapping with at least two cells to ensure a valid interpolation molecule.

Symmetry or Center Plane Condition
In order to exploit the symmetry at the center plane of a ship or a zero degree rudder and thus be able to work with half domain models, a center plane condition must be applied:

$$\frac{\partial(u, w, p)}{\partial y} = 0 \quad and \quad v = 0 \tag{8.14}$$

The condition has the same effect as the mirror image described by (8.13), the only difference is that (8.14) is applied to the boundary representing the center plane instead of the free surface boundary.

Pole Condition
The final boundary condition, which is relevant in this context, is the pole condition. This condition is applied to lines of singularities in the grid, introduced when the grid lines in a domain are collapsed into a single line. Conditions of this type may be used to model for instance the flow below a rudder with square tip as illustrated in Figure (8.1).

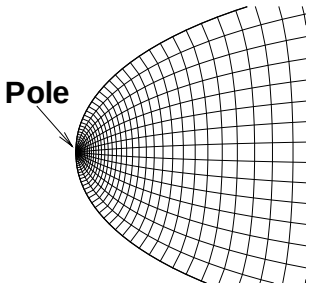

Figure (8.1) *Pole in grid.*

Instead of solving the governing equation for the nodal flow values on the singular pole boundary, the values are determined as an average of the variable values in the neighboring nodes belonging to the current grid layer.

8.5 Propeller Model

The propeller is not physically represented by its geometry in the flow. Instead the effect of the propeller is included in the model by prescribing an axial and a tangential body force distribution at the propeller disk on the basis of the propeller coefficients K_Q and C_{Th} and the advance coefficient *J*. The applied distribution is suggested by Hough and Ordway (1965) and the two force components are given as

$$fb_x = A_x r^* \sqrt{1 - r^*} \tag{8.15}$$

$$fb_\theta = A_\theta \frac{r^* \sqrt{1 - r^*}}{\left(1 - Y_h\right) r^* + Y_h} \tag{8.16}$$

where

$$A_x = \frac{C_{Th}}{\Delta x}\ \frac{105}{16\left(4+3Y_h\right)\left(1-Y_h\right)} \tag{8.17}$$

$$A_\theta = \frac{K_Q}{\Delta x\ J^2}\ \frac{105}{\pi\left(4+3Y_h\right)\left(1-Y_h\right)} \tag{8.18}$$

In these equations $f_{b\theta}$ and f_{bx} are the longitudinal and the tangential components of the force, respectively. The non-dimensional radius r^* is defined by $r^* = (y-Y_h)/(1-Y_h)$ and $Y_h = R_h / R_p$, where R_h and R_p are the hub and propeller radii, respectively. Δx is the longitudinal extension of the propeller disk and *J* is the advance coefficient defined by

$$J = \frac{u_a}{nD} \tag{8.19}$$

where u_a is the speed of advance, *n* is the number of propeller revolutions and D is the propeller diameter. The thrust coefficient C_{Th} is defined as

$$C_{Th} = \frac{T}{1/2\rho u_a^2 \pi R_p^2} \tag{8.20}$$

where T is the thrust. C_{Th} can also be expressed by *J* and K_T

$$C_{Th} = \frac{K_T}{\pi/8\ J^2} \tag{8.21}$$

where

$$K_T = \frac{T}{\rho n^2 D^4} \tag{8.22}$$

Finally, K_Q is the torque coefficient defined as

$$K_Q = \frac{Q}{\rho n^2 D^5} \tag{8.23}$$

The force component f_{bx} is aligned with the *x*-direction in the computational domain and can as such be used directly. The tangential component must be resolved into two components: One in the *y*-direction and one in the *z*-direction. The forces are imposed on the RANS grid at the points which lie within the propeller disk. When a grid point

has been identified the body force is calculated from the known distribution and then assigned to the current grid point.
It should be noted that, by adoption of this approach, only some of the interaction mechanisms can be included in a numerical rudder-propeller-hull model. It is possible to model the “propeller-on-hull” and “propeller-on-rudder” interaction, but since the body force is prescribed and therefore independent of the current flow field at the propeller the “hull-on-propeller” and “rudder-on-propeller” effects cannot be taken into account. This means that a “rudder-on-propeller” effect like the one illustrated in Section 5.4.3 in Chapter 5 will not be captured. However, in the present work, this prescribed body force approach is assumed to be sufficient, in order to simplify the model. A more realistic model would be obtained if the prescribed body force distribution was substituted by a distribution calculated interactively by a propeller performance program, but this is not within the scope of this project.

8.6 Pre- and Post-processing

In order to round off the description of the numerical methods, a comment should be made on the pre- and post-processing tools. CFDSHIP-IOWA only provides the flow solver itself, so it is necessary to use other tools for grid generation and visualization of the computational results. In the present project two commercial codes were applied. The computational grids were generated by an elliptic method implemented in Gridgen®, Pointwise, Inc., while the post-processing was performed by use of Tecplot®, Amtec Engineering, Inc.

This page is intentionally left blank.

Chapter 9

Preliminary Investigation of Numerical Interaction Model

9.1 Introduction

By recalling the findings from the studies of the mathematical model behind the simulator in Chapter 3, the model testing technique used for determination of the hydrodynamic input data in Chapter 4 and the experimental investigation of some of the interaction effects in Chapter 5, it appeared that a comprehensive model test program covering several test conditions had to be conducted in order to provide the interaction data necessary for a complete simulation. However, the idea of the numerical flow study in this context was not to provide a complete set of data for a maneuvering simulation, but rather to concentrate on a few conditions and study them in more detail, in order to obtain knowledge of the interaction effects on the integral level concerning the hydrodynamic forces and on the flow field level concerning the influence on the velocity and pressure fields.

With this objective in mind, the following plan for the computational work was outlined: First a grid around the hull with the rudder should be generated. Then a calculation should be carried out in order to ensure that the model was working. Subsequently the model should be extended by inclusion of the propeller, which was assumed to be relatively uncomplicated, since the propeller does not require additional grid generation, because it is represented by body forces applied directly to the hull-rudder grid. With the full hull-rudder-propeller model working, a limited parameter study should be carried out for different propeller loads and different rudder angles to study the interaction effects.

However, as the results in this chapter shows, it was no straightforward job to build the full hull-rudder-propeller model, because the grid generation around the stern region and the rudder was really complicated and constantly resulted in grids on which the solution did not converge. Actually, the effort did not lead to any solutions, but it was useful in the process of gaining experience in grid generation and limitations of the numerical models with respect to stability. In the present chapter the work on the hull-rudder model is described briefly, and the experience is used as a basis for outlining a new approach to building the complete numerical model.

9.2 Model Condition for Numerical Investigation

Before the numerical work was initiated it was necessary to select a model condition which enabled investigation of the rudder-propeller-hull interaction without being too complex to handle numerically. Since most of the interaction data for a maneuvering simulation is derived on the basis of experimental data measured by the PMM technique in the towing tank, it seemed to be a good idea to consider one of these test cases. By doing so, it was possible to investigate the behavior of the rudder, the propeller and the hull while different parameters like rudder angle, ship speed etc. were varied systematically. At the same time it was possible to restrict the flow to a special type of ship's motion in order to avoid cross coupling effects from different types of motions. Finally, it would also be possible to generate experimental data which could be used for comparison with the numerical results, since the numerical condition would be similar to a traditional PMM condition.
In relation to the description of the input data generation to the simulator by means of the PMM testing technique in Chapter 4, a number of different tests were mentioned. These tests covered the "static rudder", "rudder and drift", "static drift", "pure yaw", "yaw and drift" cases. Since it was planned to use a steady state RANSE method for the numerical investigation, it was not realistic to consider the two dynamic yaw tests which would require unsteady calculations. The three remaining tests were all static cases, which could be used for the investigation of the rudder-propeller-hull interaction. The tests were described in Chapter 4, but a brief summary is presented here.

"**Static rudder**":
The model travels through the tank on straight course with variations in the rudder angle.

"**Static drift**":
The model travels through the tank with variations in the drift angle. The rudder angle is set to zero.

"**Drift and rudder**":
The model travels through the tank with variations in the drift angle and the angle.

As seen from the descriptions above, two of the tests involved oblique flow, which meant that the flow would be dominated by a strong cross flow around the hull. According to Hochbaum (1998) and Ohmori et al. (1998), who made RANSE simulations for bare hulls in oblique flow, this type of flow is complicated to model, so in order to simplify the calculations during the grid generation phase and concentrate on the rudder-propeller-hull interaction without the influence of oblique flow, it was decided to consider the "static rudder" case. Even though the "static rudder" test appears to be the simplest, it still has to be kept in mind that the test plays an important role for determination of the basic propulsive and force related quantities applied in the simulator, so it is not irrelevant to consider it in the numerical study.

9.3 Numerical Hull-rudder-propeller Model

After identifying the flow situation to be considered, the numerical work was initiated. The grid was generated by means of an elliptic method implemented in the commercial code Gridgen® from Pointwise Inc., while the flow calculations were performed with the RANS-based flow solver CFDSHIP-IOWA version2.1, which was briefly described in Chapter 8.

9.3.1 Simplifying Assumptions

In order to simplify the numerical model a number of different assumptions were made. Since the work was concentrated on calculation of the flow around a tanker hull form, it was assumed that the computations could be simplified by neglecting the free surface to reduce the complexity of the model. Of course, this assumption would introduce a difference between the numerical model and the real ship, but since a tanker like the Esso Osaka is large and relatively slow and therefore operates at low Froude numbers, the flow should not be dominated by wave effects. The Esso Osaka is operating at a Froude number around 0.14 for the service condition, but for the full-scale maneuvering trials, which are relevant in this context, the Froude number was even smaller, namely Fn_{Lwl}=0.063, corresponding to a full-scale ship speed of 7 knots. At a Froude number of this magnitude the influence of the waves is small and in relation to the resistance, this quantity will mainly be dominated by viscous effects and form resistance. Finally, it should be mentioned that as regards the rudder-propeller-hull interaction the small waves at Fn_{Lwl}=0.063 should hardly influence the rudder and the propeller, which are submerged all the time. With respect to simplifications of geometry, the rudder shaft and the rudder heel were neglected in order to simplify the grid generation and moreover the ship was considered on even keel, so that the effect of squat was neglected. The draft corresponded to 21.79m in full scale and the remaining model and ship particulars are found in Appendix A.

Concerning turbulence modeling the results of the literature study for viscous CFD methods showed that, when these methods were applied to ship's flows, they seemed to perform reasonably in conjunction with the Baldwin-Lomax turbulence model. On this basis, it was assumed that this turbulence model should initially be applied to the calculations, even though the model does not apply a near wall model and therefore requires a very fine grid resolution in order to resolve the boundary layer flow.

Finally, the influence of the rudder and the hull on the propeller flow itself was neglected, since the applied Hough-Ordway propeller model prescribed the propeller force instead of allowing the force to change in accordance with the surrounding flow. However, for the grid generation phase and the initial flow study this model was assumed to be sufficient.

9.3.2 Grid Generation and Boundary Conditions

In the grid generation phase, different grids were tested to find a topology which enabled sufficient grid resolution on the hull and rudder surface to resolve the surface pressure

field and at the same time made it possible to resolve the turbulent boundary layer on the no-slip surfaces. Since the Baldwin-Lomax turbulence model, which does not use wall functions, was applied, the layer of computational cells closest to the wall was placed at a distance from the wall, which was approximately equal to 10^{-6} and consequently resulted in a non-dimensional wall distance corresponding to $y^{+}\approx 1$. In numerical ship calculations the center plane symmetry is usually exploited to reduce the size of the model. Thus only one side of the flow domain is modeled. But in this case the presence of the propeller and the need for the ability to turn the rudder destroyed the symmetry and made it necessary to model the domain on both sides of the ship. All in all these factors resulted in a quickly expanding grid size, which was critical in relation to the computational power required to solve the flow problem numerically.

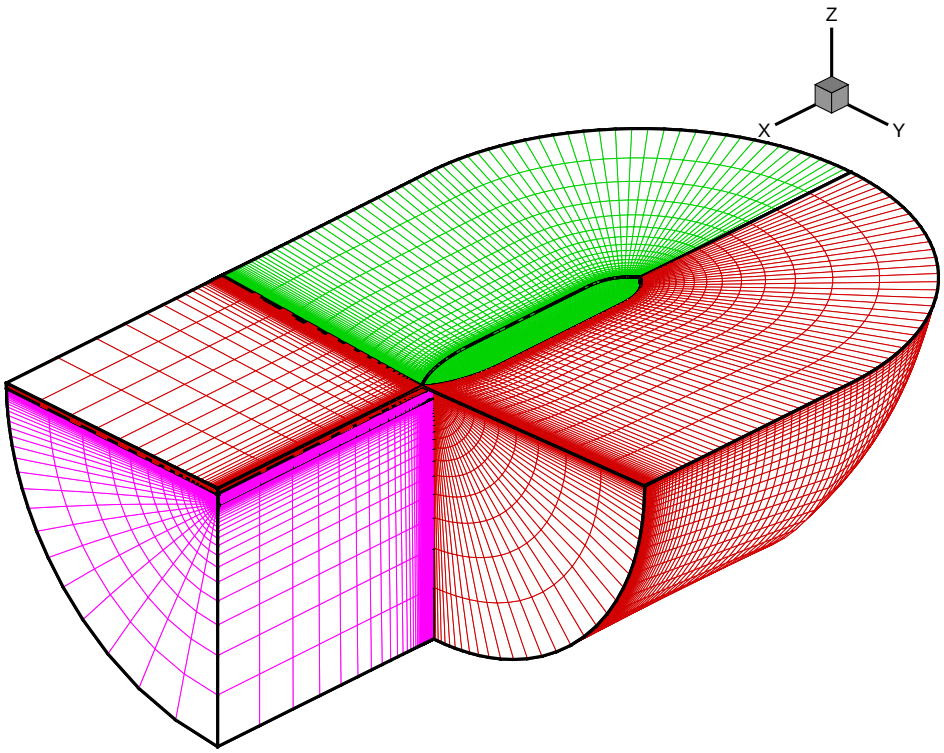

Figure (9.1) *Overall block structure for rudder-hull grid.*

It was quickly realized that it was not possible to generate the grid without using the patched and overlapping multi-block approaches, since these were the only methods which were flexible enough to allow a combination of the rudder geometry and the hull geometry. The grid generation led to several grid topologies, but they constantly resulted in numerical instabilities, causing the numerical solution to diverge in the stern region. The latest grid, which consisted of eight blocks, is shown in Figures (9.1) and (9.2). The individual blocks had the following purpose: Around the ship two blocks with C-C-topology were used to model the hull (red and green in Figure (9.1)). Each block consisted of 103 points along the hull (ξ-direction), 60 points in the direction perpendicular to the hull (η-direction) and, finally, 41 points in the girdwise direction (ζ-direction), i.e. the dimension was 103x60x41. The two blocks were patched at the center plane, while they were overlapping with the remaining blocks in the wake. Around the rudder two blocks with C-topology were used to model the lower part of the

wake of the ship and the rudder except for the upper end (magenta in Figure (9.1)). The block consisted of 93 points in the longitudinal direction (ξ-direction), 60 points in the direction perpendicular to the rudder surface (η-direction) and 40 points in the spanwise direction (ζ-direction), ending up with a total dimension of 93x60x40. Again the blocks were patched at the center plane and connected to the remaining neighboring blocks by the overlapping multi-block approach.

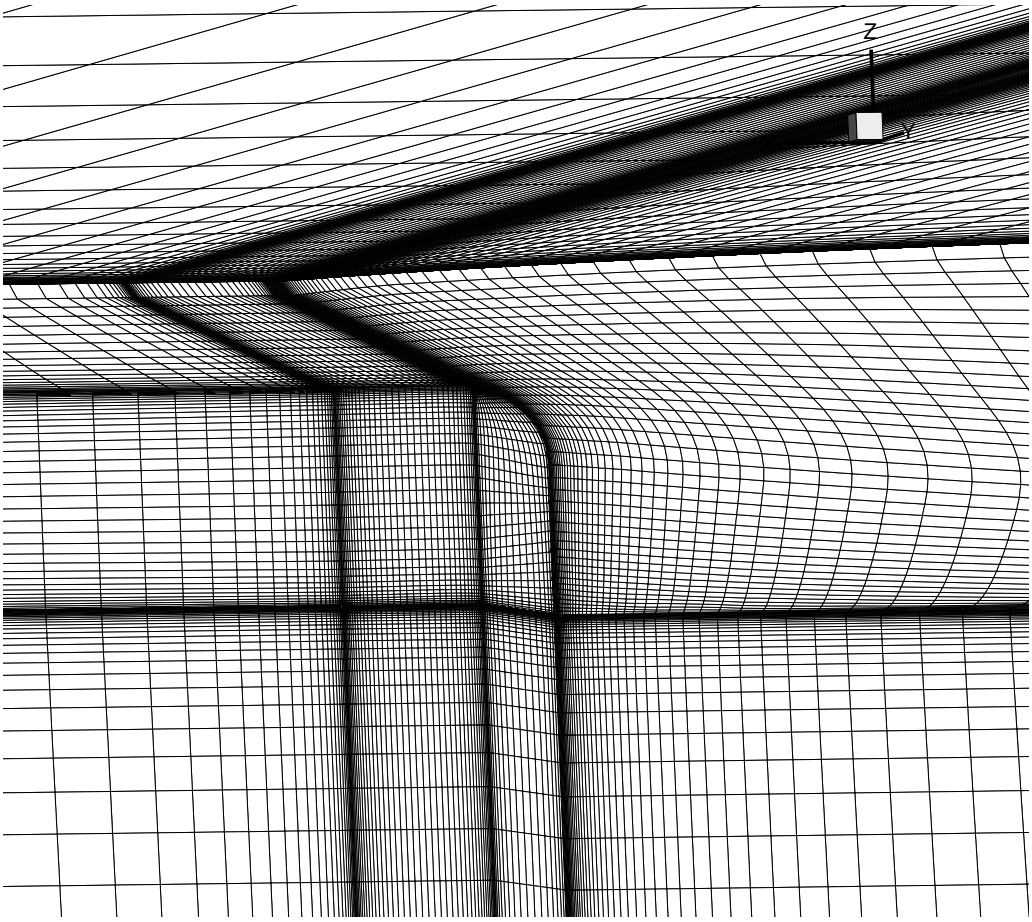

Figure (9.2) *Grid on hull and rudder.*

Above the rudder in the upper part of the wake of the ship, two blocks with H-topology were placed in order to model the wake (red in Figure (9.1)). The dimensions of these blocks were 75x60x31, where the number of points in the different coordinate directions follows the same directions as the one used for the rudder blocks. These blocks were also patched at the center plane and overlapping with the other blocks. Finally, two thin blocks were placed on the top of the rudder, where they modeled the upper end of the rudder. The dimensions of these blocks were 40x5x5. The model ended up with a total number of grid cells of 1,234,160.

Concerning the boundary conditions applied to solving the flow problem, the following conditions were used: At the block boundaries placed in the interior of the domain the multi-block boundary conditions for patched and overlapping grids were used in order to exchange data between the blocks. On the free surface, the waves were neglected and a mirror image was applied instead. At the outer boundaries, which were placed approximately one ship’s length away from the hull, a far field condition prescribing the ship speed was applied, while a zero gradient exit condition was applied to the boundary

behind the ship. Finally, the rudder and the hull surfaces were modeled by means of the no-slip condition. The individual boundary conditions are described in more detail in Chapter 8.

9.4 Experience Obtained for Future Work

On the basis of the experience obtained from the numerical work described above, it seemed to be more complicated to build the complete rudder-hull model in a single step than initially expected. Three issues were found to be difficult. The first concerned the grid quality in order to avoid numerical instabilities. When the present type of numerical methods for simulation of complex three-dimensional flow problems is dealt with, the grid is not to satisfy any stability criteria to avoid the numerical instability. It is possible to calculate the skew and the aspect ratios of the cells, which reflect the grid quality, but in the end it is up to the user to judge if the grid looks fine, on the basis of his or her experience. Actually, the only way to check the grid is to perform the calculation and see if the solution blows up. One of the reasons for the stability problems in the present case was that the fine near wall spacing, caused by the applied turbulence model, resulted in extreme cell aspect ratios. Another was that the C-H-grid approach, which generally modeled the domain along the hull well, caused the cells to be extremely skewed at the keel in the aft part of the hull as illustrated in Figure (9.3). The problems with the skewed cells would require another grid topology in the critical region as shown in a later chapter, while the problems caused by the aspect ratios could be solved by adding more points to the grid. But then the second critical issue appeared, namely that the size of the model exceeded the limitations of the available computer, which was around 1.2 million cells. So in order to refine the grid in a critical region it was necessary to make it coarser in another region. Moreover, it was really time consuming to perform a calculation to test the grid every time a change was made.

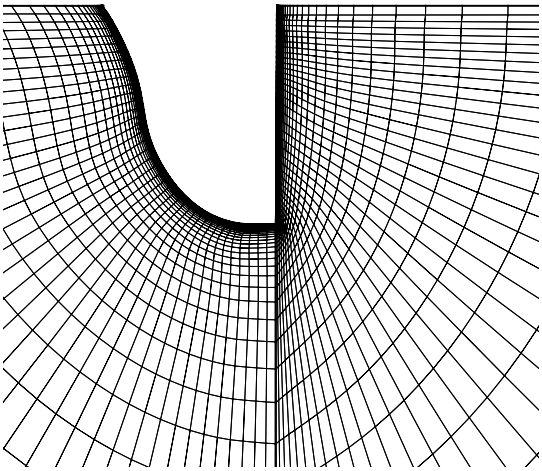

Figure (9.3) *Skew introduced by C-grid.*

Finally, the third issue concerned the necessity for experience in order to generate a grid which modeled both rudder and hull, so that the characteristic flow features for each component were captured. This knowledge could be obtained by the trial and error method applied to the full model, but the approach is time-consuming and expensive,

when numerical models of the size as in the present case are used. It would be more advantageous to have an idea of the requirements of the grid concerning the number of grid points and grid clustering for the hull and the rudder before the grid generation for the full model was initiated. This could probably help to avoid some of the problems with numerical instabilities, but also help to generate a sufficient model with respect to the size of the grid.
On the basis of the experience from the initial work it was decided to stop working on the complete rudder-hull model and to choose a more rational approach, which seemed to be a stepwise procedure where each component was investigated at a time. By doing so, it would be possible to gain knowledge of the requirements of the local grids around the hull and the rudder, but also to investigate the performance of the code for each component. Besides, it would be possible to address parts of the interaction effects, for instance between rudder-propeller and hull-rudder. The new stepwise procedure is outlined in Table (9.1).

Step	Activity
1	2-D flow around rudder profile
2	3-D flow around rudder in free stream
3	3-D flow around rudder behind a propeller
4	3-D flow around bare hull
5	3-D flow around hull with rudder
6	3-D flow around hull with rudder and propeller

Table (9.1) *Stepwise procedure for generation of complete rudder-propeller-hull model.*

9.5 Summary

In the present chapter the initial work on generation of a complete numerical model of a ship equipped with rudder and propeller was described. First a relevant ship condition was selected for consideration. It was decided to consider the ship in a condition corresponding to the “static rudder” PMM test, since this condition was found to enable a systematic study of the rudder-propeller-hull interaction. Subsequently the geometric and numerical assumptions used to simplify the model were described together with the grid and boundary conditions for the latest combined rudder-hull model.
The effort did not result in any solutions, since iterative convergence could not be achieved, but on the basis of the experience obtained from the work some critical issues were identified. It was found that the model size seemed to be critical, since 1.2 million grid cells were not enough to model the rudder-hull flow problem. In addition to this, some critical topics concerning the grid topology were detected and it was realized that more experience and knowledge of the flow problem and the requirements of the local rudder and hull grids were necessary to generate the complete rudder-propeller-hull model. Finally, a new stepwise procedure was outlined on the basis of the initial work to provide some of the knowledge and experience necessary for the completion of the full rudder-propeller-hull model.

This page is intentionally left blank.

Chapter 10

2-D Rudder Profile

10.1 Introduction

In two-dimensional viscous flow calculations around wing profiles the well known NACA0012 is probably one of the most often treated test cases. Thus, information can be found about numerical topics as well as experimental data for validation of the results in the literature. Therefore, it seemed to be a good idea to select this profile for the initial calculations, where it was tried to gain some experience in CFDSHIP-IOWA.
In the present chapter the lift and drag characteristics of a two-dimensional NACA0012 profile are calculated for angles of attack not exceeding the stall angle. The investigation covers a grid study where the uncertainty introduced by the grid is estimated, calculations for three different Reynolds numbers and, finally, comparison of the calculated lift coefficient, drag coefficient and pressure distribution with experimental data. Calculations have been performed for Reynolds numbers equal to $Re=0.76\cdot10^6$, $Re=3.0\cdot10^6$ and $Re=6.0\cdot10^6$ and angles of attack equal to $\alpha=0°$, $\alpha=3°$, $\alpha=6°$, $\alpha=9°$ and $\alpha=12°$.

10.2 Grid Generation and Boundary Conditions

The calculations were performed with a C-grid topology generated by an elliptic method implemented in Gridgen©. The coordinate system for the non-orthogonal curvilinear coordinates was oriented so that the ξ-direction ran along the profile surface, the η-direction was perpendicular to the surface and the ζ-direction ran in the spanwise direction. The first grid which was considered had 239 points in the ξ-direction, 60 points in the η-direction and 3 points in the ζ-direction. The reason for using 3 points instead of 1 in the ζ-direction is that CFDSHIP-IOWA is a 3-D code which requires more cells in this direction.
To determine how far the outer boundary of the domain should be placed away from the profile a small literature study was carried out. Guilmineau et al. (1997) gathered information from the literature about several viscous CFD calculations on two-dimensional wing profiles. According to the paper, calculations were performed with grids where the outer boundaries were placed from 3 to 48 cord lengths away from the

profile. Therefore, the outer boundaries were initially placed approximately 3 cord lengths away from the profile. The extension of the grid in the ζ-direction (coincide with *z*) corresponded to 1.4 times the cord length, see Figure (10.1). In order to resolve the boundary layer it was attempted to place the first layer of computational cells at a distance from the profile which resulted in a non-dimensional wall distance y^+ less than one. Therefore, the grid points closest to the wall were placed at a physical distance of $y=2\cdot10^{-6}$ from the wall. On the boundaries the conditions shown in Table (10.1) were applied. The definition of the boundary conditions can be found in Chapter 8.

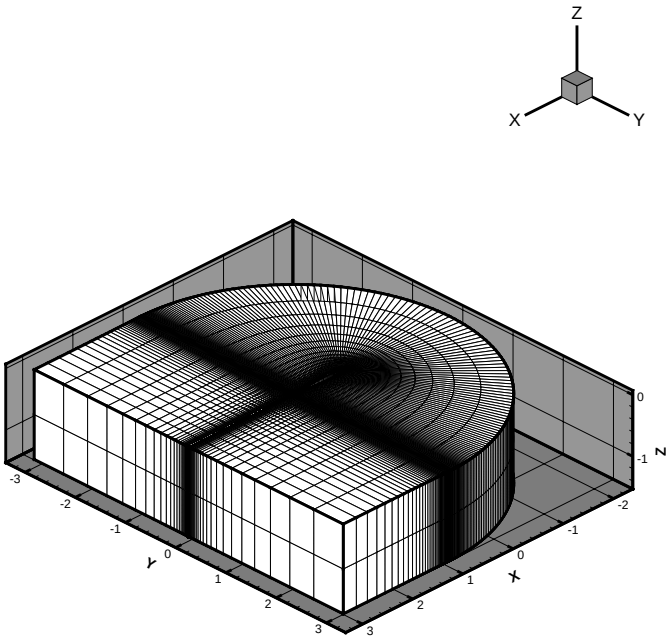

Figure (10.1) *Initial C-grid. 239x60x3*.

Type	*i*-index (ξ)	*j*-index (η)	*k*-index (ξ)
Exit	1 to 1	1 to j_{max}	1 to k_{max}
Exit	i_{max} to i_{max}	1 to j_{max}	1 to k_{max}
Cut	1 to $i_{no\text{-}slip\ start}$	1 to 1	1 to k_{max}
No-slip	$i_{no\text{-}slip\ start}$ to $i_{no\text{-}slip\ end}$	1 to 1	1 to k_{max}
Cut	$i_{no\text{-}slip\ end}$ to i_{max}	1 to 1	1 to k_{max}
Far field	1 to i_{max}	j_{max} to j_{max}	1 to k_{max}
Zero gradient	1 to i_{max}	1 to j_{max}	1 to 1
Zero gradient	1 to i_{max}	1 to j_{max}	k_{max} to k_{max}

Table (10.1) *Boundary conditions used for 2-D NACA0012 calculations.*

After calculating the flow with the grid described above, the results shown in Figure (10.2.a) were obtained. The figure shows the integral force coefficients represented by

the frictional drag C_{fx}, the pressure drag C_{ppx} and the total drag C_{totx}, which are defined by

$$C_{fx} = \frac{F_{fric,x}}{1/2\rho U^2 S} \qquad C_{ppx} = \frac{F_{press,x}}{1/2\rho U^2 S} \qquad C_{totx} = \frac{F_{tot,x}}{1/2\rho U^2 S} \tag{10.1}$$

where ρ is the density, U is the free stream speed and S is the wetted surface of the profile. $F_{fric,x}$ and $F_{press,x}$ are forces found by integrating the viscous shear stresses and the pressure-induced normal stresses over the profile and projecting the force on the x-direction, while $F_{tot,x}$ is the sum of the two components.

It was found that the solution was oscillating and that the oscillations were decaying slowly. This was also reflected in the residuals, which are shown in Figure (10.2.b), because it was observed that the residuals showed relatively slowly iterative convergence. Usually, a solution is said to be converged when the residuals have dropped at least three to four decades and this was not seen to be the case for the pressure. To make sure that the poor convergence was not caused by insufficient grid resolution an additional study was carried out for a finer grid made by a $\sqrt{2}$ refinement: 337x85x3. However, the results showed the same oscillating tendencies and poor convergence. In some cases the problems with the oscillating behavior became even worse.

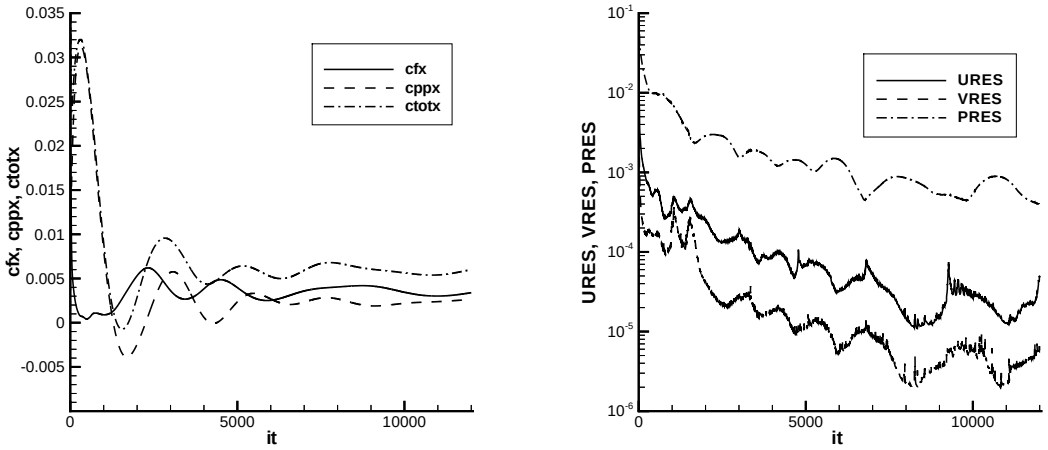

a. Drag forces *b. Residuals*

Figure (10.2) *Results from calculation with initial grid for α=0° and Re=3.0·10^6.*

The results discussed above covered the case of an angle of attack equal to α=0°, but additional calculations with angles of attack different from zero showed that convergence became more difficult to obtain as α was increased, and in some cases the solution became divergent and blew up. A study of the solutions showed that the instabilities always occurred in a region in the wake close to the trailing edge. It was found that, due to the large spanwise extension of the domain, the cells in this region had extreme aspect ratios, which apparently destroyed the solution when the profile was rotated and the flow direction changed. The solution to the problem seemed to be an

improvement of the aspect ratios of the cells by reducing the extension of the computational domain in the spanwise direction.
Another reason for the generally poor convergence could be that the outer boundaries of the computational domain were placed too close to the profile. The explanation could be that when the profile was turned it disturbed the flow farther away from the profile. If the boundaries were then placed too close to the profile they would influence the local flow and maybe destroy the solution. In this case it was decided to move the boundaries farther away, but a later study of 3-D rudder calculations showed that the main reason for the convergence problems was to be found in the large cell aspect ratios.

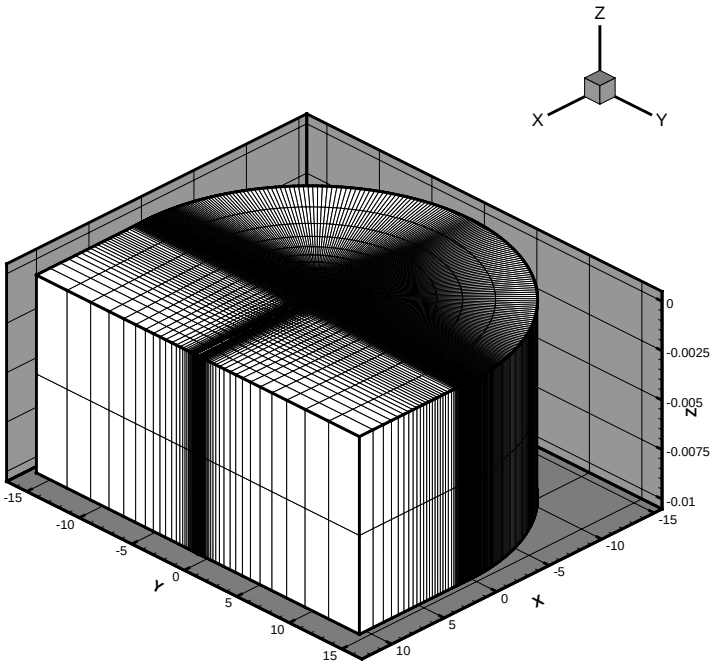

Figure (10.3) *Improved C-grid. 427x94x3.*

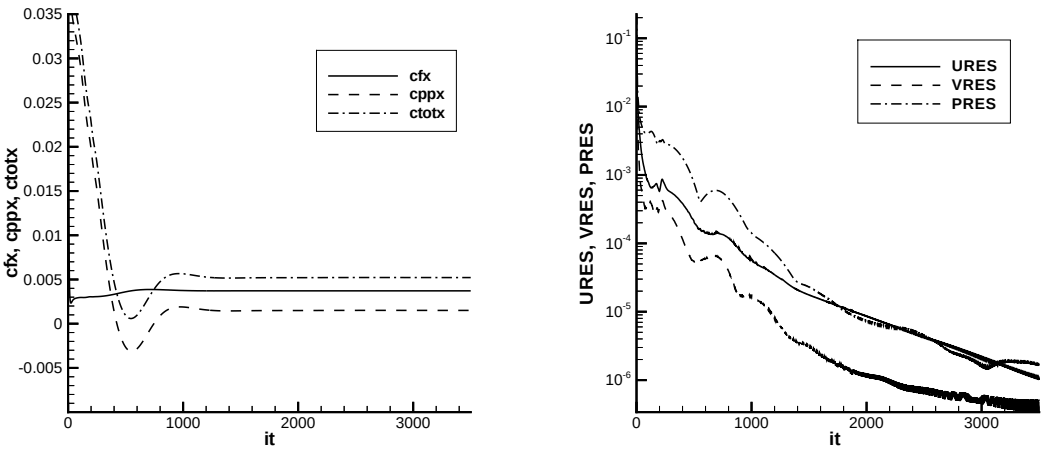

a. Drag forces *b. Residuals*

Figure (10.4) *Results from calculation with improved grid for α=0° and Re=3.0·10^6.*

After the initial study it was decided to generate a new C-grid (427x94x3), but this time the outer boundaries were placed 15 cord lengths away from the profile, and the extension of the domain in the spanwise direction was reduced to one percent of the cord length to improve the aspect ratios. The new grid is shown in Figure (10.3), while the results obtained by the grid are shown in Figure (10.4). In the first place Figure (10.4.a) shows that the solution had become stabler, meaning that the oscillations decayed faster throughout the solution. In the second place Figure (10.4.b) shows that the solution converged better with the new grid than with the old one, but it also shows that convergence was obtained faster, even though the grid was finer than the first.

On the basis of the results presented above it was decided to use a domain with the same extensions as those of the improved grid. However, before the actual calculations were carried out a grid study was conducted in order to estimate the uncertainties connected with the grid.

10.3 Verification and Validation

To be able to verify and validate the CFD calculations it is necessary to estimate the numerical uncertainties and possibly also the errors introduced by application of a given grid. In the present grid study the contributions to the numerical uncertainty and error originating from iterations and grid were investigated. It was checked if grid convergence could be achieved as the grid was refined and if the individual solutions showed iterative convergence.

The grid study was conducted with three grids made by a systematic $\sqrt{2}$ refinement: Coarse: 301x66x3, medium: 427x94x3 and fine: 598x133x3 for zero angle of attack, $\alpha=0°$ and $Re=0.76\cdot10^6$. During the grid study the number of points in the ξ- and η-directions was varied while the number of points in the ζ-direction (spanwise) was kept constantly equal to 3, since there was no flow in this direction for the two-dimensional flow. The results were evaluated on the basis of the calculated non-dimensional total drag force coefficient, which was defined in (10.1). The results are shown in Table (10.2).

	Coarse 301x66x3	Medium 427x94x3	Fine 598x133x3	R_G
$C_{totx}\cdot10^3$ ε	6.671	6.438 -3.5 %	6.374 -1.0 %	0.27

Table (10.2) *Calculated drag forces from grid study.*

The study revealed iterative convergence of all three calculations where the residuals for the pressure *p* and the velocities *u* and *v* dropped at least four decades to a level below 10^{-4}. The type of iterative convergence was characterized as a kind of mixed oscillatory/convergent for the pressure and convergent for the friction. The convergence history for all three solutions had the same shape as that shown in Figure (10.4.a). Since all the solutions actually flattened out throughout the solution, it was assumed that the iteration error and uncertainty were negligible compared to the grid error and uncertainty, which are estimated below.

The estimation of the grid uncertainty or error was made on the basis of the procedure for verification of CFD simulations presented in Stern et al. (1999) and the idea behind the method is briefly described in Chapter 7. According to this method, the grid convergence ratio R_G is used to determine if the grid convergence condition is convergent($0< R_G <1$), oscillatory($R_G <0$) or divergent($R_G >1$). R_G is defined as the ratio between the change in the solution from medium to fine grid and the change in the solution from coarse to medium grid. The R_G value equal to 0.27 in Table (10.2) indicates that the drag force was converging as the grids were refined. This means that generalized Richardson extrapolation could be used for estimation of the grid uncertainty and possibly also of the error. With the grid refinement factor r_G equal to $\sqrt{2}$ and the theoretical order of the method equal to 2, the order of the method P_G, the error $\delta_{RE,G}$, the correction factor C_G and the grid uncertainty U_G were calculated. The results obtained for the fine grid are shown in Table (10.3). It is seen that the correction factor C_G was equal to 2.64, which was so far away from 1 that the case of lacking confidence should be applied. Therefore, only the grid uncertainty was estimated and it appeared that the uncertainty U_{G1} introduced by using the fine grid was 1.6%.
Even though, the case of lacking confidence was applied, it was tried to correct the solution for numerical errors, as suggested in Chapter 7, to provide an estimate of the level of the grid independent solution or the numerical benchmark S_C. From Tables (10.2) and (10.3) it is found that the calculated drag forces for the fine grid was fairly close to this numerical benchmark S_C.

Grid	Fine
r_G	$\sqrt{2}$
P_G	3.73
$\delta_{RE,G1}\cdot 10^4$	0.242
C_G	2.64
U_{G1} in % of solution	1.6
Numerical benchmark, S_C	$6.31\cdot 10^{-3}$
Deviation between S_C and solution in %	1.0

Table (10.3) *Grid uncertainties found in grid study for rudder in free stream.*

Since the number of computational cells for the fine grid was relatively high, the computation required relatively much CPU time and memory. However, the computational effort could be reduced by using a coarser grid, e.g. the medium grid, even though this would introduce a larger grid uncertainty. Therefore, it was interesting to investigate how large the medium grid uncertainty would be. The verification method presented in Chapter 7 is derived for estimation of the uncertainty related to the fine grid, so in order to estimate the uncertainty introduced by the medium grid without making extra grids and performing extra computations, $\delta_{RE,G2}$ was estimated on the basis of the existing data in Table (10.3). According to Ferziger and Peric (1996) the derivation of the expression for the first order fine grid discretization error $\delta_{RE,G1}$ is

based on the assumption that $\delta_{RE,G1}$ is proportional to h^{P_G} and $\delta_{RE,G2}$ is proportional to $(r_G h)^{P_G}$ which also can be expressed as $r_G^{P_G} h^{P_G}$, where *h* is the fine grid spacing. Based on this relation it was therefore assumed that the medium grid discretization error was $r_G^{P_G}$ times larger than the fine grid error. Assuming that the order of the method P_G and the correction factor C_G from Table (10.3) were the same for the medium and fine grids, $\delta_{RE,G2}$ was found to be equal to $0.882 \cdot 10^{-4}$ resulting in a grid uncertainty U_{G2} equal to 5.9% of the fine grid solution. Finally, it should be noted that compared to the numerical benchmark the total drag force for the medium grid solution was 2% higher than the benchmark value.
As regards selection of the grid to be used for the calculations in this chapter, the choice was based on the results presented in Tables (10.2) and (10.3) and the considerations about the medium grid mentioned above. From the data it is observed that if the fine grid was used instead of the medium grid the total drag force would only change one percent. In addition to this, the medium grid solution was only two percent higher than the numerical benchmark compared to one percent for the fine grid. If this was seen in connection with the additional computational effort required when the fine grid was used instead of the medium grid, it seemed that the medium grid should be sufficient for the calculations. Therefore, the medium grid was applied to all the calculations. It should be mentioned that the chosen grid introduced a grid uncertainty of 5.9%, which means that validation can be achieved at no level higher than 5.9%. However, it was shown that further refinement of the grid reduced the uncertainty, so if needed this can be done.

In summary of the results obtained so far, the grid uncertainty has been estimated, while it was found that the uncertainty originating from the iterations was negligible compared to the grid uncertainty. The remaining source of uncertainty/error is the so called modeling error, which can only be investigated by comparison of the calculations with experimental data. The data used for the validation was taken from Michos et al. (1983), where results from wind tunnel tests with an NACA0012 profile at a Reynolds number equal to $Re=0.76 \cdot 10^6$ are presented together with estimates of the uncertainty related to the integral lift and drag quantities. This made it possible to determine the validation uncertainty.

	Medium 427x94x3, *S*	Fine 598x133x3, *S*	Experiment *D*
C_D	$1.324 \cdot 10^{-2}$	$1.311 \cdot 10^{-2}$	$0.79 \cdot 10^{-2}$
E	$-5.34 \cdot 10^{-3}$	$-5.21 \cdot 10^{-3}$	------
$U_S = U_G$	$7.81 \cdot 10^{-4}$	$2.49 \cdot 10^{-4}$	------
U_D	------	------	$6.32 \cdot 10^{-4}$
U_V	$1.00 \cdot 10^{-3}$	$6.79 \cdot 10^{-4}$	------

Table (10.4) *Comparison between drag forces from calculation and experiment*.

The experimental and calculated drag coefficient C_D is shown in Table (10.4) together with the estimated simulation uncertainty U_S, the data uncertainty U_D, the validation

uncertainty U_V and the comparison error *E*. It should be noted that the definition of the drag coefficient applied to the experimental results was different from the one applied to the CFD code. Therefore, the numerical results were converted to the form as in the experiment. The conversion is described later in the chapter.

	Medium 427x94x3, *S*	Fine 598x133x3, *S*	Experiment *D*
U_D % of *D*	------	------	8
E % of *D*	-68	-66	------
U_V % of *D*	13	8.5	------

Table (10.5) *Quantities used for validation of calculated drag forces.*

U_D, *E* and U_V are summarized in Table (10.5) and it is found that the calculations were quite different from the experiments, which results in a comparison error larger than the validation uncertainty, i.e. $|E|>U_V$ for both medium and fine grid. Thus, the code was not validated. The large comparison error indicated that a dominant modeling error was present, so the next step in the procedure involved identification of the problem causing the error. On the basis of results from additional calculations and the discussion presented in Section 10.4 below, it was found that the difference between calculation and experiment was most likely introduced, because the experiments were performed with profiles with smooth surfaces on which the boundary layer was laminar in a region from the leading edge to the position where transition occur, while the CFD code treated the boundary layer as being fully turbulent from the leading edge. Therefore, to compare calculations and experiments it was necessary to find some data where the boundary layer flow was turbulent all over the profile.

	Calculation *S*	Experiment *D*
C_D	$9.6\cdot10^{3}$	$9.8\cdot10^{3}$
E	$2.0\cdot10^{-4}$	------
U_S	$5.65\cdot10^{-4}$	------
U_D	------	$7.84\cdot10^{-4}$
U_V	$9.66\cdot10^{-4}$	------

Table (10.6) *Comparison between drag forces from calculation and experiment.*

In Abbott and Doenhoff (1959), measurements were performed with a profile equipped with leading edge roughness, which should enforce transition close to the leading edge and result in fully turbulent flow over most of the profile. It was therefore assumed that these results would be a better basis for the validation and a new comparison was made. The case of zero angle of attack $\alpha=0°$ was considered again, but this time at a Reynolds number equal to $6.0\cdot10^{6}$ to match the experimental conditions. A new grid study of three grids was not performed, as it was assumed that the results from the initial grid study could be used. Hence, the grid error was assumed to be 5.9% of the solution since the medium grid was used for the calculation. Concerning the experimental uncertainty, no uncertainty analysis is presented in Abbott and Doenhoff (ibid.), so it was assumed to be

8% as in Michos et al. (1983). The results from the calculation and the experiments are shown in Tables (10.6) and (10.7) together with the estimated uncertainties.

	Calculation *S*	Experiment *D*
C_D	$9.6 \cdot 10^3$	$9.8 \cdot 10^3$
E % of *D*	2	------
U_D % of *D*	------	8
U_V % of *D*	9.6	------

Table (10.7) *Comparison error, uncertainty in data and validation uncertainty*.

From the results in Table (10.7) it is observed that the agreement between the new calculation and the experiment including leading edge roughness is better than in the smooth profile case. It is also seen that the absolute value of the comparison error is smaller than the validation uncertainty, i.e. $|E| < U_V$, indicating that computations could be regarded as validated at a 9.6 percent level. It has to be kept in mind that these results were obtained with the medium grid with a grid uncertainty of 5.9%. The grid uncertainty could have been decreased by using the fine grid, since this would have introduced a grid uncertainty of 1.6%. However, due to the experimental uncertainty of 8% it would be impossible to bring the noise level or validation uncertainty below 8%. Therefore, to obtain validation at a lower level than 8% more accurate experimental data would be required.

10.4 Results and Discussion

The results are mainly presented as integral quantities, i.e. by lift and drag coefficients, since these are useful from an engineering point of view, but to obtain a little more insight into the details of the flow, the field quantities are shown for a single case.

10.4.1 Field Quantities

The field quantities presented below were calculated for a condition whith α=12° and *Re*=$0.76 \cdot 10^6$. Instead of turning the flow field the angle of attack was obtained by turning the profile and the grid relatively to the free stream. This is illustrated in Figure (10.5.b) where the free stream velocity component is parallel to the *x*-axis. The convergence history for the residuals is shown in Figure (10.5.a), from which it is observed that iterative convergence was achieved.
The calculated pressure distribution represented by the local pressure coefficient $c_p = (p - p_\infty)/(\frac{1}{2}\rho U^2)$ is shown in Figure (10.6.a), where it is plotted together with the experimentally determined distribution found in Michos et al. (ibid.). There seems to be agreement between the calculations and the experiments except in two regions. First, there is a small difference between the calculation and the experiment on the lower surface close to the trailing edge.

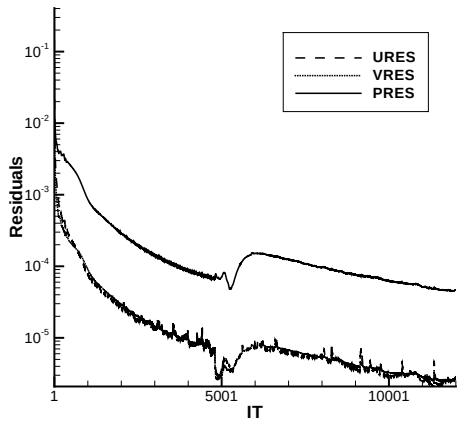

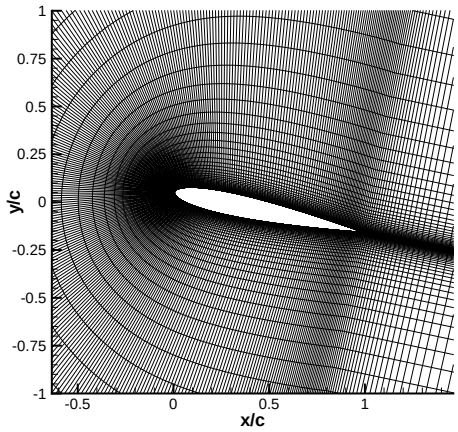

a. Residuals for u, v and p *b. Grid used for calculation with α=12°*

Figure (10.5)

Secondly, differences are observed for the pressure over the first 15% of the upper surface close to the leading edge, where the pressure peak is slightly over predicted by the calculation. There are probably two reasons for the behavior of the pressure distribution. One is found in the applied turbulence model because, according to Rizzetta and Visbal (1993), Guilmineau et al. (1997), Sanz and Platzer (1998), who have all made calculations of the flow around wing profiles with different turbulence models, it is characteristic for the Baldwin-Lomax turbulence model to overpredict the leading edge suction peak when the angle of attack increases towards the stall angle. The other is found in the assumption about steady state flow, because as the angle of attack increases and separation occurs, unsteady effects, which cannot be captured by the steady state calculation, may occur and result in differences between measurements and calculations.

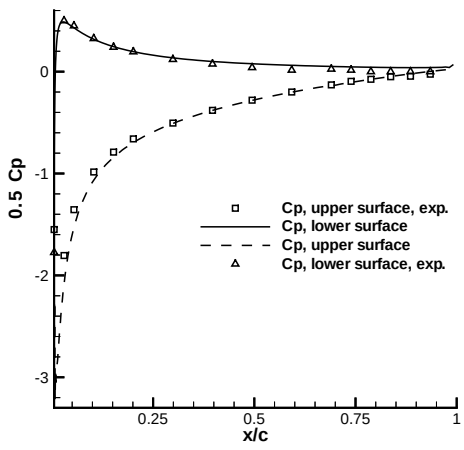

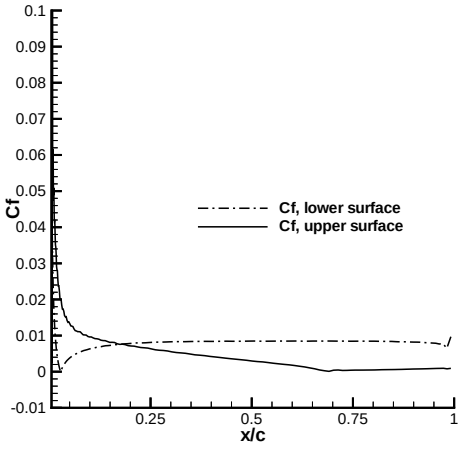

a. c_p *b. c_f*

Figure (10.6) *Calculated local pressure and frictional force coefficients.*

Concerning skin friction it was not possible to compare the calculation with experimental results since no data was available, but Figure (10.6.b) shows the local skin friction coefficient c_f, defined by $c_f = \tau_w / (\frac{1}{2}\rho U^2)$, where τ_w is the wall shear

stress, ρ is the density of the fluid and *U* is the free stream velocity. It is seen that c_f has a peak at the leading edge caused by the large velocity gradient in this region. On the upper or suction side of the profile it should be noted that c_f first decreases to a position of *x/c*≈0.7 and then starts to increase. This behavior may be explained by the fact that close to the surface there is a thin region from *x/c*≈0.7 to *x/c*≈1.0 where the flow is reversed.

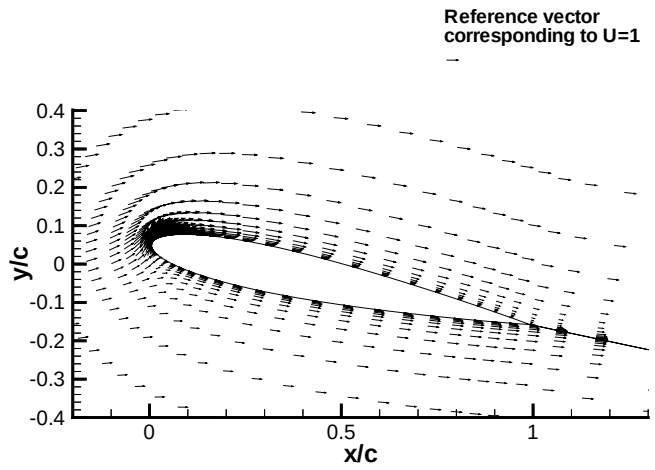

Figure (10.7) *Velocity vectors, (u, v).*

Since the reversed flow region is very thin it is difficult to see it on the vector plot of the velocities shown in Figure (10.7), but a closer study of the flow reveals that it is present. Finally, it should be noted that the vectors in the figure are shown for every 6th point along the profile and every 3rd point perpendicular to the profile.

10.4.2 Integral Quantities

The lift and drag coefficients from all the calculations are shown below together with experimental results found in the literature. Since the calculated coefficients were defined in another way than the experimental coefficients, the numerical values were converted to a format which could be compared with the experiments. For a rectangular wing the traditional lift and drag coefficients are defined as

$$C_L = \frac{L}{1/2\,\rho U^2 A} \qquad \textit{and} \qquad C_D = \frac{D}{1/2\,\rho U^2 A} \tag{10.2}$$

where L and D are the lift and drag forces, respectively, ρ is the density of the fluid, *U* is the free stream velocity and *A* is the projected wing area defined by

$$A = sc \tag{10.3}$$

where *s* and *c* are the span and cord length of the wing. However, in the CFD code the lift and drag coefficients are defined by

$$C_{toty} = \frac{L}{1/2\rho U^2 S} \qquad and \qquad C_{totx} = \frac{D}{1/2\rho U^2 S} \tag{10.4}$$

where *S* is the wetted surface area defined by

$$S = sl \tag{10.5}$$

where *l* is the arc length of the wing section. If the two definitions are combined the relation between the experimental and calculated lift and drag coefficients becomes

$$C_L = \frac{l}{c}\, C_{toty} \qquad and \qquad C_D = \frac{l}{c}\, C_{totx} \tag{10.6}$$

In the current case the cord length was c=1.0 and the arc length was l=2.0563.

The first calculations covered α equal to 0, 6 and 12 degrees at *Re*=0.76 million. and the lift and drag coefficients were compared with experimental data from Michos et al. (1983). Figure (10.8) shows the results.

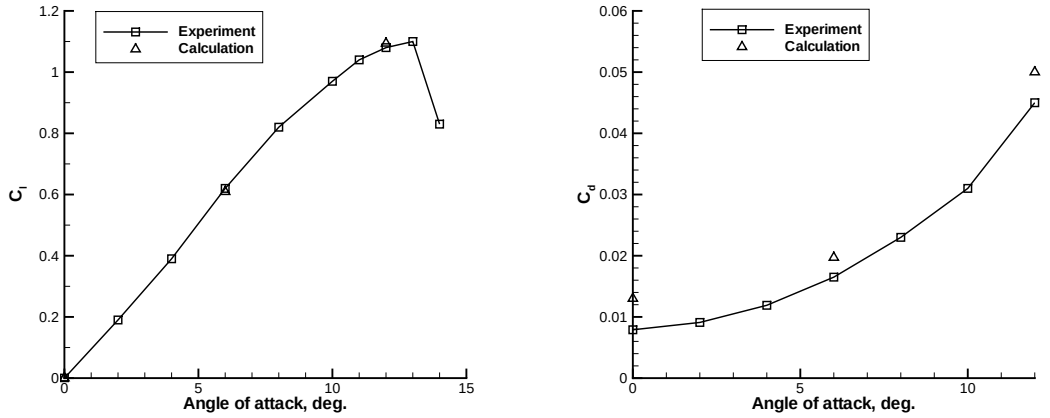

a. *Lift coefficient* b. *Drag coefficient*

Figure (10.8) *NACA0012, Re=0.76·10^6.*

Figure (10.8.a) shows good agreement between the calculated and the experimental lift coefficients for α=6°. This is also the case for α=12°, though the calculated value is predicted a little higher than that of the experiment. The overprediction is probably a consequence of the overpredicted leading edge pressure peak, caused by the applied turbulence model as discussed earlier. Concerning the drag, it is observed that the agreement between experiment and calculation is not as good as for the lift. According to Figure (10.8.b) it seems to be a general problem, since the drag is overpredicted for all the considered angles of attack. As the lift is pressure dominated and the pressure

distribution is reasonably predicted according to Figure (10.6.a), it is expected that the calculated lift should generally be in agreement with the experiments. Hence the discrepancies between numerical and experimental drag indicate that the reason to the problems should be found in the turbulence model since the drag is dominated by the frictional forces.

One reason for the poor agreement could be found in the condition of the profile surface during the experiments, because the roughness of the surface might influences the results. When the fluid meets the leading edge of the smooth profile the boundary layer starts to build up. It will initially be laminar, but at some point along the profile it will become unstable and transition to fully turbulent flow will take place. Depending on the surface quality it is possible that the transition from laminar to turbulent flow in the boundary layer takes place at different positions. This effect is not taken into account in the present CFD code where the flow is assumed to be fully turbulent all over the profile.

Johansen and Sørensen (1998) investigated the influence of transition on lift and drag characteristics for wing profiles at Reynolds numbers of an order of magnitude of $o(10^6)$. On the basis of experimental data and calculations with and without transition, they conclude that it is important to model the transition when CFD calculations are made since the laminar/turbulent properties of the boundary layer have important influence on the skin friction and separation, which again influences the lift and drag characteristics of the profile. One of the considered profiles is an NACA0012 profile at $Re=3.0\cdot10^6$. It is shown that if transition is not taken into account in this case it will result in slight underprediction of the lift and overprediction of the drag. Since the drag is to a large degree influenced by the skin friction and the lift by the pressure the largest difference is observed for the drag. In Michos et al. (1983), no detailed information about the surface condition is available, but the behavior of the drag coefficient seems to be the same as in Johansen and Sørensen (1998), even though the Reynolds number is different in the two cases. However, in order to investigate the influence of the transition three calculations were performed for the same condition as in Johansen and Sørensen (ibid.), i.e. $Re=3.00\cdot10^6$, to see if the tendencies of lift and drag presented by Johansen and Sørensen (ibid.) could also be found in the results calculated by the present method. It should be noted, that Johansen and Sørensen (ibid.) use Menter's two-equation k-ω turbulence model, which is different from the present algebraic Baldwin-Lomax model.

The results of the calculation at $Re=3.00\cdot10^6$ are shown in Figure (10.9) together with experimental data from Abbott and Doenhoff (1959). The data was obtained with a smooth profile. The results plotted in Figure (10.9) show that the fully turbulent calculated data had the same behavior as described in Johansen and Sørensen (1998), i.e. too high drag and too low lift compared with the experimental smooth profile data. This indicates that the problem was most likely caused by the missing transition model. Therefore, if the calculations should be compared with experiments there are two options. One would be to use experimental data for a profile with a boundary layer which was fully turbulent over most of the profile during the measurement and another would be to implement a transition model in the CFD code. However, the latter option was not within the scope of the project so the first option was chosen.

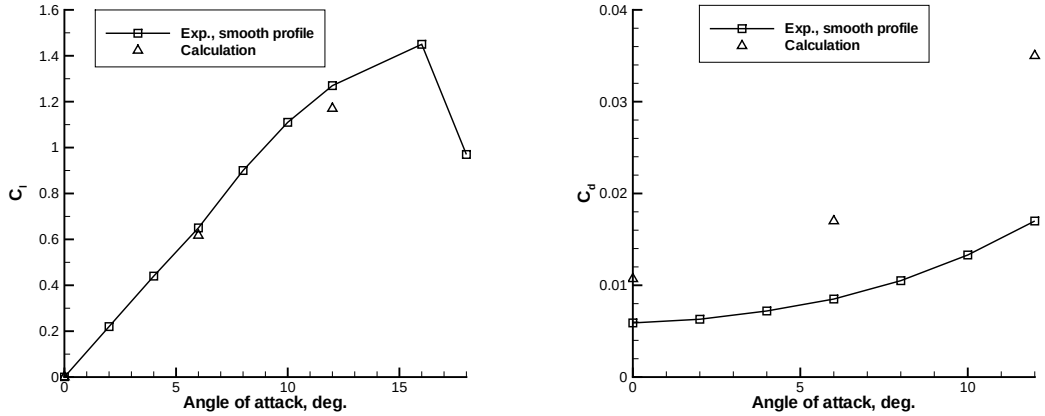

a. *Lift coefficient* b. *Drag coefficient*

Figure (10.9) *Lift and drag, Re=3.0·10*^{6}.

In Abbott and Doenhoff (1959) lift and drag data is presented for a 0.6 m cord profile at *Re*=6.0·10^6, equipped with 0.28 mm carbon grains applied to the surface of the profile at the leading edge over a surface length of 0.08*c*. The grains were thinly spread to cover 5 to 10 percent of the surface area. The presence of the grains should enforce transition close to the leading edge or at least at *x*=0.08c and result in fully turbulent flow over most of the profile. Thus, this data should be in better agreement with the calculations than the smooth profile data was. In order to test the assumption a new set of calculations was performed for angles of attack equal to 0, 3, 6, 9 and 10 degrees and *Re*=6.0·10^6, and the results were compared with data for a profile with and without leading edge roughness. The results in Figure (10.10) show that the agreement between calculation and experiment was generally best for the data found with roughness. For angles of attack between 0 and 9 degrees lift and drag are predicted well, but for larger angles the lift is overpredicted, which was probably caused by the turbulence model, because of its tendency to overpredict the leading edge pressure peak as mentioned earlier.

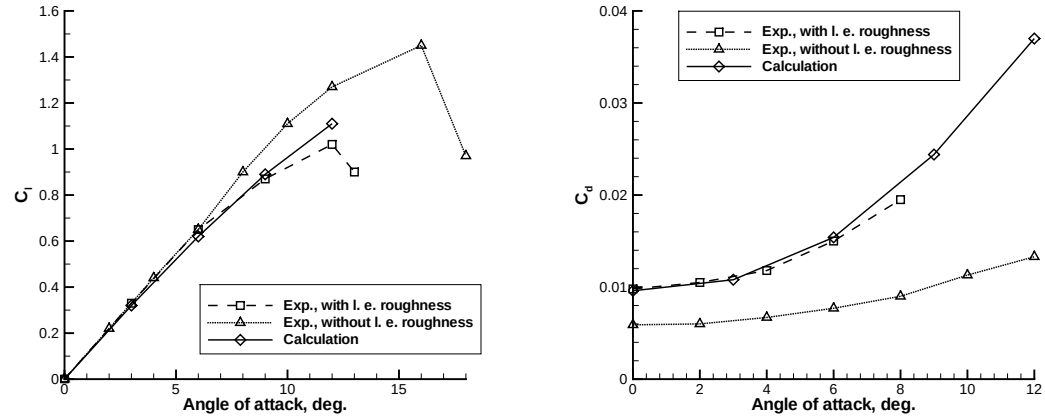

a. *Lift coefficient* b. *Drag coefficient*

Figure (10.10) *NACA0012 with and without leading edge roughness, Re=6·10*^{6}.

Concerning the drag, no data was available for $\alpha>8°$, but for $\alpha=8°$ the calculation and the experiment began to differ a little. This behavior was also found in Rizzetta and Visbal (1993), where it was shown that for 2-D steady state calculations with the Baldwin-Lomax turbulence model the best results for the NACA0012 profile were found for $\alpha<9°$.

10.5 Summary

In this chapter steady state RANS calculations were performed for an NACA0012 profile by means of the CFD code CFDSHIP-IOWA. The calculations were made with a C-grid topology consisting of 120414 computational cells and the turbulence was modeled by the algebraic Baldwin-Lomax turbulence model. The profile was considered for different angles of attack between 0 and 12 degrees and three different Reynolds numbers in the range from 0.76 million. to 6.0 million.

The computations were compared with experimental data and it was found that good agreement could be obtained if the experiments were performed with leading edge roughness. The reason for this is found in the CFD code, which treats the boundary layer as fully turbulent from the leading edge and therefore does not take the transition from laminar to turbulent flow in the boundary layer into account. However, this is only a problem when small model scale rudders are considered. If the code is applied to ship's rudder calculations it is most likely that the boundary layer will be turbulent relatively close to the leading edge because of the surface quality and, furthermore, if a propeller is working in front of the rudder, this will also destroy the laminar boundary layer. Though, it should be noted that in order to simulate model scale flows where a relative large part of the boundary layer may be laminar a transition model could be implemented, but this is not within the scope of the present work.

The best results are obtained for angles of attack smaller then 9°, since both lift and drag coefficients are in fair agreement with the experimental data for these angles. For larger angles the lift was overpredicted, so it was not possible to capture the decrease in the lift which is usually observed when the angle of attack is increased towards the stall angle. According to the literature this behavior was not unusual when steady state calculations were performed with the Baldwin-Lomax turbulence model. There are two possible reasons for this: 1) For angles larger than 8 to 9 degrees the flow starts to separate, which introduces some unsteady effects not to be captured in a steady state solution and 2) the Baldwin-Lomax model has a tendency to overpredict the leading edge pressure peak on the suction side of the profile which results in too high lift.

Finally, the calculations were verified by a grid study of three grids. Both iterative and grid convergences were achieved and the grid uncertainty introduced by the grid applied to the calculations was estimated to 5.9%. It was shown that this uncertainty could be decreased to 1.6% by using a finer grid, but 5.9% was assumed to be sufficient in this context to reduce the computational requirements. Taking the grid uncertainty of 5.9% and the experimental uncertainty of 8% into account resulted in validation of the code at a 10% level. This level could be improved by application of the fine grid and more accurate experiments.

This page is intentionally left blank.

Chapter 11

Rudder in Free Stream

11.1 Introduction

After finishing the calculations of the flow around the two-dimensional NACA0012 profile the next step involves a numerical investigation of the flow around a three-dimensional rudder in free stream and behind a propeller. This case is important from a maneuvering point of view, since the performance of the rudder plays an important role for the maneuverability of the ship and it is interesting to find out if the numerical method is capable of predicting the rudder performance.
As the flow around a rudder is complex to handle numerically it is necessary to validate the results by experiments. However, experimental data which can be used for this purpose is sparser than in the two-dimensional case, and especially so when the influence of a propeller is taken into account. However, in Molland and Turnock (1991) three different rudders with an NACA0020 profile were investigated in a wind tunnel. The rudders were tested in free stream and behind a modified Wageningen B4.40 propeller. On the basis of this data it was decided to perform the rudder calculations with two of the rudders. The work on the free stream rudder is described in this chapter while the rudder-propeller configuration is described in a later chapter.

11.2 Existing Experimental Data

As mentioned above the numerical results from the present rudder flow study were compared with experimental data from Molland and Turnock (ibid.). The considered rudder model consisted of a wall-mounted all-movable rudder built of a symmetric NACA0020 section and it was equipped with a square rudder tip. The two rudders relevant to the present project had the same cord length equal to 667 mm, but two different aspect ratios equal to 1.5 and 1.8, respectively. Both rudders were rectangular so that the taper ratio was equal to 1. The aspect ratio Λ and the taper ratio T_r are defined as

$$T_r = \frac{c_t}{c_r} \qquad \Lambda = \frac{s}{c_m} \tag{11.1}$$

where c_t and c_r are the cord lengths at the tip and the root, respectively, s is the rudder span and c_m is the mean cord length.

The rudders were tested in a 3.5m x 2.5m low-speed wind tunnel at free stream wind speeds of U=10m/s and U=25m/s, corresponding to cord-length-based Reynolds numbers equal to 0.4 million and 1.0 million. Both rudders had a 12 mm wide roughness strip, attached to each side close to the leading edge. The strip consisted of thinly spread 0.15mm diameter carbon grains, which should trigger the turbulence and impose transition from laminar to turbulent flow relatively close to the leading edge and ensure the turbulence of the boundary layer flow over most of the rudder. The roughness strip and the resulting wide extension of the turbulent boundary layer were important factors when the experimental data was chosen for the comparison. The reason for this is found in Chapter 10, where the numerical model assumed the boundary layer to be turbulent from the leading edge. Hence, if the numerical and the experimental results should be comparable, it was necessary to use experimental data obtained for a fully turbulent flow condition.

Finally, it should be noted that the comparison between calculations and experiments was made on the basis of the lift and drag characteristics for the rudders plus the spanwise distribution of the sectional rudder normal force. The sectional normal force was defined as the force acting in a direction perpendicular to the cord of the rudder, and it was determined by integrating the pressure around the rudder profile for constant spanwise position. Concerning the validation, it should also be noted that no estimate of the uncertainties of the experimental data was available for the validation of the calculations.

11.3 Empirical Data

Besides the use of experiments, it was also possible to estimate the free stream lift and drag characteristics for a rudder by empirical formulas. In Brix (1993), Söding proposes two expressions for the lift and drag coefficients based on potential theory and experiments:

$$C_L = \frac{2\pi\Lambda(\Lambda+1)}{(\Lambda+2)^2}\sin\delta + C_q \sin\delta\,\left|\sin\delta\right|\cos\delta \tag{11.2}$$

$$C_D = 1.1\,\frac{C_L^2}{\pi\Lambda} + C_q\,\left|\sin\delta\right|^3 + C_{D0} \tag{11.3}$$

In these expressions C_L and C_D are the lift and drag coefficients. Λ is the aspect ratio and δ is the rudder angle. $C_q \approx 1$ is a resistance coefficient used for rudders with square tips, i.e. sharp ends. Finally, the term C_{D0} accounts for the surface friction and it is given as 2.5 times the ITTC friction line:

$$C_{D0} = 2.5\,\frac{0.075}{(\log_{10} Re - 2)^2} \tag{11.4}$$

As mentioned above the expressions for C_L and C_D are empirical and partly based on potential theory and as such they have some limitations. They can only be applied to angles of attack below the stall angle and, in addition to this, they do not take the profile shape into account. According to Brix (ibid.), the reason for omitting the profile shape is that it mainly influences the stall angle δ_s and the maximum lift properties. The lift and drag forces below δ_s should be less influenced. Besides these two restrictions it is also seen that the expressions only account for the Reynolds number effect in the term C_{D0}. However, according to Brix (ibid.), results obtained by the two expressions are in fair agreement with experimental data for rudders at Reynolds numbers around one million and with aspect ratios in the range of 1 to 3. Therefore, they were used as a supplement to the experimental rudder data from Molland and Turnock (1991) in the comparison with the numerical data.

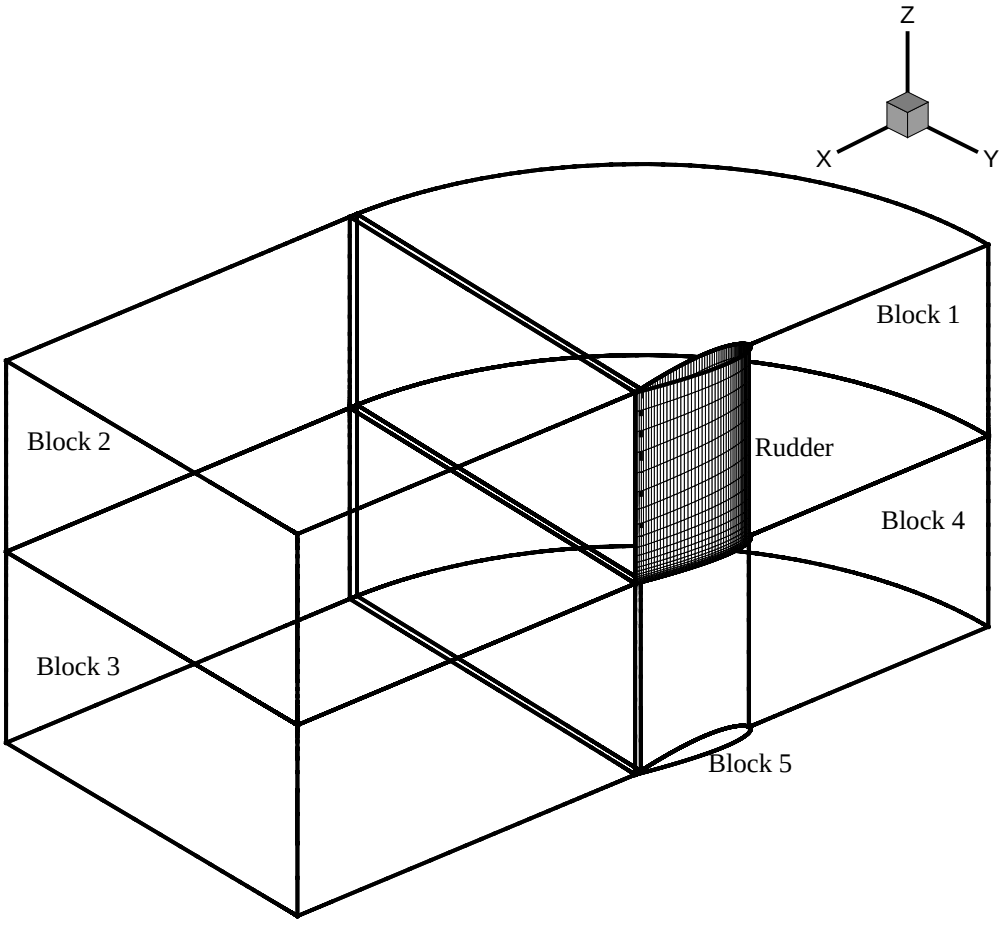

Figure (11.1) *Definition of blockcs in rudder grid topology.*

11.4 Grid Topology and Boundary Conditions

The calculations were performed with a C-grid topology generated by use of an elliptic method implemented in Gridgen®. To be able to model the square tip and to obtain a grid resulting in a converged solution, it was necessary to use nine blocks. Four blocks

were placed on each side of the vertical symmetry plane of the rudder and one block was placed just below the rudder. Five of the blocks are shown in Figure (11.1). Referring to the block numbers in the figure, block 1 included the rudder surface represented by a no-slip condition. To ensure that the grid was fine enough to resolve the boundary layer, the grid points in the cell layer next to the rudder surface were placed so close to the wall that the non-dimensional wall distance y^+ was smaller than 1, which resulted in a physical wall distance of approximately $2 \cdot 10^{-6}$. In addition to this, the grid was clustered in the tip region in order to resolve the tip vortex and the boundary layer at the tip.
Initially, block 1 was just extended into the wake instead of using block 2, but this resulted in solution divergence when the rudder was given an angle of attack. It was found that the divergence originated from the cells in the wake just behind the trailing edge and that it was caused by extreme aspect ratios of the cells in this region. The large aspect ratios were a result of the continuation of the thin cells on the rudder surface into the wake. For zero angle of attack there was no problem, but when the rudder was turned and the cells were no longer parallel to the streamlines, the problem arose. To solve the problem a separate block 2 with less extreme aspect ratios had to be used in the wake behind the rudder. Since the aspect ratios in block 2 were improved by using a larger grid spacing, the overlapping multi-block approach had to be used between blocks 1 and 2 because point to point exchange of boundary data was no longer possible.

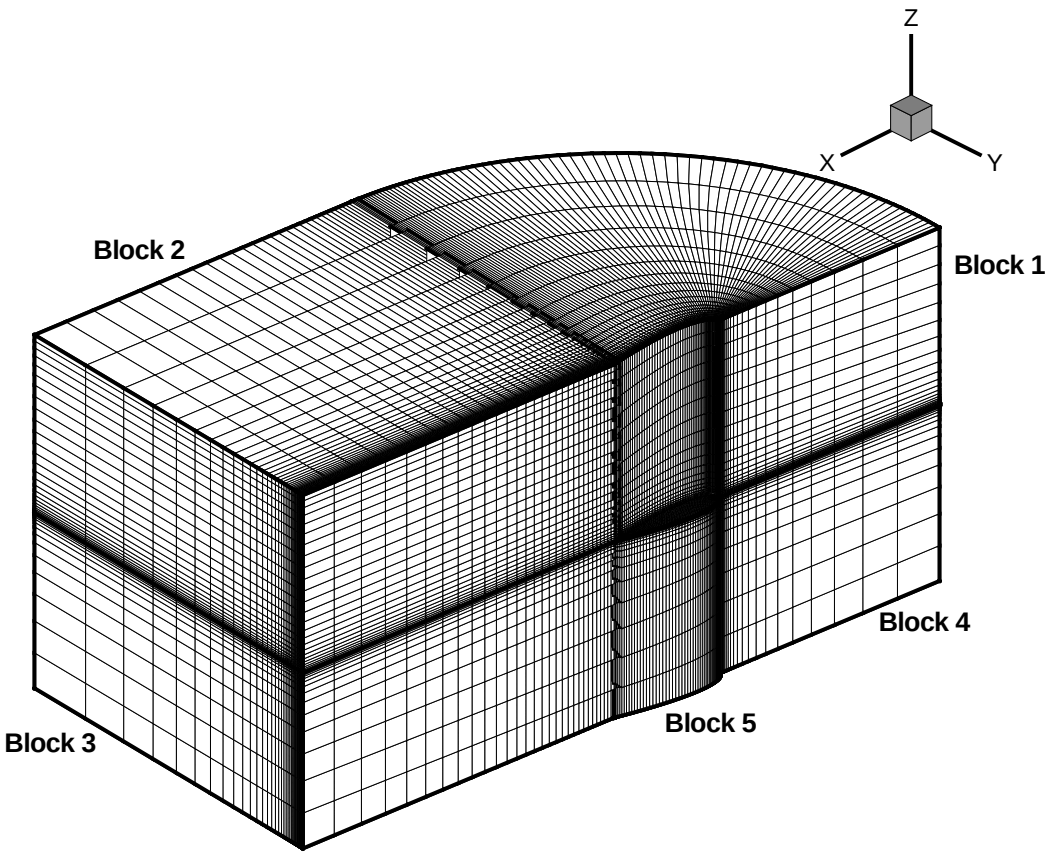

Figure (11.2) *Rudder grid topology.*

Block 5 was placed just below the rudder where it modeled the no-slip surface at the tip and the flow field below the rudder. Again the grid cells were placed close to the wall to resolve the boundary layer and at the same time the tip vortex. Blocks 3 and 4 modeled the flow domain below blocks 1 and 2 and they were connected by use of the overlapping grid technique as it was the case for blocks 1 and 2. The remaining four blocks, which are not shown in the figure, were identical to blocks 1,2,3 and 4 and they were connected point to point with the shown blocks at the center plane by means of the patched multi-block approach.
The coordinate system for the non-orthogonal curvilinear coordinates used in the individual blocks was oriented so that the ξ-direction ran along the profile surface and into the wake, the η-direction was perpendicular to the surface and the ζ-direction ran in the spanwise direction.

The boundary conditions applied to each boundary of the individual blocks are not described here, but in summary the following boundary conditions were applied: At the outer boundaries below and around the rudder a far field condition was applied, prescribing the free stream velocity for the velocity components and a zero gradient for the pressure. At the outer boundary behind the rudder an exit condition was used and at the upper boundary at the root of the rudder a symmetry condition was applied. The rudder surface was modeled by a no-slip condition. Finally, the boundary data at the boundaries of the individual blocks in the interior of the domain were exchanged by using a combination of the patched and overlapping multi-block approaches. A description of the individual types of boundary conditions was presented in Chapter 8 were the numerical method was also described.
The extension of the computational domain was investigated and it was found that placing the outer boundaries 6 cord lengths away from the profile instead of 3 only had a minor influence on the flow. It was therefore assumed that 3 cord lengths were sufficient to ensure that the flow was not influenced by the boundaries.
Finally, one of the problems in connection with the three-dimensional rudder calculations, was the quickly expanding size of the grid because of limitations of the available memory of the computer. Since the symmetry of the flow could not be exploited due to the use rudder angles different from zero and since the turbulence model without wall function required fine near wall grid resolution, the model size quickly reached the critical limit of approximately 600000 cells. However, with the maximum grid size in mind a grid consisting of 601952 was generated and Table (11.1) below shows the dimensions of the individual blocks.

Block	ξ, η and ζ dimensions i_{max} x j_{max} x k_{max}
1 (x 2 because of other side of domain)	79 x 48 x 26
2 (x 2 because of other side of domain)	35 x 48 x 26
3 (x 2 because of other side of domain)	79 x 48 x 26
4 (x 2 because of other side of domain)	35 x 48 x 26
5	79 x 16 x 26
Total number of cells	601952

Table (11.1) *Dimensions of grid used for rudder in free stream.*

It should be noted that the calculations were performed on a CRAY C92 vector machine and that one calculation with a grid of this size required 760 MB of RAM and 26 CPU hours.

11.5 Verification

When CFD calculations are made it is important to keep in mind that the quality of the solution is strongly influenced by the quality of the grid and that it is important to investigate the errors and uncertainties introduced by using a certain grid. Today most of the grid generation is done by means of interactive computer programs where the user can see the grid during the generation process. This makes the grid generation easier, but it does not ensure that the grid has a good quality since this usually depends on the skills and the experience of the user. When a grid is generated it is often impossible to tell if it is fine enough, if the cells are good enough to ensure numerical stability or if it is refined at the right locations, and the more complex the geometry, the more difficult to find the right answer.
Usually, tools for checking cell aspect ratios, skewness and jacobians are available in the grid generation programs, but there are no requirements of the values of these quantities, so it is up to the user to judge if it looks realistic. Thus, the grid generation often relies on visual judgment based on the experience of the user.
When a grid has been generated it is usually necessary to perform a calculation to investigate if the grid results in a stable solution, i.e. if the solution shows iterative convergence. However, iterative convergence is not enough to ensure a good solution because it is also necessary to know if the grid is fine enough, i.e. to know how close the solution, obtained by the current grid, is to the grid-independent solution and which errors and uncertainties the grid introduces. This requires a grid study where the grid is systematically refined.

Before the calculations for the study of the 3-D rudder flow were made, the computational grid was examined. It was decided to carry out verification and validation on the basis of the total rudder drag, expressed by the rudder drag coefficient C_{totx} in the case of angle of an attack equal to zero degree. Three grids were generated for the grid study by application of a grid refinement factor of r_G =1.12, which resulted in a coarse (3), medium (2) and fine (1) grid with 307671 cells, 426671 cells and 601952 cells, respectively. It should here be observed that r_G =1.12 was relatively small compared to a $\sqrt{2}$ or 2 refinement. However, it was impossible to use these factors, because it would result in grid sizes which required a computational effort exceeding the performance of the available computer.
As in the two-dimensional case the validation and verification procedure presented by Stern et al. (1999) was followed and the verification was performed with respect to iterative and grid convergence studies as described in Chapter 7. From the convergence history of the residuals for the three solutions, it was observed that the solution showed iterative convergence where the residuals dropped to a level between 10^{-4} and 10^{-5}. Moreover, it was observed that the calculated forces were oscillating during the first 1000 iterations, but then flattened out throughout the solution, which indicated that the iterative error and uncertainties became negligible compared to the grid errors and

uncertainties, i.e. $\delta_I << \delta_G$ and $U_I << U_G$. Therefore, Equation (7.3) for the simulation numerical error δ_{SN} and uncertainty U_{SN} in Chapter 7 could be reduced to

$$\delta_{SN} = \delta_G \qquad U_{SN} = U_G \tag{11.5}$$

The convergence history for the residuals and forces for the fine grid is shown in Figures (11.3.a) and (11.3.b), respectively. It should be noted that the solutions obtained with the coarse and medium grid showed the same behavior.

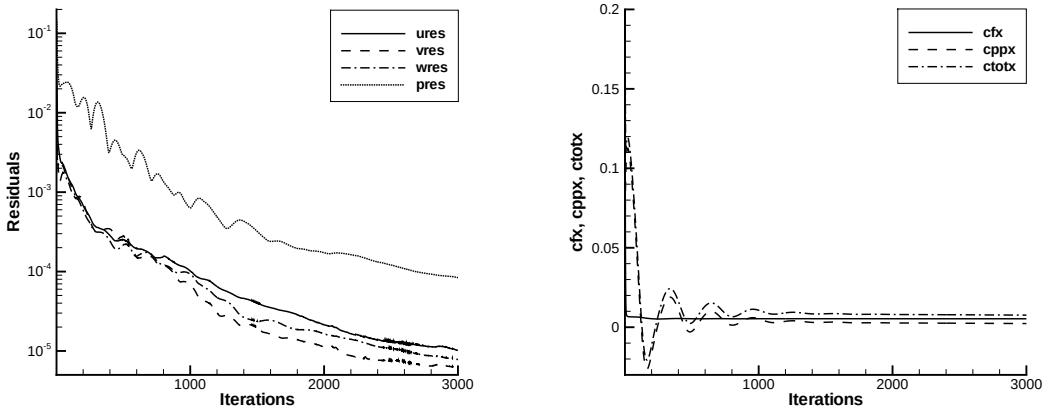

a. Residuals *b. Rudder forces*

Figure (11.3) *Results from fine grid calculation for δ=0° and Re=0.4·10^6.*

Since the iterative error and uncertainty were found to be negligible the next step in the verification procedure involved estimation of the error and uncertainty introduced by the grid. By following the procedure described in Chapter 7 the quantities were estimated on the basis of results obtained with three grids generated by systematic grid refinement. The results of the grid convergence study are shown in Table (11.2), where the frictional C_{fx} and the pressure C_{ppx} components of the drag force coefficient plus the total force coefficient C_{totx} are presented.

	Coarse 307671	Medium 426374	Fine 601952	R_G	Numerical benchmark
$C_{fx} \cdot 10^3$ ε	5.141	5.265 2.4 %	5.311 0.9 %	0.37	----------
$C_{ppx} \cdot 10^3$ ε	2.882	2.635 -8.6 %	2.519 -4.4 %	0.47	----------
$C_{totx} \cdot 10^3$ ε	8.023	7.900 -1.5 %	7.830 -0.9 %	0.57	7.555

Table (11.2) *Calculated drag forces from grid study for rudder in free stream.*

By considering the R_G values, which were calculated by Equation (7.9) in Chapter 7, it was observed that all the values were in the interval from 0 to 1. This indicates that the

numerical solution was converging as the grid was refined and that Richardson extrapolation could therefore be used for a first order estimate of the grid error $\delta_{RE,G1}$ for the fine grid. Thus, on the basis of the grid refinement factor equal to r_G =1.12 and the ε-values presented in Table (11.2) the estimated order of accuracy P_G was calculated from (7.12) and then applied to calculation of $\delta_{RE,G1}$ from (7.11). Both values are shown in Table (11.3). Following the idea presented in Stern et al. (ibid.), the calculation of both δ_{G1} and U_{G1} or just U_{G1} was based on a correction of $\delta_{RE,G1}$. Depending on the value of C_G, two different cases could arise according to the theory. If C_G turned out to be close to 1, meaning that the solutions were in the asymptotic range, both the error δ_{G1} and the uncertainty U_{G1} should be estimated, but if C_G turned out to be too far away from 1, indicating that the solutions were not in the asymptotic range, only the uncertainty U_{G1} should be estimated. Hence, in order to investigate which case was relevant to the present problem, the correction factor was calculated by means of (7.13) with a theoretical order of accuracy of the method P_{th} equal to 2. The result is shown in Table (11.3).

r_G	1.12
P_G	4.97
$\delta_{RE,G1} \cdot 10^4$	0.925
C_G	2.98
U_{G1} in % of fine solution	5.8
Numerical benchmark, S_C	$7.555 \cdot 10^{-3}$
S_C /(fine solution)	0.96

Table (11.3) *Grid uncertainties found in grid study for rudder in free stream.*

From the results presented in Table (11.3) it is observed that the C_G value for the total *x*-force was not close to 1, which leads to the assumption that the solutions were not in the asymptotic range. It was therefore decided not to have confidence in the equation for δ_{G1} and only calculate the grid uncertainty, ending up in 5.8% of the fine grid solution. It should be noted that as in the NACA0012 case, a numerical benchmark solution was estimated by correcting the numerical fine grid solution with the numerical error in order to obtain an indication of the level of the grid independent solution.

11.6 Validation

As mentioned earlier the validation was made on the basis of experimental data taken from Molland and Turnock (1991), where results from wind tunnel tests with a wall-mounted wing are presented. No uncertainty estimate is presented for the experiments, so it was assumed to be 10 % of the data value. The experimental and calculated drag force coefficients C_{totx} are shown in Table (11.4) together with the estimated simulation uncertainty U_S, the data uncertainty U_D, the validation uncertainty U_V and the comparison error *E*.

	Re=0.4·10^6		
	Calculation, S	Experiment, D	
	Λ=1.5	Λ=1.5	Λ=1.8
C_{totx}	$7.83 \cdot 10^{-3}$	$2.8 \cdot 10^{-3}$	$10.3 \cdot 10^{-3}$
E	$-5.0 \cdot 10^{-3}$	------	------
$U_S = U_G$	$4.54 \cdot 10^{-4}$	------	------
U_D	------	$2.8 \cdot 10^{-4}$	------
U_V	$5.3 \cdot 10^{-4}$	------	------

Table (11.4) *Comparison between forces from calculation and experiment.*

By relating E and U_V to the data, the results shown in Table (11.5) were obtained and it was found that the calculations were overpredicted in comparison with the experiments, which resulted in a comparison error larger than the validation uncertainty, i.e. $|E| > U_V$ so the code was not validated.

	Re=0.4·10^6	
	Calculation, S	Experiment, D
	Λ=1.5	Λ=1.5
U_D % of D	------	10
E % of D	-179	------
U_V % of D	19	------

Table (11.5). *Quantities used for validation of calculated forces.*

To find the reason for the discrepancy between calculation and experiment, various factors were considered. The first concerned the difference between the physical and the numerical model. In the experiment a wall-mounted wing with an aspect ratio equal to 1.5 was modeled, so that the flow in the root region was influenced by the boundary layer on the floor of the wind tunnel. The numerical model corresponded to half of a free wing with an aspect ratio equal to 3.0, since the influence of the wall boundary layer was neglected and the wind tunnel floor was treated as a symmetry plane instead of a no-slip surface. In Hörner (1965), the effect of the presence of a wall at the end of a wing has been examined. It was found that when the wing adjoins the wall the boundary layers on the wall and on the wing will interact and result in additional pressure drag. According to this, the experimental drag should have been higher than the calculated drag, which was seen not to be the case. Therefore, the difference between calculation and experiment had to be found somewhere else. According to the results from the two-dimensional rudder profile calculations presented in Chapter 10, one of the problems in connection with the comparison between experiments and calculations was the difference originating from laminar/turbulent boundary layer flow. It was found that if the boundary layer flow was not fully turbulent during the experiment, the measured drag would be lower than the calculated drag. It was also found that the presence of leading edge roughness could reduce the problem and lead to better agreement. As mentioned earlier in this chapter the considered rudder was equipped with leading edge roughness consisting of 0.15 mm carbon grains, so the boundary layer was assumed to be turbulent all over the profile. However, since the Reynolds number was relatively low, Re=0.4 million, the flow may have been less influenced by the leading edge

roughness than expected. According to White (1991), Feindt in 1957 reported some results for the influence of distributed sand grain roughness on the transition. These results indicated that the roughness did not show any effect on transition in both favorable and adverse pressure gradients until the roughness-based Reynolds number Re_k satisfied

$$Re_k = \frac{Uk}{\nu} \approx 120 \tag{11.6}$$

where U is the speed, k is the diameter of the roughness grains and ν is the viscosity. For $Re_k > 120$ the transition point x_{tr} was found to decrease markedly with increasing Re_k. In the present case corresponding to Re=0.4 million, where k=0.00015 m and U=10m/s, the roughness-based Reynolds number was calculated to be Re_k=94, which was smaller than 120. Thus, it was possible that the boundary layer flow had been partly laminar during the experiment and that the measured drag was therefore lower than the calculated one.

	$Re=1.0\cdot10^6$ and $\Lambda=1.5$	
	Calculation, S	Experiment, D
C_{totx}	$7.665 \cdot 10^{-3}$	$8.4 \cdot 10^{-3}$
E	$7.3 \cdot 10^{-4}$	------
$U_S = U_G$	$4.44 \cdot 10^{-4}$	------
U_D	------	$8.4 \cdot 10^{-4}$
U_V	$9.5 \cdot 10^{-4}$	------

Table (11.6) *Comparison between forces from calculation and experiment.*

	$Re=1.0\cdot10^6$	
	Calculation, S	Experiment, D
	$\Lambda=1.5$	$\Lambda=1.5$
U_D % of D	------	10
$\|E\|$ % of D	8.7	------
U_V % of D	11.3	------

Table (11.7) *Quantities used for validation of calculated forces.*

In order to study a condition where the roughness based Reynolds number was higher than the critical value, i.e. $Re_k > 120$, the flow was calculated for the case of U=25m/s which also was tested experimentally by Molland and Turnock (1991). The condition corresponded to Re=1.0 million and Re_k=234 and based on the results shown in Table (11.6) it is seen that the agreement between experiment and calculation was better in this case. On the basis of the summary of the results in Table (11.7) it was concluded that at the higher Reynolds number the comparison error was smaller than the validation uncertainty, i.e. $|E| < U_V$, which meant that the code was validated at a 11.3% level. However, it must still be kept in mind that the wall boundary layer was neglected in the numerical model.

11.7 Results and Discussion

The work on verification and validation was followed by a study of the flow around the two three-dimensional rudders to investigate the flow for different rudder angles and two different aspect ratios. The experimental investigation of the with- and without-propeller condition was performed for a free stream Reynolds number equal to *Re*=0.4 million, so with regard to comparison all the calculations were performed at the same Reynolds number. Both field and integral quantities are considered below, but the presentation of the field quantities is restricted to one single case, which will be used as test example for both the free stream rudder and the rudder behind the propeller. The test example covers the 10 degrees rudder angle case, i.e. δ=10°.

11.7.1 Integral Quantities

Seen from the point of view of maneuvering simulation it is important to be able to predict reasonably the drag and especially the lift characteristics of the rudder since these forces play a central role in the maneuvering prediction. In order to investigate the possibility of calculating the rudder forces numerically, the flow around the rudder was calculated for two different aspect ratios.

11.7.1.1 Lift and Drag Characteristics

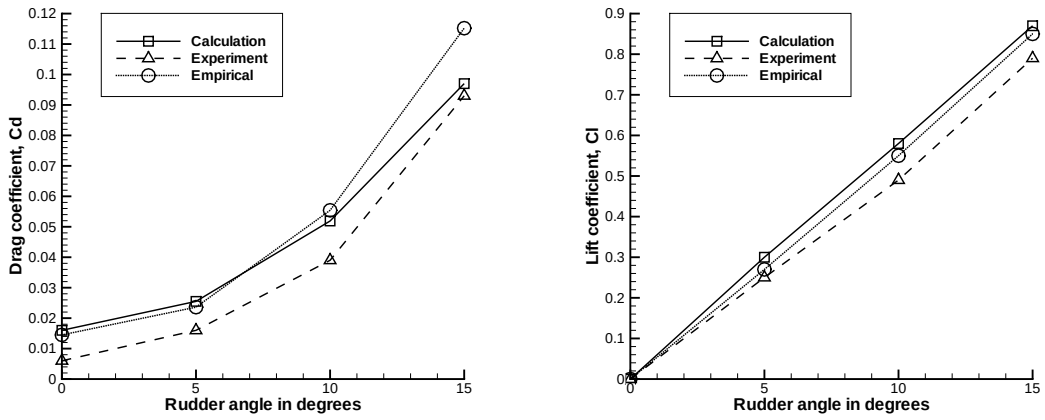

a. Drag force *b. Lift force*

Figure (11.4) *Lift and drag characteristics for Λ=1.5 and Re=0.4· 10^6.*

The numerically determined lift and drag characteristics for the two different aspect ratios, Λ=1.5 and Λ=1.8, are shown in Figure (11.4) and Figure (11.5), respectively, together with the corresponding experimental lift and drag characteristics from Molland and Turnock (1991) and the empirical characteristics from Equations (11.2) and (11.3).
As regards the calculated lift there is generally and independently of the aspect ratio the same tendency in the results when they are compared with the experiments and the empirical values, i.e. overprediction of the calculated lift. According to the results in

Figures (11.4.b) and (11.5.b), the agreement is best between the calculation and the empirical expression, because it is found that the lift coefficient can be determined within 10 to 16 percent of the experimental value, while it is determined within 2 to 10 percent of the empirical value. For the drag there is no clear tendency in the comparison. The drag for Λ=1.5 in Figure (11.4.a) shows that for rudder angles up to 10 degrees the numerical values are in reasonable agreement with the empirical drag, while the experimental drag is smaller. For δ equal to 15 degrees the agreement with the experiment becomes better, but then the empirical drag is higher than the calculated drag. For Λ=1.8 there is again fair agreement between the calculation and the empirical results according to Figure (11.5.a), but also with the calculation for δ=5° and δ=10°. However, for δ=0° the experimental drag coefficient is somewhat higher than the calculation.

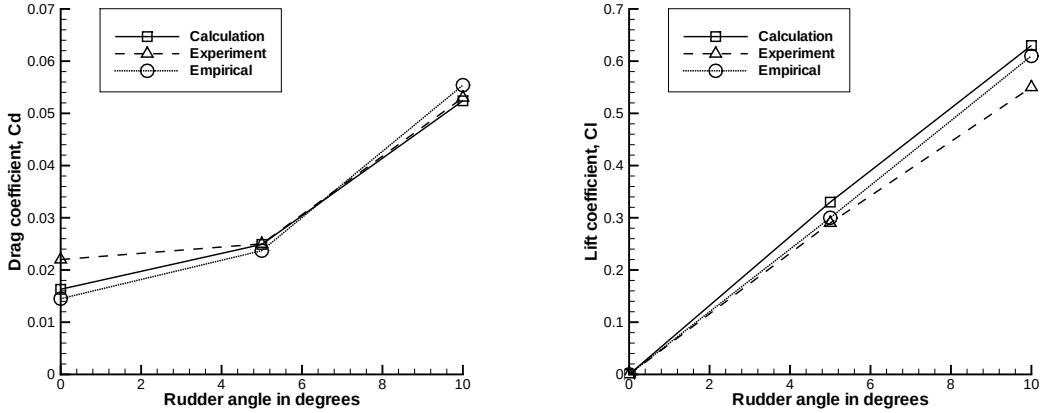

a. Drag force *b. Lift force*

Figure (11.5) *Lift and drag characteristics for Λ=1.8 and Re=0.4 10^6.*

The explanation for the difference between the experimentally and numerically determined drag coefficients in Figure (11.4.a) is probably found in the idea of the transition from laminar to turbulent boundary layer flow, which was described in Section 11.6. Since the experiment was carried out at a critical roughness-based Reynolds number, it is most likely that the boundary layer flow was not fully turbulent when the data in Figure (11.4.a) was generated, while it was close to fully turbulent for the data in Figure (11.5.a), as the calculation and the experiment were in better agreement in this case. However, it has still to be kept in mind that a difference between the numerical and the experimental model was introduced by neglecting the wall boundary layer at the root of the rudder in the numerical model. This could possibly also explain some of the observed difference for the lift and the drag in comparison with experiments. In Pope and Harper (1966), different phenomena influencing the results of low-speed wind tunnel measurements are discussed. One of the topics is the effect of exploiting the symmetry of wings and rudders by testing half models instead of complete models. With respect to small models (half model span < 0.6*h*, where *h* in this case is the width of the tunnel) it is stated that due to vortex shedding occurring in the boundary layer where the half model joins the tunnel wall, the lift curve slope is lower and the drag slightly higher for the half model than for the corresponding complete model. Due to these effects, the performance of a wing, investigated by means of a wall-mounted

half model, corresponds to the performance of a wing with a virtual span smaller than the geometric span, *b*. In order to compensate for the difference, the idea of an effective span, b_e, of the wing or the rudder is introduced as illustrated in Figure (11.6).

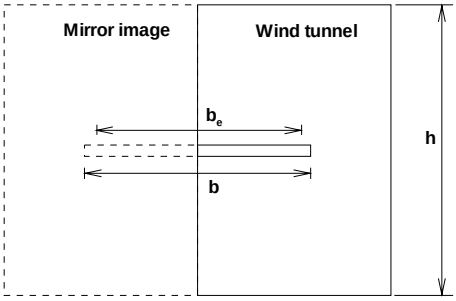

Figure (11.6) *Definition of effective rudder span.*

For the present experiments the span of the half model, *s*, was equal to 1.0 m for Λ=1.5 and 1.2 m for Λ=1.8 and the wind tunnel height, *h*, was equal to 3.5 m. Thus, it was found that the criterion $s<0.6h$ was satisfied for both rudders, which so that both models could be characterized as being small and that the effective span could be calculated by the method proposed in Pope and Harper (ibid.).

Geometric span of full model b	Geometric aspect ratio of full model Λ	Effective span of full model b_e	Effective aspect ratio of full model Λ_e
2.0	3.0	1.84	2.76
2.4	3.6	2.22	3.33

Table (11.8) *Geometric and effective spans and aspect ratios for full rudder models.*

It is seen from Table (11.8) that when the tested rudders were assumed to be half models like the numerical rudder model, they actually performed as rudders with effective aspect ratios Λ_e, which were approximately 8% smaller than in the numerical model where $\Lambda_e = \Lambda$. Since the lift is relatively sensitive to changes in the aspect ratio, the reduced effective aspect ratio probably explains some of the difference between the experiments and the numerical calculations. Finally, the effect of the effective aspect ratio can also explain the generally better agreement between the calculations and the empirical expressions (11.2) and (11.3), since these were evaluated with the geometric aspect ratio, corresponding to the numerical case.

11.7.1.2 Local Normal Force Distribution

To illustrate the spanwise load distribution along the rudder, the local normal force distribution was calculated for different rudder angles. The normal force coefficient C_n was found by integration of the local pressure coefficient around the profile at a constant spanwise position. During the integration the forces were projected in the direction normal to the center plane of the rudder. The load distributions for the two different aspect ratios are shown in Figures (11.7) and (11.8). It is seen from the results that the

load was highest at the root and that it was decreasing to zero towards the tip, where the pressure on the suction side equaled the pressure on the pressure side of the rudder. For the case of $\delta=10°$ the calculated normal force distribution was compared with the experimental distribution for both aspect ratios.

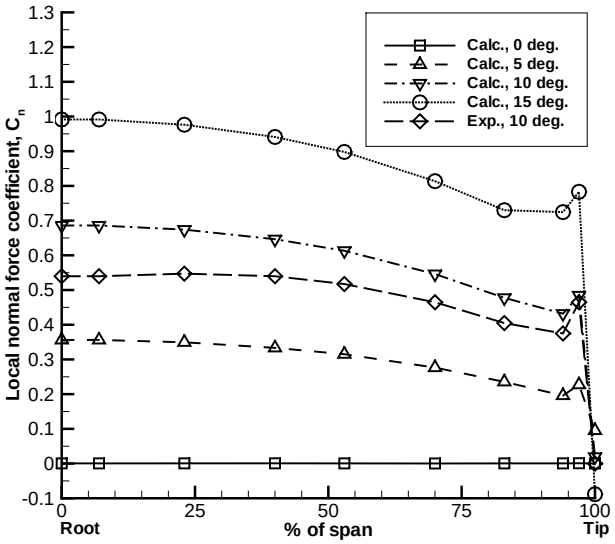

Figure (11.7) *Local normal force distribution for* $Re=0.4\ 10^6$ *and* $\Lambda=1.5$.

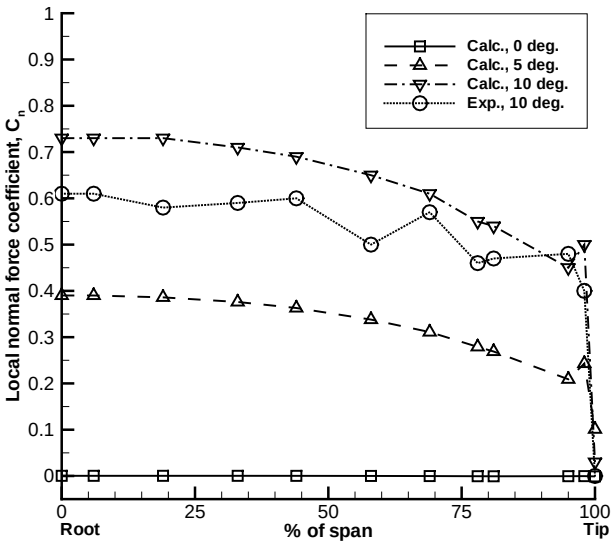

Figure (11.8) *Local normal force distribution for* $Re=0.4\ 10^6$ *and* $\Lambda=1.8$.

It is observed that the calculation generally overpredicted the load along the span by approximately 15 to 18%, which agrees with the size of the overprediction of the lift at the same rudder angle. It is also seen that the difference between calculation and experiment was larger at the root than at the tip, probably due to the presence of the wall boundary layer. Finally, it is found that for fixed rudder angle the local normal force

increased with increased aspect ratio. This is to be expected since the influence of the pressure loss at the tip is decreasing with increasing aspect ratio.
To round off the description and discussion of the integral quantities, it should be noted that on the basis of the calculated lift and drag characteristics presented above it was found that a change in the aspect ratio hardly affected the drag coefficient, while it resulted in a slightly increased lift coefficient. This tendency is in agreement with the findings in Chau (1998), where CFD calculations with the *K*-ε turbulence model were performed for different rudders.

	$\left.\frac{dC_L}{d\delta}\right\|_{\delta=0}$		
Λ	Calculation	Experiment	Empirical
1.5	0.060	0.050	0.054
1.8	0.066	0.058	0.060

Table (11.9) *Influence on lift curve slope from changes in aspect ratio.*

The effect of the increase in the lift coefficient with increased aspect ratio is also reflected in the slope of the lift curve, which is illustrated in Table (11.9). It is seen that both the experimental and empirical lift showed the same tendency, even though the slopes were quantitatively different.

11.7.2 Pressure and Velocity Components

The integral quantities presented above only provide information about the overall flow features, so in order to study the flow closer and provide more detailed information about the flow pattern, different field quantities were investigated for the test case covering $\delta=10°$ and $Re=0.4\cdot10^6$.

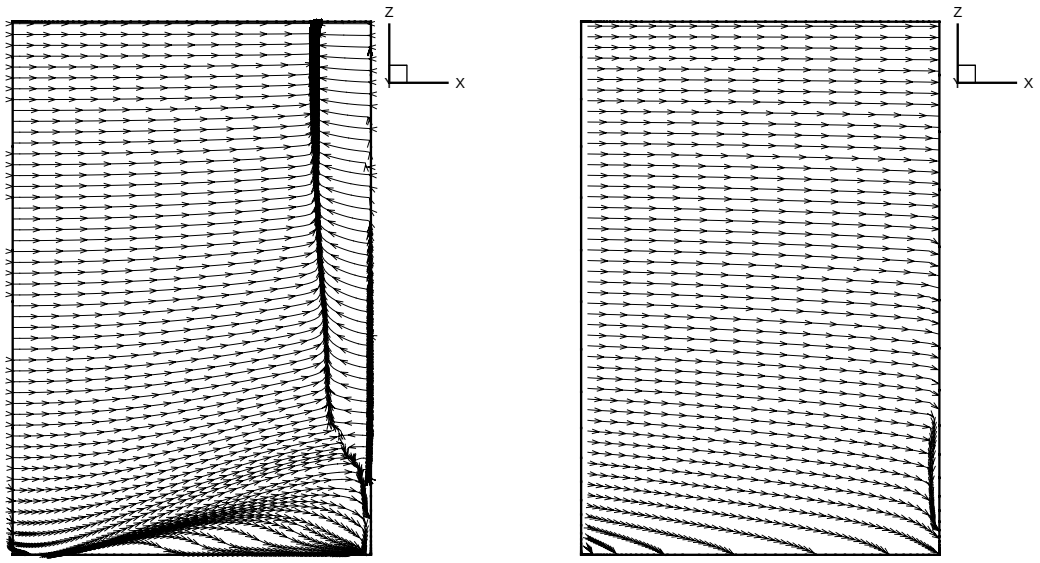

a. Suction side *b. Pressure side*

Figure (11.9) Limiting streamlines on rudder surface at $\delta=10°$.

Figures (11.9.a) and (11.9.b) show the calculated limiting streamlines on the suction side and the pressure side of the rudder, respectively. The picture of the flow pattern on the suction side reveals the presence of a region with reversed flow close to the trailing edge. The zone of reversed flow extended along the whole rudder span, but in a region close to the tip its cordwise extension was reduced due to the influence of the tip vortex, which was running along the tip of the rudder. A closer study of the zone of reversed flow shows that it actually was very thin, as illustrated in Figure (11.10), so that no heavy separation took place.

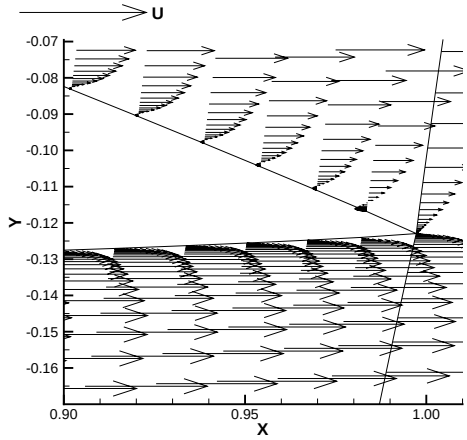

Figure (11.10) Extension of the zone of reversed flow, z=0.

On the pressure side of the rudder the picture is somewhat different, because the flow was generally not reversed on this side except for a small region near the tip in the rear of the rudder. This reversed flow zone was probably caused by the circulating flow from the rudder because of the tip vortex on the other side of the rudder.

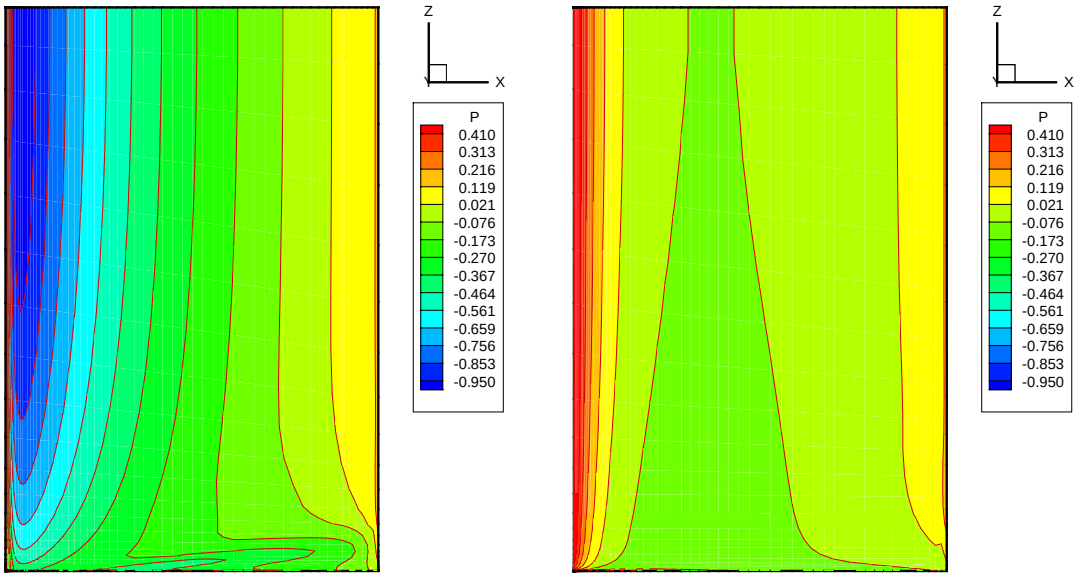

a. Suction side *b. Pressure side*

Figure (11.11) *Pressure distribution on rudder surface at δ=10°.*

Additionally, it was observed that the flow over a part of the rudder was directed towards the tip and that the fluid close to the tip was actually flowing around the tip due to the pressure difference between the pressure and suction sides.
The pressure distribution on the rudder surface is shown in Figure (11.11). It is seen that both the stagnation zone on the pressure side and the peak zone on the suction side are reduced due to the presence of the tip, but also that the accelerated flow in the tip vortex results in a low-pressure region along the tip on the suction side. The presence of this region explains why the normal force distribution shown earlier in Figure (11.7) increases a little close to the tip.

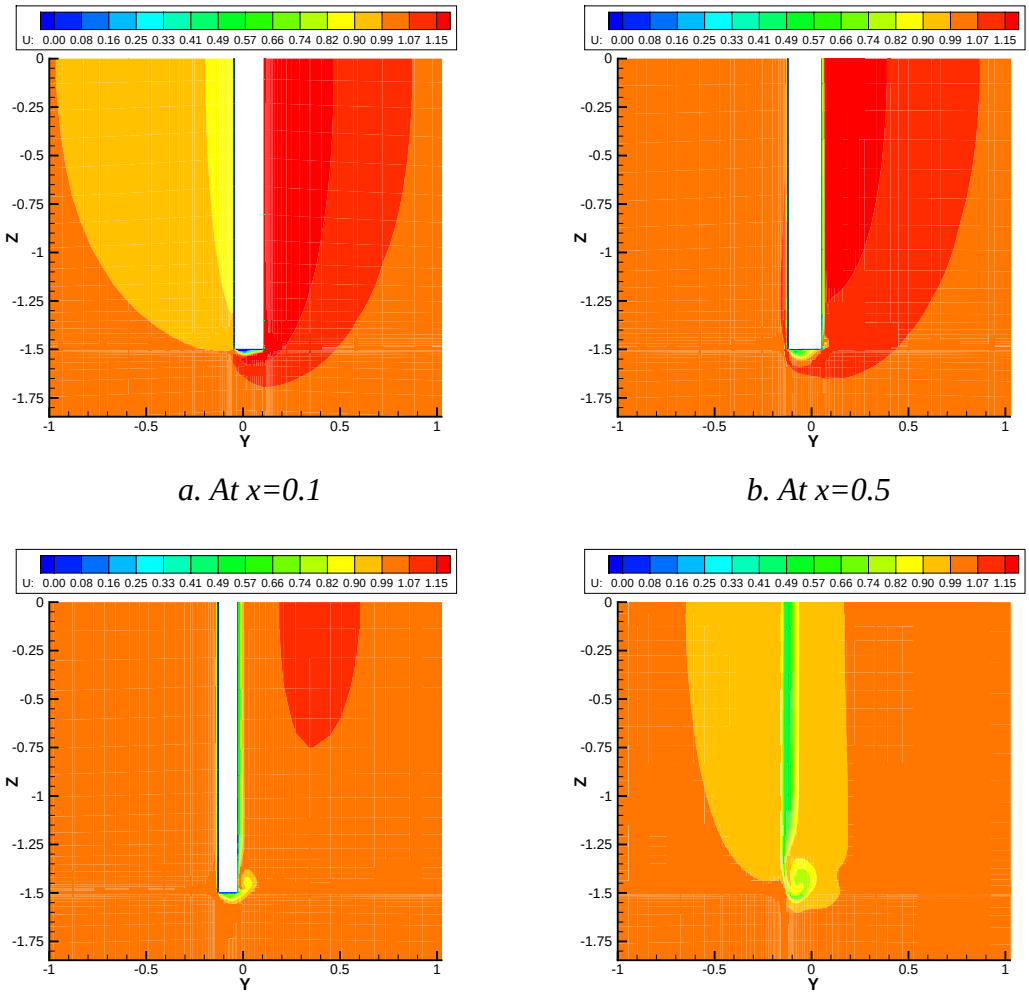

a. At x=0.1 *b. At x=0.5*

c. At x=0.75 *d. At x=1.1*

Figure (11.12) *x-velocity contours at different x-positions.*

The final field quantity, which was considered, covered the *x*-velocity contours at four *x*-positions along the rudder. The calculated velocity contours are shown in Figures (11.12.a) to (11.12.d), while the individual *x*-positions are illustrated in Figure (11.13). The plots in Figure (11.12) show the rudder flow seen from aft in upstream direction, which means that the pressure side is on the port side of the rudder while the suction side is on the starboard side. It is seen that at *x*=0.1 the flow is retarded on the pressure side due to the stagnation region, while it is accelerated below the rudder and on the suction side.

Further down the profile at the mid-cord position x=0.5, a region with increased x-velocity is still observed on the suction side together with a thin region on the pressure side.

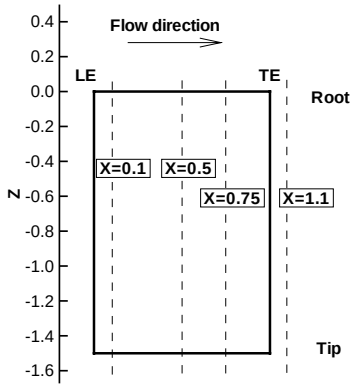

Figure (11.13) *Definition of x-positions.*

At the same time, a thin boundary layer develops around the rudder. In the tip region a tip vortex also develops. At x=0.75 the boundary layer thickness is increased due to the reduced rudder thickness. However, in a small region on the suction side close to the tip the boundary layer is disturbed because the tip vortex forces higher velocity fluid into the boundary layer region. Finally, in the wake right behind the rudder at x=1.1 the velocity defect caused by the presence of the rudder is clearly seen. However, again because of the tip vortex the low velocity band is disturbed.

11.8 Summary

In the present chapter the flow around two rudders in free stream was calculated numerically for different rudder angles in the range of 0 to 15 degrees and a cord-based Reynolds number equal to 0.4 million. The rudders were based on the same NACA0020 profile, but they had two different aspect ratios equal to Λ=1.5 and Λ=1.8. The calculations were performed with a C-grid topology consisting of nine blocks and a total number of computational cells equal to 601952, and the turbulence was modeled by use of the algebraic Baldwin-Lomax turbulence model. During all the computations, the boundary layer at the wind tunnel wall at the root of the rudder was neglected and a symmetry plane was applied instead.

The calculated lift and drag characteristics were compared with both experimental and empirical characteristics. Concerning the lift the CFD code generally showed a tendency to overpredict the lift coefficient when compared with the experiments and the empirical formula. A part of the numerical overprediction could be explained by the presence of the wall during the experiment, which resulted in an effective aspect ratio smaller than the geometric one and therefore reduced the lift curve slope. The deviation between calculations and experiments was found to be in the range of 10 to 16 percent, while it was 2 to 10 percent for the empirical values. Finally, the calculations showed that if the aspect ratio was increased, the lift curve slope would also increase and result in slightly higher lift coefficients for Λ=1.8 than for Λ=1.5. Concerning the drag, the calculations were generally in fair agreement with the empirical expression except for δ=15°.

However, the picture was somewhat different for the experiments. For some of the values the agreement was fair, while for others deviations of more than 100 % were observed. The explanation for these large deviations was probably that at the considered Reynolds number the applied leading edge roughness had a critical grain size which in some cases triggered the boundary layer turbulence and in other cases did not. As expected, comparison of the calculated drag coefficients for the two different aspect ratios did not show any significant influence on the drag coefficient from changes in the aspect ratio.

The field quantities were investigated for the case of the Λ=1.5 rudder at δ=10°, and it generally seemed that the code was capable of capturing the gross features of the rudder flow. The study revealed that the flow was separating in a region on the suction side of the rudder close to the trailing edge, but also that the numerical method was able to capture the vortex developing at the tip of the rudder.

Finally, the numerical method was verified and validated for the zero rudder angle case. The verification was done on the basis of a grid study performed with three systematically refined grids and both iterative convergence and grid convergence were achieved. The grid study showed that the numerical uncertainty introduced by application of the fine grid could be estimated to be 5.8% of the rudder drag coefficient. On the assumption that the experimental uncertainty was 10% of the measured drag coefficient, the code was validated at a level of 11%. In connection with the validation two points should be made. First, the method was validated on the basis of experimental results, which included the effect of a wall at the root leading to an effective aspect ratio approximately 8% smaller than the geometric one. Thus, the computation should have been performed for a rudder with a geometric aspect ratio equal to this effective ratio in order to make the comparison. However, since the validation was performed on the basis of the drag, which is relatively insensitive to small changes in Λ, the result most likely would have been the same. Second, the numerical uncertainty may be higher for rudder angles different from zero, since these flow situations are different from the case of δ=0°.

From the results presented in this chapter, it is concluded that as long as considered flow problems involve boundary layer flows which are close to fully turbulent, the performance of the numerical steady state method seems reasonable in relation to rudders in free stream at rudder angles in the range of 0 to 10 degrees. Since the boundary layer flow around most ship’s rudders is turbulent due to the surface roughness it should therefore be possible to use the present method for prediction of the rudder performance in relation to maneuvering problems. Finally, it should be noted that in case it is necessary to compute flows which involve partly laminar boundary layers due to transition, it could be useful to implement a transition model in the code as mentioned in Chapter 10.

This page is intentionally left blank.

Chapter 12

Rudder behind Propeller

12.1 Introduction

As regards the maneuverability of ships, the interaction between the propeller and the rudder plays an important role, since it is usually observed that the rudder on the ship is placed in the slipstream of the propeller. There are mainly two reasons for placing the rudder at this position. The first is that the presence of a profiled rudder increases the propulsive efficiency by utilizing some of the rotational energy in the propeller slipstream. The second, which concerns the maneuverability, is that the rudder lift force is increased considerably because of the accelerated flow over the part of the rudder in the propeller slipstream. This is not only advantageous in the normal service condition, because at low speeds where a free stream rudder will normally lose its efficiency, the effect of a rudder behind the propeller can be increased by increasing the number of propeller revolutions for short periods.

In order to create the full numerical model of the maneuvering ship, which is capable of dealing with the rudder-propeller interaction, it is important to have knowledge of the rudder-propeller flow itself and to investigate the performance of the numerical method when applied to rudder-propeller flows. Moreover, this information about the flow around the pure rudder-propeller configuration makes it possible to investigate the hull influence on the rudder-propeller flow when a full model is available.

According to the plan for the computational work presented in Chapter 9, this knowledge should be obtained by use of a numerical study of a rudder-propeller configuration. The work presented in this chapter is a continuation of the work presented in Chapter 11, where two rudders in free stream were investigated. The study of the rudder-propeller condition is based on the same two rudder models, but they are extended by applying the body force propeller, which was described in Chapter 8. Finally, some of the results will be compared with experimental data presented in Molland and Turnock (1991).

12.2 Existing Experimental Data

As mentioned earlier Molland and Turnock (ibid.) made a comprehensive experimental study of three different wall-mounted rudders in free stream and of the interaction between the three rudders and a modified Wageningen B4.40 propeller in a low-speed wind tunnel. In the present project two of the three rudders were selected for a numerical study of the performance in free stream and behind the propeller. The free stream case was treated in Chapter 11 where subjects concerning rudder profile, rudder geometry and surface quality were also dealt with. The overall propeller data is shown in Table (12.1), while additional information should be found in Molland and Turnock (ibid.).

Number of blades	4
Diameter, mm	800
Hub diameter, mm	200
Blade area ratio	0.40
Pitch ratio	0.95

Table (12.1) *Propeller data.*

The experimental rudder-propeller data was measured in the 3.5m wide and 2.5m high wind tunnel by means of the test rig shown in Figure (12.1). The idea of the test was to investigate the influence of propeller loading, rudder geometry and longitudinal rudder-propeller separation on the rudder performance and provide a set of data covering spanwise normal force distribution, rudder surface pressure distribution and lift and drag characteristics.

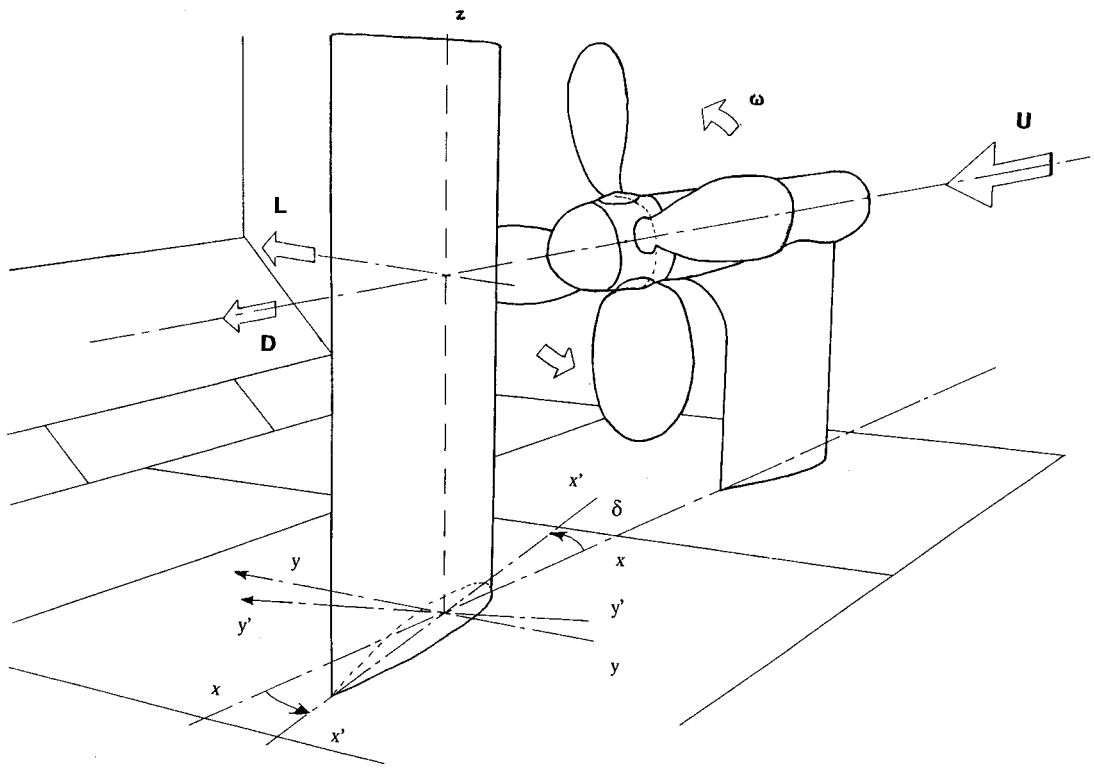

Figure (12.1) *Rudder-propeller configuration. From Molland and Turnock (1991).*

As in the without-propeller case all the tests were carried out for a free stream velocity equal to 10m/s, which corresponded to a cord-based Reynolds number equal to 0.4 million. In order to keep the free stream speed constantly equal to 10m/s and compensate for the working propeller, the speed in the wind tunnel was adjusted with the propeller running before each measurement. Concerning the spanwise position of the propeller for the two considered rudders, it was constantly 0.9 cord length from the wall for both rudder cases. Thus, the rudder tip was placed just inside the propeller slipstream for the small rudder aspect ratio Λ=1.5 and outside the slipstream for Λ=1.8. See Figure (12.2).

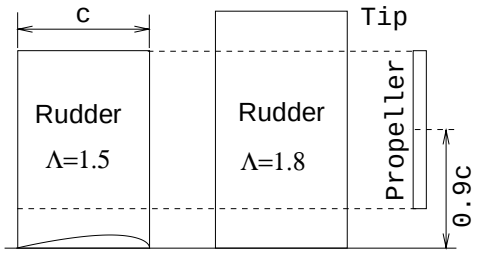

Figure (12.2) *Vertical position of propeller.*

Finally, since a large number of configurations were tested it was necessary to select a few to be used for comparison with the calculations. This is described in the following section.

12.3 Computational Conditions

As mentioned in the introduction, the two considered rudder geometries were the same as in Chapter 11. The same two rudders were chosen for comparison of the rudder performances in the with- and without-propeller condition and hence for investigation of the effect of placing the rudder in the propeller slipstream. Besides, the same computational grids and boundary conditions were applied to the with- and without-propeller cases. These subjects are treated in more detail in Chapter 11. By applying the same grids it was intended not to introduce additional numerical errors in the calculated results and in this way avoid performing a new grid study. However, from the experience from the rudder-propeller work, it was later found that instead of adopting the same grid approach, it had probably been a better idea to generate a new grid because of the different flow patterns of the conditions. This is discussed later.
The with-propeller calculations were performed for a condition where the free stream velocity was the same as in the free stream rudder case in Chapter 11. Thus, the calculations were performed at a free stream Reynolds number equal to *Re*=0.4 million. Concerning the model of the propeller rig shown in Figure (12.1), only the effect of the propeller was included. The rig itself was not modeled, which probably introduced additional differences between the numerical and the physical models. As regards the applied propeller model it was found that care should be taken when the body force was imposed on the computational grid. Due to the curved C-lines around the rudder profile and the spanwise stretching of the grid, it was difficult to obtain a smooth distribution of the body force over the propeller disk and consequently the exact thrust and torque

values shown in Table (12.2) could not be obtained. For each calculation the total thrust T and torque Q, imposed on the RANS grid, were calculated and compared with the values corresponding to an ideal circular disk and it was found that T and Q could be applied within a tolerance of 5 to 8%.
A total of twelve calculations was performed for different combinations of propeller loads and rudder angles. For Λ=1.5 nine conditions were investigated in order to study the influence of propeller loading on the flow. Additionally three cases for Λ=1.8 were considered in a study of the influence of changes in the aspect ratio. The influence of longitudinal rudder-propeller separation was not investigated, so the propeller was constantly positioned at x_p=-0.468.

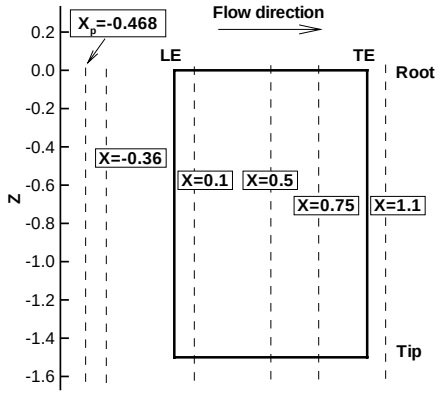

Figure (12.3) *Definition of longitudinal propeller-rudder positions.*

The leading edge of the rudder at zero degree rudder angle was positioned at *x*=0 and the longitudinal position of the propeller in relation to the rudder is illustrated in figure (12.3). Finally, the list of calculated cases is summarized in Table (12.2), where δ is the rudder angle, J the coefficient of advance, C_{Th} the thrust loading coefficient, K_Q the torque coefficient and Λ is the aspect ratio. The results of the computational work are presented below.

δ (deg.)	J	C_{Th}	10 K_Q	Λ
0	0.51	2.24	0.374	1.8
5	0.51	2.24	0.374	1.8
10	0.51	2.24	0.374	1.8
0	0.94	0.13	0.146	1.5
5	0.94	0.13	0.146	1.5
10	0.94	0.13	0.146	1.5
0	0.51	2.24	0.374	1.5
5	0.51	2.24	0.374	1.5
10	0.51	2.24	0.374	1.5
0	0.35	5.86	0.437	1.5
5	0.35	5.86	0.437	1.5
10	0.35	5.86	0.437	1.5

Table (12.2) *List of computed flow situations.*

12.4 Results and Discussion

The presentation of the results covers both field and integral quantities. The field quantities are presented to provide information about the flow pattern itself, while the integral quantities like the spanwise normal force distribution and the lift and drag characteristics show the overall behavior of the rudder. The latter characteristics are interesting from a maneuvering point of view, as they can be applied to maneuvering simulation. Due to lack of velocity data, the velocity related field quantities will be related qualitatively to other rudder-propeller flows from the literature, while the pressure distribution at different spanwise positions for a single case will be compared with data from Molland and Turnock (ibid.). Finally, the integral quantities will be compared with data from the same reference.

12.4.1 Field Quantities

Before studying the behavior of the lift and drag characteristics for the rudders behind the propeller, the flow pattern around the rudders was investigated to provide some information about the details in the flow. The flow field was considered in two cases at the same rudder angle, δ=10°, but with different aspect ratios. The propeller loading was kept constantly corresponding to a coefficient of advance equal to 0.51 and C_{Th}=2.24. The study included the limiting streamlines and the pressure distribution on the rudder surface plus the axial velocity (*x*-velocity component) contours and cross flow vectors at different *x*-positions.

12.4.1.1 Limiting Streamlines on Rudder Surface

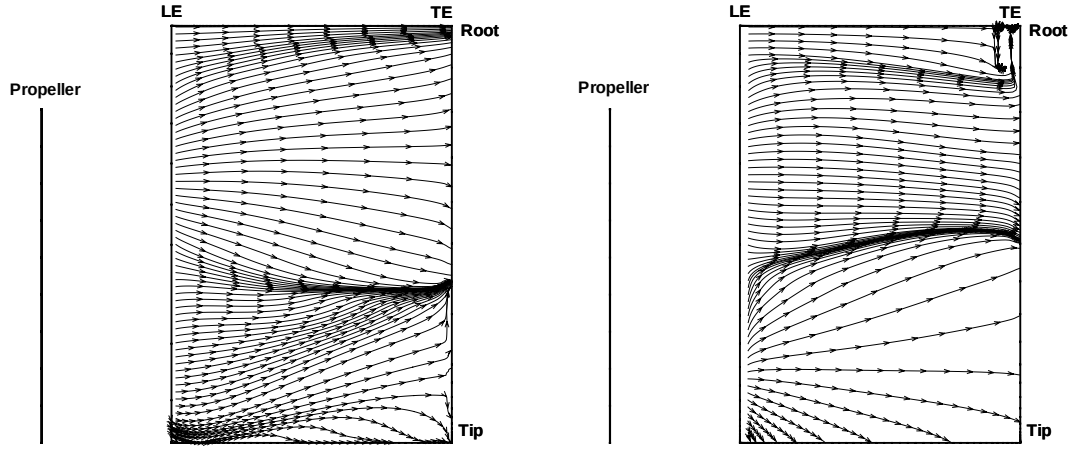

Λ=1.5, suction side *Λ=1.5, pressure side*

Figure (12.4) *Limiting streamlines over the rudders for δ=10° and J=0.51.*

The flow pattern over the rudder surface was illustrated by the limiting streamlines, shown in Figures (12.4) and (12.5). For both rudders it was found that on the upper part of the suction side of the rudders where the swirl in the propeller slipstream hit the

rudder surface, the streamlines were diverging or fanning out. Thus, some of the streamlines were running towards the root of the rudder while others were running downwards, where they met the streamlines coming up from the tip at a line of converging streamlines approximately at the midspan position. On the lower part of the suction side, which was not hit by the swirl, the streamlines were forced upwards towards the line of converging streamlines, by the fluid flowing around the tip. Moreover, a thin region of reversed flow was present at the trailing edge. The same phenomenon of diverging streamlines was observed on the lower part of the pressure side where the swirl also hit the rudder surface. Some of the streamlines were running towards a line of converging streamlines approximately in the middle of the rudder while others were running downwards, where they continued around the rudder tip to form the tip vortex caused by the pressure difference between the two sides of the rudder. Finally, on the upper part of the pressure side of the rudder the flow was affected by a region of reversed flow close to the root above the propeller slipstream.

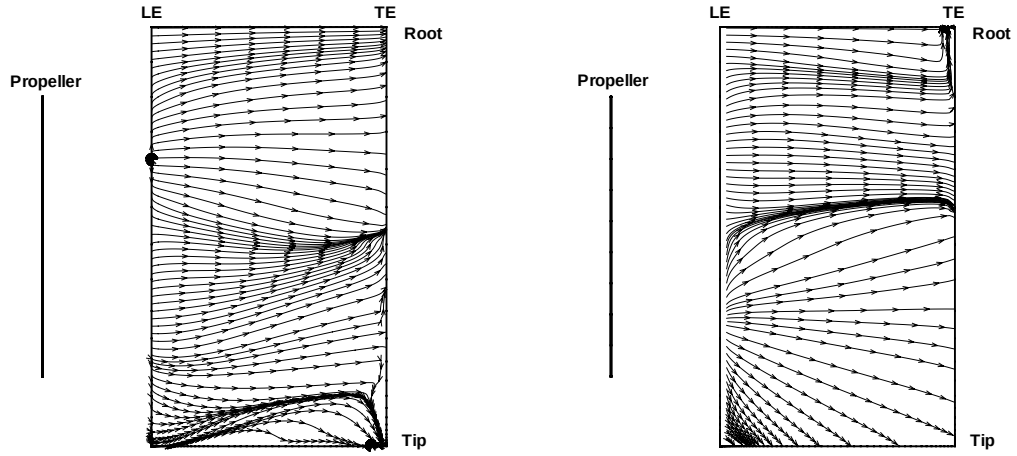

Λ=1.8, suction side *Λ=1.8, pressure side*

Figure (12.5) *Limiting streamlines over the rudders for δ=10° and J=0.51.*

Concerning the influence of the different aspect ratios on the streamline patterns, the two flows were generally similar except for the tip flow, which was less pronounced for the small aspect ratio. Since the tip in this case was placed inside the propeller slipstream, the observed effect was probably caused by a kind of flow straightening effect from the accelerated flow in the slipstream. It was found that the presence of the propeller changed the flow compared to the free stream flow presented in Chapter 11. It was seen that the zone of reversed flow at the trailing edge of the suction side of the free stream rudder was strongly reduced and almost removed in the with-propeller case. The same was the case for the zone of reversed flow on the lower part of the pressure side, even though a new zone was developing at the upper part of the trailing edge.

It was not possible to compare the calculated streamline pattern with experiments since such data did not exist for the considered rudder-propeller configuration. However, based on an H-grid topology, Ichikawa (1995) performed numerical calculations for a large aspect ratio NACA0010 rudder behind a propeller by means of a RANS method, including the Baldwin-Lomax turbulence model and the Hough-Ordway propeller model, and the presented field quantities seemed to be in qualitative agreement with experimental data found for the corresponding rudder-propeller configuration. Even though Ichikawa (ibid.) neglected the tip effects of the rudder due to the large aspect

ratio, the streamline pattern over the part of the rudder in the propeller slipstream showed tendencies of diverging and converging streamlines similar to the streamline patterns in Figure (12.5).

12.4.1.2 Velocity Components in Propeller Slipstream

The three calculated velocity components *u*, *v* and *w* were investigated at different *x*-planes in the flow domain. Figure (12.6.a) shows the axial velocity component at *x*=-0.36 in the slipstream just behind the propeller (see Figure (12.3)) for the case of Λ=1.5, δ=10°, *J*=0.51 and C_{Th}=2.24. From Figure (12.6.a) it is seen that in the propeller slipstream the fluid was accelerated to a maximum level around 1.6 to 1.7 times the free stream velocity. Above and below the slipstream a region of reduced axial velocities was observed. According to Figure (12.6.b) the axial velocity for the free stream rudder at the same *x*-position showed the same region of retarded flow, so the low-speed region was most likely caused by the presence of the rudder, which was placed farther downstream. Since no experimental data for the velocity distribution was available for comparison with the calculation, it was difficult to check if the velocity field was correctly calculated. However, according to the momentum theory including corrections for the slipstream contraction, which was presented in relation to the maneuvering model in Chapter 3, the axial mean velocity was found to be U_{mean}=1.53 in the slipstream at *x*=-0.36. This looked reasonable compared to the velocity distribution shown in Figure (12.6.a).

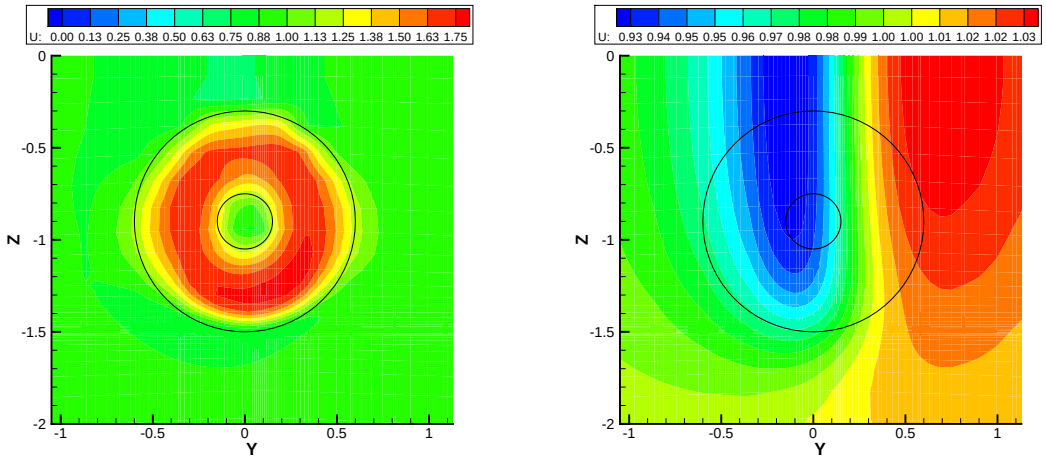

a. With propeller *b. Without propeller*

Figure (12.6) *Axial velocity contours behind propeller at x=-0.36 for δ=10° and J=0.51.*

Seen in relation to the cross flow properties of the slipstream, Figure (12.7.a) shows the calculated cross flow vectors just behind the propeller at *x*=-0.36 and, as expected, a rotational motion induced by the propeller was observed. The presence of the swirl in the propeller slipstream influences the rudder flow, since it changes the local inflow angle to the rudder. As an illustration of this, the local twist angle β was calculated along a line parallel to the vertical center line of the propeller, corresponding to *y*=0 in Figure (12.6.a). The twist angle is defined as

$$\beta = Arctan\left(\frac{v}{u}\right) \tag{12.1}$$

where v and u are the calculated velocity components in the y- and x-directions, respectively. The results are plotted in figure (12.7.b) and it is found that upstream of the rudder at x=-0.36 the twist angle is in the range from -17° to 22° for the case of Λ=1.5, δ=10° and J=0.51. It is also seen that β is not symmetric around β=0°, which is probably caused by the presence of the turned rudder disturbing the propeller flow upstream.

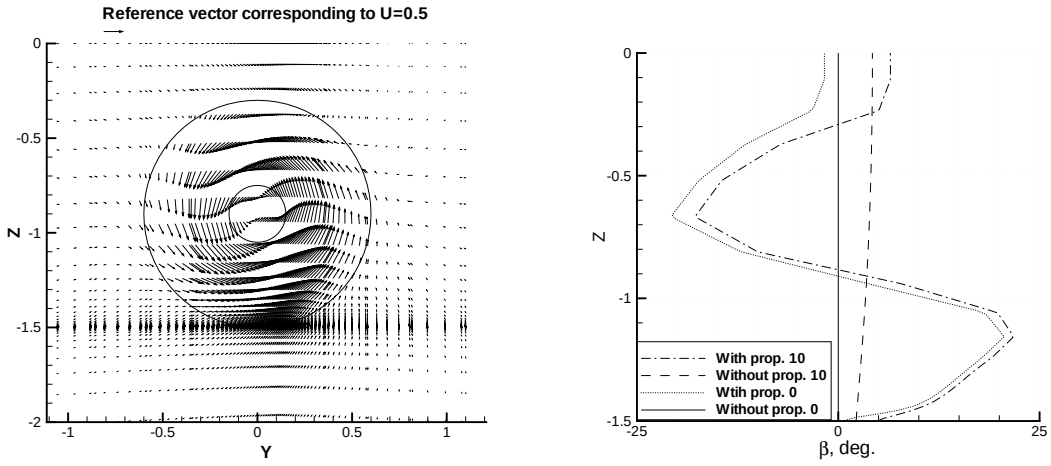

a. Cross flow vectors b. Twist angle

Figure (12.7) *Cross flow properties behind propeller at x=-0.36 for δ=10° and J=0.51.*

In order to investigate this idea the influence from the rudder alone in free stream is also plotted in Figure (12.7.b). It is seen that the presence of the rudder actually introduces a cross flow at the considered x-position, resulting in positive beta-values in the range from 2° to 4° along the rudder. Since no experimental velocity data is available for comparison with the calculation, it is tried to compare the twist angle with a theoretical value calculated on the basis of the axial and tangential mean velocity components in the propeller slipstream. The applied expression for the mean twist angle was proposed by Rohman and Thieme (1957) on the basis of the vortex cylinder theory presented in Gutsche (1956). The expression is found to be

$$\beta_{theory} = Arctan\left(\frac{1.3\,K_Q / K_T}{k_m + 1/\left(\sqrt{1+C_{Th}} - 1\right)}\right) \tag{12.2}$$

where K_Q and K_T are the torque and thrust coefficients, respectively. C_{Th} is the thrust loading coefficient and k_m is a factor accounting for the variation of the slipstream velocity with respect to the non-dimensional distance x/D from the propeller. The k_m factor corresponds to κ in Chapter 3. At the considered longitudinal position, k_m was equal to 0.64 according to Gutsche (ibid.) and with C_{Th}=2.24, K_Q=0.0374 and K_T=0.2288 the absolute value of the twist angle was calculated to be β_{Theory}=6.4°.

From the plot of β for the without-propeller case in Figure (12.7.b) it is seen that for δ=0° the twist angle is equal to zero, so in order to avoid the rudder influence on β, which is observed for δ=10°, the case of δ=0° is used for the comparison with the theoretical twist angle. For δ=0° the calculated beta-values are found to be in the range from -20.5° to 20.5°. When compared with the theoretical mean value, the numerically determined twist angle is somewhat larger than the theoretical angle, which indicates that the numerically calculated flow is more rotational than the one predicted by the simple cylinder vortex theory.

12.4.1.3 Velocity Fields around Rudders

In order to study the influence of the propeller on the flow around the rudder, which was placed farther downstream at x=0, the axial velocity contours and the cross flow vectors were calculated at three positions along the rudder at x=0.1, x=0.5, x=0.75, and at one just behind the trailing edge, at x=1.1 (see Figure (12.3)). The results were plotted in Figures (12.8.a) to (12.8.d) together with two circles illustrating the propeller with the hub. The plots show the flow seen in the upstream direction, which means that the suction side of the rudder is on the starboard side and the pressure side is on the port side of the rudder. As regards the axial velocity component, it was found that the effect of the propeller influenced the rudder flow all along the rudder, since it resulted in a region of high axial velocity over the part of the rudder placed inside the slipstream. Relatively close to the leading edge at x=0.1, the fluid was accelerated over the suction side compared to the slipstream velocity in Figure (12.6.a), while the velocity was less influenced over the pressure side. In addition to this, the vortex at the tip was developing. At the stations farther downstream at x=0.5 and x=0.75 the tip vortex, which was caused by the pressure difference between the pressure and the suction sides, was seen to develop further. This pressure difference in conjunction with the rotation of the flow probably caused the high-velocity region on the pressure side to move downwards and even around the tip and the region on the suction side to move towards the root. The same tendency was seen in the wake just behind the rudder as illustrated in Figure (12.8.d)

With the results of the study of the streamlines shown in Figure (12.4) in mind, it was observed that the streamlines fanned out over the lower part of the pressure side and over the upper part of the suction side due to the swirl hitting the rudder surface. This effect was also reflected in the velocity contour plots. From Figure (12.8.b) it was seen that on the upper part of the suction side close to the rudder surface, the high-velocity region spread out to an extension outside the propeller diameter and inside the hub region illustrated by the two circles in the figure. The same tendency was observed near the lower part of the pressure side where it actually seemed to help force the flow towards the tip. Concerning the propeller hub it was not included in the model, but it was reflected in the propeller body force distribution, which was only applied in the blade region and not in the hub region inside the small circle. The missing propeller body force in this region explained the presence of the regions of low-speed flow on each side of the rudder which were observed in the Figures (12.8) and (12.9). On the pressure side the region seemed to be positioned a little higher than on the suction side.

The cross flow properties of the flow are also plotted in Figure (12.8).

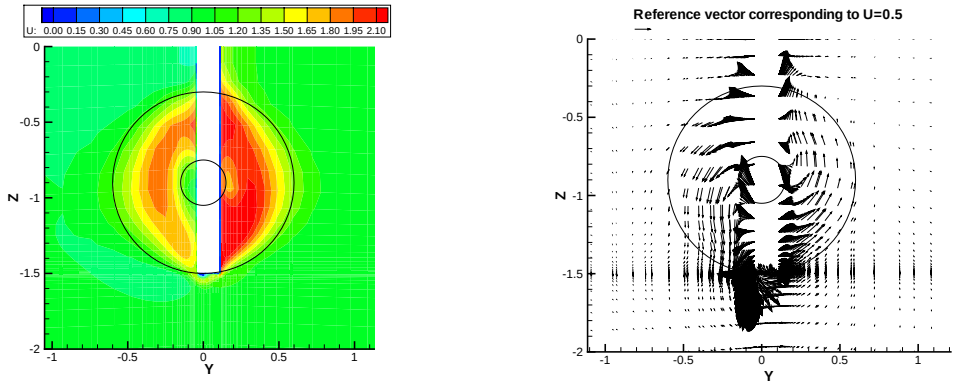

a. At x=0.1c

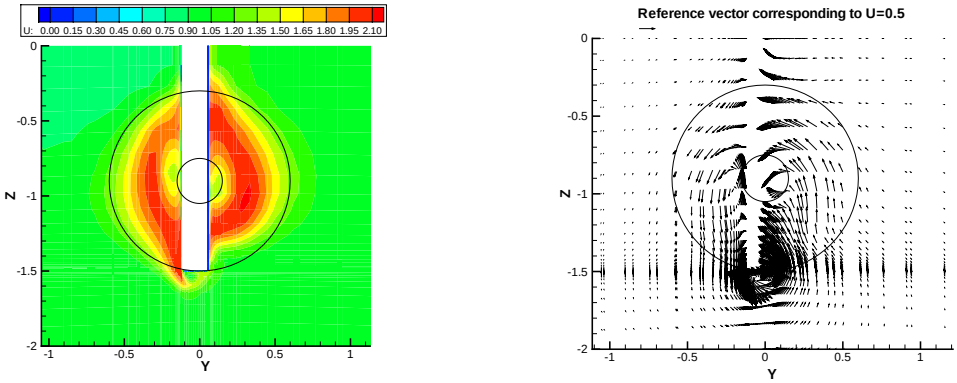

b. At x=0.5c

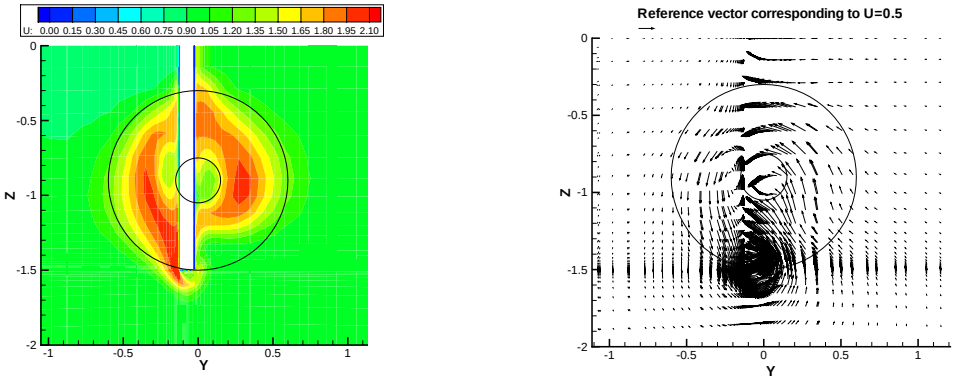

c. At x=0.75c

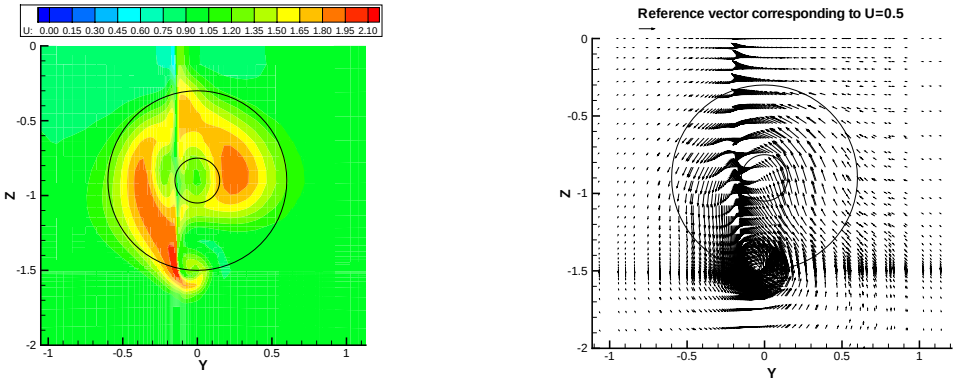

d. At x=1.1c

Figure (12.8) *Axial velocity contours and cross flow vectors at different x-positions. Λ=1.5, δ=10°.*

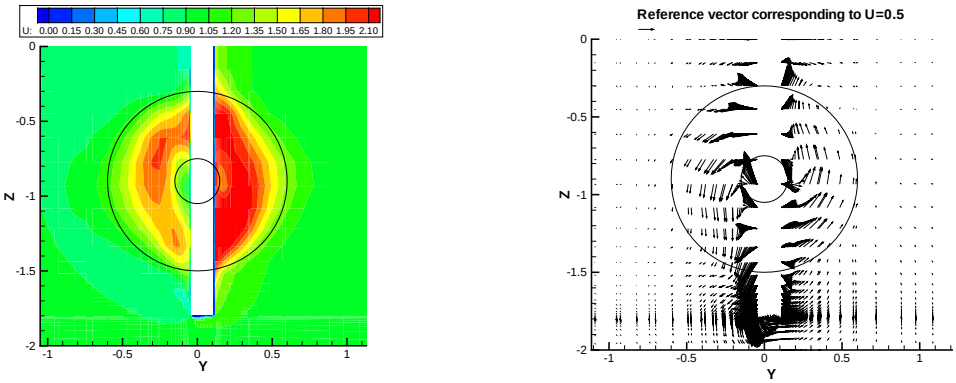

a. At x=0.1c

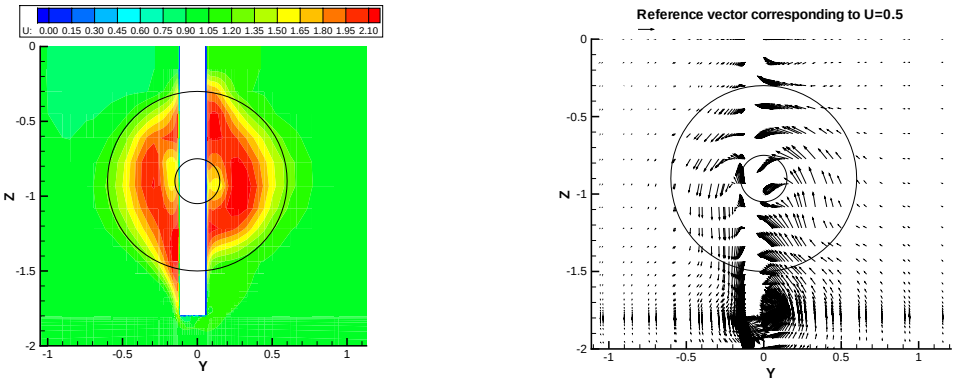

b. At x=0.5c

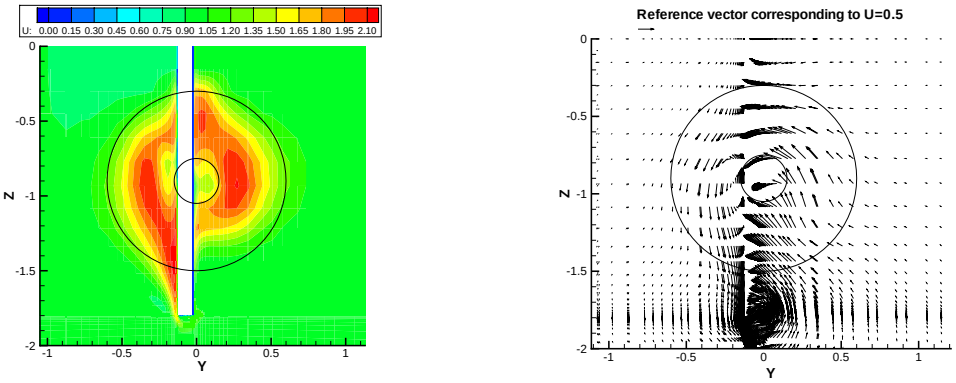

c. At x=0.75c

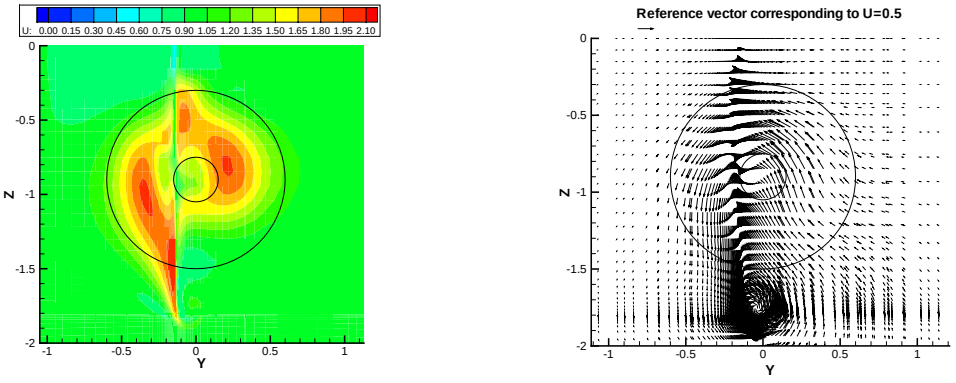

d. At x=1.1c

Figure (12.9) *Axial velocity contours and cross flow vectors at different x-positions. Λ=1.8, δ=10°.*

For x=0.1 the cross flow generally seemed to be directed away from the rudder in a region close to the surface. This can be explained by the growing thickness of the rudder profile in the considered region, which caused the fluid to be forced to each side. However, the presence of the swirl was still observed since the flow within the propeller disk was forced downwards on the pressure side and upwards on the suction side of the rudder.

Moreover, a relatively strong cross flow around the tip was observed, which indicated that the tip vortex was developing. It was also found that with the applied propeller orientation the rotation in the slipstream actually helped to drive the tip vortex for the considered positive rudder angles. Regarding the other two x-stations at x=0.5 and x=0.75, the overall picture in the outer flow field appeared to be the same, i.e. the cross flow was directed downwards on the pressure side and upwards on the suction side due to the rotation and developing the tip vortex. On the inner flow field close to the rudder surface a few comments should be made. In the region beside the upper part of the suction side the cross flow vectors indicated that the flow arriving perpendicularly to the surface in one region was forced upwards and in another downwards because of the presence of the rudder, blocking the rotation. The same effect was partly observed along the lower part of the pressure side where some of the cross flow vectors were pointing upwards and some downwards. However, the incoming flow was more parallel than perpendicular to the rudder because of the presence of the tip. In the wake just behind the rudder at x=1.1 the rudder no longer blocked the rotation, but as seen from Figure (12.8.d) the influence from the rudder was still strong.

To be able to investigate the influence of changing the aspect ratio, i.e. the effect of moving the tip outside the propeller slipstream, the flow pattern was calculated at the same x-positions for the rudder with Λ=1.8 as for Λ=1.5. On the basis of the results in Figures (12.9.a) to (12.9.d) the overall picture was the same for the two aspect ratios. However, four points concerning the axial velocity should be mentioned. The first and most obvious difference between the two rudders was the reduction in the way the pressure side high-speed region was forced below the rudder tip. The elongation of the rudder to a large degree prevented the slipstream from being sucked around the tip of the rudder, even though the tip effect still forced the slipstream downwards. Second, the part of the slipstream on the suction side was not displaced as far away from the tip as in the case of the small aspect ratio. Third, the axial velocity seemed to be a little higher in some regions for Λ=1.8 compared to Λ=1.5. Finally, the small region of accelerated flow close to the root on the suction side, seen all along the small aspect ratio rudder, disappeared as the aspect ratio was increased. This could be a consequence of the previously mentioned smaller vertical displacement of the slipstream. As regards the cross flow properties of the rudder flow, also shown in Figure (12.9), no significant changes were observed in the region above the hub. In the region around the lower part of the rudder the effect of the larger aspect ratio was more clearly seen, since the cross flow around the tip seemed to be weaker after the tip was removed from the propeller slipstream. However, except for this, the gross features of the two rudder flows were much the same.

12.4.1.4 Pressure Distribution on Rudder Surface

The last investigated field quantity, was the pressure distribution on the rudder surface. The pressure distribution plays an important role for to the rudder performance, since it practically alone determines the lift of the rudder. According to the calculated pressure distribution in Figure (12.10), the influence of the propeller on the pressure is clear on both suction and pressure sides of the rudder with Λ=1.5 at δ=10°. In the figure two zones of high and low pressure are observed close to the leading edge of each side of the rudder. The high-pressure regions were caused by the swirl of the slipstream, which hit the upper part of the suction side and the lower part of the pressure side with the applied propeller orientation. At the same spanwise positions as the high-pressure regions, but on the opposite rudder side, the two low-pressure regions were caused by the shadow effect of the rudder, which stopped the rotational motion.

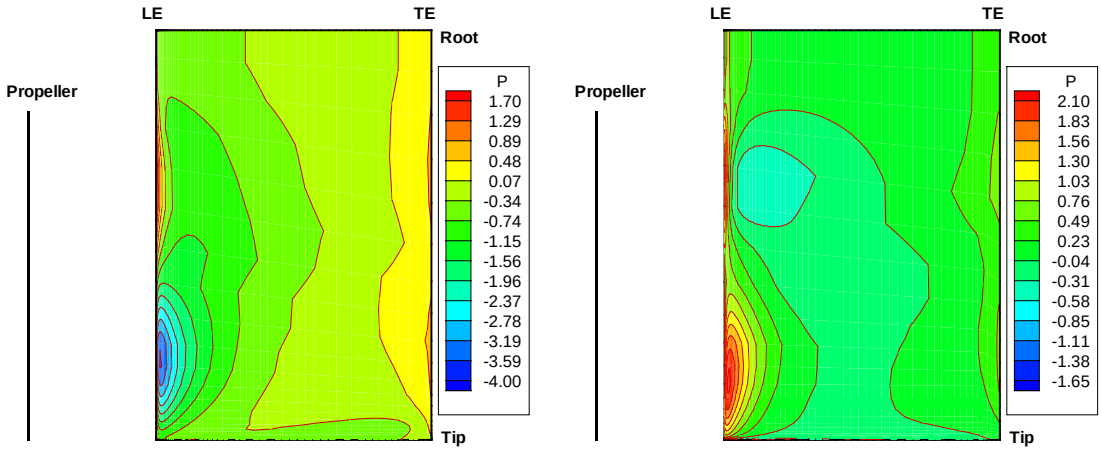

a. Suction side *b. Pressure side*

Figure (12.10) *Pressure distribution on rudder surface for Λ=1.5 at δ=10°.*

Further along the profile in the streamwise direction just behind the two high- and low-pressure regions, a low-pressure zone was observed within the slipstream on each side of the rudder. These zones, were probably caused by the accelerated flow in the slipstream and extended to the tip region, where they widened out and almost covered the tip over the complete cord length. This behavior was expected, since the accelerated fluid forming the cross flow around the tip resulted in decreasing pressure. A comparison with the without-propeller case in Chapter 11 showed that the propeller introduced higher pressure peaks, both positive and negative, than in the free stream case, which explains the increasing lift coefficient for a rudder behind a propeller. This is illustrated later.

By comparison of the pressure distributions for the two different aspect ratios, it was found that they generally showed the same tendencies over the rudder except for the tip region. In the Figures (12.11) and (12.10) it is seen that the low-pressure regions close to the tip on both sides of the rudder were reduced when the tip was removed from the propeller slipstream as in the case of Λ=1.8. The reduced pressure difference between the two rudder sides consequently reduced the cross flow around the tip, which explained the observed cross flow behavior discussed previously.

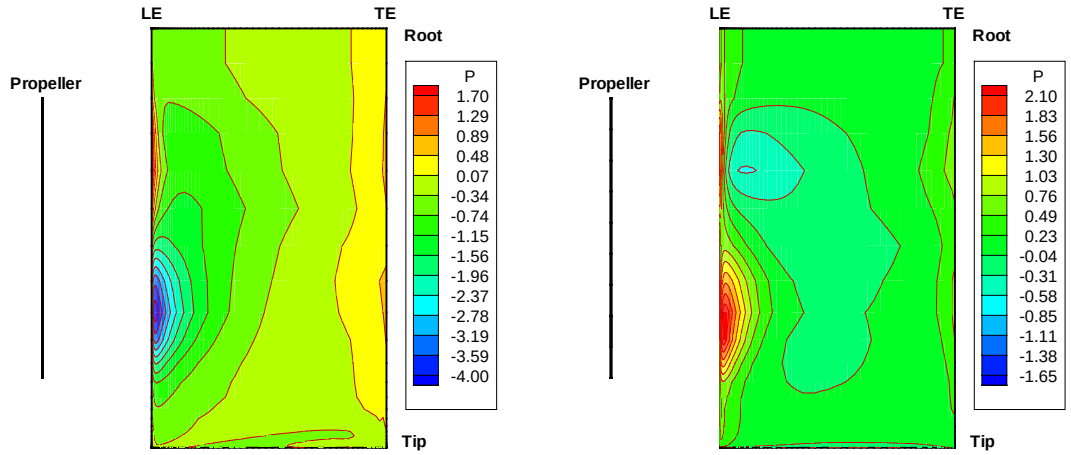

a. Suction side *b. Pressure side*

Figure (12.11) *Pressure distribution on rudder surface for Λ=1.8 at δ=10°.*

In order to investigate the performance of the code, seen in relation to quantitative prediction of the pressure distribution on the rudder surface, the calculated pressure along the rudder surface at different constant spanwise positions was compared with the corresponding experimental values from Molland and Turnock (1991). Eight different *z*-positions over the rudder were considered. With *z*=0 at the root of the rudder they were placed at *z* equal to -0.07*s*, -0.23*s*, -0.40*s*, -0.53*s*, -0.70*s*, -0.83*s*, -0.94*s* and -0.97s, where s is the rudder span. The calculated and experimental pressure distributions were compared for the smallest aspect ratio Λ=1.5 at δ=10° and a propeller loading corresponding to *J*=0.51 and C_{Th}=2.24. The results were plotted in Figures (12.12.a) to (12.12.h). The pressure was represented by the local pressure coefficient c_p defined by

$$c_p = \frac{p - p_\infty}{1/2 \rho U^2} \qquad (12.3)$$

where $p - p_\infty$ is the local pressure, ρ is the density and *U* is the free stream velocity. Figure (12.12.a) shows that close to the wall and outside the propeller slipstream at *z*=-0.07*s* the calculated pressure was in fairly good agreement with the experiment on the pressure side of the rudder, while the calculation overpredicted the magnitude of the pressure on the suction side. Farther away from the wall and just inside the propeller slipstream, at *z*=-0.23*s*, Figure (12.12.b) shows that the code overpredicted the pressure on the pressure side and overpredicted the magnitude of the negative pressure peak on the first half of the suction side. Nearer to the trailing edge the agreement was better. When the center of the slipstream was approached Figures (12.12.c) and (12.12.d) illustrate that the pressure on the pressure side of the rudder was still overpredicted, while agreement between the calculated and the experimental pressure improved on the suction side. On the other side of the center of the slipstream at *z*=-0.70*s*, Figure (12.12.e) shows that the computed pressure peak values were slightly underpredicted on both suction and pressure sides. Closer to the tip the results in Figures (12.12.f) to (12.12.h) reveal that the agreement was generally fair, except for the region on the suction side close to the trailing edge at the *z*-position closest to the tip.

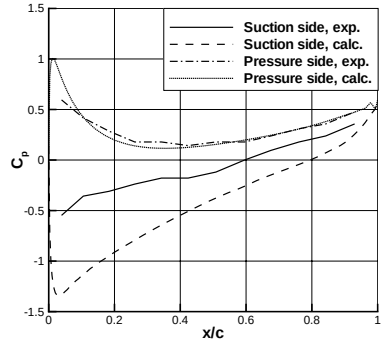

a. z=-0.07 span

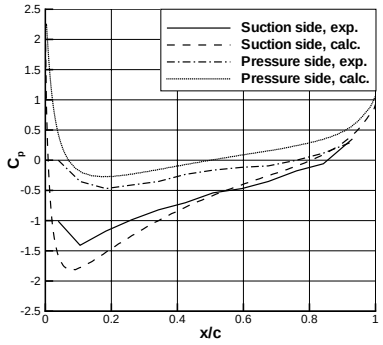

b. z=-0.23 span

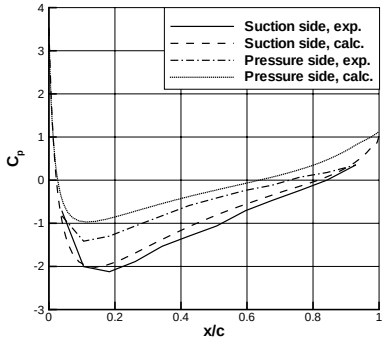

c. z=-0.40 span

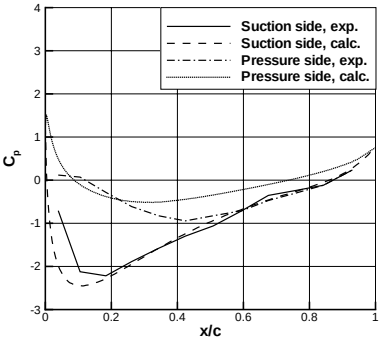

d. z=-0.53 span

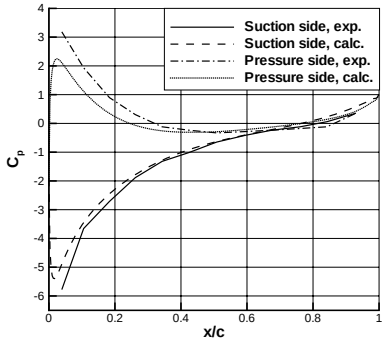

e. z=-0.70 span

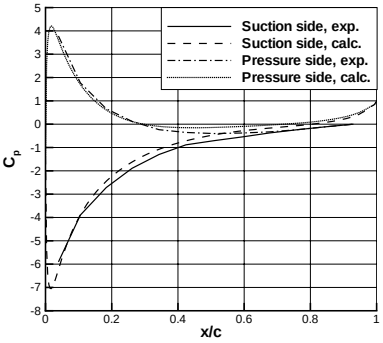

f. z=-0.83 span

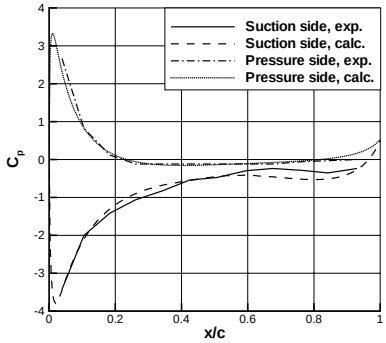

g. z=-0.94 span

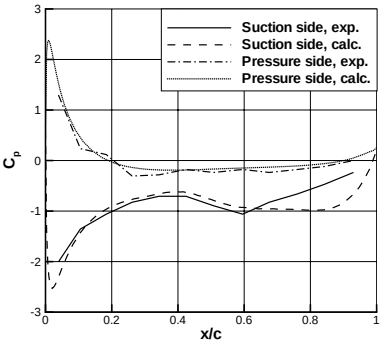

h. z=-0.97 span

Figure (12.12) *Numerical and experimental* c_P *values. J=0.51,* Λ*=1.5 and* δ*=10°.*

In order to summarize and comment on the results of the comparison between experiments and calculations, it was found that the numerical results qualitatively showed the same overall tendency as the experiments and that there was actually fairly good agreement between the two sets of data in the tip region of the rudder. There were probably two reasons for the observed differences in Figures (12.12.a) to (12.12.d). The first was the missing wall condition at the root of the rudder. By neglecting the no-slip condition in the numerical model, the effect of the interaction between the wall and the rudder boundary layers at the root could not be modeled. According to Pope and Harper (1966), vortex shedding in the root boundary layer results in reduced lift for wall-mounted half-wings compared to models of complete wings, as discussed in Chapter 11.
By the application of the symmetry boundary condition instead of the wall, the numerical model corresponded to a complete wing model. Since the lift is pressure dominated, the pressure difference between the suction and pressure sides in the root region should be reduced for the experimental wall-mounted wing compared to the numerical full model, which also was the case according to Figure (12.12.a). The second reason could be in insufficient grid resolution. As mentioned earlier it was assumed that the free stream rudder grid could be applied to the behind-propeller calculation. However, on the basis of the study of the pressure distributions for the with- and without-propeller condition a special grid should have been generated for the propeller calculation. According to Figure (11.11) in Chapter 11 no significant pressure gradient in the spanwise direction was observed on the upper part of the free stream rudder. Thus, a relatively coarse grid resolution could be applied in the z-direction for this case. However, as seen from Figures (12.10) and (12.11) the presence of the propeller changed the pressure distribution and introduced relatively large spanwise variations in the pressure. Consequently, the grid should not only be refined in the tip region, but also in the remaining part of the rudder in order to resolve the pressure field in the spanwise direction. The idea of the insufficient grid resolution was supported by the behavior of the results, since the agreement between experiment and calculation was best in the tip region where the grid was relatively fine in order to resolve the tip vortex.
Regarding the tip vortex, the difference observed in Figure (12.12.h) at the tip in the aft part of the rudder could be explained by the presence of this vortex. It was possible that the vortex introduced some unsteady effects not to be captured by the steady state solver and, besides the relatively simple algebraic isotropic turbulence model could be insufficient for the complicated tip flow leading, to some discrepancies between the numerical and the experimental results. However, it could also be that the difference in the region was caused by inaccuracy of the measurements, due to the complex flow around the tip.
Finally, it should also be kept in mind that the body force could not be distributed perfectly smooth over the propeller disk, which probably also introduced some differences between the experiment and the calculation.

12.4.2 Integral Quantities

In order to investigate the influence of the propeller on the rudder performance the spanwise normal force distribution and the lift and drag characteristics were calculated for different propeller loads.

12.4.2.1 Non-dimensionalization

Concerning the non-dimensionalization of the rudder propeller data, there are different approaches. One is the traditional approach based on the free stream velocity as demonstrated in Chapter 11. Another involves both the free stream velocity and the number of propeller revolutions and the propeller diameter to include the effect of the propeller loading and, finally, a third method is based on the free stream and the propeller slipstream velocities. This approach is mainly used in maneuvering simulations as described in Chapter 3. The good thing about the first approach is that for a constant free stream velocity it reflects the physics, i.e. when the propeller loading is changed, the change in the force coefficient will reflect whether the rudder force increases or decreases. This is not the case for the propeller parameter based approaches, where for instance increased propeller loading will not necessarily result in increasing lift force coefficients as seen from the experimental results in Chapter 5. However, for some applications like maneuvering simulation some propeller parameters have to be included in the non-dimensionalization. In this context the traditional method will be used in order to study the physical influence of the propeller loading on the lift, drag and normal forces.

12.4.2.2 Drag Characteristics

The calculated drag characteristics of the two rudders are shown in Figure (12.13). Concerning the influence of the propeller loading on the drag force, which is illustrated in Figure (12.13.a), the numerical results showed that if the propeller loading was increased from light, J=0.94 and C_{Th}=0.13, to medium, J=0.51 and C_{Th}=2.24, the drag coefficient would increase except for δ=0°, where the change was relatively small. If the propeller loading was increased further, corresponding to J=0.35 and C_{Th}=5.86, the drag was decreasing and it actually became negative for δ=0° and δ=5°.

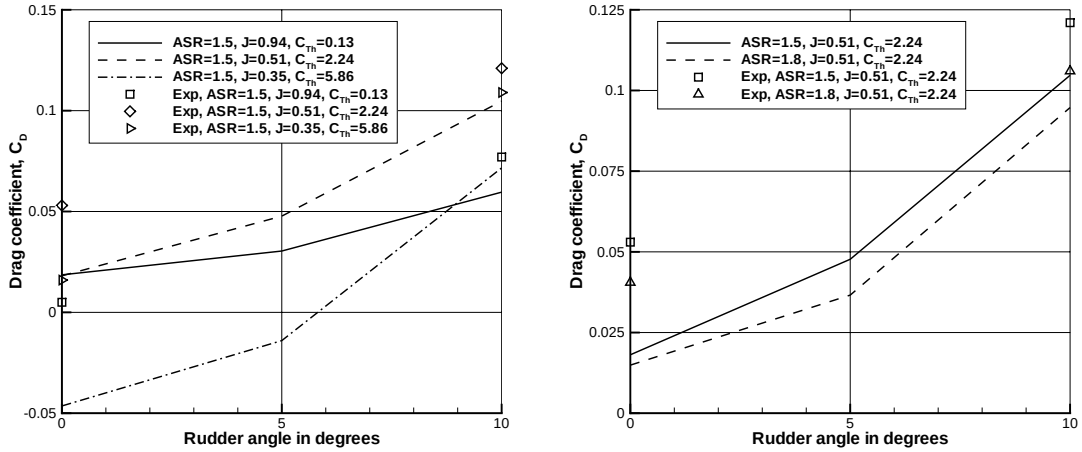

a. Drag, influence of propeller loading *b. Drag, influence of aspect ratio*

Figure (12.13) *Calculated and experimental drag characteristics.*

It is seen from a comparison with the experimental drag coefficients that the calculated coefficients were generally underpredicted, but also that they showed the same

tendencies as the experiments, i.e. increasing C_{Th} from 0.13 to 2.24 increased the drag, while increasing C_{Th} from 2.24 to 5.86 decreased the drag.

The deviation between the experiments and the calculations is probably due to the same factors as discussed in connection with the field quantities, namely the wall effect, the grid resolution and the turbulence model. According to Hörner (1965), the drag for the wall-mounted experimental rudder should be higher than that for the numerical rudder due to the root vortex, so this could explain some of the difference. The presence of the working propeller relatively close to the wall could also influence the root flow and increase the effect of the root vortex. Next, the relatively coarse grid resolution away from the tip region probably caused additional problems, because the pressure and the suction peaks at the leading edge were not properly resolved. Since the *x*-component of the normal to the rudder surface is large at the leading edge, the local drag coefficient is dominated by the pressure contribution in this region. Therefore, if the leading edge pressure and suction peaks were not calculated accurately enough, it could lead to inaccurate drag coefficients. Finally, if the turbulence model was not sufficient to model the flow, it would influence the frictional forces, which also play an important role in relation to the drag. As to the influence of the aspect ratio on the drag coefficient, Figure (12.13.b) shows a small decrease in the calculated drag coefficient as the aspect ratio was increased from 1.5 to 1.8. This behavior was also observed for the experimental results, even though the increase in the drag was a little larger than predicted by the calculation. For both aspect ratios the calculated drag was underpredicted in comparison to the experiment.

12.4.2.3 Lift Characteristics

The computed lift coefficients for the two rudders are shown in Figure (12.14). From Figure (12.14.a) it is seen that in contrast to the free stream rudder, the rudder behind the propeller had a lift coefficient different from zero for $\delta=0°$. The reason for this is that the rotation in the slipstream in conjunction with the axial velocity introduced a local angle of attack, similar to the twist angle described earlier, over the part of the rudder placed in the slipstream. This local angle of attack usually results in a net lift force different from zero. For the present calculation the lift force was negative and it is observed that when the propeller loading was increased, the magnitude of the negative lift force was increasing as well. It is difficult to say if the this behavior was correct because it depended on the local angle of attack induced by the rotation in the slipstream, but compared to experimental lift coefficients at $\delta=0°$, the magnitude seemed to be overpredicted, and especially so for the heavy propeller loading. For larger rudder angles, i.e. $\delta=5°$ and $\delta=10°$, the lift force became positive and since an increased propeller loading leads to higher axial velocity in the propeller slipstream, it was expected that the lift force would increase with increasing propeller loading for $\delta=5°$ and $\delta=10°$. Therefore, the observed behavior of the calculated results in Figure (12.14.a) is found to be qualitatively reasonable. By comparison of the calculations with experiments it is seen that for $\delta=10°$ the computations and the experiments followed the same tendency and that the computations seemed to overpredict the lift a little. Common to all three propeller loads was that the differences resulted in larger lift curve slopes for the computations compared to the experiments. Compared to the lift of the rudder in free stream shown in Chapter 11, the lift was increased considerably when the rudder was

placed in the slipstream of the propeller for C_{Th}=2.24 and C_{Th}=5.86. For C_{Th}=0.13 there was no significant increase in the lift.

The influence of the different aspect ratios is illustrated in Figure (12.14.b). It is seen that for δ=0° the aspect ratio equal to 1.5 resulted in a slightly higher calculated lift coefficient than Λ=1.8. For δ=5° and δ=10° the calculated lift coefficients were practically identical. The experimental lift forces followed a trend where Λ=1.5 resulted in a slightly higher lift coefficient than Λ=1.8 for both δ=0° and δ=10°. By comparing the two sets of data it is seen that the calculations predicted a higher lift curve slope and that the experimentally observed reduction in the lift caused by the increased aspect ratio was not present in the calculations. Seen in relation to the free stream rudder case, the effect of changing the aspect ratio was generally smaller when the rudder was working in the slipstream and concerning the experimental results, they actually showed the opposite behavior than observed in the free stream case.

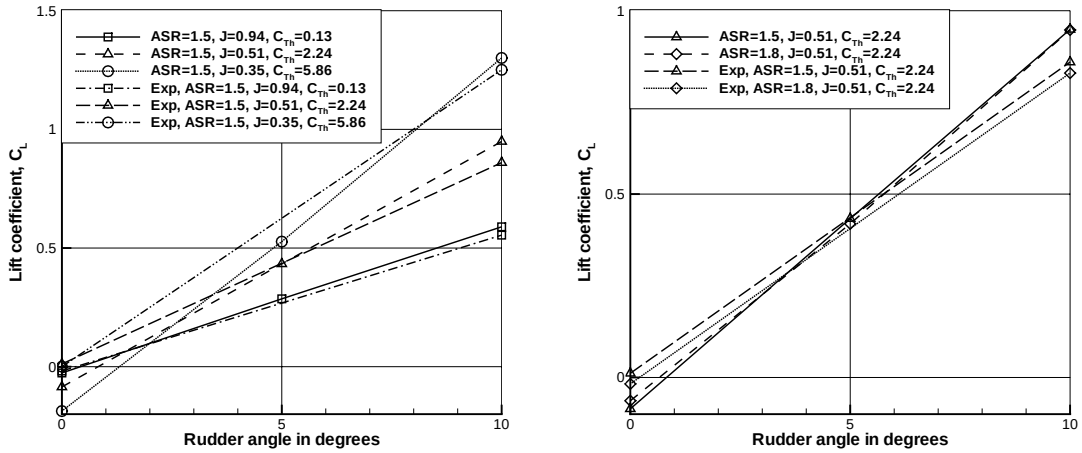

a. Lift, influence of propeller loading *b. Lift, influence of aspect ratio*

Figure (12.14) *Calculated and experimental lift characteristics.*

12.4.2.4 Local Normal Force Distribution

The study of the lift and drag characteristics only provided information about the overall behavior of the rudder lift, so in order to study the influence of the propeller on the local load over the rudder, the normal force distribution was calculated at different spanwise positions and plotted in Figure (12.15). For the lightly loaded propeller, *J*=0.94 and C_{Th}=0.13, Figure (12.15.a) reveals that the influence of the propeller was relatively weak and that it was most clearly seen for δ=0°, where it resulted in a negative normal force from the root to the center of the slipstream at 60 % span. On the other side of this position the normal force changed sign and became positive. With the applied direction of the propeller rotation this seemed reasonable since the rotation in the slipstream should result in local angles of attack along the span, following the sign of the normal force shown in Figure (12.15.a). As the rudder angle was increased, the propeller influence was less pronounced. From Figures (12.15.b) and (12.15.c) it is seen that the magnitude of the local force was generally increasing with the propeller loading and that it had a negative peak in the upper part of the propeller slipstream and a positive peak in the lower part at the tip for δ=0°, which was in agreement with the sign of the twist

angle or the local angle of attack illustrated in Figure (12.7.b). Figure (12.15.d) shows that if the tip was moved away from the propeller slipstream, by changing the aspect ratio of the rudder, the normal force over the part of the rudder outside the slipstream in the tip end would decrease to approximately the same level as in the region outside the slipstream at the root.

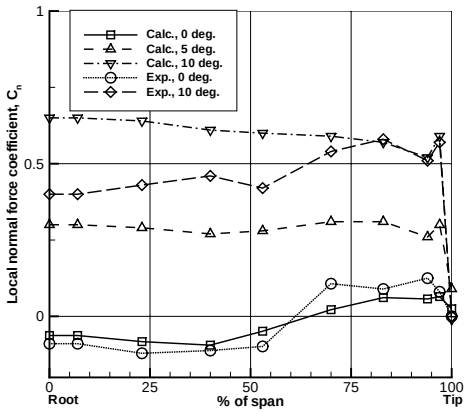

a. Λ=1.5, J=0.94 and C_{Th}=0.13

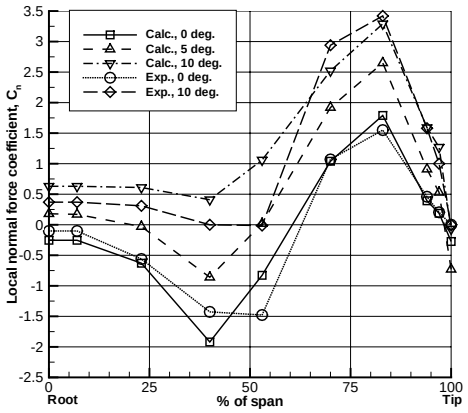

b. Λ=1.5, J=0.35 and C_{Th}=5.86

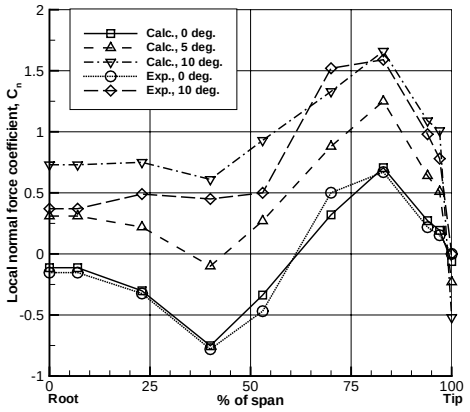

c. Λ=1.5, J=0.51 and C_{Th}=2.24

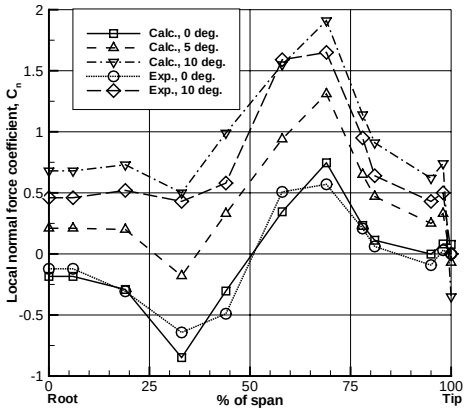

d. Λ=1.8, J=0.51 and C_{Th}=2.24

Figure (12.15) *Local normal force distributions for different rudder angles and propeller loads.*

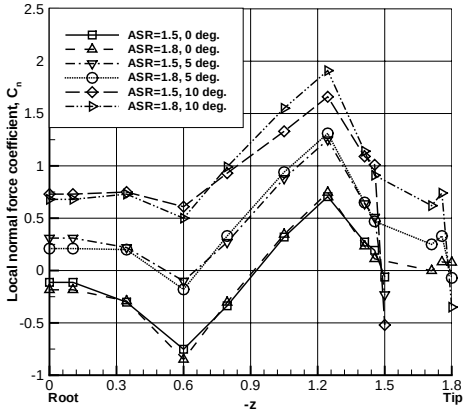

Figure (12.16) *Influence of Λ on C_n. J=0.51.*

As an illustration the actual effect of changing the aspect ratio the normal force distributions for the two rudders are plotted in Figure (12.16). From the figure it is seen that increasing Λ would decrease the normal force in the region from z=0 to z=-0.7 and increase it on the other side of z=-0.7. Moreover, it was found that the effect was most significant for the largest rudder angle.
With the results from Figure (12.14.b) in mind, it was found that the calculated lift coefficient was practically not affected by the aspect ratio. However, as seen from Figure (12.16) the local load was actually influenced by the aspect ratio, but the load probably changed in a way which lead to the same lift coefficient.
If Figure (12.15) is returned to where the experimental normal force data is also shown for the rudder angle equal to 0° and 10°, it is observed that the overall tendency was generally the same for the calculations and the experiments. However, concerning the quantitative agreement there are some differences. For the low aspect ratio rudder Figures (12.15.a) to (12.15.c) show that the calculated normal force for δ=10° was higher than the experimental force from the root to a position at approximately 75% of the span, while the agreement was better closer to the tip. For Λ=1.8 in Figure (12.15.d) the calculation was higher than the experiment over most of the rudder. At the rudder angle equal to zero, the tendency was not so clear. For Λ=1.5 and J=0.51 the agreement was fair, but for J=0.94 the absolute value of the normal force was generally underpredicted and for J=0.35 it was overpredicted. This was also the case for Λ=1.8. However, since the normal force distribution to a large degree determines the lift of the rudder, the overprediction of the normal force for δ=10° explains why the lift was over-predicted.

12.5 Summary

In the present chapter the flow around two different NACA0020 section rudders behind a propeller was calculated numerically by means of a RANS method including the Baldwin-Lomax turbulence model and a body force propeller model based on a circulation distribution proposed by Hough and Ordway (1965). The purpose of the work was to study the flow and the interaction between the rudder and the propeller, but also to gain experience of the numerical method, which could be used in the process of generating a complete numerical rudder-propeller-hull model. The computations covered 12 different conditions. For Λ=1.5 three rudder angles were considered at three different propeller loads, in order to study the influence of the propeller loading on the rudder performance, and for Λ=1.8 one propeller loading and three rudder angles were considered for investigation of the effect of changing the aspect ratio. A study of the field quantities was made for the two different rudders at the same rudder angle, δ=10°, and the same propeller loading corresponding to J=0.51 and C_{Th}=2.24, to provide some information about the flow pattern around the rudder. As regards the velocity field it was found that the propeller accelerated the flow axially, over the part of the rudder in the slipstream and thus reduced the extension of the zones of reversed flow at the trailing edge, which were observed in the free stream case. Besides, the rotation of the flow in the slipstream changed the local angle of attack along the rudder and enforced the cross flow around the tip. When the tip was removed from the slipstream by increasing the aspect ratio, the cross flow seemed to be a little weaker.

Seen in relation to the pressure on the rudder surface, the propeller appeared to increase considerably the magnitude of the pressure and suction peaks at the leading edge within the slipstream, resulting in a different pressure field compared to the free stream case. In addition to the study of the general features of the pressure field, the calculated pressure distributions along the cord of the rudder for eight different spanwise positions were extracted and compared with experimental distributions for the same positions. The comparison revealed that the computation and the experiment generally agreed qualitatively. At the *z*-stations in the tip region the agreement was fair, while some deviation was observed closer to the root.

Concerning the integral quantities, it was found that when the rudder was placed behind the propeller the lift would increase with increasing propeller loading. For the heavy and medium propeller loads the resulting lift was considerably higher than the free stream lift, while no significant change was observed for the light loading. This behavior was also reflected in the experimental lift characteristics, even though the numerical method predicted higher positive lift coefficients at $\delta=10°$ and larger negative lift for zero rudder angle than the experiment. As to the drag, the numerical method qualitatively predicted the same tendency of increasing and decreasing drag depending on the propeller loading as the experiment, but quantitatively it predicted the drag to be smaller than the experiment.

The effect of increasing the aspect ratio for the case of medium propeller loading was numerically found to be decreasing drag while the lift did not change significantly. For the experimental drag the tendency was the same, but for the lift, the experiment indicated a small decrease of the lift with increased aspect ratio. However, the behavior was different from the free stream case, where an increase of the aspect ratio led to an increase of the lift and no significant change in the drag.

The study of the local spanwise normal force distribution revealed that the presence of the propeller influenced the local rudder load significantly and in a way which reflected the influence of the local angle of attack along the rudder span caused by the swirl in the slipstream. Additionally, it was found that when the propeller load was increased the normal force increased accordingly. As to the influence of changing the aspect ratio, the normal force was slightly decreased in the root region and the upper part of the slipstream closest to the root and slightly increased in the part of the slipstream closest to the tip. When compared with the experimental normal force distribution, the calculation overpredicted the normal force over the portion of the rudder from the root to 75% of the span, while the agreement was better over the remaining 25% of the rudder span. This overprediction probably explains the overprediction of the lift mentioned earlier.

The reasons for the observed difference between calculation and experiment could be a number of different factors caused by assumptions and numerical topics. As regards assumptions, the following three assumptions were made in order to simplify the numerical rudder model: First, the no-slip effect of the wall was substituted by a symmetry condition. The missing wall effect could explain why the calculated pressure field and normal force distribution deviated in the root region. As to the free stream case the neglected wall mainly influenced the lift, but it is possible that the influence on the drag was larger when the propeller was included. Second, the propeller rig itself was neglected. This device could have some flow straightening effect, which consequently would be omitted. Third, the propeller forces were prescribed, meaning that the influence of the rudder flow on the propeller flow was neglected. Regarding the

numerical topics, the grid resolution was probably too coarse away from the rudder tip as a consequence of applying the grid from the free stream case. In addition to this, the C-grid topology prevented a completely smooth distribution of the body force. Finally, the isotropic algebraic turbulence model could be insufficient for the complicated flow problem.

In order to round off the chapter and relate the performance of the numerical method to the rudder-propeller-hull model, it is concluded that with the grid resolution applied to this study, the numerical method would be able to give a qualitative picture of the flow features in the rudder-propeller flow, so for this purpose it should be possible to apply the method to a rudder-propeller-hull model. Concerning the integral quantities, the method was also capable of giving a reasonable estimate of the lift, but to judge the quantitative performance, the grid should be changed in accordance with the experience gained in this chapter. Thus, the grid should be redistributed in order to resolve the slipstream flow better and allow a smoother distribution of the body force. Moreover, a grid study should be conducted and the calculation should be compared with data for an experimental condition similar to the numerical model.

This page is intentionally left blank.

Chapter 13

Calculation of Flow around Tanker Hull Form

13.1 Introduction

Following the stepwise procedure outlined in Chapter 9, the next step in the process of building the complete numerical rudder-propeller-hull model involved a calculation of the flow around the bare hull. This plays an important role since an accurate prediction of the flow around the hull and especially the stern is essential for a good prediction of the propeller and rudder performance, when they are working behind the ship. However, viscous calculations of the flow around tanker hull forms are generally complex to perform seen from a numerical point of view, because the numerical model must deal with a flow involving strong pressure gradients in the aft ship and strong curvature of the hull which results in regions of separated flow and converging and diverging streamlines. Besides, the relatively rapid change of the cross-sectional shape of the ship results in a relatively thick boundary layer around the aft ship and in strong vortices running along the hull and into the wake. All in all these factors make the modeling difficult and they lead to strong requirements of turbulence modeling, quality and size of the grid and computer capacity. By considering the bare hull it was intended to investigate the requirements of the grid in order to capture the flow features well and to study the performance of CFDSHIP-IOWA when applied to a tanker hull form with the Baldwin-Lomax turbulence model. But it was also intended to study the flow closer in order to get an idea of the flow field in which the rudder and the propeller are working.
With respect to comparison between numerical and experimental data for tanker flows only sparse information is available for the field quantities, because it is difficult and time-consuming to obtain this kind of data. For the integral quantities like the resistance it is different, because this quantity can be measured relatively easily by means of standard equipment in the towing tank. In the present case involving the tanker Esso Osaka the calculated resistance was compared with the model resistance obtained from a resistance test performed at the Danish Maritime Institute. Concerning the field quantities, it was not within the scope of this project to perform detailed field measurements. Therefore, to find out if the calculated results were reasonable, it was decided to look at the flow pattern for the HSVA and Mystery tankers and see if the tendencies in these flows were present in the simulation.

13.2 Considered Ship Condition

Most of the full-scale maneuvers for the Esso Osaka were performed at approach speeds in the range of 7 to 10 knots, so it was decided to consider a condition corresponding to a speed in this range. Since the effect of the free surface was neglected in the calculation, the final choice of a speed equal to 7 knots was made in order to consider a condition which would match this simplification as well as possible. Based on the length of the ship at the water line, the speed of 7 knots corresponded to a Froude number equal to 0.063. This Froude number was so small that it was assumed that the resistance would be dominated by viscous drag and form drag, which meant that the assumption about neglecting the free surface seemed reasonable.
Generally, it is difficult to perform CFD calculations for full-scale Reynolds numbers, which are of the order of 10^9, because it requires grids with millions of cells to resolve the flow properly in this case. Therefore, in order to avoid this problem and to avoid the effects of scaling the measured model resistance to full-scale resistance before the comparison with the calculation, the computation was performed at model scale Reynolds number, and the results were compared directly with the measured model resistance found in the towing tank. Based on scaling in accordance with Froude's law and a model scale of 1:43.4783, the speed of 7 knots corresponded to a model-scale Reynolds number equal to Re=3.609 million. The ship and the model particulars of the considered case are found in Appendix A.

13.3 Computational Grid

As for the previous CFD calculations the grid generation was also time-consuming in this case. Especially, because it was tried to generate a grid around the hull, which satisfied the requirement of a good description of the geometry and at the same time was partly prepared for inclusion of rudder and propeller.

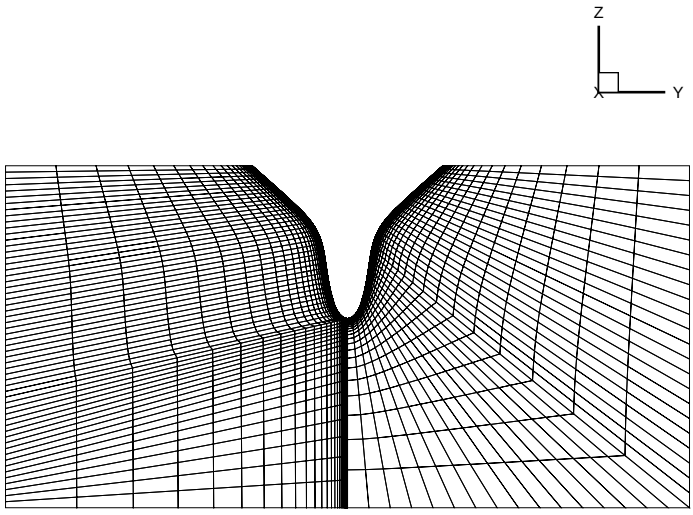

Figure (13.1) *Combined C (right) and H (left) grid.*

In order to generate a grid with these qualities it was natural to rely on the experience obtained from the previous CFD work. In summary, the results from Chapter 9 show that with a C-H-grid the computational cells were distorted in the aft ship due to the geometry of the ship, so that another type of grid had to be found. It was also realized that to include the rudder it was necessary to use the multi-block approach to create a "hole" in the hull grid, in which a block with a separate rudder grid could be inserted. Finally, the work on the rudder-propeller configuration presented in Chapter 12 showed that it was difficult to apply the propeller body force distribution to curved grid lines, because it was impossible to distribute the force smoothly. Therefore, the grid at the propeller plane needed to consist of plane layers of cells.
Based on these considerations, the idea behind the new hull grid structure was to apply the C-C-grid topology around the fore end and the C-H-topology along most of the hull as done in Chapter 9. To avoid the problem with poor grid quality around the stern caused by the C-H-topology it was decided to apply a grid technique proposed by Hochbaum (1998). The purpose of the method was to substitute the pure C-H-grid topology by a combination of blocks with C-H-topology in the outer domain and H-topology in the inner domain around the hull and in the wake behind the ship. Figure (13.1) illustrates the grids in blocks 3 and 5 at the *x*-position where the grid changed from C-H- to H-topology. At the position shown, the C-H-grid seemed to be as good as the H-grid, but as soon as the cross-sectional area was decreasing towards the stern the H-grid was better. The block numbers refer to the numbers used in Figures (13.2) and (13.3).

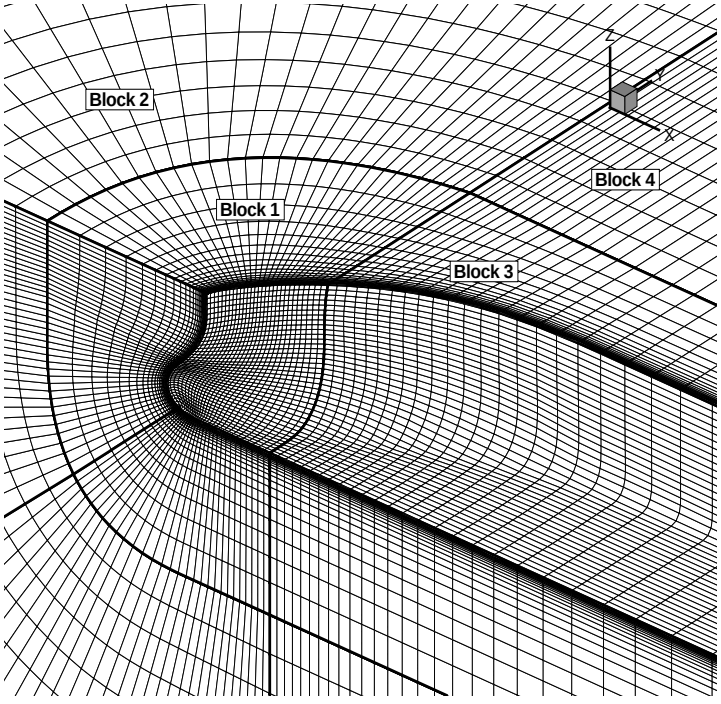

Figure (13.2) *Block structure of grid around fore body.*

With respect to the inclusion of the rudder and the propeller, the grid was constructed so that it was possible to change the grid locally in the region just behind the hull (block 7) without affecting the rest of the grid. The positions of the individual blocks in the overall structure around the bow and the stern are shown in Figures (13.2) and (13.3), respectively. Finally, the grid generation resulted in a topology consisting of 10 blocks

with a total number of 497250 computational cells. The overall grid structure is shown in Figure (13.4).

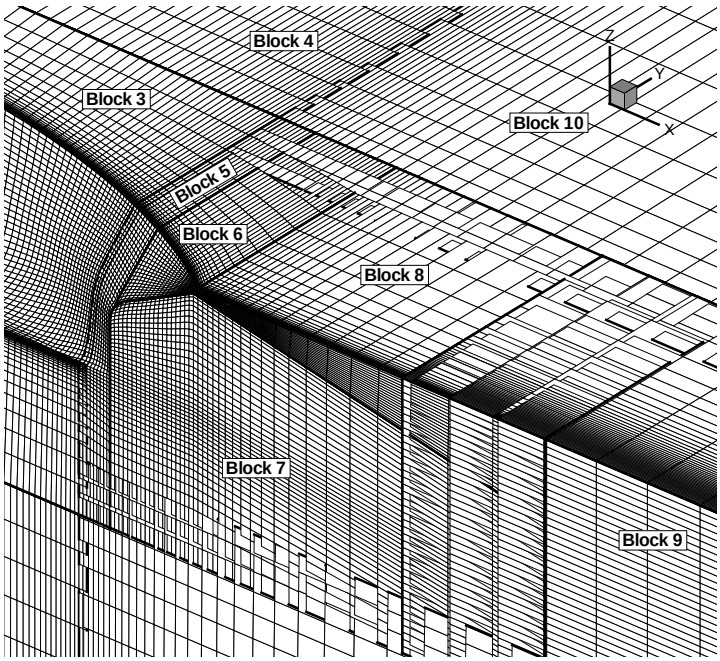

Figure (13.3) *Block structure of grid around aft body.*

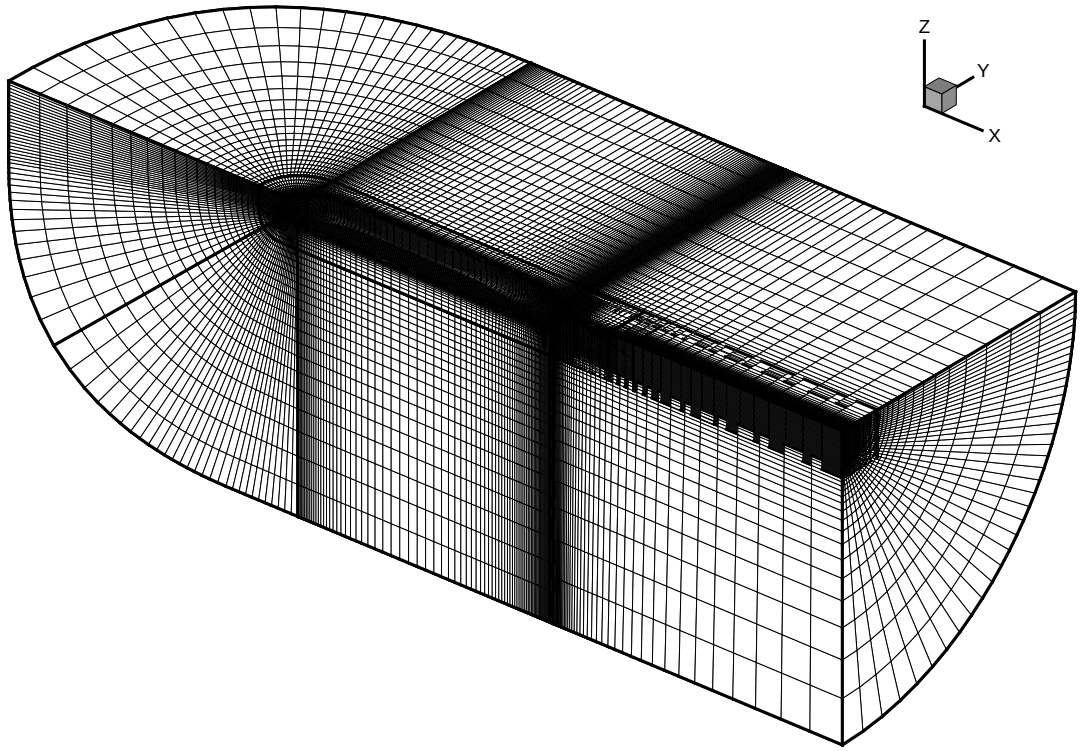

Figure (13.4) *Overall grid structure.*

Additional information about the grid type, the region which the grid modeled and the dimension is shown for each block in Table (13.1). The *i*, *j* and *k* values in Table (13.1) refer to the dimensions in the coordinate system for the non-orthogonal curvilinear coordinates ξ, η and ζ. The coordinates were oriented so that the ξ-direction ran

positively along the hull from bow to stern, the η-direction was perpendicular to the hull surface, positive away from the surface, and the ζ-direction ran positively in the girdwise direction from keel to water surface. The hull surface was modeled by 5320 cell faces and clustering was employed in the bow and stern in order to resolve the large velocity and pressure gradients in these regions. As in the previous CFD calculations the first layer of grid points next to the wall was placed at a non-dimensional wall distance of $y^+ < 1$, where $y^+ = yv^*/\nu$, and the wall friction velocity is defined by $v^* = \sqrt{\tau_W / \rho}$. In the physical domain this corresponded to a wall distance approximately equal to $y = 2 \cdot 10^{-6}$. The outer boundaries of the domain were placed one ship's length away from the hull in all directions.

Block No.	Topology	Region	ξ, η and ζ dimensions i_{max} x j_{max} x k_{max}
1	C-C	Hull	30x45x40
2	C-C	Outer domain	30x20x40
3	C-H	Hull	83x45x40
4	C-H	Outer domain	83x20x40
5	H	Hull, aft	10x45x59
6	H	Hull, aft	20x45x20
7	H	Wake	40x45x40
8	H	Wake	21x45x20
9	H	Wake	20x45x40
10	C-H	Outer domain	40x20x40

Table (13.1) *Type, position and size of the individual blocks.*

13.4 Boundary conditions

Seven different boundary conditions were applied to the block boundaries. They will just be mentioned briefly in this chapter, since they are described in more detail in Chapter 8, where the CFD method is described.

As said in the beginning of this chapter, the effect of the free surface was neglected, so instead of the free surface condition, a mirror image or symmetry condition was applied. On the boundaries representing the center plane of the domain an impermeable slip boundary condition was employed to enforce center plane symmetry on the flow. On the hull itself a no-slip condition was used, while a free stream velocity field was prescribed on the outer boundaries by means of a far field condition. Finally, an exit or zero-gradient condition was used on the boundaries of the domain behind the ship.

On the remaining block boundaries in the interior of the domain, the boundary data was exchanged by use of the two multi-block approaches. For neighboring blocks with the same boundary dimensions the data was exchanged by means of the patched multi-block condition, while the overlapping multi-block approach was applied in the cases where the blocks had different boundary dimensions and therefore had to be overlapped.

13.5 Results and Discussion

The results of the calculations consisted of two types of data: The field quantities, which provided detailed information about the flow features, and the integral quantities, which provided information about the overall influence of the flow on the ship. Below some field data is presented for a study of the flow pattern around the hull. As mentioned in the beginning of the chapter, no experimental field data was available for the Esso Osaka, so a quantitative comparison between calculations and experiments was not possible. Instead, it was tried to make a qualitative comparison with field data from other tanker flows to see if similar flow features were present. Concerning the integral quantities the calculated resistance was compared quantitatively with experimental data, measured in the present project. It should be noted that due to the time limitation of the project no verification with respect to numerical errors was performed for the tanker flow, and it was therefore not possible to give a level of validation for the code in this case. However, according to the convergence history of the residuals and the resistance shown in Figure (13.5), convergence was achieved for the considered solution. As seen in Figure (13.5.a) the residuals were decreasing throughout the solution to a level below 10^{-5}. This was also reflected in the resistance shown in Figure (13.5.b), since the oscillations of the solution were decaying throughout the solution.

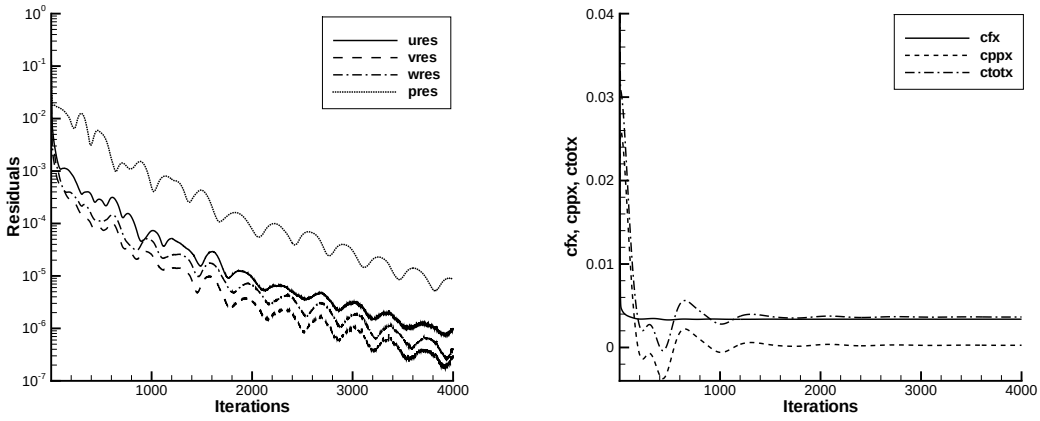

a. *b.*

Figure (13.5) *Convergence history. a. Residuals for u, v, w and p. b. Resistance: frictional* c_{fx}, *pressure* c_{ppx} *and total* c_{totx}.

13.5.1 Field Quantities

To obtain information about the flow pattern around the hull, the limiting streamlines were calculated and shown in Figure (13.6). It is seen from Figure (13.6.b) that when the fluid particles approached the upper part of the bow near the water surface, they flowed around the shoulders and followed a path along the side of the ship. If the particles approached the bow at a position deeper in the water, it is seen, that they were forced downwards below the hull along a path on the bottom of the ship. In the stern region the flow pattern was found to be much more complex than in the bow region, because the calculated streamlines revealed a complex pattern of regions with reversed flow and

diverging and converging streamlines, cf. Figure (13.6.a). When the streamlines on the side of the hull came close to the rear of the ship they were diverging at the saddle point C. Afterwards, the streamlines above C were continuing over the stern post towards the water surface, following the line of convergence at D, while the lines below C were running towards the keel following the line of convergence at B. However, before the latter streamlines reached the keel they were seen to meet the streamlines coming up from the bottom at the third line of converging streamlines at A. Aft of the two lines of converging streamlines B and D a zone of reversed flow was observed, but it was split into two regions at the saddle point C. In the upper region the streamlines were running towards the water surface, while below C the streamlines were running towards the keel.

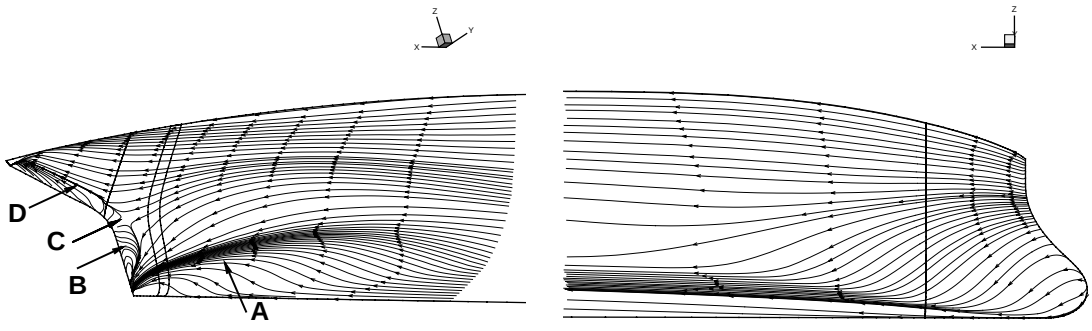

a. *b.*

Figure (13.6) *Limiting streamlines. a. Aft body. b. Fore body*

Since the flow pattern over the Esso Osaka has not been examined experimentally it is impossible to say whether the calculation was correct or not. However, results from experiments with the HSVA tanker and the Mystery tanker, found in Sotiropoulos and Patel (1995), showed flow features similar to those of the present calculation. For the HSVA tanker two lines of converging streamlines were observed at A and B as well as the saddle point at C and the zone of reversed flow at B. However, the line of converging streamlines at D was not observed, but this may be explained by the different hull forms in this region, because the HSVA tanker is U-shaped, while the Esso Osaka is V-shaped. For the Mystery tanker all the flow features shown in Figure (13.6.a) were present including the line at D. The presence of this line may be due to the fact that the Mystery tanker is V-shaped like the Esso Osaka in the considered region. Finally, the experiments with both tankers showed that the line of converging streamlines at B was S-shaped, which was not the case for the Esso Osaka according to Figure (13.6.a). The reason for this missing feature may be insufficiencies in the relatively simple Baldwin-Lomax turbulence model. However, based on these two experimental cases it was found that the calculated near-wall flow pattern looked reasonable from a qualitative point of view.

The next field quantity to be considered was the pressure distribution on the hull surface, which is important to predict correctly to be able to calculate the pressure related resistance. The calculated pressure distribution on the hull in the fore end of the ship is shown in Figure (13.7) where it is seen that at the bow a region with high pressure was present, which looks reasonable since the stagnation zone was located here. Aft of the stagnation region the pressure decreased at the shoulders of the ship and the presence of a low-pressure region at the bilge parallel to the keel was detected. By recalling the flow pattern from Figure (13.6.b) it is seen that this low-pressure region was caused the

streamlines to follow a path below the ship. Further down the hull the pressure was increasing again towards zero, which looked reasonable since the cross-sectional shape in this part of the hull was becoming constant.

Figure (13.7) *Pressure distribution on hull in the fore end of the ship.*

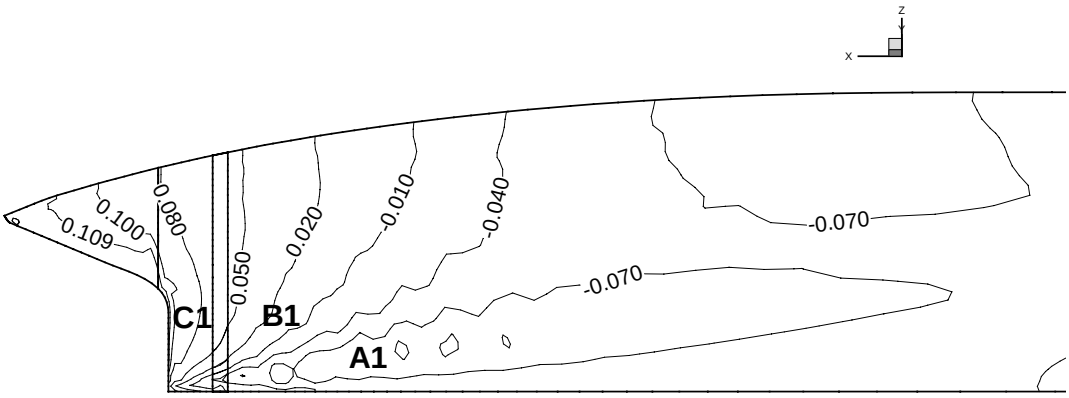

Figure (13.8) *Pressure distribution on hull in stern region.*

The calculated pressure distribution on the hull surface in the stern region is shown in Figure (13.8). It should be noted that a relatively large region (A1) of low pressure parallel to the keel was developed, which caused the streamlines to diverge outwards from the keel and move upwards as illustrated in Figure (13.6.a). Above the low-pressure region the pressure is seen to increase towards the rear of the hull, resulting in adverse pressure gradients in the x-direction. This was probably the cause of the reversed flow region at the propeller boss (C1), observed at B in Figure (13.6.a). Due to the high-pressure region (B1), the water next to the side of the hull flowed towards the low-pressure region parallel to the keel, where it met the previously mentioned upcoming flow at the line of converging streamlines denoted by A in Figure (13.6.a). A1,B1 and C1 refer to the regions in Figure (13.8). As in the case of the limiting streamlines, no experimental data was available for comparison, not even for the two other tankers mentioned earlier. Instead the calculated pressure distribution was compared with calculations for the HSVA tanker and the Mystery tanker. The calculations were performed by Sotiropoulos and Patel (ibid.), who applied two different turbulence models, namely a K-ε model and a Reynolds stress model. The comparison

revealed that the present calculation produced a pressure distribution which qualitatively showed the same features as the distributions for the two other tankers.
So far the results have been concentrated on the near-wall flow features, so in order to investigate the features of the flow around the hull, and especially in the near wake of the hull where the propeller and the rudder are usually located, the axial velocity contours and the cross flow vectors were calculated at the propeller plane.

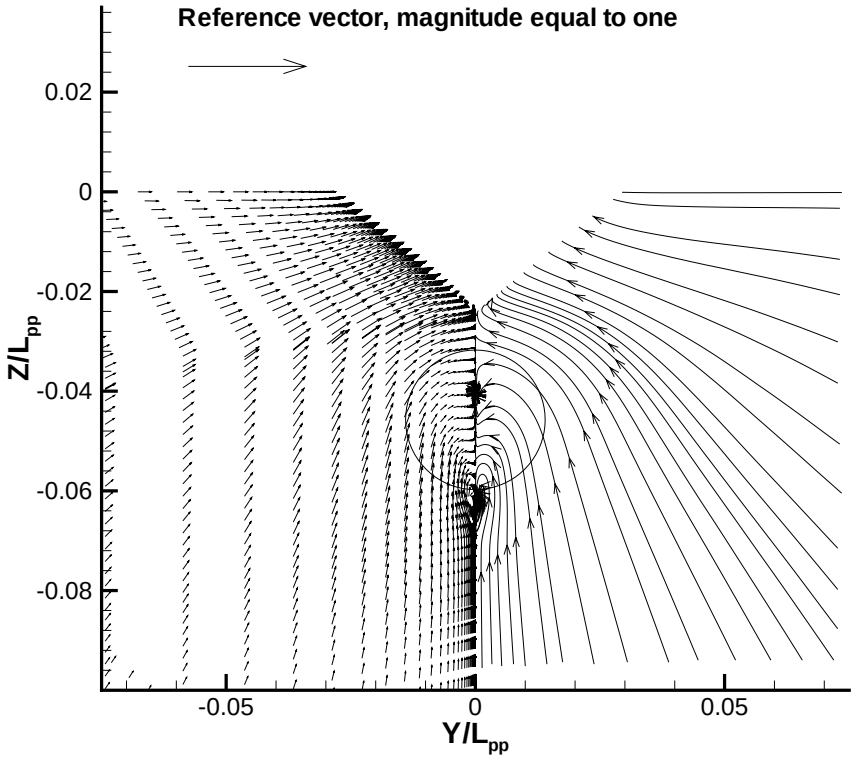

Figure (13.9) *Cross flow vectors at propeller plane, $X/L_{pp}=0.984$.*

Figures (13.9) and (13.10) show the calculated properties of the three velocity components *u, v* and *w* at the propeller plane. The two cross flow components *v* and w are plotted together as cross flow vectors as illustrated in Figure (13.9). From the plot of these vectors and the stream traces, it is seen that there is a vortex structure close to the center plane at the propeller position. Compared with the experimental cross flow features of the HSVA and Mystery tankers found in Sotiropoulos and Patel (ibid.), the calculation generally shows a flow pattern which is qualitatively similar to the two others. This also includes presence of the vortex structure in the wake, although the calculated vortex seems to be less pronounced and positioned closer to the keel than in the other cases.
In order to study the last velocity component *u*, the axial velocity contours are plotted in Figure (13.10). The figure shows that, due to the thick boundary layer in the stern region the near-wake flow of the ship is strongly retarded over a relatively large region. This information is important from a propulsive point of view since the performance of the propeller is determined by the inflow velocity field. By illustrating the propeller disk by the circle in Figure (13.10) it is seen that the axial velocity is actually approximately half of the ship speed over a relatively large portion of the disk.

When the calculated contours were compared with experimental data for the other two tanker flows found in Sotiropoulos and Patel (ibid.), it was found that the calculated bulging of the outer contours was also present in the experiments. However, in the inner low-velocity region close to the center plane, the experimental flow was somewhat more complicated.

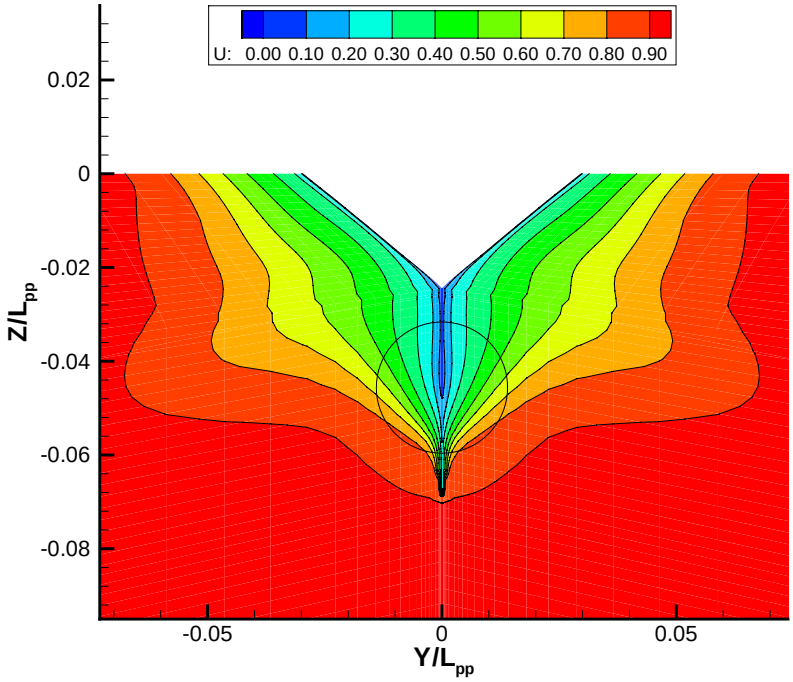

Figure (13.10) *Axial velocity contours at propeller plane, $X/L_{pp}=0.984$.*

Instead of the smooth contours found in the calculation, the experiment showed hook-shaped contours originating from the disturbance introduced by the vortex discussed previously in connection with Figure (13.9). Since the calculated vortex seemed to be relatively weak, the influence on the axial velocity contours was consequently not strong enough to result in the hook-shaped contours in the low velocity region close to the center plane. However, since the considered results were found for three different ships it was impossible to say if the calculated contours were correct or not, but it may be that the calculated vortex was predicted to be too weak, because the algebraic Baldwin-Lomax turbulence model was not able to model the flow or because the grid in the wake was too coarse to resolve the flow properly. With regard to the limitation of the turbulence model, Shiotani and Kodama (1998) studied the influence of using different versions of the Baldwin-Lomax turbulence model (with and without pressure correction) on the flow around the stern of the SR196C tanker hull form. They found that when the Baldwin-Lomax turbulence model was applied in its basic form, i.e. without pressure gradient correction, it predicted the bulging of the outer contours, but not the hook-shape of the center plane contours, which was predicted by the experiments. This was in agreement with the present results, obtained by the Baldwin-Lomax model without pressure correction. Furthermore, it indicated that the calculated flow probably showed the features which were possible to capture with a turbulence model of the kind applied in the present case. The axial velocity contours were only shown at one *x*-position in the

wake in this chapter, but plots for 12 additional positions along the complete hull can be found in Appendix E.
Finally, it should be mentioned that from a qualitative point of view the calculated flow features were generally in agreement with the features observed for other full form ships. However, it must still be kept in mind that the calculations should be compared with experimental data for the ship concerned in order to investigate the quantitative correctness of the simulated field quantities. In the present project the comparison will be based on integral quantities, as described in the following section.

13.5.2 Integral Quantities

If the description of the mathematical model used for maneuvering simulation is recalled, it was shown that the integral quantities or the hydrodynamic forces play an important role in the simulation, since they are used as input to the simulator when the equations of motion are solved for the motion of the ship. For the ship sailing straight ahead in calm water the important quantity is the resistance. Traditionally, this quantity is assumed to consist of contributions from the wave resistance, the frictional resistance and the form resistance. In model scale it can be expressed as

$$C_T = C_R + (1+k)\,C_f \tag{13.1}$$

In this expression C_T is the total resistance coefficient of the model defined as

$$C_T = \frac{R}{1/2\,\rho\, S_m\, U^2} \tag{13.2}$$

where R is the model resistance, ρ the density of the water, S_m the wetted surface area of the model and U the model speed. C_f is the frictional resistance coefficient of the model and C_R is the residual resistance coefficient due to waves, and k is the form factor accounting for the form resistance of the ship. Usually, k lies in the range from 0 to 0.25. Seen in relation to a traditional resistance test in the towing tank, the only quantity in (13.1) which is measured directly is C_T.
The frictional resistance coefficient C_f is estimated by means of the ITTC 1957 friction line:

$$C_f^m = \frac{0.075}{(\log_{10}(Re)-2)^2} \tag{13.3}$$

where Re is the model Reynolds number.
The form factor k is estimated from C_T and C_f values which are found at Froude numbers around 0.1. The idea is to plot C_T/C_f at low speeds as a function of Fn^4/C_f and assume that the curve is approximately a straight line. The form factor is then found from the C_T/C_f ratio at the value corresponding to Fn=0. Figure (13.11) shows the plot

used for determination of the form factor for the Esso Osaka. Finally, when C_T, C_f and k are known, C_R is calculated from (13.1).

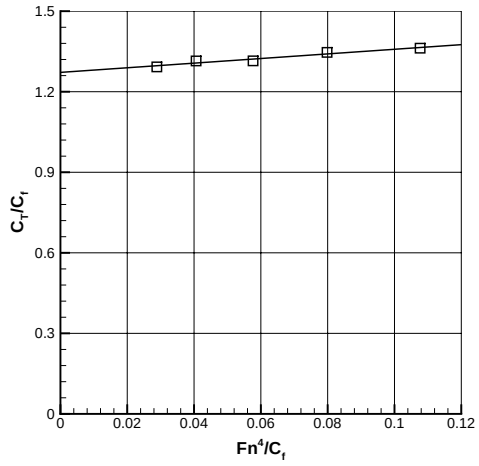

Figure (13.11) *Determination of form factor.*

Numerical calculation of the hydrodynamic forces is done by integration of the pressure-induced normal stresses and the frictional shear stresses over the wetted surface. The axial component of these forces is the resistance, which in non-dimensionalized form can be written as

$$C_{totx} = C_{ppx} + C_{fx} \tag{13.4}$$

where C_{totx} is the total resistance coefficient, C_{ppx} is the resistance coefficient from the pressure and C_{fx} is the frictional resistance coefficient.

Since the free surface was neglected in the present calculation, C_{ppx} in (13.4) was assumed to express the form resistance of the model, and it was therefore tried to use it for calculation of the form factor *k*. By neglecting the free surface the residual resistance C_R in (13.1) was assumed to be equal to zero so that the expression could be written as

$$C_T = k\,C_f + C_f \tag{13.5}$$

and by comparison between (13.4) and (13.5) it was found that *k* could be expressed as

$$k = \frac{C_{ppx}}{C_{fx}} \tag{13.6}$$

In order to investigate the performance of the code, the calculated resistance coefficient C_{totx} and the form factor *k* were compared with experimental data, while the calculated frictional resistance C_{fx} was compared with the ITTC 1957 friction line. The results of the calculation and the resistance test are shown in Table (13.2). The comparison between the results in the table reveals that the numerically computed frictional

resistance coefficient is in fair agreement with the friction line. It is somewhat more difficult to draw conclusions about the remaining components of the forces, since the experiment included a contribution to the resistance from the waves. However, the total resistance coefficient C_T found in the towing tank was observed to be higher than the calculated resistance coefficient, which seemed to be reasonable since the experimental C_T included the wave resistance. After splitting up the experimental resistance in order to separate the form resistance and the wave resistance by means of the form factor method, the wave resistance appeared to be small seen in relation to the total resistance coefficient. This was reasonable, since the ship was considered at a relatively low Froude number. Concerning the form resistance expressed by the form factor, the calculation underpredicted the form factor compared to the experiment.

Data source	$C_f \cdot 10^3$	$C_p \cdot 10^3$	$C_R \cdot 10^3$	$C_T \cdot 10^3$	Form factor $(1+k)$
Calculation	3.451	0.281	0.000	3.733	1.08
ITTC 1957	3.609	-----	-----	-----	-----
Experiment	-----	-----	0.09	4.67	1.27

Table (13.2) *Comparison between, calculation, ITTC friction line and experiment.*

A few comments should be given on the results in Table (13.2). Apparently, the pressure contribution caused most of the deviation between the calculated and the experimental total resistance. It was difficult to say if the two pressure forces could be compared directly because of the difference between the numerical and the experimental models introduced by the omission of the free surface in the numerical model. However, at the considered model speed the free surface effect was probably of minor importance, so that it could not explain the total difference. Another factor, probably more important, was the applied grid resolution, which was not investigated in order to study the grid sensitivity. Since the pressure resistance is based on a balance between the pressure forces acting on the bow and the pressure forces acting on the stern, almost outbalancing each other, the numerical pressure resistance is relatively sensitive to insufficient grid resolution. This could explain some of the difference. A third and also important factor concerned the turbulence model as mentioned earlier. It is most likely that the applied isotropic algebraic turbulence model, which generally performs well for slender ships, was not capable of modeling the complex three-dimensional flow around the aft part of a full form ship. The assumption about isotropic turbulence was probably not valid in this type of flow. Moreover, the omission of a pressure gradient correction, may also have caused some of the problems, since the present flow to a large degree involves this phenomenon. All together, these factors most likely influenced the flow field and consequently also the pressure field, resulting in inaccurate prediction of the pressure itself or for instance the extension of the separation zones in the aft ship. This would of course influence the resistance. For further investigation of the problem the method should be verified and validated at both integral and field level to be able to quantify the numerical error and modeling error originating from the turbulence model, and if it turns out that the modeling error is large, a more complex turbulence model should be tried to reduce the error.

13.6 Summary

In the present chapter the flow around the tanker Esso Osaka was calculated in order to study the flow, gain experience of the grid topology and investigate the performance of the CFD code in relation to full form ships. The computation was performed on a computational grid built of 10 blocks and consisting of a total number of cells equal to 497250. The grid was generated so that future inclusion of the rudder was possible by substitution of a grid block in the wake by a grid including the rudder grid. The computation was performed on the assumption that the free surface could be neglected and a mirror image was applied instead. Finally, the turbulence was modeled by the algebraic Baldwin-Lomax turbulence model.

The numerical results were studied on the basis of the limiting streamlines and the pressure distribution on the hull surface and the axial velocity contours and the cross flow vectors at the propeller plane. A complex flow pattern including converging and diverging streamlines, adverse pressure gradients and vortex structures was revealed. On the basis of the field quantities for other tanker hull forms, it was found that the present results were generally in qualitative agreement with these except in the inner wake close to the center line. In this region it was shown that the numerical method did not predict some of the expected near-wake flow features in the velocity field close to the center plane, which could be due to insufficient grid resolution in the region and to the applied algebraic Baldwin-Lomax turbulence model.

The resistance was compared with experimental data measured in the towing tank. The comparison showed that the total calculated resistance was approximately 20% lower than the experimental value and that the difference mainly was originated from the pressure or the form resistance. Three possible reasons for the observed deviation between experiment and calculation were suggested. The first was omission of the free surface in the calculation, the second insufficient grid resolution and the third insufficiency of the applied algebraic turbulence model.

Generally, it appeared to be possible to use the numerical results for a qualitative visualization of the flow pattern around the hull. But in order to use the results quantitatively and perhaps improve the method, the errors and uncertainties introduced by the three factors mentioned above should be quantified. Thus, the numerical method should be verified to estimate the numerical error and uncertainty introduced by the grid and validated to quantify the modeling error introduced by turbulence modeling and omission of the free surface.

Chapter 14

Conclusion and Recommendations for Future Work

14.1 Conclusion

In recent years attention has increasingly been focused on the requirements of the education of the officers sailing the ships and of the maneuverability of the ships in order to increase the safety at sea. This has of course increased the interest in the numerical maneuvering simulators, which are a strong tool for investigation of the maneuverability of the ship and for training of the crew members. At the same time it has also resulted in stronger requirements of the quality, accuracy and reliability of the methods. So far, the simulators are doing well today, but there are still areas where additional knowledge could be useful to improve the models. One of these areas is the interaction between the rudder, propeller and hull, which plays an important role in good modeling of the maneuvering problem. Hence, the objective of the project was to study the flow phenomena related to the rudder, propeller and hull flows by means of a numerical method. Since application of numerical simulations of the complex rudder, propeller and hull flow is rare, the project should also give information about the future possibilities of using numerical tools in maneuvering related flow problems.

14.1.1 Existing Maneuvering Models and Rudder-propeller-hull Interaction Models

The conclusion of studies of the different kinds of maneuvering simulation applied today is that the state of the art within methods for maneuvering simulation covers the full mission simulators, based on numerical solution of the equations of motion in conjunction with a comprehensive set of experimental hydrodynamic data. This data is mainly determined by means of captive model testing techniques like the planar motion mechanism (PMM). Concerning the interaction effects between the rudder, propeller and hull, they were found to be considered at the integral level, and they were either accounted for in the non-dimensionalization of the forces or by data directly derived from the measured forces. The interaction could be studied in two ways: The first

approach consists of systematic experimental parameter studies of the forces and the second of a detailed numerical study of the flow patterns considered to gain a better understanding of the complex flow phenomena.
To exemplify the first approach and to provide an experimental basis for the numerical work a full PMM test program was designed and a PMM test was carried out in the towing tank with a model of the tanker Esso Osaka. Results from the test were used to illustrate some of the basic interaction effects. The examples revealed relatively large variations in the parameters due to the interaction, but since they were derived at the integral level it was found that this approach did not provide information to be used as an explanation of the real cause of the interaction.

14.1.2 Application of Numerical Tools to Maneuvering Related Flow Problems

After the study of the maneuvering model and the experimental methods used for generation of hydrodynamic input data to the simulator, the remaining work focused on numerical investigations of the flow. Since the objective was to study the local flow features, a method was needed which included real fluid effects. Therefore, all the numerical calculations were performed by the CFD code CFDSHIP-IOWA, a so-called RANS code based on solution of the Reynolds-averaged Navier-Stokes equations. The turbulence was modeled by the isotropic algebraic Baldwin-Lomax turbulence model, while the effect of the propeller was given by a prescribed body force distribution calculated from the Hough-Ordway model.

On the basis of the initial attempts to make the full rudder-propeller-hull model in one step, it was concluded that due to the complexity and size of the model and to the need for knowledge of suitable grid topologies, a complete model should be generated in more than one step. A new procedure was then proposed and it covered: 1) 2-D rudder profile, 2) 3-D rudder in free stream, 3) 3-D rudder behind a propeller, 4) bare hull, 5) hull with rudder and 6) hull with rudder and propeller. However, due to the time limitations of the project it was not possible to finish items 5 and 6.

Concerning the 2-D rudder profile case, the flow around an NACA0012 profile was calculated for different angles of attack and different Reynolds numbers. The computations were compared with experimental data, and it was found that fair agreement could be obtained if the experiments were performed with leading edge roughness. By using leading roughness in the experiment the transition in the boundary layer was forced to take place relatively close to the leading edge. This resulted in fully turbulent boundary layer flow over most of the profile, which was in agreement with the numerical model which is based on the assumption that the boundary layer is fully turbulent from leading to trailing edge.
The best results seemed to be obtained for angles of attack smaller than 9°, where both lift and drag coefficients were in fair agreement with the experimental data. By taking the limitations of the numerical method into account, it was concluded that with the applied grid resolution the code performed well for the 2-D rudder profile case.

In the case of the rudder in free stream, the flow was calculated around two NACA0020 rudders with different aspect ratios at different rudder angles and a Reynolds number equal to 0.4 million. When compared with experimental and empirical data, the CFD code generally showed a tendency to overpredict the lift coefficient by 2 to 16 percent. The largest deviation was detected for the experimental data, but it was partly caused by differences between the boundary conditions for the numerical model and the experimental model. As to the drag, the calculations were generally in fair agreement with the empirical expression, while the agreement with the experiments to a large degree seemed to depend on the applied leading edge roughness. The effect of changing the aspect ratio was also reflected in the numerical results, which showed that if the aspect ratio was increased, the lift curve slope would increase accordingly, while the drag coefficient was relatively unaffected. With regard to the field quantities, the code was generally capable of capturing the gross features of the rudder flow with respect to reversed flow and the vortex developing at the tip of the rudder. The conclusion to be drawn from the results from the rudder in free stream is that as long as the considered flow problems involved boundary layer flows close to being fully turbulent, the performance of the numerical steady state method seemed reasonable for rudders in free stream at rudder angles in the range of 0 to 10 degrees. Since the boundary layer flow around most ship rudders is turbulent due to the surface roughness, it should therefore be possible to use the present method for prediction of the rudder performance in relation maneuvering problems. In order to improve the results for cases involving partly laminar boundary layer flows, a transition model should be implemented either by prescribing a line of transition or by using a model which describes the problem mathematically.

In the case of the rudder behind the propeller, the flow around the same two rudders as in the free stream case was calculated numerically for 12 different combinations of rudder angles and propeller loads. The purpose of the work was to study the flow and the interaction between the rudder and the propeller, but also to gain experience of the numerical method, which could be used in the process of building the complete numerical rudder-propeller-hull model.

As regards to the interaction effects between the rudder and the propeller the study showed that the presence of the propeller increased the axial velocity over the portion of the rudder placed in the slipstream, and that it introduced a swirl in the flow which changed the local angle of attack over the rudder. Consequently, the magnitude of the pressure and of the suction peaks on the rudder surface was increased over the part of the rudder in the slipstream, resulting in increased lift compared to the free stream rudder. The propeller also influence the strength of the cross flow around the tip of the rudder depending on the rudder angle. In the present case for positive rudder angles the propeller enforced the cross flow around the rudder tip, even though the effect was reduced when the aspect ratio was increased and the tip was moved away from the slipstream. In the case where a negative rudder angle were considered the propeller reduced the cross flow. However, all these flow features were actually in agreement with the expected behavior, which indicated that the method was capable of capturing the important features of the flow. As for the forces on the rudder, the increased aspect ratio caused the drag to decrease, while the lift was relatively unaffected.

In order to relate the performance of the numerical method to the rudder-propeller-hull model, it was concluded that with the grid resolution applied in this study, the numerical method would give a qualitative picture of the flow features of the rudder-propeller

flow, so for this purpose it should be possible to apply the method to a rudder-propeller-hull model. In the case of the integral quantities the method was also capable of giving a reasonable estimate of the lift, while the drag was predicted too low. However, for a judgment of the quantitative performance, the grid should be changed in accordance with the experience obtained in the work. Thus, the grid should be redistributed to resolve the slipstream flow better and allow a smoother distribution of the body force. In addition to this, a grid study should be conducted and the calculation should be compared with data for an experimental condition similar to the numerical model.

Concerning the bare hull condition, the flow around the tanker Esso Osaka was calculated to study the flow, gain experience of the grid topology and investigate the performance of the CFD code in relation to full form ships. The computation was performed on the assumption that the free surface could be neglected and a mirror image applied instead. The numerical results were studied on the basis of the limiting streamlines and the pressure distribution on the hull surface and the axial velocity contours and the cross flow vectors at the propeller plane. By comparing the calculated results with other experimentally visualized tanker flows, it was found that the numerical method was generally in qualitative agreement with these. However, in the inner wake close to the center line the famous hook shape of the axial velocity contours was lacking, which was probably caused by the Baldwin-Lomax turbulence model. With respect to the resistance a comparison with experimental data showed that the calculated resistance was lower than the experimental ditto, which was expected since the free surface was neglected in the calculation and the contribution to the resistance from the waves therefore lacked. However, after splitting the resistance into wave, frictional and form or pressure contributions it was found that the largest deviation between calculation and experiment originated from the pressure resistance represented by the form factor. The relatively large deviation could be explained by the grid sensitivity of the solution and by the simple algebraic Baldwin Lomax turbulence model, which was probably incapable of modeling the flow field in the stern region of the full form ship, where a correct prediction of the pressure field is essential for a correct resistance calculation. It should be kept in mind that the numerical method was not verified to estimate the numerical error or uncertainty introduced by the applied grid, so it was not possible to validate the calculation and thus quantify the modeling error introduced by turbulence modeling and omission of the free surface. The conclusion from the bare hull case was that for the purpose of investigation of the flow pattern around the hull, the numerical method was able to capture the overall features of the flow, while for the purpose of calculation of the integral quantities a verification and validation had to be made for a judgment of the quantitative correctness of the calculation.

To round off the conclusion a final comment must be made on the future application of the numerical method. The possibility of applying viscous CFD methods to calculation of maneuvering related flow problems seems to have a potential in the future, even though a full rudder-propeller-hull model may consist of around two millions computational cells and the method is time-consuming. The method will not be able to compete with the experimental methods with respect to generation of the large amounts of integral quantities, i.e. hydrodynamic data to the simulator. It may be that the method can produce quantitative, accurate data, but this requires additional studies with respect to verification and validation. However, the method seems to be able to capture the

gross features of the considered flows. Thus, the viscous CFD method may be a good tool for visualization of the flow, which can be useful in order to understand the complex rudder-propeller-hull flow problems and perhaps improve the mathematical maneuvering models.

14.2 Recommendations for Future Work

Based on the experience obtained in the present work, the following subjects should be considered in order to continue the work and improve the method.

- The grid for the rudder-propeller configuration should be redistributed in the span-wise direction to resolve the slipstream flow better and the model should be verified and validated.

- Concerning the bare hull model, the uncertainty of the experimental data should be estimated and the numerical model should be verified and validated to estimate the numerical uncertainty and the error originating from the omission of the free surface and the application of the Baldwin-Lomax turbulence model.

- Based on the experience gained in the present work, the proposed stepwise procedure for generation of the combined rudder-propeller-hull model should be completed, i.e. the initiated work on the combined hull and rudder model should be continued and the propeller should be included. The final model should be verified and a validation on the basis of experimental data, for which the experimental uncertainties are estimated, should be performed

- Experimental field quantities should be generated for the ship with rudder and propeller. The measurements should include assessment of the experimental uncertainties in order to use the data for validation of the numerical ruder, propeller and hull model.

- Relatively small rudder angles in the range from 0 to 15 degrees were considered in the present work, but the possibility of performing calculations for larger rudder angles should be investigated, even though this may require numerical solutions which are unsteady and therefore have to be calculated accurately with regard to time.

- The algebraic Baldwin Lomax turbulence model is probably sufficient in the grid generation phase, but more complex turbulence models should be tried.

- The overlapping multi-block grid approach, required for the flexibility of the grid generation, could be improved. As it is now, a lot of manual work is needed to generate the block structure, but this work could be reduced by adopting a full Chimera approach. Moreover, the method for identification of orphaned grid points should be improved.

- Since the prescribed body force propeller lacks the influence of the rudder and hull flow on the propeller, an interactive solution between the RANS code and a propeller performance code should be implemented.

- Concerning the treatment of laminar/turbulent boundary layer flow conditions which occurred in connection with the rudder calculations in model scale, the problem could probably be reduced by implementation of a transition model.

- As regards the quickly expanding size of the complete numerical rudder-propeller-hull model, the computations should be performed by means of parallel processing so that the large numerical problem can be solved in a reasonable time.

Bibliography

Abbott, I. H. and Doenhoff, A. E. (1959)
Theory of Wing Sections, Dower Publications Inc., New York, 1959.

Abkowitz, M. A. (1964)
Lectures on Ship Hydrodynamics - Steering and Manoeuvrability, Report No. Hy-5, Hydro- og Aerodynamisk Laboratorium, Lyngby, 1964.

Brix J., ed. (1993)
Manoeuvring Technical Manual, Seehafen Verlag GmbH, Hamburg, 1993.

Chislett, M.S. (1996)
A generalized math model for manoeuvring, *Proceedings of MARSIM '96,* International Conference on Marine Simulation and Ship Manoeuvrability, Balkema, Rotterdam, 1996, pp. 593-606.

Cebeci, T. and Smith, A. M. O. (1974)
Analysis of Turbulent Boundary Layers, Academic Press, London, 1974.

Chau, Shiu-Wu (1998)
Computation of Rudder Force and Moment in Uniform Flow, *Schiffstechnik*, Bd. 45, 1998/Ship Technology Research, Vol. 45, 1998.

Crane, L. C. (1979)
Maneuvering Trials of a 278 000-DWT Tanker in Shallow and Deep Waters, *SNAME Transactions,* Vol. 87, 1979, pp. 251-283.

Crane, L. C., Eda, H. and Landsburg, A. (1989)
Controllability, *Principles of Naval Architecture*, Vol. 3, 1989.

Ferziger, J. H. and Peric, M. (1996)
Computational methods for fluid dynamics, Springer-Verlag Berlin Heidelberg, 1996.

Fujino, M. (1996)
Prediction of ship manoeuvrability: State of the art, *Proceedings of MARSIM '96,* International Conference on Marine Simulation and Ship Manoeuvrability, Balkema, Rotterdam, 1996, pp. 371-387.

Guilmineau, E., Piquet, J. and Queutey, P. (1997)
Two-dimensional Turbulent Viscous Flow Simulation Past Airfoils at Fixed Incidence, *Computers & Fluids*, Vol. 26, No. 2, 1997, pp.135-162.

Gutsche, F. (1955)
Die Induktion der axialen Strahlzusatzgeschwindigkeit in der Umgebung der Schraubenebene, *Schiffstechnik*, No. 12/13, 1955.

Gronarz, Andreas (1993)
A Mathematical Model for Manoeuvring Simulation on Shallow Water, *Proceedings of MARSIM '93*, International Conference on Marine Simulation and Ship Manoeuvrability, St. John's, Canada, 1993, pp. 143-152.

Harvald, Sv. Aa. (1976)
Wake and Thrust Deduction at Extreme Propeller Loadings for Ship Running in Shallow Water, The Technical University of Denmark, April 1976.

Harvald, Sv. Aa. (1967)
Wake and Thrust Deduction at Extreme Propeller Loadings, *SSPA publication* No. 61, 1967.

Hearn Grant, E. and Clarke, David (1993)
Manoeuvring of Ships and Estimation Schemes (Moses): The Influence of Vortices on the Calculation of Hull Derivatives, *Proceedings of MARSIM '93*, International Conference on Marine Simulation and Ship Manoeuvrability, St. John's, Canada, 1993, pp. 171-178.

Hochbaum, A. C. (1998)
Computation of the Turbulent Flow around a Ship Model in Steady Turn and in Steady Oblique Motion, *Twenty-Second Symposium on Naval Hydrodynamics, August 9-14, Preprints*, Washington, D.C, 1998, pp. 198-213.

Hooft, J.P. and Quadvlieg, F. H. H. A. (1996)
Non-linear hydrodynamic hull forces derived from segmented model tests, *Proceedings of MARSIM '96*, International Conference on Marine Simulation and Ship Manoeuvrability, Balkema, Rotterdam, 1996, pp. 399-409.

Hooft, J. P. and Nienhuis, U. (1994)
The Prediction of the Ship's Maneuverability in the Design Stage, *SNAME Transactions*, Vol. 102, 1994, pp. 419-445.

Hough, G. R. and Ordway, D. E. (1965)
The Generalized Actuator Disc, *Developments in Theoretical and Applied Mechanics*, Vol. 2, Pergamon Press, Atlanta, Ga., 1965, pp. 317-336.

Hörner, S. F. (1965)
Fluid-dynamic drag, 1965.

HSVA (1986)
Untersuchung zur Korrelation von Manövrierversuchen bei völligen Schiffen, *HSVA Report* 31/86, 1986.

Ishiguro, T., Tanaka, S. and Yoshimura, Y. (1996)
A study on the accuracy of the recent prediction technique of ship's manoeuvrability at early design stage, *Proceedings of MARSIM '96*, International Conference on Marine Simulation and Ship Manoeuvrability, Balkema, Rotterdam, 1996, pp. 547-561.

Ichikawa, M. (1995)
Propeller-rudder interaction, m*aster thesis* from Department of Global Architecture, Osaka University, Japan, 1995.

Ishikawa, S. (1994)
Application of CFD to Estimation of Ship's Viscous Resistance -A Series of Full Hull Forms, *Transactions of West Japan Society of Naval Architechts*, No. 87, 1994, pp. 81-92.

ITTC's Manoeuvrability Committee (1996)
Final Report and Recommendations to the 21st ITTC, 1996, pp. 378-381.

ITTC (1999)
Proceedings of 22nd International Towing Tank Conference, Vol. 2, 1999, pp. 498-505.

Jensen, A.G. and Martinussen, K. (1987)
Assessment of ship manoeuvring, *Nordic Seakeeping Project*, nstm, DMI, 1987.

Jensen, P. S. (1993)
DEN-Mark1 - An Innovative and Flexible Mathematical Model for Simulation of Ship Manoeuvrability, *Proceedings of MARSIM '93*, International Conference on Marine Simulation and Ship Manoeuvrability, St. John's, Canada, 1993, pp. 219-227.

Johansen, J. and Sørensen, J. N. (1998)
Prediction of Laminar/Turbulent Transition in Airfoil Flows, Paper 98-0702 at the *AIAA* 36th Aerospace Sciences Meeting & Exhibit, Reno, NV, January 12-15, 1998.

Key P., Rhee (1993)
Evaluation of Hydrodynamic Derivatives from PMM Test by System Identification, *Proceedings of MARSIM '93*, International Conference on Marine Simulation and Ship Manoeuvrability, St. John's, Canada, 1993, pp. 489-497.

Kijima, K., Asai, S. and Yamakami N. (1986)
Prediction of manoeuvrability in deep water, *Bulletin of the Society of Naval Architects of Japan*, No. 668, February 1986.

Kijima, K., Nakari, Y., Katsuno, T. and Furukawa, Y. (1990)
On the manoeuvering performance of a ship with the parameter of loading condition, *Journal* of the Society of Naval Architects of Japan, Vol. 168, 1990, pp. 141-148.

Kijima, K., Tanaka, S., Furukawa, Y. and Hori, T. (1993)
On a Prediction Method of Ship Manoeuvring Characteristics, *Proceedings of MARSIM '93*, International Conference on Marine Simulation and Ship Manoeuvrability, St. John's, Canada, 1993, pp. 285-294.

Kose, K. (1982)
On a New Mathematical Model of Manoeuvring Motions of a Ship and Its Application, *International Shipbuilding Progress*, Vol. 29, No. 336, August 1982, pp. 205-220.

Kose, K., Yoshimora, Y. and Hamamoto, Y. (1986)
Mathematical Models and Model Tests for Predicting Manoeuvrability, *Bulletin of the Society of Naval Architects of Japan*, No. 668, February 1986.

Kose, K., Misiag, W.A. and Xiong, X. (1996)
Systematic approach for ship manoeuvrability prediction, *Proceedings of MARSIM '96*, International Conference on Marine Simulation and Ship Manoeuvrability, Balkema, Rotterdam, 1996, pp. 535-545.

Landsburg, C. Alexander et al. (1983)
Design and Verification for Adequate Ship Manoeuvrability, *The Society of Naval Architects and Marine Engineers*, No. 12, New York, 1983.

Li, D. Q. and Dyne, G. (1995)
Study of Propeller-Rudder Interaction Based on a Linear Method, *Int. Shipbuilding Progress*, Vol. 42, No. 431, 1995, pp. 235-258.

Mathematical Model Description (1993)
Documentation of the mathematical model used in the DEN-Mark1 manoeuvre model. (*Confidential*).

Michos, A., Bergeles, G. and Athanassiadis, N. (1983)
Aerodynamic Characteristics of NACA0012 Airfoil in Relation to Wind Generators, *Wind Engineering*, Vol. 7, No. 4, 1983.

Molland, A. F. and Turnock, S. R. (1991)
Windtunnel investigation of the influence of propeller loading on ship rudder performance. *Ship Science Report No. 46*, University of Southampton, March 1991.

Nonaka, Koji (1993)
Estimation of hydrodynamic forces acting on a ship in manoeuvring motion, *Proceedings of MARSIM '93*, International Conference on Marine Simulation and Ship Manoeuvrability, St. John's, Canada, 1993, pp. 437-446.

Ohmori, T. and Miyata, H. (1993)
Oblique Tow Simulation by a Finite-Volume Method, *Journal of The Society of Naval Architects of Japan*, Vol. 173, 1993, pp. 27-34.

Ohmori, T., Fujino, Masataka and Miyata, H. (1998)
A study on flow field around full ship forms in maneuvering motion, *Journal of Marine Science and Technology*, Vol. 3, No. 1, 1998, pp. 22-29.

Pope, A. and Harper, J. J. (1966)
Low-Speed Wind Tunnel Testing, John Wiley & Sons, Inc., New York, 1966.

Rizzetta, D. P. and Visbal, M. R. (1993)
Comparative Numerical Study of Two Turbulence Models for Airfoil Static and Dynamic Stall, *AIAA Journal*, Vol. 31, No. 4, April 1993, pp. 784-786.

Rohman, K. and Thieme, H. (1957)
Zur Wahl der Balancefläche von Rudern im Propellerstrahl, *Schiffstechnik*, No. 21, 1957.

Sanz, W. and Platzer, M. F. (1998)
Numerical investigation of the stall onset behavior of the GA(W)-1 airfoil, *Computers & Fluids*, Vol. 27, Nos. 5-6, 1998, pp. 681-687.

Sotiropoulos, F. and Patel, V.C. (1995)
Application of Reynolds-Stress Transport Models to Stern and Wake Flows, *Journal of Ship Research*, Vol. 39, No. 4, December 1995, pp. 263-283.

Shiotani, S. and Kodama, Y. (1998)
Numerical analysis on free surface waves and stern viscous flow of a ship model, *Journal of Marine Science and Technology*, Vol. 3, 1998, pp. 130-144.

Stern, F., Kim, H. T., Zhang, D. H., Toda, Y., Kerwin, J. and Jessup, S. (1994)
Computation of Viscous Flow Around Propeller-Body Configurations: Series 60 C_B = 60 Ship Model, *Journal of Ship Research*, Vol. 38, No. 2, June 1994, pp. 137-157.

Stern, F., Paterson, E.G. and Tahara, Y. (1996)
CFDSHIP-IOWA: Computational Fluid Dynamics Method for Surface-Ship Boundary Layer, Wakes and Wave Fields, *IIHR Report No. 381*, Iowa Institute of Hydraulic Research, College of Engineering, The University of Iowa, Iowa City, Iowa 52242 USA, 1996.

Stern, F., Wilson, R. V., Coleman, H. W. and Paterson, E.G. (1999)
Verification and validation of CFD simulations, *Proceedings of the 3rd ASME/JSME joint fluids engineering conference*, July 18-23, 1999, San Francisco, California.

Strøm-Tejsen, J. and Chislett, M. S. (1966)
A Model Testing Technique and Method of Analysis for the Prediction of Steering and Manoeuvring Qualities of Surface Vessels, Report No. Hy-7, Hydro- og Aerodynamisk Laboratorium, Lyngby, 1966.

Söding, H. (1982)
Prediction of Ship Steering Capabilities, *Shiffstechnik*, Bd. 29 - 1982, pp. 3-24.

Tahara, Y. and Himeno, Y.
Computation of Isotropic and Anisotropic Turbulent Flows around Tanker Forms, source unknown.

Tahara, Y. and Stern, F. (1996)
A Large-Domain Approach for Calculating Ship Boundary Layers and Wakes and Wave Fields for Nonzero Froude Number, *Journal of Computational Physics*, Vol. 127 No. 2, 1996, pp. 398-411.

Turnock, S. (1993)
Prediction of ship rudder-propeller interaction using a panel method, *19th WEGEMT School*. Numerical Simulation of Hydrodynamics: Ships and Offshore Structures. Propeller and Lifting Surfaces, Nantes, 1993.

Tzabiras, George D. (1997)
A Numerical Study of Additive Bulb Effects on the Resistance and Self-Propulsion Characteristics of a Full Ship Form, *Schiffstechnik* Bd. 44-1997/Ship Technology Research, Vol. 44, 1997, pp. 98-108.

White, Frank M. (1991)
Viscous Fluid Flow, Second Edition, McGraw-Hill International Editions, Mechanical Engineering Series, 1991.

Wilson, R., Paterson, E. and Stern, F. (1998)
Unsteady RANS CFD Methods for Naval Combatants in Waves, *Twenty-Second Symposium on Naval Hydrodynamics*, August 9-14, *Preprints*, Washington, D.C, 1998, pp. 198-213.

Wilcox, David C. (1994)
Turbulence Modeling for CFD, DCW Industries Inc. La Cañada, California, 1994.

Yasukawa, H., Yoshimura, Y. and Nakatatake, K. (1996)
Hydrodynamic forces on a ship with constant rudder angle: A thoretical treatment of rudder angle test, *Proceedings of MARSIM '96*, International Conference on Marine Simulation and Ship Manoeuvrability, Balkema, Rotterdam, 1996, pp. 435-447.

Zhang, D.H., Broberg, L., Larson, L. and Dyne, G. (1991)
A method for computing stern flows with an operating propeller, *Transactions, Royal Institution of Naval Architects*, Vol. 134, 1991, pp. 245-259.

Zou, Z. J. (1995)
Calculation of the Three-Dimensional Free-Surface Flow About a Yawed Ship in Shallow Water, *Schiffstechnik*, Vol. 42, 1995.

Zou, Z. J. and Söding, H. (1994)
A Panel Method for Lifting Potential Flows around Three-dimensional Surface-Piercing Bodies, *20th Symposium on Naval Hydrodynamics*, Santa Barbara, USA, 1994.

Appendix A

Ship and Model Data

A.1 Ship and Model Particulars

The Esso Osaka PMM: 278,000 DWT tanker			
		Ship	Model
Scale	-	1 : 1	1 : 43.4783
L_{PP}	m	325.00	7.475
L_{WL}	m	335.00	7.705
B_{mld}	m	53.00	1.219
T_m	m	21.79	0.501
S, incl. rudder	m^2	27671	14.638
∇	m^3	311609.8	3.791
Δ	ton	319400	3.791
C_b	-	0.805	0.805

Table (A.1) *Ship and model particulars for test condition.*

		Ship	Model
Scale	-	1 : 1	1 : 43.4783
Number of blades, Z	-	5	4
Diameter, D	m	9.100	0.2093
Pitch ratio, $P_{0.7} / D$	-	0.715	0.728
Area ratio, A_e / A_P	-	0.682	0.644

Table (A.2) *Propeller data for ship and model.*

		Ship	Model
Scale	-	1 : 1	1 : 43.4783
Rudder cord	m	9.00	0.207
Aspect ratio		1.54	1.54
Rudder area	m^2	124.65	0.066

Table (A.3) *Rudder data for ship and model.*

A.2 Body Plan

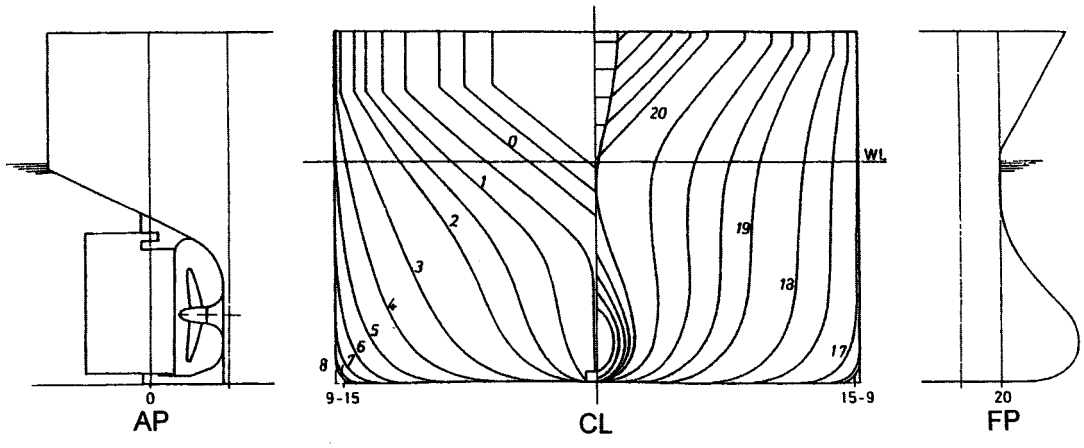

Figure (A.1) *Body plan of the Esso Osaka.*

Appendix B

PMM Test Program

In this appendix the PMM test program applied in connection with the Esso Osaka experiment at DMI is shown. Compared to a traditional test program this one is slightly extended since it involves a few runs with reversed propeller revolutions.

B.1 Static Test Program

U_C	U_C/U_0	Rudder angle, δ (deg.)	n/N_0
0.780	1.00	-35, -30, -20, -10, -5, 0, 5, 10, 20, 30, 35	1.0
0.624	0.80	-35, -30, -20, -10, -5, 0, 5, 10, 20, 30, 35	1.0
0.546	0.70	-35, -30, -20, -10, -5, 0, 5, 10, 20, 30, 35	1.0
0.468	0.60	-35, -30, -20, -10, -5, 0, 5, 10, 20, 30, 35	1.0
0.312	0.40	-35, -30, -20, -10, -5, 0, 5, 10, 20, 30, 35	1.0
0.000	0.00	-35, -30, -20, -10, -5, 0, 5, 10, 20, 30, 35	1.0
		Reversed propeller	
0.312	0.40	-35, -30, -20, -10, -5, 0, 5, 10, 20, 30, 35	-0.50

Table (B.1*) "Static rudder"*.

U_C	U_C/U_0	Drift angle, β (deg.)	n/N_0
0.780	1.00	-6, -4, -3, -2, -1, -0.5, 0, 0.5, 1, 2, 3, 4, 6	1.0
0.624	0.80	-10, -8, -6, -4, 0, 4, 6, 8, 10	1.0
0.546	0.70	-36,-30,-24, -20, -16, -10, -6, -4, 0, 4, 6, 10, 16, 20, 24, 30, 36	1.0

Table (B.2) *"Static drift"*

U_C	U_C/U_0	Drift angle, β (deg.)	n/N_0
0.468	0.60	-36, -30, -24, -18, -12, -6, 0, 6, 12, 18, 24, 30, 36	1.0
0.312	0.40	-36, -30, -24, -18, -12, -6, 0, 6, 12, 18, 24, 30, 36	1.0
		Reversed propeller	
0.312	0.40	-36, -30, -24, -18, -12, -6, 0, 6, 12, 18, 24, 30, 36	-0.5

Table (B.2) continued. *"Static drift"*.

U_C	U_C/U_0	β (deg.)	Rudder angle, δ (deg.)	n/N_0
0.312	0.40	36	-35, -30, -20, -10, -5, 0, 5, 10, 20, 30, 35	1.0
0.312	0.40	24	-35, -30, -20, -10, -5, 0, 5, 10, 20, 30, 35	1.0
0.312	0.40	12	-35, -30, -20, -10, -5, 0, 5, 10, 20, 30, 35	1.0
0.468	0.60	24	-35, -30, -20, -10, -5, 0, 5, 10, 20, 30, 35	1.0
0.468	0.60	16	-35, -30, -20, -10, -5, 0, 5, 10, 20, 30, 35	1.0
0.468	0.60	10	-35, -30, -20, -10, -5, 0, 5, 10, 20, 30, 35	1.0
0.780	1.00	6	-35, -30, -20, -10, -5, 0, 5, 10, 20, 30, 35	1.0
0.468	0.60	-10	-35, -30, -20, -10, -5, 0, 5, 10, 20, 30, 35	1.0
0.468	0.60	-16	-35, -30, -20, -10, -5, 0, 5, 10, 20, 30, 35	1.0
0.468	0.60	-24	-35, -30, -20, -10, -5, 0, 5, 10, 20, 30, 35	1.0
0.312	0.40	-12	-35, -30, -20, -10, -5, 0, 5, 10, 20, 30, 35	1.0
0.312	0.40	-24	-35, -30, -20, -10, -5, 0, 5, 10, 20, 30, 35	1.0
0.312	0.40	-36	-35, -30, -20, -10, -5, 0, 5, 10, 20, 30, 35	1.0
			Reversed propeller	
0.312	0.40	24	-35, -30, -20, -10, -5, 0, 5, 10, 20, 30, 35	-0.50
0.312	0.40	12	-35, -30, -20, -10, -5, 0, 5, 10, 20, 30, 35	-0.50
0.312	0.40	-12	-35, -30, -20, -10, -5, 0, 5, 10, 20, 30, 35	-0.50
0.312	0.40	-24	-35, -30, -20, -10, -5, 0, 5, 10, 20, 30, 35	-0.50

Table (B.3) *"Drift and rudder"*.

n/N_0	U_C	U_C/U_0
1.00	0.000, 0.078, 0.156, 0.234, 0.312, 0.546, 0.780	0.00, 0.10, 0.20, 0.30, 0.40, 0.70, 1.00
0.75	0.000, 0.078, 0.156, 0.234, 0.312, 0.546, 0.780	0.00, 0.10, 0.20, 0.30, 0.40, 0.70, 1.00
0.50	0.000, 0.078, 0.156, 0.234, 0.312, 0.546, 0.780	0.00, 0.10, 0.20, 0.30, 0.40, 0.70, 1.00
0.25	0.000, 0.078, 0.156, 0.234, 0.312, 0.546, 0.780	0.00, 0.10, 0.20, 0.30, 0.40, 0.70, 1.00
0.00	0.078, 0.156, 0.234, 0.312, 0.546, 0.780	0.10, 0.20, 0.30, 0.40, 0.70, 1.00
-0.25	0.000, 0.078, 0.156, 0.234, 0.312, 0.546, 0.780	0.00, 0.10, 0.20, 0.30, 0.40, 0.70, 1.00
-0.50	0.000, 0.078, 0.156, 0.234, 0.312, 0.546, 0.780	0.00, 0.10, 0.20, 0.30, 0.40, 0.70, 1.00
-0.75	0.000, 0.078, 0.156, 0.234, 0.312, 0.546, 0.780	0.00, 0.10, 0.20, 0.30, 0.40, 0.70, 1.00
-1.00	0.000, 0.078, 0.156, 0.234, 0.312, 0.546, 0.780	0.00, 0.10, 0.20, 0.30, 0.40, 0.70, 1.00

Table (B.4) *"Runs for estimation of effective wake fraction: $\delta=0°$ and $\beta=0°$"*.

B.2 Dynamic Test Program

N_{PMM} =1.5			
U_C	U_C/U_0	Sway-mm	β
0.780	1.0	86.7	2
0.780	1.0	173.6	4
0.546	0.7	244.3	8
0.546	0.7	306.5	10
0.312	0.4	284.8	16
0.312	0.4	361.5	20

Table (B.5) *"Pure sway"*.

N_{PMM} =1, 2, 3			
U_C	U_C/U_0	Sway-mm	β
0.0	0.0	100.0	90
0.0	0.0	200.0	90
0.0	0.0	300.0	90

Table (B.6) *"Space surge"*.

N_{PMM}=1, 2, 3			
U_C	U_C/U_0	Sway-mm	β
0.0	0.0	100.0	0
0.0	0.0	200.0	0
0.0	0.0	300.0	0

Table (B.7) *"Space sway"*.

N_{PMM}=1, 2, 3			
U_C	U_C/U_0	Yaw-mm	β
0.0	0.0	100.0	90
0.0	0.0	200.0	90
0.0	0.0	300.0	90
0.1[#]	0.0	300.0	90

Table (B.8) *"Space yaw"*.

N_{PMM}=2.0						
U_C	U_C/U_0	Sway-mm	Yaw-mm	r'	$\dot{r}'$	ψ
0.780	1.0	50	13.4	0.054	0.108	1.5
0.780	1.0	100	26.9	0.108	0.216	3.1
0.780	1.0	140	37.6	0.151	0.303	4.3
0.780	1.0	190	51.0	0.205	0.411	5.8
0.780	1.0	300	80.6	0.323	0.649	9.2
0.468	0.60	50	22.4	0.150	0.501	2.6
0.468	0.60	100	44.8	0.299	1.002	5.1
0.468	0.60	140	62.7	0.419	1.402	7.1
0.468	0.60	200	89.5	0.599	2.003	10.1
0.468	0.60	270	120.8	0.808	2.704	13.6
0.468	0.60	310	138.7	0.928	3.105	15.5

Table (B.9) *"Pure yaw"*.

U_C	U_C/U_0	Sway-mm	Yaw-mm	r'	$\dot{r}'$	ψ	N_{PMM}
Frequency dependence							
0.780	1.0	270	72.5	0.291	0.584	8.3	2.0
0.780	1.0	170	57.1	0.286	0.718	6.5	2.5
0.780	1.0	120	48.3	0.291	0.876	5.5	3.0
Speed dependence							
0.780	1.00	310	83.2	0.334	0.671	9.5	2.0
0.546	0.70	150	57.5	0.330	0.946	6.6	2.0
0.468	0.60	110	49.2	0.329	1.102	5.6	2.0

Table (B.10) *"Pure yaw", check for speed and frequency dependence.*

[#] A run where the model is yawing, while it is towed with the side to the flow direction, β=90.

N_{PMM}=2.0							
U_C	U_C/U_0	Sway mm	Yaw mm	r'	$\dot{r}'$	β	δ
0.468	0.60	50	22.4	0.150	0.501	2	-10,-20,-35
0.468	0.60	140	62.7	0.419	1.402	10	-10,-20,-35
0.468	0.60	310	138.7	0.928	3.105	24	-10,-20,-35
0.468	0.60	140	62.7	0.419	1.402	-10	10, 20, 35

Table (B.11) *"Yaw and drift and rudder"*.

N_{PMM}=2.0						
U_C	U_C/U_0	Sway-mm	Yaw-mm	r'	$\dot{r}'$	β
0.780	1.00	50	13.4	0.054	0.108	2, 6
0.780	1.00	140	37.6	0.151	0.303	2, 6
0.780	1.00	50	13.4	0.054	0.108	-2, -6
0.780	1.00	140	37.6	0.151	0.303	-2, -6
0.468	0.60	50	22.4	0.150	0.501	2, 6
0.468	0.60	100	44.8	0.299	1.002	6, 10
0.468	0.60	140	62.7	0.419	1.402	10, 16
0.468	0.60	200	89.5	0.599	2.003	16, 20
0.468	0.60	270	120.8	0.808	2.704	20, 24
0.468	0.60	310	138.7	0.928	3.105	20, 24
0.468	0.60	50	22.4	0.150	0.501	-2, -6
0.468	0.60	100	44.8	0.299	1.002	-6, -10
0.468	0.60	140	62.7	0.419	1.402	-10, -16
0.468	0.60	200	89.5	0.599	2.003	-16, -20
0.468	0.60	270	120.8	0.808	2.704	-20, -24
0.468	0.60	310	138.7	0.928	3.105	-20, -24

Table (B.12) *"Yaw and drift"*.

This page is intentionally left blank.

Appendix C

Open Water Test Program

C.1 Test Program

In order to provide an open water propeller diagram covering all four quadrants, the following open water test program was applied.

β^* (deg.)	Speed (m/s)	Rpm	Quadrant
Propeller orientation corresponding to forward-sailing ship			
0	0.00	391	I
10	0.52	385	I
20	1.03	367	I
30	1.50	339	I
40	1.93	300	I
50	2.30	251	I
60	2.60	196	I
70	2.82	134	I
80	2.95	68	I
90	3.00	0	I
110	2.82	-134	II
130	2.30	-251	II
150	1.50	-339	II
160	1.03	-367	II
170	0.52	-385	II
180	0.00	-391	II
Propeller orientation corresponding to astern-sailing ship			
-180	0.00	391	IV
-160	1.03	367	IV
-140	1.93	300	IV
-120	2.60	196	IV
-110	2.82	134	IV
-100	2.95	68	IV

Table (C.1) *Open water test program.*

β^* (deg.)	Speed (m/s)	Rpm	Quadrant
-90	3.00	0	IV
-80	2.95	-68	III
-60	2.60	-196	III
-40	1.93	-300	III
-20	1.03	-367	III
-10	0.52	-385	III

Table (C.1) continued. *Open water test program.*

Appendix D

Resistance Test Program

D.1 Test Program

For determination of the resistance and the form factor of the bare hull of the Esso Osaka, a resistance test was carried out in the towing tank at the Danish Maritime Institute. The case of U_{Ship}=7 knots was used for the comparison with the CFD calculation of bare hull flow, so the measurement in this condition was repeated several times to assess the precision error or random error in a later uncertainty analysis. This is not done in the present project. It should be noted that the test was carried out without propeller and rudder.

U_{Ship} (knots)	U_{Ship} (m/s)	U_{Model} (m/s)	*Fn*, based on L_{WL}
7	3.601	0.546	0.063
15	7.717	1.170	0.135
7	3.601	0.546	0.063
14	7.202	1.092	0.126
7	3.601	0.546	0.063
13	6.688	1.014	0.117
7	3.601	0.546	0.063
12	6.173	0.936	0.108
7	3.601	0.546	0.063
11	5.659	0.858	0.099
7	3.601	0.546	0.063
10	5.144	0.780	0.090
7	3.601	0.546	0.063
9	4.630	0.702	0.081
7	3.601	0.546	0.063
8	4.116	0.624	0.072
7	3.601	0.546	0.063
6	3.087	0.468	0.054

Table (D.1) *Test program.*

U_{Ship} (knots)	U_{Ship} (m/s)	U_{Model} (m/s)	Fn, based on L_{WL}
7	3.601	0.546	0.063
5	2.572	0.390	0.045
7	3.601	0.546	0.063
4	2.058	0.312	0.036

Table (D.1) continued. *Test program.*

Appendix E

Calculated Velocity Properties for Tanker Flow

E.1 Plots of Velocity Components

As an illustration of the calculated velocity field around the Esso Osaka at other *x*-stations than the one corresponding to the propeller plane, the axial velocity contours and the cross flow vectors were extracted for 12 additional *x*-positions, and the results were plotted in the present appendix. The results were calculated for a Froude number equal to *Fn*=0.063 and a model Reynolds number equal to *Re*=3.609 million.

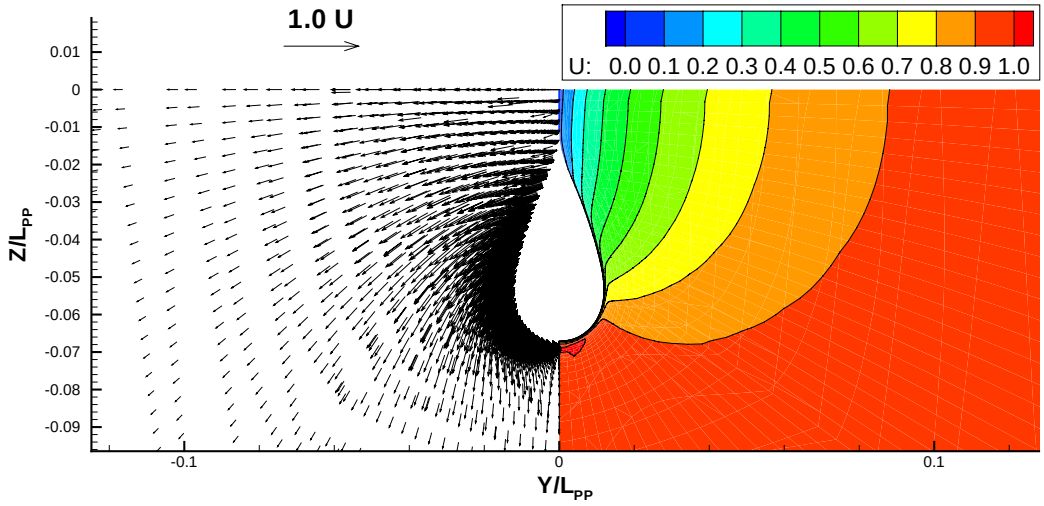

Figure (E.1) *X/L_{PP}=0.0. Left cross flow vectors and right axial velocity contours.*

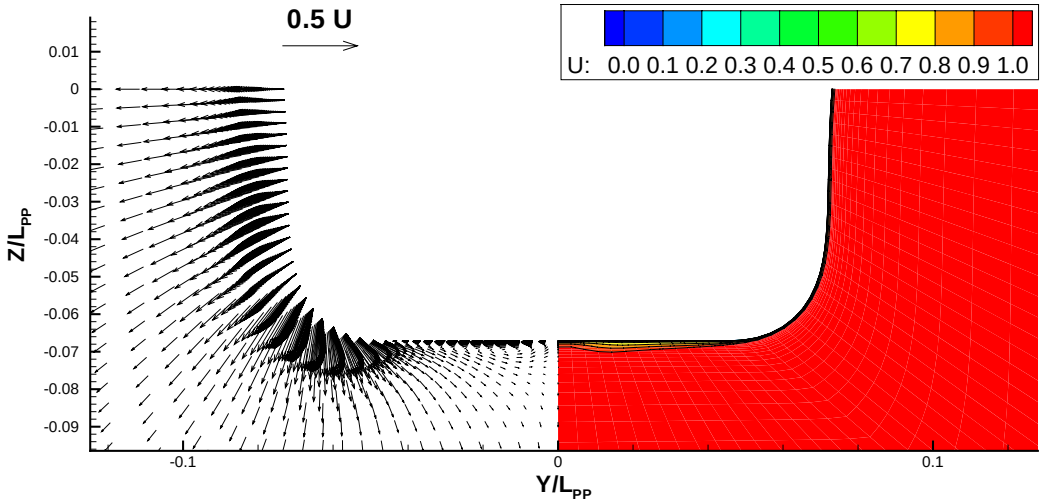

Figure (E.2) *X/L_{PP}=0.1. Left cross flow vectors and right axial velocity contours.*

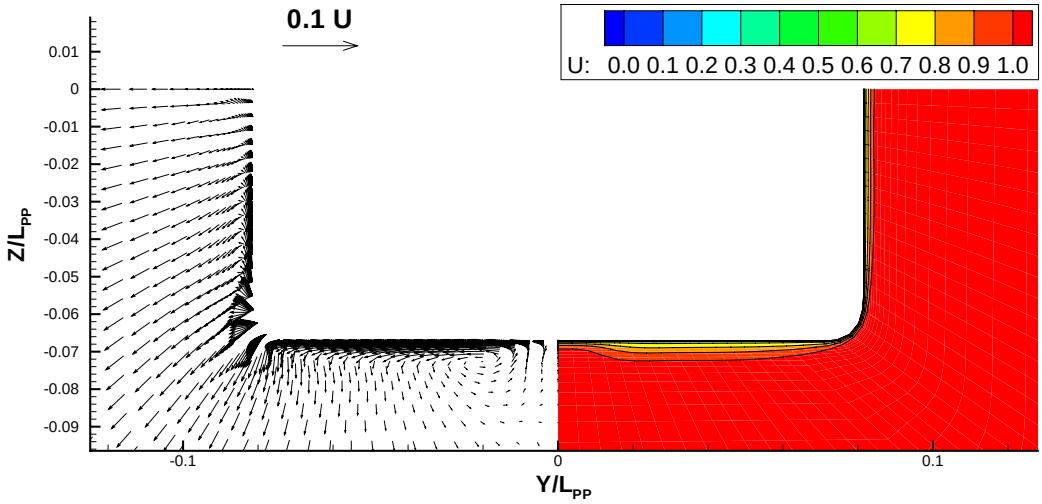

Figure (E.3) *X/L_{PP}=0.2. Left cross flow vectors and right axial velocity contours.*

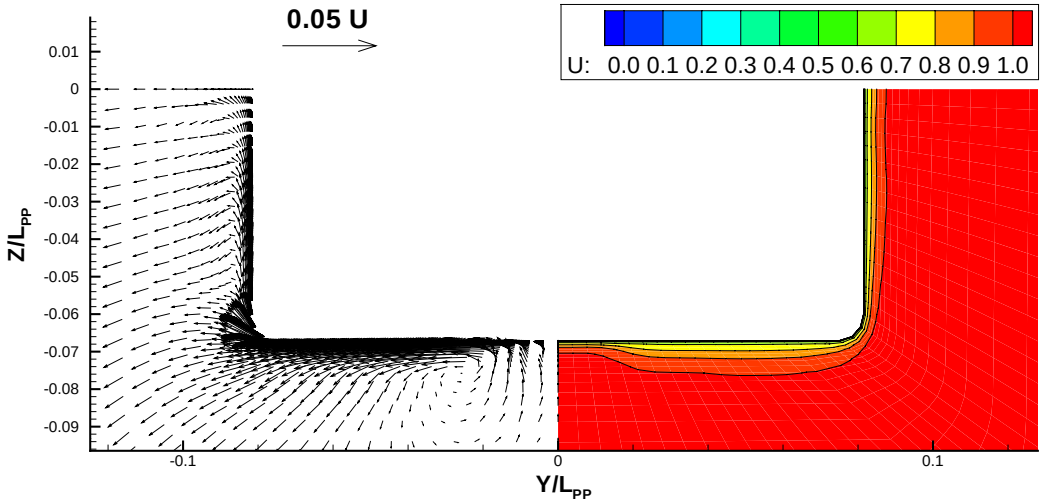

Figure (E.4) *X/L_{PP}=0.3. Left cross flow vectors and right axial velocity contours.*

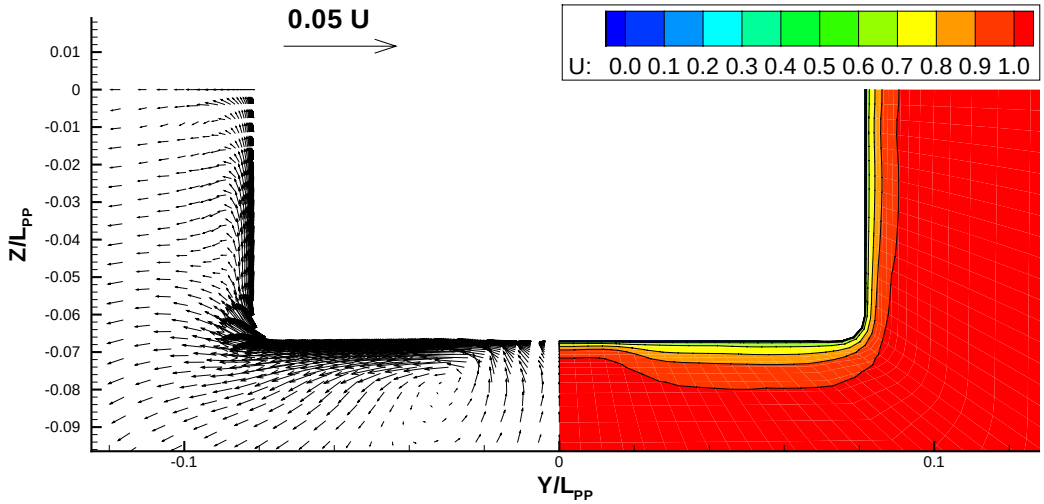

Figure (E.5) *X/L_{PP}=0.4. Left cross flow vectors and right axial velocity contours.*

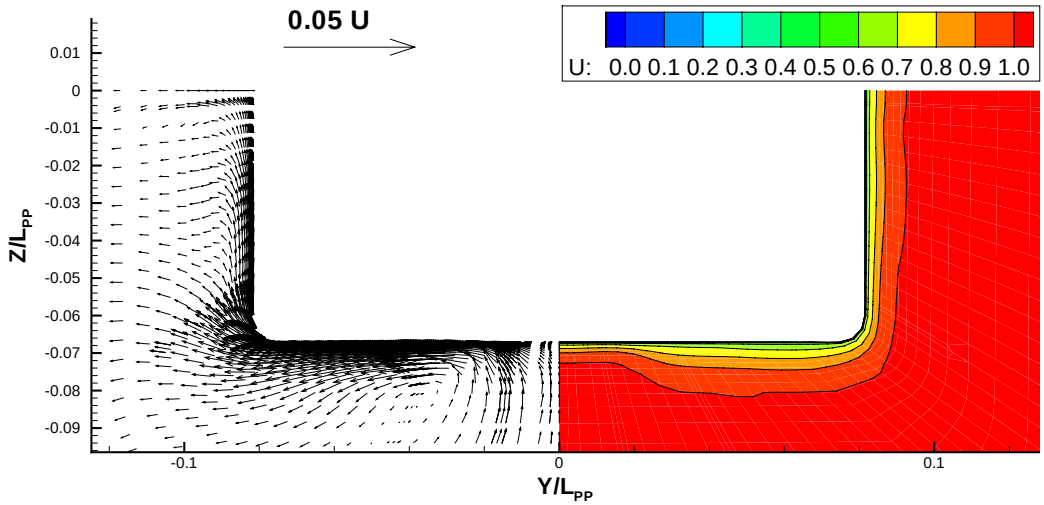

Figure (E.6) *X/L_{PP}=0.5. Left cross flow vectors and right axial velocity contours.*

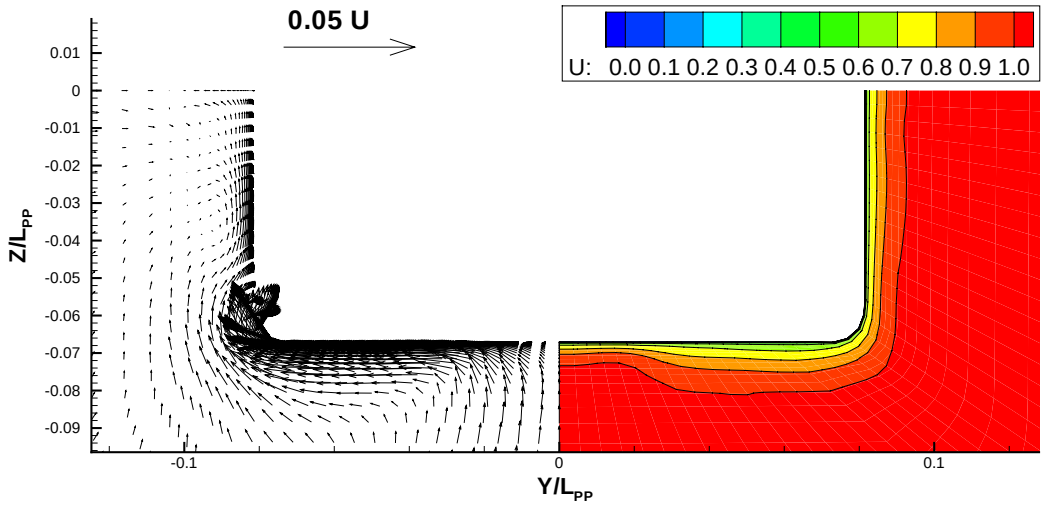

Figure (E.7) *X/L_{PP}=0.6. Left cross flow vectors and right axial velocity contours.*

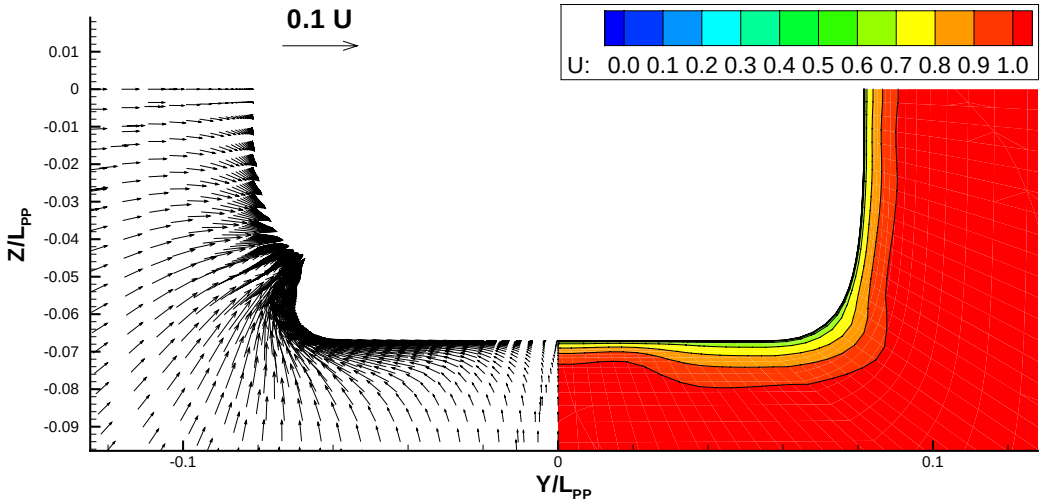

Figure (E.8) *X/L_{PP}=0.7. Left cross flow vectors and right axial velocity contours.*

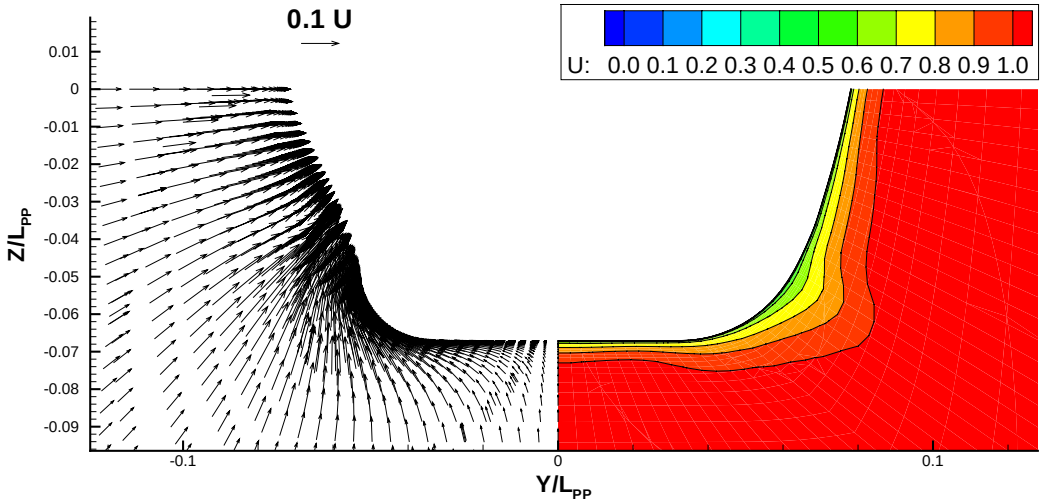

Figure (E.9) *X/L_{PP}=0.8. Left cross flow vectors and right axial velocity contours.*

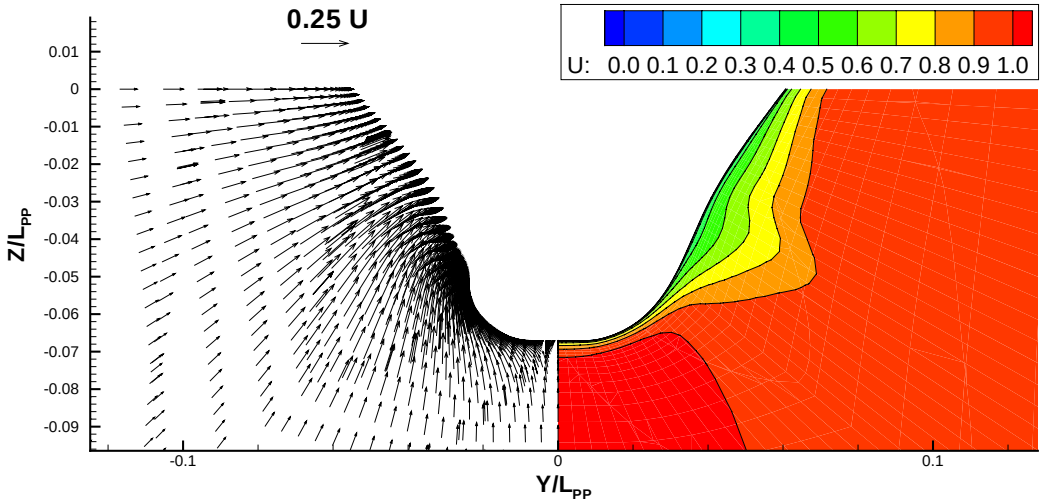

Figure (E.10) *X/L_{PP}=0.9. Left cross flow vectors and right axial velocity contours.*

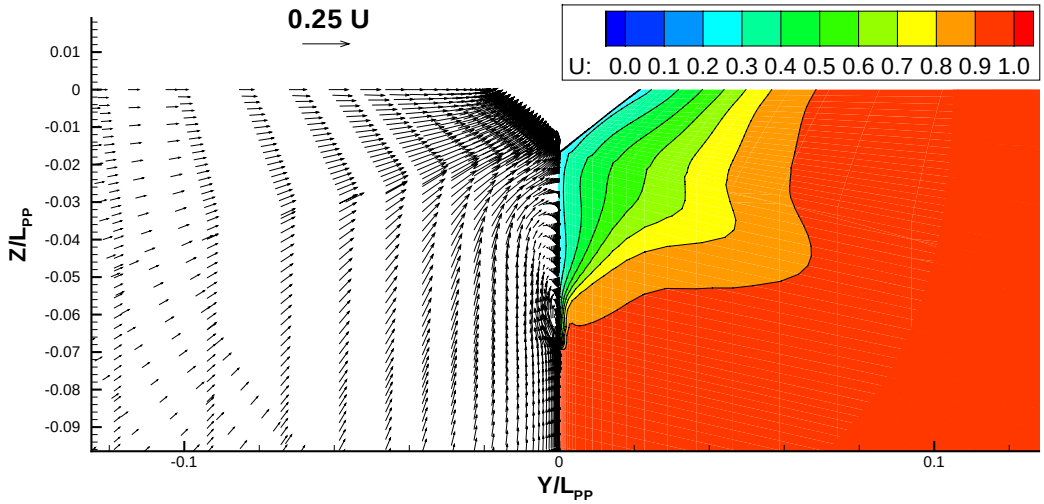

Figure (E.11) *X/L_{PP}=1.0. Left cross flow vectors and right axial velocity contours.*

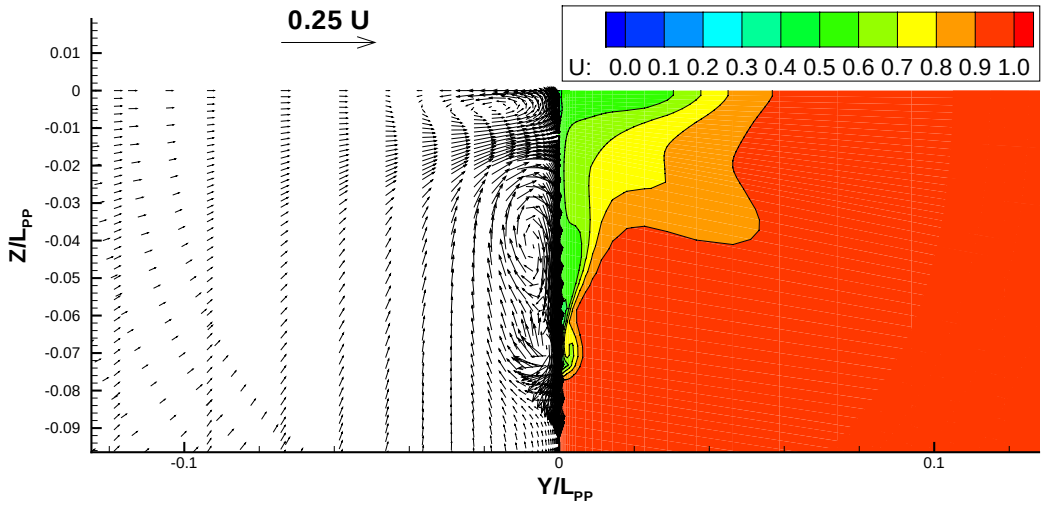

Figure (E.12) *X/L_{PP}=1.1. Left cross flow vectors and right axial velocity contours.*

This page is intentionally left blank.

PhD Theses
Department of Naval Architecture and Offshore Engineering
Technical University of Denmark · Kongens Lyngby

List of PhD Theses Available from the Department

1961 Strøm-Tejsen, J.
Damage Stability Calculations on the Computer DASK

1963 Silovic, V.
A Five Hole Spherical Pilot Tube for three Dimensional Wake Measurements

1964 Chomchuenchit, V.
Determination of the Weight Distribution of Ship Models

1965 Chislett, M.S.
A Planar Motion Mechanism

1965 Nicordhanon, P.
A Phase Changer in the HyA Planar Motion Mechanism and Calculation of Phase Angle

1966 Jensen, B.
Anvendelse af statistiske metoder til kontrol af forskellige eksisterende tilnærmelsesformler og udarbejdelse af nye til bestemmelse af skibes tonnage og stabilitet

1968 Aage, C.
Eksperimentel og beregningsmæssig bestemmelse af vindkræfter på skibe

1972 Prytz, K.
Datamatorienterede studier af planende bådes fremdrivningsforhold

1977 Hee, J.M.
Store sideportes indflydelse på langskibs styrke

1977 Madsen, N.F.
Vibrations in Ships

1978 Andersen, P.
Bølgeinducerede bevægelser og belastninger for skib på lægt vand

1978 Römeling, J.U.
Buling af afstivede pladepaneler

1978 Sørensen, H.H.
Sammenkobling af rotations-symmetriske og generelle tre-dimensionale konstruktioner i elementmetode-beregninger

1980 Fabian, O.
Elastic-Plastic Collapse of Long Tubes under Combined Bending and Pressure Load

1980 Petersen, M.J.
Ship Collisions

1981 Gong, J.
A Rational Approach to Automatic Design of Ship Sections

1982 Nielsen, K.
Bølgeenergimaskiner

1984 Nielsen, N.J.R.
Structural Optimization of Ship Structures

1984 Liebst, J.
Torsion of Container Ships

1985 Gjersøe-Fog, N.
Mathematical Definition of Ship Hull Surfaces using B-splines

1985 Jensen, P.S.
Stationære skibsbølger

1986 Nedergaard, H.
Collapse of Offshore Platforms

1986 Yan, J.-Q.
3-D Analysis of Pipelines during Laying

1987 Holt-Madsen, A.
A Quadratic Theory for the Fatigue Life Estimation of Offshore Structures

1989 Andersen, S.V.
Numerical Treatment of the Design-Analysis Problem of Ship Propellers using Vortex Lattice Methods

1989 Rasmussen, J.
Structural Design of Sandwich Structures

1990 Baatrup, J.
Structural Analysis of Marine Structures

1990 Wedel-Heinen, J.
Vibration Analysis of Imperfect Elements in Marine Structures

1991 Almlund, J.
Life Cycle Model for Offshore Installations for Use in Prospect Evaluation

1991 Back-Pedersen, A.
Analysis of Slender Marine Structures

1992 Bendiksen, E.
Hull Girder Collapse

1992 Petersen, J.B.
Non-Linear Strip Theories for Ship Response in Waves

1992 Schalck, S.
Ship Design Using B-spline Patches

1993 Kierkegaard, H.
Ship Collisions with Icebergs

1994 Pedersen, B.
A Free-Surface Analysis of a Two-Dimensional Moving Surface-Piercing Body

1994 Hansen, P.F.
Reliability Analysis of a Midship Section

1994 Michelsen, J.
A Free-Form Geometric Modelling Approach with Ship Design Applications

1995 Hansen, A.M.
Reliability Methods for the Longitudinal Strength of Ships

1995 Branner, K.
Capacity and Lifetime of Foam Core Sandwich Structures

1995 Schack, C.
Skrogudvikling af hurtiggående færger med henblik på sødygtighed og lav modstand

1997 Simonsen, B.C.
Mechanics of Ship Grounding

1997 Olesen, N.A.
Turbulent Flow past Ship Hulls

1997 Riber, H.J.
Response Analysis of Dynamically Loaded Composite Panels

1998 Andersen, M.R.
Fatigue Crack Initiation and Growth in Ship Structures

1998 Nielsen, L.P.
Structural Capacity of the Hull Girder

1999 Zhang, S.
The Mechanics of Ship Collisions

1999 Birk-Sørensen, M.
Simulation of Welding Distorsions of Ship Sections

1999 Jensen, K.
Analysis and Documentation of Ancient Ships

2000 Wang, Z.
Hydroelastic Analysis of High Speed Ships

2000 Petersen, T.
Wave Load Prediction - a Design Tool

2000 Banke, L.
Flexible Pipe End Fitting

2000 Simonsen, C.D.
Rudder, Propeller and Hull Interaction by RANS

DEPARTMENT OF NAVAL ARCHITECTURE AND OFFSHORE ENGINEERING
TECHNICAL UNIVERSITY OF DENMARK
BUILDING 101E
DK-2800 LYNGBY
DENMARK
PHONE +45 4525 1360
TELEFAX +45 4588 4325
EMAIL ish@ish.dtu.dk
INTERNET http://www.ish.dtu.dk

ISBN 87-89502-27-2